

APPENDIX A

2014-02-13 KME512 / PR.263.1.49

Department: Chemistry and Materials Technology

Author: Annika Stålenheim

Security class: Internal [S2]

Attention: KME 512 project group

ADDED AMOUNT OF ADDITIVE - BACKGROUND

The amounts of additives to be used in the tests at SP were decided based on available information from the literature on previous tests with the additives and the expected mechanisms for the corrosion inhibiting effect of the additives. The reasoning behind this for the different additives is presented below.

1 SEWAGE SLUDGE

Sewage sludge addition has been shown to reduce bed agglomeration, deposit formation, and superheater corrosion in fluidised bed boilers, through tests in the Chalmers research CFB and in the E.ON waste-fired boiler P14 at the Händelö plant in Norrköping, Sweden. [1], [2]

The mechanism behind the positive effects is not yet fully clarified, but in [1] it is suggested to be the conversion of alkali chlorides to alkali sulphates and alkali phosphates. Based on this theory, threshold limits have been suggested for some ratios that should be achieved to achieve an alkali chloride content below 10 ppm in the flue gases and a low chlorine content in the deposits and thus a reduced risk for superheater corrosion.

If it is assumed that a reduction in waterwall corrosion will be achieved by the same mechanism, i.e. conversion of alkali chlorides to alkali sulphates and alkali phosphates, the ratios suggested in [1] should be useful also for estimating the effect of adding sewage sludge for this purpose as well. However, since the conditions at the waterwalls is very different from those around the superheaters and since many reactions take place later in the flue gas path one cannot assume that the effect of sewage sludge addition will be the same in the two positions. (Sulphation probably to a large extent probably takes place after the flue gases have passed the waterwalls. Flue gas temperature and composition in the two regions as well as the temperatures of waterwalls and superheater surfaces differ very much.)

It is also possible that the addition of sewage sludge could be beneficial through other mechanisms, such as alkali metal or heavy metal adsorption by clay minerals (e.g. alumino silicates) in the sludge.

Calculation of the ratios from [1] using the compositions of the fuel and the sludge that are used in this project leads to unrealistically large amounts of sludge to be

VATTENFALL RESEARCH AND DEVELOPMENT AB

ADDRESS TELEPHONE SE-814 26 Älvkarleby, Sweden +46 26 835 00

ONE VAT NUMBER 35 00 SE556390-5891

VISITING ADDRESS Älvkarleby Laboratory TELEFAX +46 26 836 70 SE336390-369

added. Instead it is suggested to use realistic amounts that could be added in a boiler and that also probably will be used at the Idbäcken plant. At Idbäcken additions of 4-5% were planned and it was decided to use 4% in the tests at SP as well. In the second set of tests at SP this amount was doubled.

Figure 1 Calculated ratios for mixtures of sewage sludge and waste wood fuel according to [1]

Ratio	(2S+3P)/alkali	(2S+3P)/CI	Ca/(S+1,5P)	S/CI
Limit	>6	>15	<1	>4
Waste wood	0,6	1,9	4,1	0,7
100% sludge	30,6	297	0,33	32
4% sludge	1,5	5,1	1,7	1,1
8% sludge	2,5	8,5	1,2	1,5
12% sludge	3,5	12,0	0,9	1,9
16% sludge	4,5	15,9	0,8	2,4
22% sludge	6,0	22,1	0,6	3,1
29% sludge	7,8	30,3	0,5	4,0

2 KAOLIN

A stoichiometric value for kaolin has been calculated with 2 mol (K, Na) corresponding to 1 mol kaolin, resulting in the amount 21 g/kg ds fuel. However, considering such things as equilibrium and kinetics as well as not perfect mixing, a higher amount is needed. It was decided to use 30 g/kg ds fuel.

3 LIME

Lime is probably not a good additive to reduce waterwall corrosion. It will probably not reduce the content of alkali chlorides in the flue gases to any larger extent, possibly even increasing it. It might however adsorb heavy metals. The other additives to be used in the project, sulphur, kaolin, foundry sand, sewage sludge are all expected to bind or convert alkali chlorides.

Using lime in one test could lead to a better understanding of reactions/mechanisms that influence waterwall corrosion and the mechanisms for the other additives.

Since it is not known if and how lime will influence waterwall corrosion it is suggested to use the same amount as for kaolin, 30 g/kg ds fuel.

4 FOUNDRY SAND

Foundry sand is used to make forms for metal casting, and contains quartz or feldspar sand grains covered with bentonite clay. Foundry sand can also contain organic additives and kaolin. Its composition may vary considerably depending on sand used (quartz, feldspar, olivine), clay mineral (bentonite, kaolin) and the metal used in the casting process.

Sand from iron casting usually contains 3-9% bentonite and is usually made from Baskarp sand.

Bentonite is a geological term for soil materials with a high content of a swelling mineral, which usually is montmorillonite. High-quality commercial bentonites normally contain over 80% of montmorillonite. However, the other minerals in bentonite may vary substantially within, and especially between, different quarries.

Montmorillonite is hydrated sodium calcium aluminium magnesium silicate hydroxide (Na,Ca)0.33(Al,Mg)2(Si4O10)(OH)2·nH2O.

Potassium, iron, and other cations are common substitutes, the exact ratio of cations varies with source.

The foundry sand used in this project is sand from iron casting (Volvo). It is a finer fraction with a higher content of bentonite than the main part of the foundry sand available. Its main constituent is Baskarp sand and it contains 17,4% active bentonite and 11,7% C.

Foundry sand could probably be used as bed material without previous sieving.

The largest addition of foundry sand to the boiler is probably achieved if it is used as bed sand and the upper limit for the amount of foundry sand to be used should then be set by the exchange rate of bed sand. The exchange rate at the Jordbro boiler is 2% and this is considered an extremely high rate. The exchange rate at Idbäcken is 0.6%.

It is suggested to add a slightly higher amount than what could be used in a real boiler, 3% or 30 g/kg ds fuel. This is to maximise the chances of seeing an effect on the waterwall corrosion, but still not too far from a realistic value.

5 SULPHUR

Sulphur is used as a reference additive since it has been used in many boilers for other purposes, such as reduction of superheater corrosion and CO reduction.

Since sulphation of alkali chlorides to a large extent occurs later in the boiler, it is possible that the influence on waterwall corrosion is small. The ratios for determining the appropriate amount of sulphur to be added for superheater reduction is also of limited value to use for the purpose of determining the amount to be used to reduce waterwall corrosion. However, these ratios have still been calculated to give an idea of what would be a reasonable amount to add. If too much sulphur is added there will be problems with e.g. emissions and low temperature corrosion.

It is suggested to add a fairly high amount of sulphur, 10 g/kg ds fuel, to maximise the chances of seeing an effect on the waterwall corrosion, but still not too far from a value that would be realistic in a real boiler.

Figure 2 Calculated ratios for mixtures of sulphur and waste wood fuel according to [1]

Ratio	(2S+3P)/alkali	(2S+3P)/CI	Ca/(S+1,5P)	S/CI
Limit	>6	>15	<1	>4
Waste wood	0,6	1,9	4,1	0,7
5 g S / kg fuel	2,5	8	1,0	3,8
6 g S / kg fuel	2,9	9	0,9	4,4
11 g S / kg fuel	4,8	15,4		
15 g S / kg fuel	6,3			

6 REFERENCES

- [1] Herstad Svärd S, Åmand L-E, Bowalli J, Öhlin J, Steenari B-M, Pettersson J, Svensson J-E, Karlsson S, Larsson E, Johansson L-G, Davidsson K, Bäfver L, Almark M, Ramprogram Åtgärder för samtidig minimering av alkalirelaterade driftproblem, Etapp 3, Värmeforsk report no 1167, January 2011
- [2] Pettersson J, Svensson J-E, Skog E, Johansson L-G, Folkeson N, Froitzheim J, Karlsson S, Larsson E, Israelsson, N, Enestam S, Tuiremo J, Jonasson A, Arnesson B, Andersson B-Å, Heikne B, Evaluation of different fuel additives´ ability to master corrosion and deposition on steam superheaters in a waste fired CFB-boiler, KME 411, Konsortiet Materialteknik för termiska Energiprocesser, 2010



Owner	Changed by	Latest change		
Michal Glazer		Thursday, 13 February 2014	Page 1 (25)	
Subject		Project	Project No	
HSC MODELLING RESULTS FOR KME – 512 PROJECT		KME 512		PR.620.4.3

Distribution List:	Receiver:
Stålenheim Annika (ER-RC); Gårdman Lennart (ER-RC)	

HSC MODELLING RESULTS FOR KME – 512 PROJECT

SUMMARY:

In the frame of the KME-512 project chemical equilibrium calculations have been performed. The calculations have been done using the HSC modelling software. The goal was to validate assumptions regarding the impact of the tested additives on the deposit chemistry at different conditions (e.g. additive selection, different Cl concentrations, etc). As the initial step in order to fine tune the HSC Chemistry software comparison with the calculations done by Åbo Akademi (ÅA) within the KME-512 project has been performed.

The KME-512 project focused on different fuel additives in order to prevent/decrease problems related to corrosion and deposit formation, especially waterwall corrosion. During the project, sewage sludge has been selected as additive and extensively tested experimentally. This additive has been also simulated using the HSC equilibrium software. In order to simulate the system and learn more about the basic, fundamental reactions responsible for the equilibrium, the sludge composition has been added to the system. The substantial increase of Ca and P, coming from sludge, was responsible to move the equilibrium towards more Ca/P based components.

In order to test varying CI concentrations and check applicability of the HSC software, additional calculations with three different CI concentrations have been performed. Two times more, four times more of chlorine and ten times less of chlorine in the system were simulated. For the KME-512 the case with four times more chlorine and the sludge added (high case 80 g of sludge / kg of fuel) were tested. The results of the chemical equilibrium describe the interactions between the components, reveal no substantial change for alkali chlorides and indicate that phosphates start to play more important role in the system where sludge has been added. The results are discussed in details.

TABLE OF CONTENTS

1	BASIC INFORMATION	4
1.1	Overall goals (frame) of the KME-512	4
2	GOALS AND METHODOLOGY	5
2.1	Goals for the thermodynamic equilibrium calculations	5
2.2	Objectives	
2.3	Methodology	5
Resu	ılts	7
2.4	Fuel composition and calculation cases	7
4.	Adding sludge to the system	8
2.5	40 g of sludge / kg of fuel – results	
2.6	80 g of sludge / kg of fuel – results	9
3	Varying the chlorine content of the system	10
3.1	Chlorine content x 2 – results	
3.2	Chlorine content x 4	
3.3	Chlorine content x 0.1	
3.4	Chlorine content x 4 + sludge 80 g sludge / kg fuel	12
4	Discussion and conclusions	
4.1	Comparing the experimental findings - deposits analysis by SP	
4.2	Discussion on chemical equilibrium modelling	
4.3	Chemical equilibrium calculations – applicability and limitations	
4.4	Conclusions	
5	References:	19
6	Appendix 1 – Fine tuning between HSC and FactSage	20
6.1	ÅA pellets at lambda 1.2	
6.2	Sulphur addition in steps – influence on the system	
6.3	Summary	25

1 BASIC INFORMATION

The vision for the KME programme is to improve the electrical and total efficiency by material technology development when utilizing climate neutral fuels in thermal energy conversion processes. The long-term vision includes research for erection of a new full-scale demonstration CHP plant in 2017-2018, fired with renewable bio fuels and refuse fractions, with at least 3-4 % points higher electrical efficiency than commercial plants built today.

Wide fuel mixes are of interest for many energy companies due to increasing prices and reduced availability of clean biomass. However, wide fuel mixes (including e.g. waste wood) contain components causing corrosion in the furnace and convective superheaters. Especially wall corrosion is a problem in plants that operate today at conventional / commercial steam data levels. Therefore, to be able to increase the steam data level in a demonstration plant, it must be shown that the corrosion can be limited to levels that allow cost-effective operation of the plant.

The KME projects (KME-508, KME-512) evaluated, based on laboratory-scale combustion tests, corrosion and deposit building propensity, the effectiveness of bed/fuel additives as a means to reduce furnace wall corrosion during combustion of a wide fuel mix/waste wood in CHPs. The results will add to the basis of information needed to compare different alternative measures to reduce furnace wall corrosion on a cost/benefit basis.

1.1 Overall goals (frame) of the KME-512

The project identified and then evaluated the use of additives and fuel blends to reduce furnace wall, and possibly also superheater, corrosion for wide biomass fuel mixes including waste wood. The project will give a recommendation if the identified additives are a viable way to reduce corrosion and, in that case, recommend some promising additive candidates for further evaluation. The project will evaluate the use of thermodynamic equilibrium calculations for predicting the chemical composition of the deposits formed at different temperatures, with different additives and under different combustion conditions.

2 GOALS AND METHODOLOGY

2.1 Goals for the thermodynamic equilibrium calculations

Thermodynamic equilibrium calculations have been performed, using the chemical composition of the fuel and additives in order to check ability of the software to predict/simulate the system from the chemical point of view.

Two different calculation tools have been evaluated and compared. Åbo Akademi has used FactSage and. Vattenfall has used HSC Chemistry.

2.2 Objectives

The objective was to simulate the wood pellets based system with addition of sludge in order to compare the simulation results with the experimentally collected data and to test the effectiveness of sludge as a means to reduce furnace wall corrosion during combustion. The response of the system to the sludge addition, different sulphur and chlorine concentrations were under the investigation.

2.3 Methodology

HSC Chemistry software has been used to perform the calculations. HSC Chemistry offers powerful calculation methods for studying the effects of different variables on the chemical system at equilibrium. The software calculates the defined state at equilibrium for gas/liquid/solid compounds. As a first step in order to collect experience with the software and fine tune the system response the simulation results for different conditions were compared with the results of the Åbo Akademi and done with FactSage software.

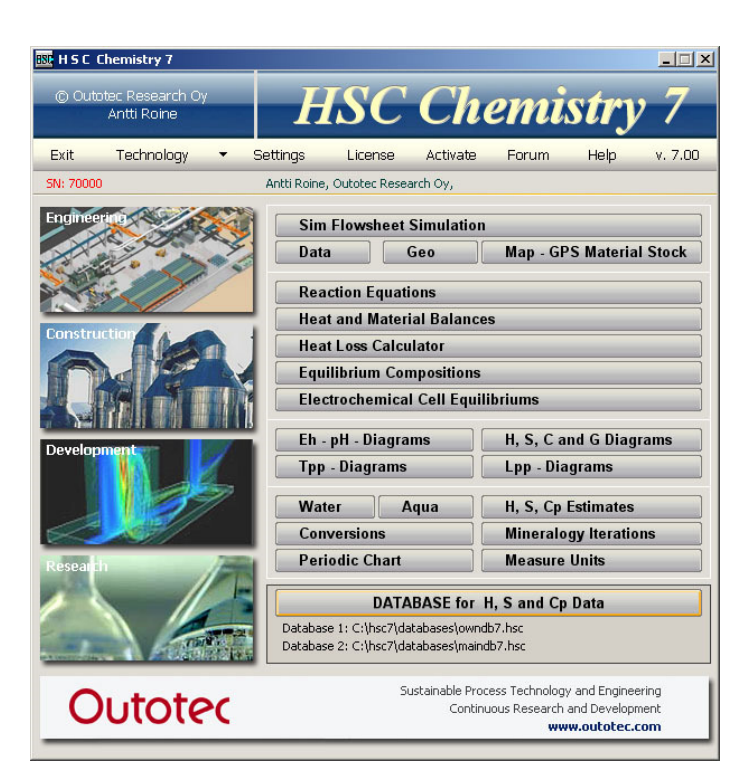


Figure 1 – HSC Chemistry 7

An overview of the all simulated cases is presented in Table 1 $\,$

	Simulated case	Lambda	Purpose
1	ÅA-Pellets with Al, Si, Fe	1.2	Fine tunning HSC
2	ÅA-Pellets without Al, Si, Fe	1.2	Fine tunning HSC
3	Sulphur added in steps - no saturation reached	1.2	Fine tunning HSC
4	Sulphur added in steps - saturation reached	1.2	Fine tunning HSC
5	40 g of sludge / kg of fuel	1.2	Sludge as additive
6	80 g of sludge / kg of fuel	1.2	Sludge as additive
7	Clx2	1.2	Varying chlorine content
8	Clx4	1.2	Varying chlorine content
9	Clx0.1	1.2	Varying chlorine content
10	80 g of sludge / kg of fuel + Clx4	1.2	High chlorine + sludge

Table 1 – Overview of the all simulated cases

RESULTS

2.4 Fuel composition and calculation cases

The equilibrium system has been calculated with the fuel composition provided by Åbo Akademi (Figure 2). The main focus was on the ÅA-Pellets sample (the red circle) and this composition has been used for all calculations. Additionally, the sewage sludge composition was used (the grey circle)

Ash, w-% 9.6 8.6 33.8 S 1 430 1 000 12 670 CI 1 860 2 600 740 Ca 6 450 (8 630) 7 140 22 870	fuel on dry basis)		fuel on dry	Pellets, ÅA-sample (Spring 2012)	SP Test Pellets (data from SP presentation 2013-02-21)		Sewage sludge			
CI 1 860 2 600 740	Ash, w-%	A		Ash, w-%	9.6		8.6		33.8	
	S	S	1 430		1 000		12 670			
Ca 6 450 (8 630) 7 140 22 870	CI	Cl	1 860		2 600		740			
	Ca	Ca	6 450 (8 630)	7 140			22 870			
K 1 590 1 630 3 540	К			K	1 590		1 630		3 540	
<u>Na</u> 1 950 2 150 1 880	<u>Na</u>			<u>Na</u>	1 950		2 150		1 880	
P 189 232 26 660	Р			Р	189		232		26 660	
Pb, Zn, Cu 376, 212, 1 050 361, 602, 43 11.8, 451, 254	Pb, Zn, Cu		Pb, Zn, Cu	376, 212, 1 050		361, 602, 4	3	11.8, 451, 254		

Figure 2 – Fuel composition used in calculations

4. Adding sludge to the system

The composition of the sludge presented in Figure 2 has been used. It can be seen that the sludge has much higher content of sulphur, calcium and phosphorus than the ÅA-pellets. Especially the sulphur is expected to act as sulphating agent for corrosive alkali metals based compounds when sludge is added as additive to the combustion process. In order to test this approach and see if there is influence of sulphur on the whole system together with side effect of Ca and P, addition the sludge has been simulated with the HSC chemistry software. Two different amounts of sludge have been added to the system, 40 g of sludge/kg of fuel and 80 g of sludge /kg of fuel. The whole temperature range between 300°C and 1300°C has been shown in order to show and track the changes between components predicted by the chemical equilibrium. One can observe that (figure 3) at 300°C the alkali metals are at equilibrium in solid form. It has to be stressed that the system presented at the underlying figures does not always represent the reality in the boiler but indicate the chemically stable compounds at the certain temperature range. The actual release of the alkali metals may follow other paths and depends on heating rates, combustion technology and is discussed in chapter 6.

2.5 40 g of sludge / kg of fuel – results

It can be seen (Figure 3) that sludge addition causes some shifts in the global equilibrium of the system comparing to the base case scenario (Figure A2), especially in Ca and P chemistry. One can observe that calcium and phosphorus are much more present (Figure 3 – red circle). From other side there is little effect on alkali system and related sulphating type of reactions.

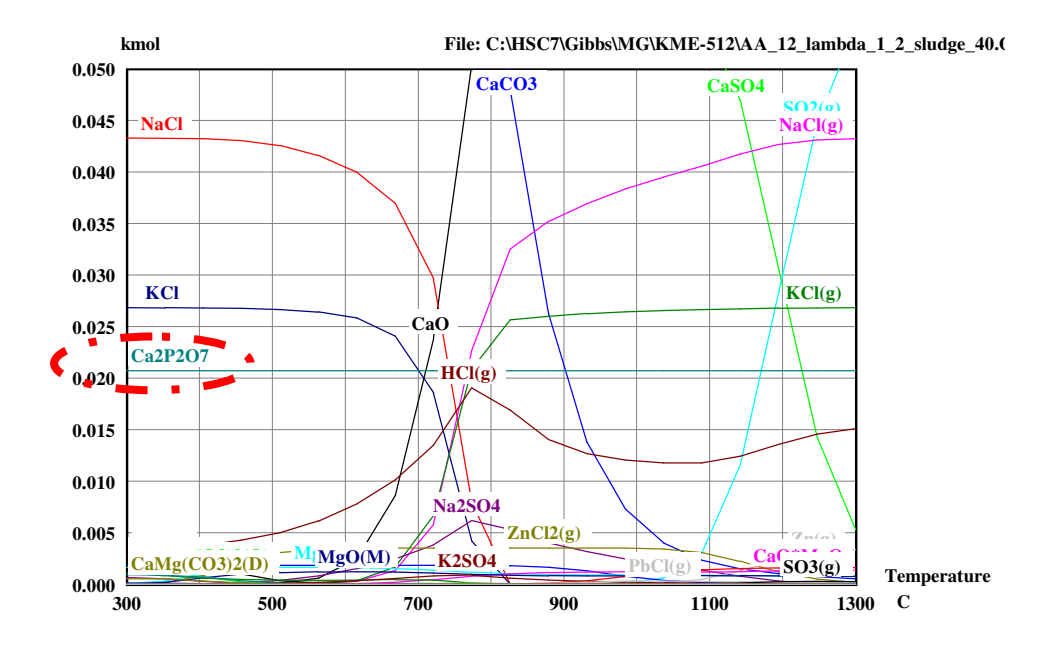


Figure 3 – The equilibrium system for the fuel ÅA-pellets. 40 g of sludge / kg of fuel added to the system, some shift towards formation of Ca/P compounds visible (red circle)

2.6 80 g of sludge / kg of fuel – results

As the next step the double amount of sludge has been used, namely 80 g of sludge per kg of fuel has been added. It means even more Ca, P and S present in the system. It can be seen (Figure 4) that sludge addition causes some shifts in the global equilibrium of the system especially in Ca and P chemistry comparing to the base case scenario (Figure 3) and the shift is stronger than in the 40 g/kg case. Twice as much of $Ca_2P_2O_7$ is present in the system according to the equilibrium software. There is little effect on alkali system and related sulphating type of reactions.

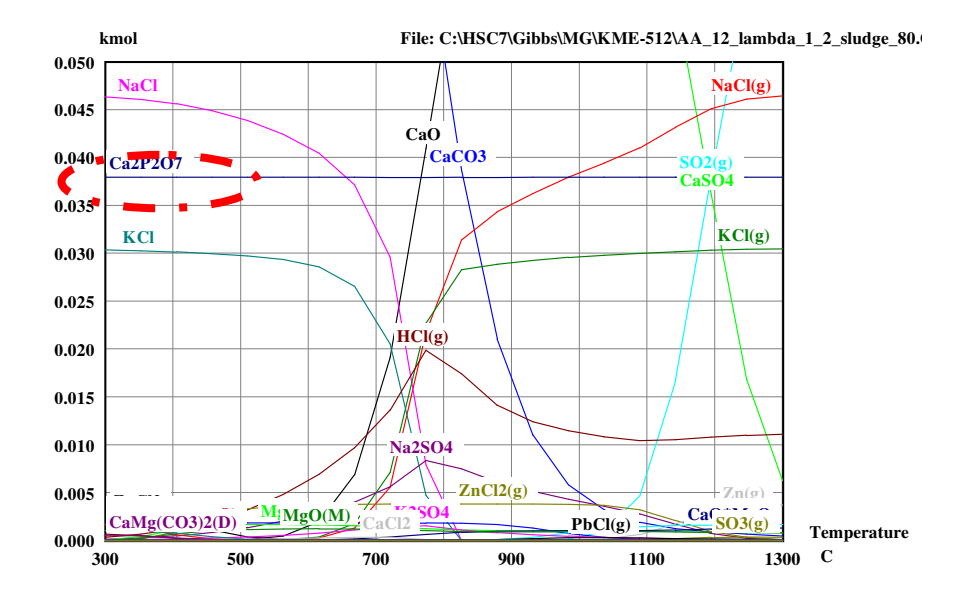


Figure 4 – The equilibrium system for the fuel ÅA-pellets. 80 g of sludge / kg of fuel added to the system, some shift towards formation of Ca/P compounds visible (red circle)

3 VARYING THE CHLORINE CONTENT OF THE SYSTEM

In order to test the system sensitivity to the chlorine content the chlorine content in the fuel has been changed (calculated S/Cl ratio – see Table 2). The equilibrium conditions have been calculated for:

- chlorine content x 2
- chlorine content x 4
- chlorine content x 0.1

Additionally to that for the case where 4 times more of chlorine was present in the system also 80 g of sludge composition has been added and calculated.

Table 2: The sulphur to chlorine ratio for the simulated cases

Ratio		Comments
2S/CI=	3.01	base case
2S/CI=	1.51	Clx2
2S/CI=	0.75	Clx4
2S/CI=	30.11	Clx0.1

3.1 Chlorine content x 2 – results

It can be seen (Figure 5) that the increased chlorine content causes an increased HCl presence comparing to the base system presented in Figure 3. The amount of KCl is at the same level comparing to the base case (Figure A2 - Appendix). It means that no more potassium is available or the reaction to form HCl is preferable.

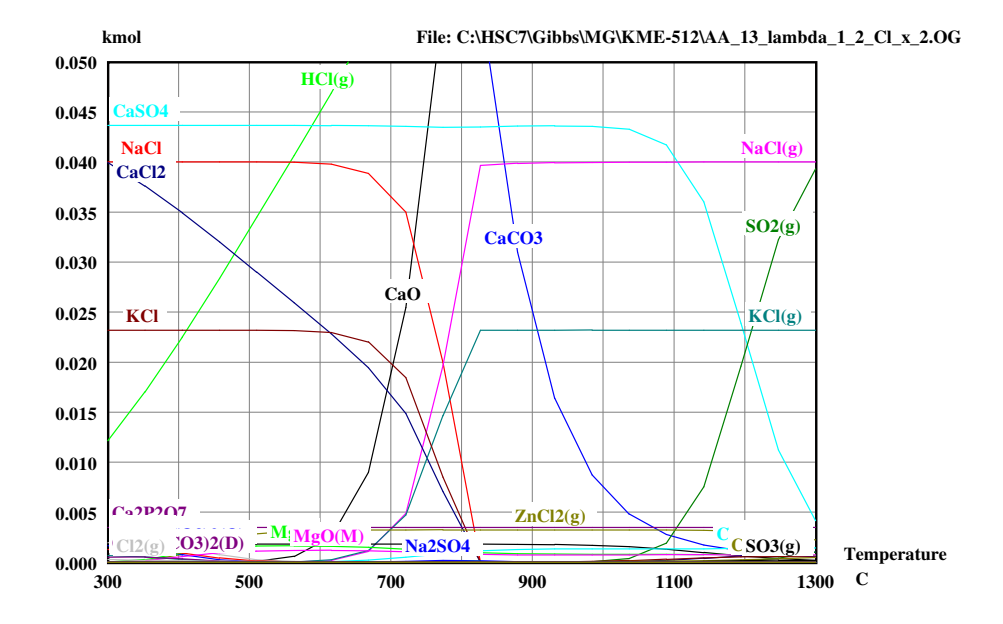


Figure 5 – ÅA-pellets with chlorine content x 2

3.2 Chlorine content x 4

It can be seen (Figure 6) that the increased CI content caused even more radical increased of HCI presence comparing to the base case system presented in Figure A2 (Appendix).

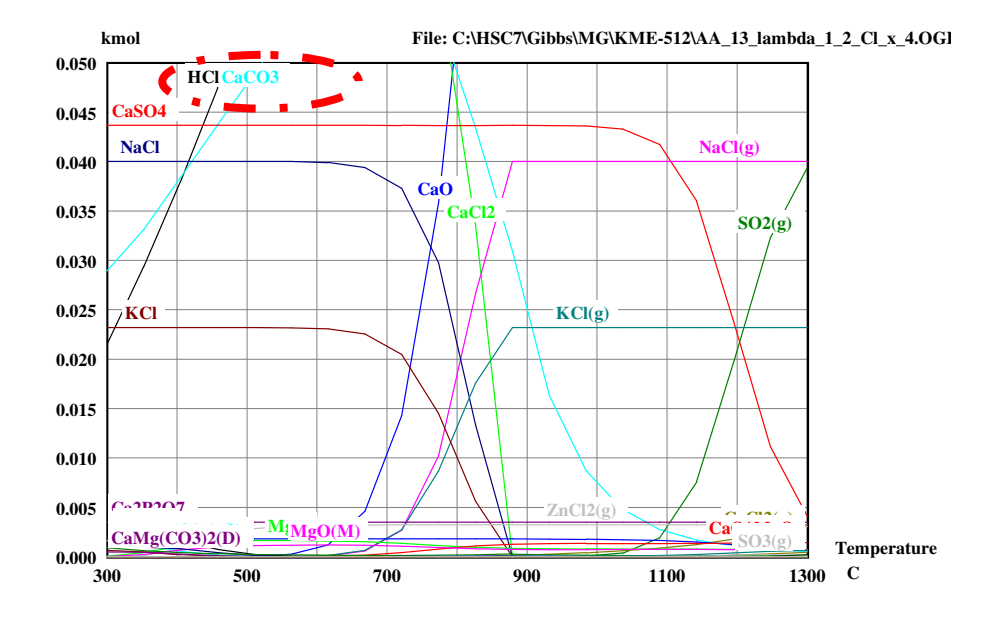


Figure 6 – AA-pellets with chlorine content x 4

The HSC software predicts that at equilibrium the additional chlorine added to the system is being released as HCl. Also $CaCl_2$ is present on much higher concentrations than for the case chlorine x 2 (Figure 5). Other compounds seem to be not much influenced. The KCl concentrations are at the same level as for the case with double chlorine amount (Figure 5) and at the same level comparing to the base case Figure A2 (Appendix). The formation of KCl is limited by the K availability. Calcium carbonate is predicted to be the most stable Ca based compound.

3.3 Chlorine content x 0.1

It is visible that ten times lower chlorine content (Figure 7) caused very significant changes in the system comparing to the base case Figure A2 (Appendix) scenario. The amount of NaCl and KCl is much lower than in other scenarios. Also the HCl(g) is not visible in the gas phase. All available chlorine is being present as alkali chlorides. Calcium carbonate is predicted to be the most stable Ca based compound.

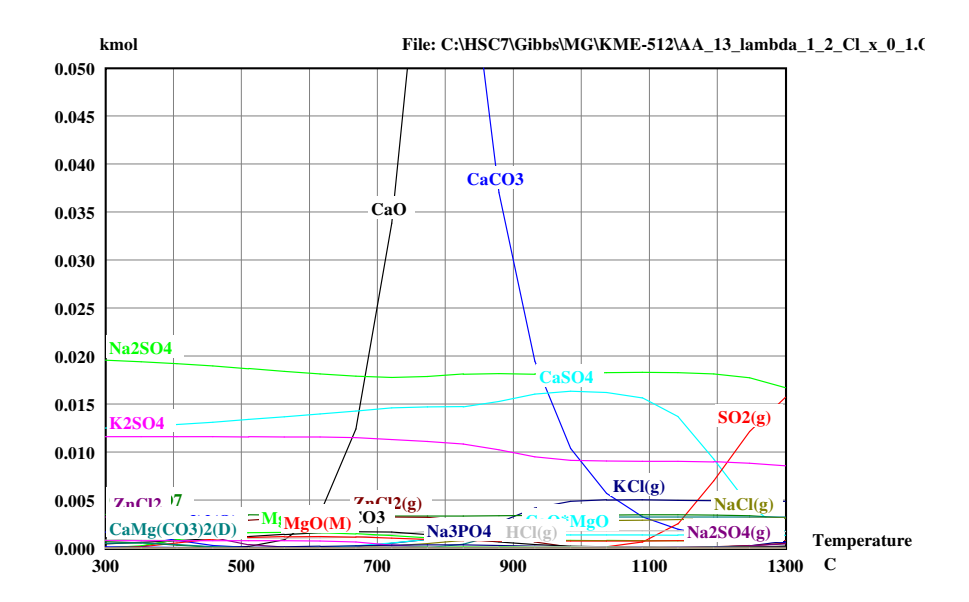


Figure 7 – ÅA-pellets with chlorine content x 0.1

3.4 Chlorine content x 4 + sludge 80 g sludge / kg fuel

In order to check the interactions of increased chlorine content in combination with increased sulphur amount originating from sludge, a case with increased chlorine content and sludge addition has been simulated.

The results reveal that there is little difference on the chlorine/sulphur chemistry comparing the case chlorine content x 4 (Figure 6) with the case chlorine + sludge case (Figure 8, mind scale difference comparing with Figure 6). With sludge some potassium and sodium has been added to the system and as a result the concentration of alkali chlorides increased. There is much more influence on the Ca/P system as observed previously with the sludge only simulations.

According to the HSC software this amount of sludge was not able to lower the gaseous KCl and NaCl content with help of more present sulphur in the gas phase but even increased the amount of KCl and NaCl slightly due to more K and Na present in the system originating from the sludge.

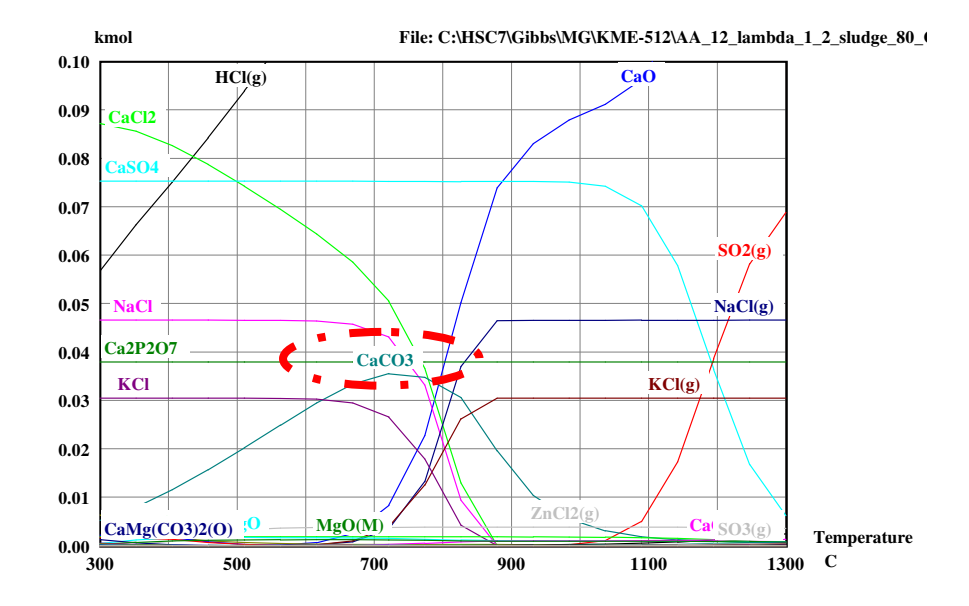


Figure 8 – ÅA-pellets with chlorine content x 4 and sludge added (80 g of sludge/kg of fuel)

4 DISCUSSION AND CONCLUSIONS

4.1 Comparing the experimental findings - deposits analysis by SP

In order to relate the results of simulations with the experimental findings delivered within the project by SP a comparison is made between the outcome of the calculations and of the composition of the deposits collected during the tests at SP. The operational conditions for the SP tests have been summarized in the Table 3. Figure 9 presents the fly ash composition as collected and analysed by SP and Figure 10 presents SH deposits and their composition as collected and analysed by SP. It can be assumed that the temperature in the SP reactor varied depending on the location and was between $770 - 930^{\circ}$ C.

Table 3 – Operational parameters for the SP tests

·	Ref pellets	SWS1	S	Kaolin	SWS2
O2 [%, d.g.]	4,9	5,07	5,22	5,14	5,18
CO [ppm,d.g.]	37	19	34	36	30
NO [ppm, w.g.]	267	287	280	339	300
SO2 [ppm, w.g.]	11	20	284	24	43
HCl [ppm, w.g.]	213	244	348	248	227
H2O [%, w.g.]	12,4	12,6	13	13	12,3
CO2 [%, w.g.]	13,9	14,5	14,6	14,7	14,3
Tbed [°C]	799	799	800	800	800
T_1 [°C]	907	911	903	878	871
T_2 [°C]	924	936	935	924	919
T_3 [°C]	779	779	785	784	782

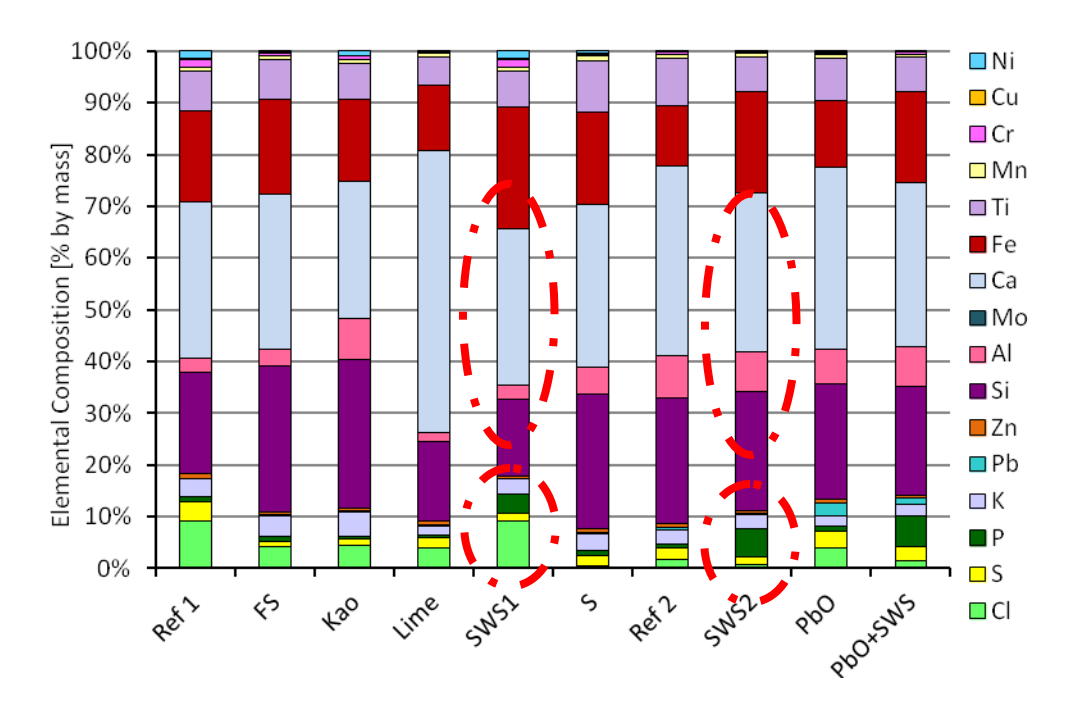


Figure 9– Fly ash composition – SP tests

It is visible that the fly ash composition has been influenced by the sludge composition (SWS1) added to the system as one of the additives. One can observe that P content for sludge (SWS) in the fly ash and SH deposits are clearly higher than for all other cases. The Ca content remains constant (Figure 9 + Figure 10) but there is no increase as in case of lime addition. The sludge added to the system adds also these elements. This was predicted with HSC equilibrium software where the formation of Ca and P based compounds was clearly visible after the sludge addition. Looking at the fly ash composition one can observe that also the chlorine content remains quite high after the sludge addition. For the SH ash it is not the case any more. Also for the double amount of sludge case (SWS2) the chlorine content both in the fly ash and in the superheater deposits was lower.

One has to be aware of different mechanisms which may take place. It is still open which mechanism is responsible for the corrosion reduction observed by SP in case of sludge addition. It can be related to the sulphur present and sulphating reaction taking place primary or secondary in deposits reducing the chlorine attack. It can be also related to the alumina-silicates present in sludge. The reaction between alkalis and alumina-silicates with release of chlorine are thermodynamically favourable and may be result of the sludge addition.

Analysing the Ca-P based HSC response and comparing it with the experimental findings from SP one has to be careful when modelling a system with phosphates being present. The thermodynamical data for solid and liquid phosphates in the commercial databases as HSC are usually very scarce [Lindberg et al. 2013]. Many of the K-Ca-phosphates even lack experimental determination of the thermodynamic properties. It means that the HSC response to phosphates present in the sludge may not always be correct.

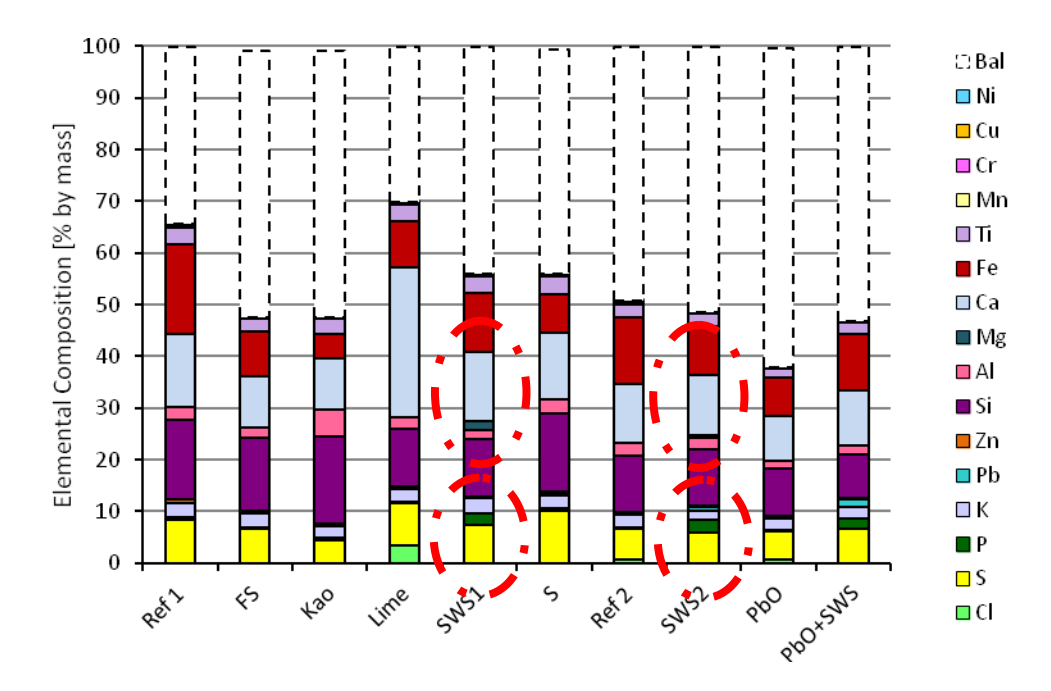


Figure 10 – SH deposits composition

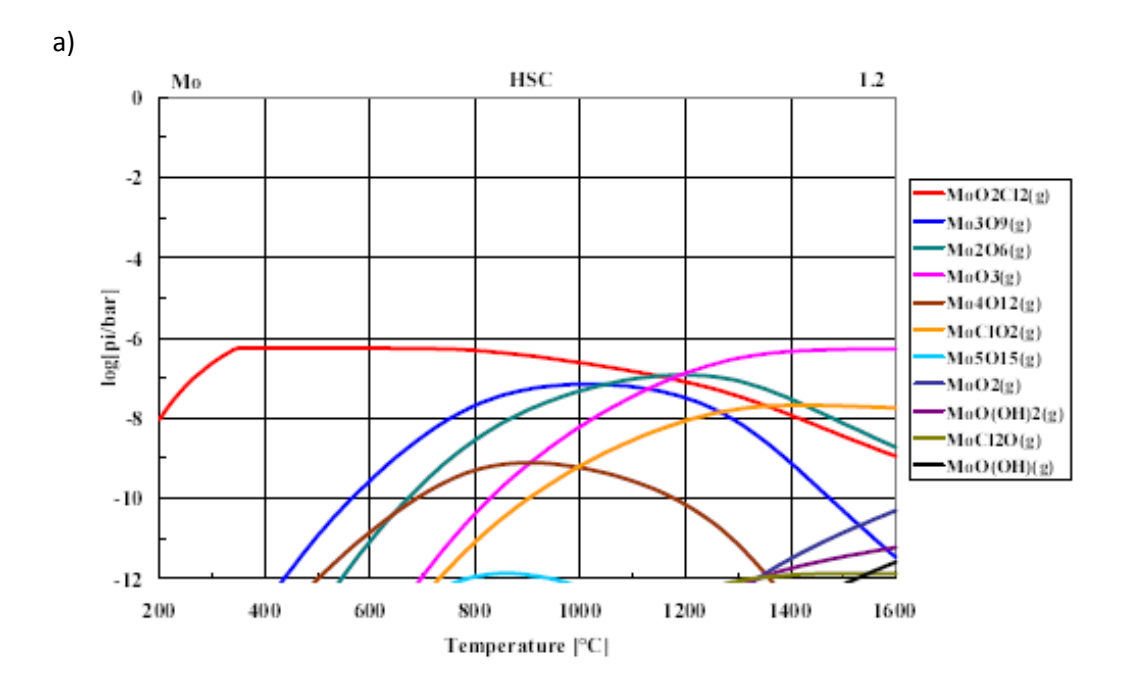
One can observe that the SH deposits show a similar trend. Only for the lime addition, the Ca content in fly ash and SH deposits were higher in Ca, but this is due to lime added to the system. In case of SH deposits there was no Cl found which could indicate deposits sulphation. This type of reaction is very difficult to predict with HSC due to the programme limitations to the gas phase mostly.

4.2 Discussion on chemical equilibrium modelling

Chemical equilibrium analysis is a useful tool in the study of a variety of processes, and it has been widely used to evaluate many environmental, geochemical, and technical processes. Moreover, equilibrium studies have proven valuable in verifying and understanding the chemistry of heavy metals in combustion systems.

Equilibrium predictions are highly sensitive to the input data. All relevant species of the system must be taken into account, and the numerical values of the constants must be correct and consistent. If some important species are omitted from the calculations or the data is not correct, the results can be very misleading. In practice, investigators often attribute the discrepancies between the experimental data and the results of calculations to the absence of chemical equilibrium in the system or to incorrect parameters in the model used, while the actual reason may be errors in the thermodynamic data. Even in cases where equilibrium is not actually reached, equilibrium analysis might still be the best approximation possible since kinetic data are not always available for the chemical systems that occur in combustion systems [11].

There appear to be significant differences in the thermodynamic values of compounds in different databases. Figure 11 shows all the gaseous molybdenum compounds that are formed under oxidizing conditions according to the HSC and FACT databases. It can be clearly seen that there are far more gaseous compounds formed according to HSC than according to FACT. While most of the compounds are also present in the FACT database, their thermodynamic values are so different that they do not become stable.



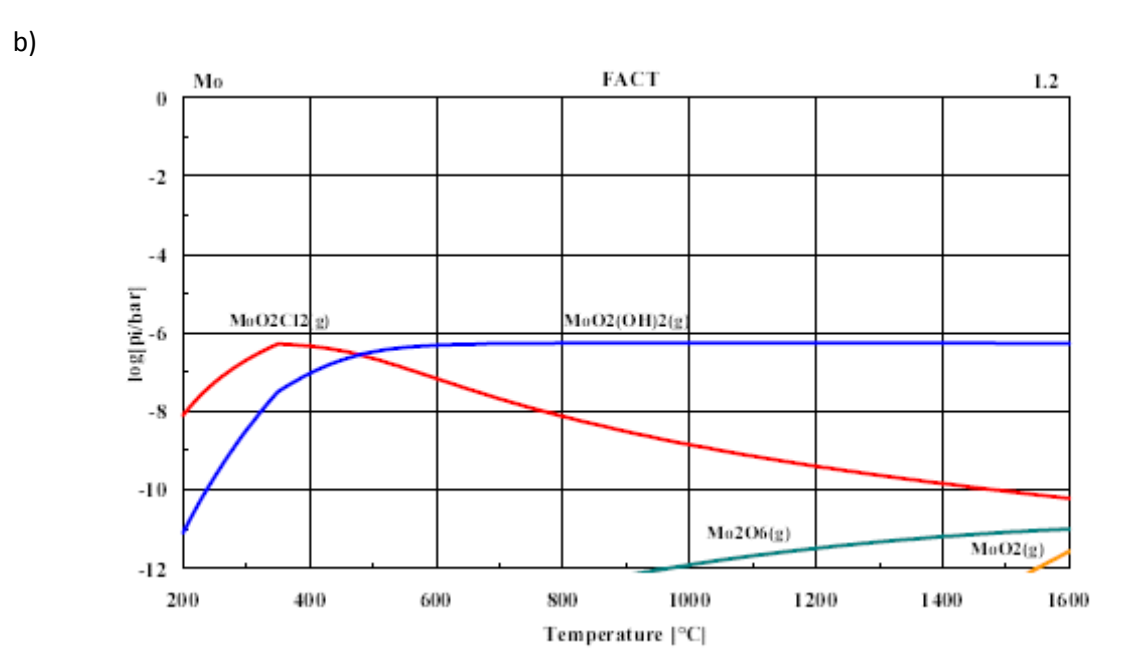


Figure 11 – Comparison between HSC and FactSage and their ability to predict the equilibrium for Mo compounds. The Figure illustrates the possible significant differences between the results

4.3 Chemical equilibrium calculations – applicability and limitations

Chemical equilibrium calculations can be a useful tool for R&D and operational engineers when dealing with new (biomass) fuel types and mixtures and helping with operational issues like corrosion or deposits formation. Of course the method will not provide all answers but may indicate problem areas.

The equilibrium calculation itself takes into account only the chemistry of the system and based on the mathematical calculations tries to minimize the Gibbs free energy of the system to check at which composition the system is at equilibrium. The equilibrium calculation process assumes infinite amount of time available for the chemical reactions to happen which is in contrary to the situation in real boilers. In reality some reactions will happen faster and some slower, all of them controlled by kinetics. One has to be careful when analysing the results. One example can be alkali release and the secondary sulphation reactions of alkali metals which happens in two steps and one step is kinetically slow (Figure 11).

During the first stages of decomposition fuel particles dry and devolatilize. In this process hydrocarbons, CO, CO₂ and H₂O are released from the fuel particle. It has been suggested that the alkali release in case of biomass may already start during the devolatilisation of the biomass fuel at relatively low temperatures (around 400°C). Further increase in the temperature causes an increased amount of alkalis detected. It is believed that there are two different types of alkalis, namely the pyrolysis alkalis, organically bound in the structure of the fuel and the ash alkalis emitted in the higher temperature range. Moreover Davidsson [12] observed that small particles release more alkali per unit initial particles mass than large ones.

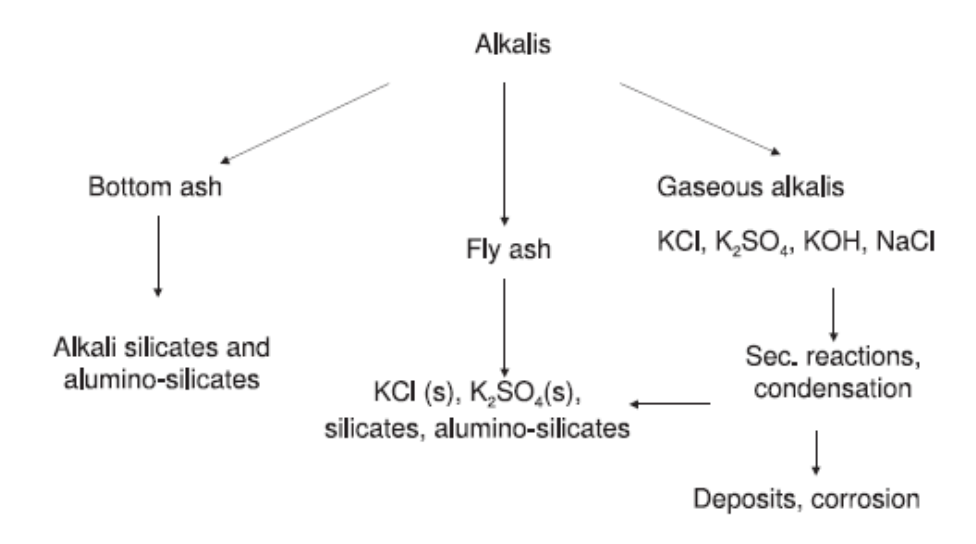


Figure 12 – Fate and release of the alkali metal in a typical combustion system [Glazer, 2007]

According to literature, if the temperature is high enough several inorganic transformations take place. Especially the alkali metals will experience surface migration, vaporization to the gas phase or coalescence with incorporation into the fuel silicate structures or for coal into alumino-silicate structures [13]. Not all alkalis from high alkali biomass are released to the gas phase (Figure 12). Cl acts as a shuttle in transporting potassium from the fuel structure to the outside. Depending on the conditions in a reactor (reducing, oxidizing environment) the alkalis can be released in the form of chlorides, hydroxides or sulphates or transferred to sulphates in secondary reactions. The form, composition and place of deposits depend also on the flow conditions and the temperature field in the boiler. The chemical equilibrium method does not take into account anything related to the flow conditions in the boiler and boiler geometry which may influence the deposits formation and composition.

Summarizing, HSC software is a great tool for some initial analysis of any new fuel and its influence on the boiler. It can be also use to help analyse the operational problems experienced at the site. Process optimization like optimal fuel mix for a certain specific type of boiler is also a possible application. Nevertheless one has to be careful and always an expert knowledge needs to be applied when analysing the results. The results often need to be supported by experimental findings and sound thermodynamical databases.

4.4 Conclusions

The calculated results show that HSC chemistry can be effectively used to predict the reactions in the gas phase from the fuel or/and (new) fuel mixtures. The HSC tool can be used to check potential influence of a fuel blend and the dominant chemical reactions in the system.

Additional sulphur addition led to the formation of calcium sulphate and with further addition of sulphur, the surplus of S is being released as SO₂. In case of Cl addition one could observe an increase in HCl emissions and a slight increase in KCl and NaCl.

Adding sludge to the system caused substantial shift in Ca toward compounds with P, due to the high Ca and P content. The use of sludge as additive in a case with increased Cl content (the last simulated case) did not modify the corrosive alkali-chlorine system in a substantial way.

According to the HSC software the sludge was not able to lower the gaseous KCl and NaCl content with help of more present sulphur in the gas phase but even increased the amount of KCl and NaCl slightly due to more K and Na present in the system originating from the sludge. The measurements performed by SP revealed that sludge was effective in reducing chlorine induced corrosion and the amount of chlorine observed in deposits collected experimentally was lower. It can be related to the alumina-silicates present in sludge. The reaction between alkalis and alumina-silicates with release of chlorine are thermodynamically favourable and may be result of the sludge addition. This can be related to secondary sulphation reactions which are not being represented properly by HSC chemistry.

HSC software could be great help and tool for some initial analysis of any new fuel and its influence on the boiler. It can be also use to help analyse the operational problems experience at the site. Nevertheless caution and proper analysis is required.

5 REFERENCES:

- 1. Project meeting knowledge exchange Åbo Akademi Vattenfall April 2013
- 2. J. Helble, The behaviour of coal minerals under combustion conditions. Atlanta Coal Cnference, 1991
- 3. M. Aho, "Reduction of superheater corrosion by co-firing risky biomass with sewage sludge" Fuel 89 (2010)
- 4. A. Pettersson, "Leaching of ashes from co-combustion of sewage sludge and wood", halmers, 2008
- 5. L. Wang, "A critical review on additives to reduce ash related operation problems in biomass combustion applications" Energy Procedia 20 (2012)
- H. Wee "The effect of combustion conditions on mineral matter transformation and ash deposition in a utility boiler fired with a sub-bituminous coal", Proceedings of the Combustion Institute 30 (2005) 2981–2989
- 7. H. Yao "Using sorbents to control heavy metals and particulate matter emission during solid fuel combustion" Particulogy 7 (2009) 477–482
- 8. X. Wei "Behaviour of gaseous chlorine and alkali metals during biomass thermal utilization, Fuel 84 (2005) 841–848
- 9. E. ferrer, "Fluidized bed combustion of refuse-derived fuel in presence of protective coal ash", Fuel Processing Technology, Volume 87, Issue 1, December 2005, Pages 33-44
- 10. I. Obernberger "Novel Characterisation methods for biomass fuels and their application case study straw", Fuel Quality Impacts Conference, 2012
- 11. Tarja Talonen, Chemical Equilibria of Heavy Metals in Waste Incineration: Comparison of Thermodynamic Databases, Åbo Akademi, report 08-02, 2008
- 12. Davidsson, K. O., Engvall, K., Hagstrom, M., Korsgren, J. G., Lonn, B., and Pettersson, J. B. C. (2002a). A surface ionization instrument for on-line measurements of alkali metal components in combustion: Instrument descriptionand applications. Energy&Fuels, 16:1369–1377
- 13. Jensen, P., Frandsen, F., Dam-Johansen, K., and Sander, B. (2000b). Experimental investigation of the transformation and release to gas phase of potassium and chlorine during straw pyrolysis. Energy & Fuels, 14:1280–1285.
- 14. Lindberg, D. Backmann, R., Chrtrand, P., Hupa, M. "Towards a comprehensive thermodynamic databse for ash-forming elements in biomass and waste combustion Current situation and future developments" Fuel Processing Technology 105 (2013) 129-141

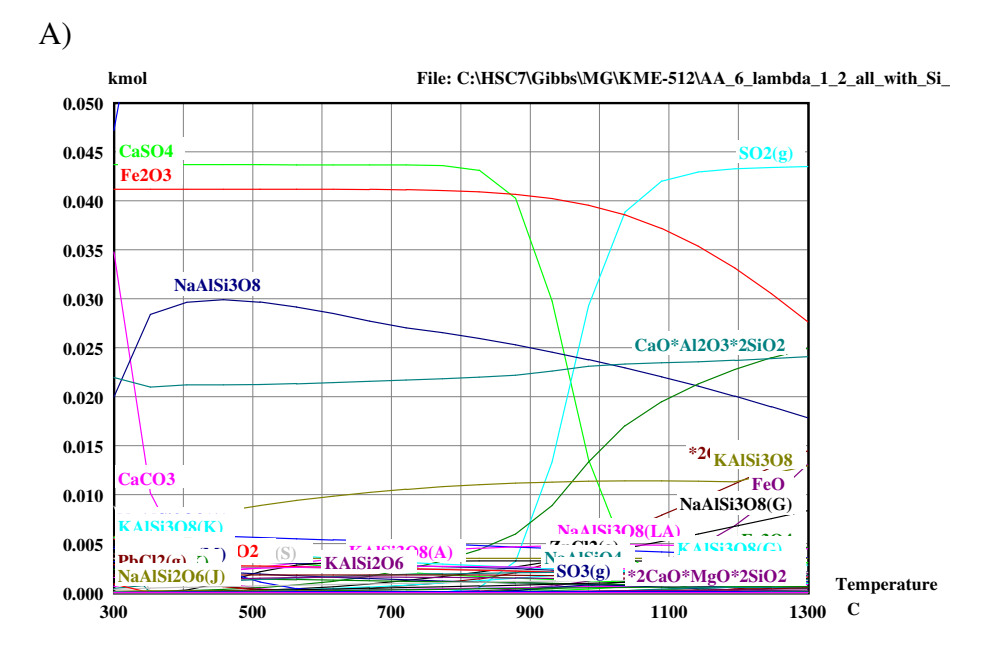
6 APPENDIX 1 – FINE TUNING BETWEEN HSC AND FACTSAGE

6.1 ÅA pellets at lambda 1.2

The system at equilibrium has been simulated using the ÅA-pellets composition as specified in Figure 2

- The system simulated with Al, Si, Fe

In order to check the influence of the Al, Si and Fe on the system, the system was calculated with these elements included according to the fuel composition presented in Figure 2. It is visible (Figure A1) that the system is dominated with Al, Si and the equilibrium composition is shifted towards formation of alkali alumina silicates (M-Al-Si). It is know that the reactions of alkali metals with alumina silicates are preferred from the equilibrium point of view. It is visible at Figure A1 (a + b) that different forms of K, Na, Ca based alumina silicates dominate over the whole temperature range. However, the system where the Al-Si dominate the system completely is far from reality. In reality not all reactions with alumina silicates take place. In Figure A2 (a and b) the results without Al, Si and Fe are presented. In this figure formation of CaO and CaCO₃ together with decomposition of solid NaCl and KCl into the gaseous forms is visible. The simulation of the system without Al, Si and Fe let to check the response of the system to these elements and let better track the fate of alkali chlorides. The results presented in Figures 3 and 4 comply with the results from Åbo Akademi done with the help of FactSage software. All further calculations done with HSC for the purpose of the KME-512 were performed without Al, Si, Fe being included.



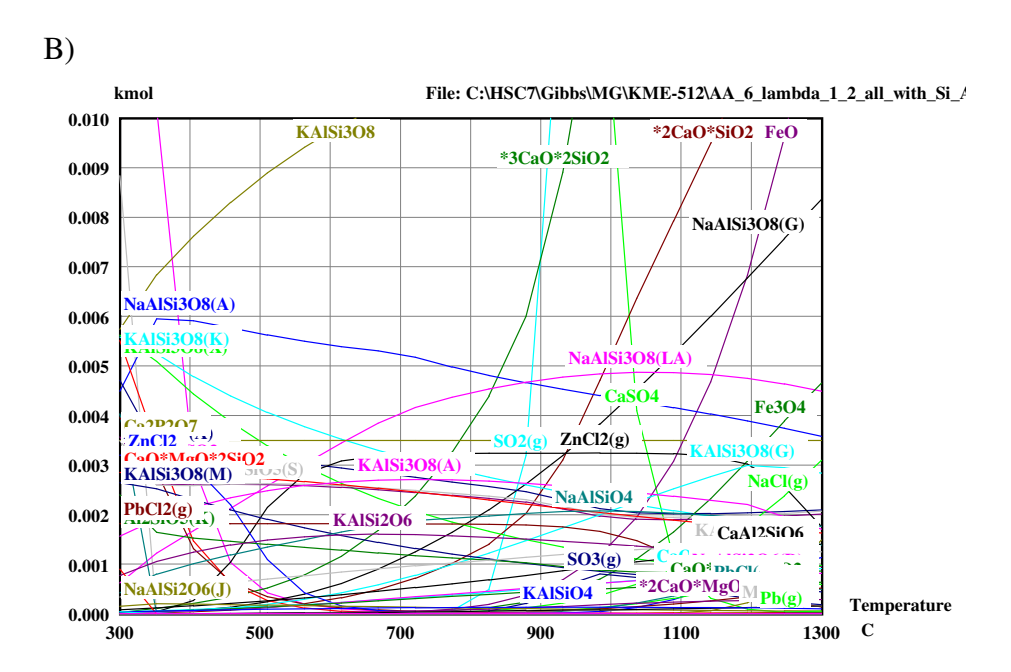
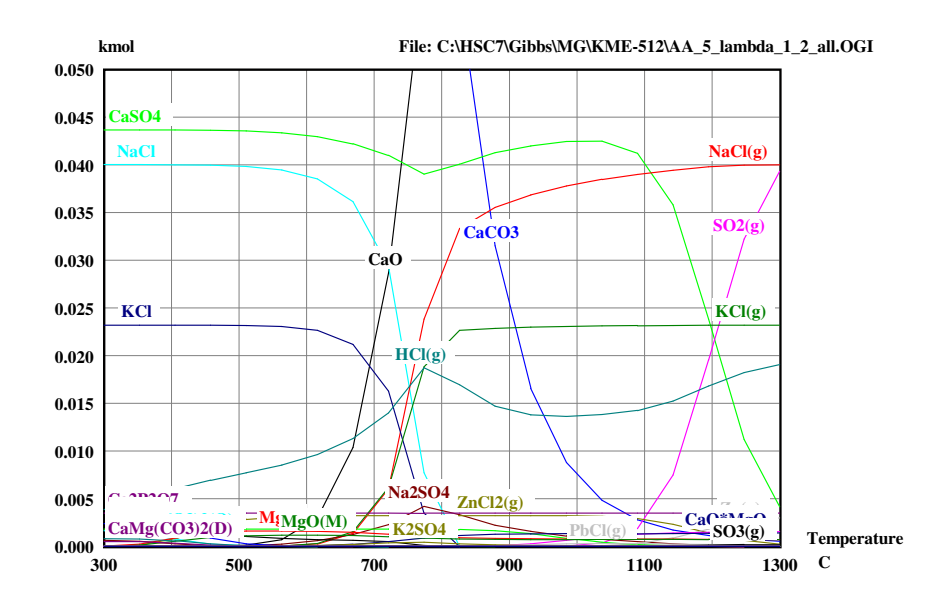


Figure A1 – The equilibrium system for the fuel ÅA-pellets with Al, Si, Fe included. Figure A scale bis 0.05 kmol, Figure B scale bis 0.01 kmol – compounds with lower concentrations visible.

The system without Al, Si, Fe

A)



B)

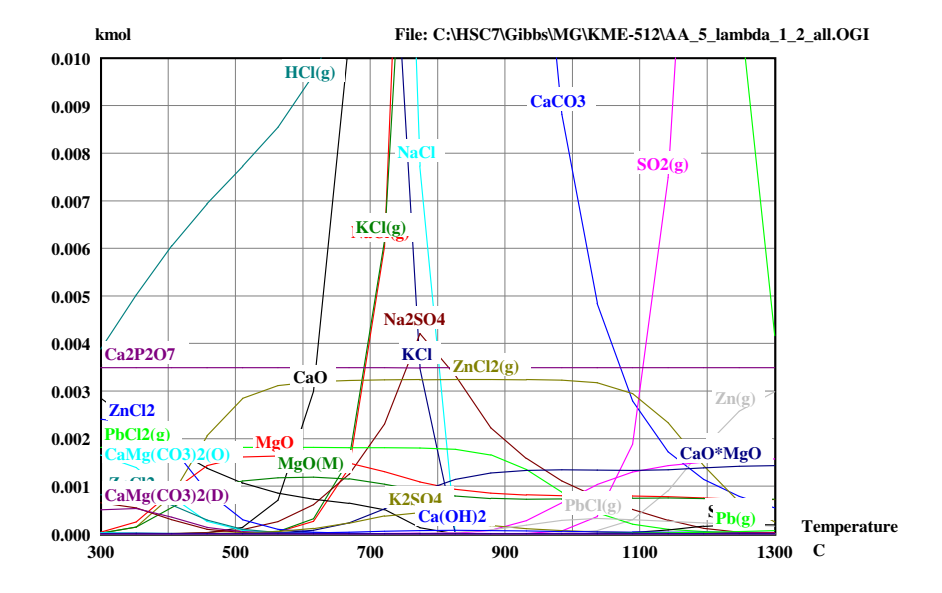


Figure A2 – Base equilibrium system for the fuel ÅA-pellets, Al, Si, Fe have been excluded from the system. Figure A scale bis 0.05 kmol, Figure B scale bis 0.01 kmol – compounds with lower concentrations visible

6.2 Sulphur addition in steps – influence on the system

The response of the system to the sulphur addition has been tested. An arbitrary amount of 0.006 kmol of S per step has been added to the system (Figure A3). With this amount of sulphur there has been no increase in SO_2 emissions visible comparing to the base case (Figure A2). There have been enough calcium in the system and all sulphur available in the system has been "consumed" to form calcium sulfate.

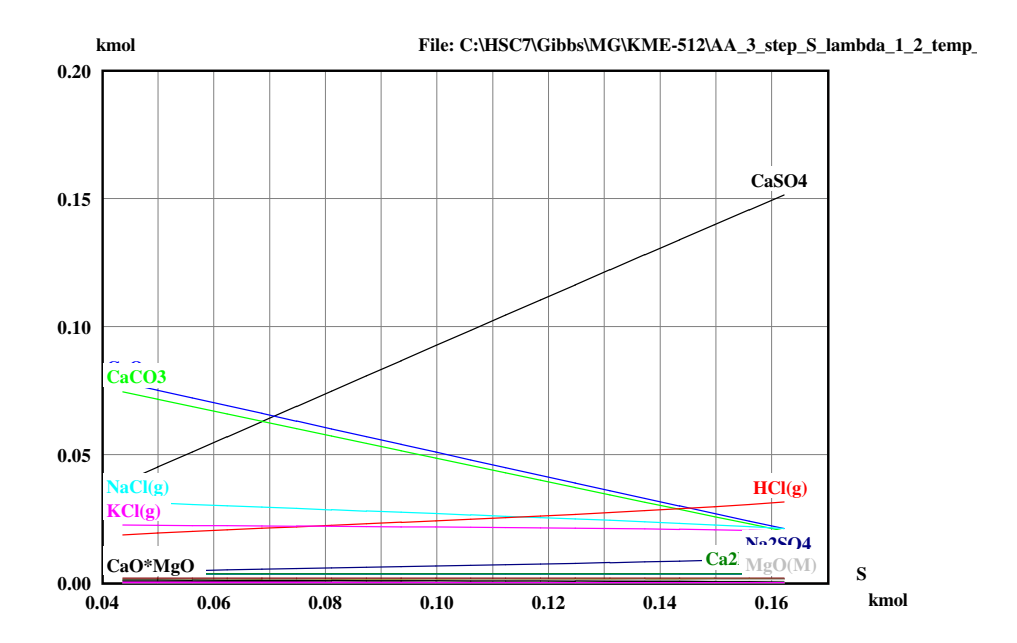


Figure A3 – The equilibrium system for the fuel ÅA-pellets, 0.006 kmol of Sulphur added per step

As the next step in order to check the sulphur sensitivity the double amount of added S $(0.012 \text{kmol}\ \text{of}\ \text{S}\ \text{per}\ \text{step})$ has been used. It could be observed that the SO_2 emissions start to increase when all Ca has been "consumed" and transformed to $CaSO_4$. After the amount of Calcium Sulphate stabilise the additional sulphur in the system is being released in the form of SO_2 (g) – Figure A4

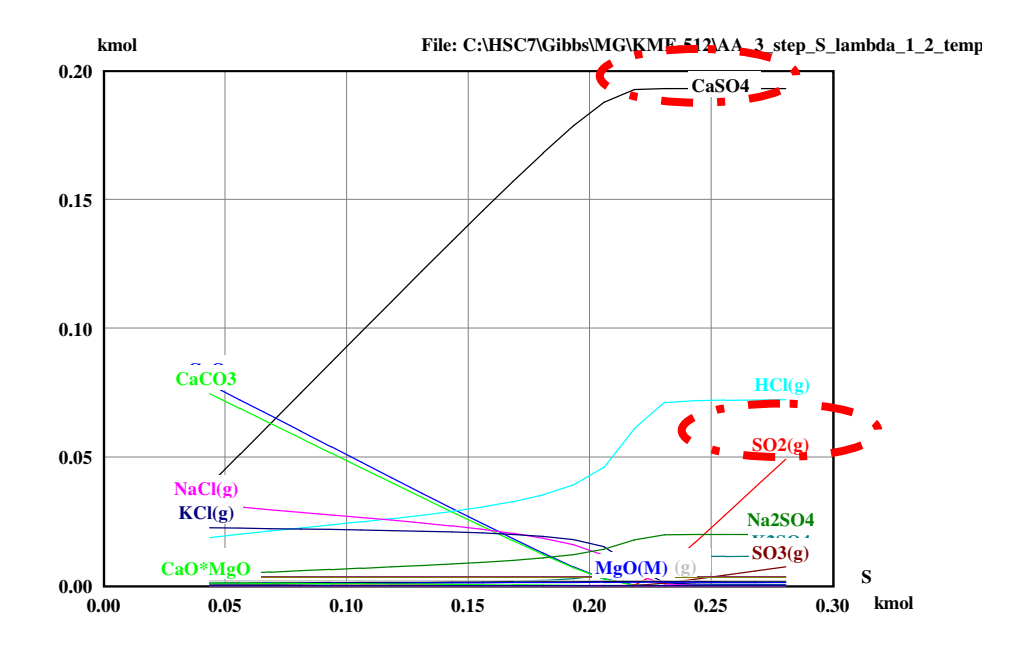
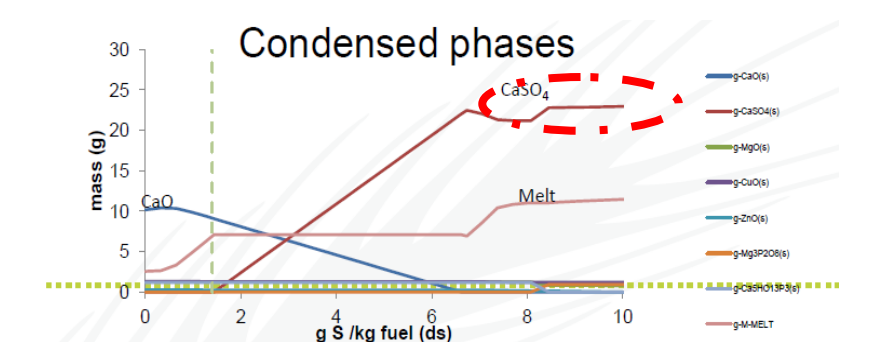


Figure A4 – The equilibrium system for the fuel ÅA-pellets, 0.012 kmol of Sulphur added per step

The results have been compared with the calculations performed by Åbo Akademi. The results of the two methods are in agreement. (Figure A4 and Figure A5). Åbo Akademi also showed increased formation of $CaSO_4$ and that when $CaSO_4$ reaches it maximum, the additional sulphur in the system forms SO_2 in gas form with increasing concentration.



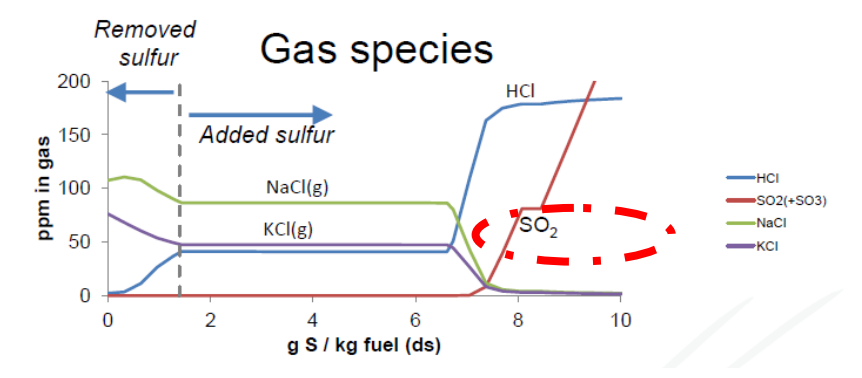


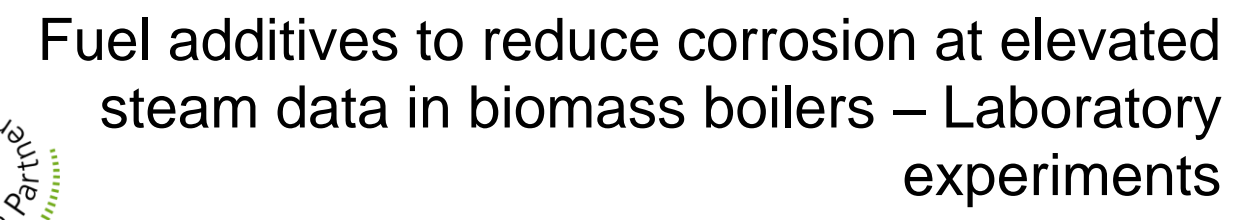
Figure A5 – The equilibrium system as calculated by Åbo Akademi

6.3 Summary

The finetuning of HSC and resulting comparison between the Åbo Akademi calculations (FactSage) and Vattenfall calculations (HSC) reveals that the oxidizing conditions cases were characterized in a similar way by the both calculation tools.

The main conclusions (lessons learned) from the comparison between two software can be summarized:

- Molten slags were not well represented by the HSC software used by Vattenfall. HSC software
 has in general limited ability to predict molten slags sue to database limitations. For this area
 FactSage shows better performance.
- K₂Si₄O₉ (s,I), K₂Si₄O₅ (s,I) not present in the HSC database. It has been realized that the
 thermodynamical data for these two compounds were not present in HSC database. These
 compounds are/might be present during biomass (straw) combustion and form sticky deposits.
- The equilibrium system is heavily influenced by Si and Al presence. Addition of Si and Al based on the <u>ÅA</u> pellet composition moved the whole equilibrium system heavily into the aluminasilicates formation. Although the effect of silica-alumina binding is positive in general such a strong influence will not occur in the reality. Therefore in order to test the influence of other elements (like sulphur and chlorine) Al, Si and Fe have been excluded. During 100% biomass combustion no (or little) stable (alkali) alumina silicates are formed because the Si and Al in biomass are of different, (simpler) form than the alumina silicates in coal (or kaolin). Investigation of the saturated kaolinite by means of XRD reveals that it contains primarily nephelite and carnegieite which are sodium aluminosilicates polymorphs with the chemical formula Na₂O· Al₂O₃ · 2SiO₂. These compounds are stable and have high melting temperatures. In pure biomass combustion is it less probable they will be formed. That is the reason <u>ÅA</u> removed the Si + Al from the system. The Vattenfall investigation using HSC showed similar system results meaning the HSC software was responding in a similar way as FactSage
- Sulphur addition to the system has been tested. In general all sulphur added formed CaSO₄ until
 there has been free Ca present in the system. When the level of Ca (CaSO₄) stabilised the
 concentration of SO₂ increased. These results from HSC response are also in agreement with the
 results from FactSage.



Fredrik Niklasson, Anders Hjörnhede

KME-512 Fuel additives to reduce corrosion at elevated steam data in biomass boilers – Laboratory experiments

Fredrik Niklasson, Anders Hjörnhede

Abstract

The purpose of this work is to study the effect of different additives to a base fuel of waste & demolition wood on boiler wall corrosion at relatively high temperature. The background is that boiler wall corrosion is a problem occurring in large scale boilers firing demolition wood. In contrast to superheater corrosion, which has been extensively studied, boiler wall corrosion in the furnace occurs mainly at reducing gas conditions, i.e. under-stoichiometric conditions, implying different corrosion mechanisms.

The laboratory tests was performed in a fluidized bed reactor fired with demolition wood mixed with different additives. The additives tested were kaolin, sewage sludge, lime, foundry sand and sulphur. Corrosion probes were inserted in two positions. One probe was located in the primary combustion zone with gas conditions similar to boiler wall conditions in the lower part of the furnace in a large-scale unit. The other probe was located close to the exit of the reactor, and exposed at conditions similar to a superheater. The material temperatures of the two probes were 400°C and 550°C, respectively. The corrosion probes were exposed for 8 hours per test, and each probe carried three metal ring samples parallel mounted, of three different steels: 16Mo3, 253 MA and Kanthal-A1.

The deposits formed on the exposed sample rings were weighed and chemically analysed by handheld XRF. After removal of the deposits, the sample rings were studied by optical microscopy. Selected rings were also analysed by SEM-EDX. Furthermore, analyses were also made on bottom ashes, fly ashes, wall deposits and the gas concentrations of NO_x , SO_2 , HCl and CO_2 were monitored by FTIR-instrument.

It was possible to give a tentative ranking between test cases based only on visual inspection of the corrosion attacks on the sample rings. It was found that the additives kaolin and sewage sludge were among the most effective additives counteracting the corrosion both at the boiler wall and superheater conditions. The lime additive showed poor corrosion limiting abilities.

SP Sveriges Tekniska Forskningsinstitut SP Technical Research Institute of Sweden

SP Arbetsrapport 2013:51 ISBN 978-91-87461-39-2 ISSN 0284-5172 Borås 2013

Contents

1 Background	7
2 Methods	8
2.1 Laboratory reactor	8
2.2 Fuels	9
2.3 Test procedure	9
2.4 Measurement methods	10
3 Results	15
3.1 Gas concentrations and temperatures	15
3.2 Fly Ash	15
3.3 Bottom Ash	17
3.4 Deposits	20
3.5 Study of selected elements in the deposits	25
3.6 XRD Analyses	33
3.7 Distribution of selected elements in ash, deposit as	nd flue gas 35
4 Corrosion analysis	39
4.1 BW comparison (first set of tests)	39
4.2 BW comparison between Ref 2 and SWS2 (second	d set of tests) 44
4.3 BW comparison between: PbO and PbO+SWS (see	
4.4 BW Comparisons between Ref 1 and Ref 2 (secon	
4.5 BW comparison between SWS1 and SWS2 (secon	nd set of tests) 72
4.6 SH comparison (first set of tests)	73
4.7 SH comparison between Ref 2 and SWS2 (second	l set of tests) 77
4.8 SH comparison between: PbO and PbO+SWS (see	cond set of tests) 81
4.9 SH Comparisons between Ref 1 and Ref 2	87
4.10 SH comparison between SWS1 and SWS2	89
4.11 Summary of corrosion analysis of second set of te	ests 91
4.12 Ranking of additives based on observations	92
Appendix A Chemical composition of deposits of	on BW probe 1
Appendix B Chemical composition of deposits of	on SH probe 1
Appendix C Fuel analyses	1
Appendix D Photos of deposit probes directly at	fter exposure 1
Appendix E XRD Diffraction Spectra	1

Preface

This project has been financed through the programme KME, which is a consortium with material technology development as a base to make thermal energy processes more effective. The programme is financed by industries (60%) and by the Swedish Energy Agency (40%). The work presented in present report is the experimental part of a project denoted KME-512. Other parts of the project, such as inventory of possible additives, chemical fractionation, thermodynamic equilibrium calculations, and cost estimates of additives, are reported within the project.

The vision for the KME program period 2010-2013 is to improve the electrical and total efficiency by material technology development when utilising climate neutral fuels in thermal energy conversion processes. The long-term vision includes research for erection of a new full-scale demonstration CHP plant in 2017-2018, fired with renewable bio fuels and refuse fractions, with at least 3-4 % points higher electrical efficiency than commercial plants built today.

The project partners in the KME-512 project are: Vattenfall Research and Development AB, E.ON Värme, E.ON Climate and Renewables, Metso, Outokumpu, Sandvik Heating Technology, Åbo Akademi and SP Technical Research Institute of Sweden.

Summary

Waste wood fuel with and without different additives have been fired in a lab-scale fluidised bed reactor. Material samples of steel types 16Mo3, 253 MA and Kanthal-A1 were exposed in the reactor for 8 hours at two different positions, which were chosen to replicate the conditions found at the furnace boiler wall (BW) and superheater (SH) in a large scale unit.

The tested additives were: foundry sand, kaolin, lime, dried sewage sludge and sulphur. In addition, two tests were conducted with fuel spiked with PbO, to study its effect on the corrosion of the steels. PbO was added to the waste wood without additives in one of these tests, and both PbO and sewage sludge were added to the fuel in the other test. Two reference test runs were conducted without any addition of additives to the fuel.

After the tests, deposits on the steel samples rings were analysed chemically by handheld XRF instrument. After removal of deposits, the corrosion on the steel surfaces were studied by optical microscopy. In some selected cases, the in-depth corrosion were also analysed on cross-sections by SEM/EDX.

The additives that showed the best results in decreasing the corrosion at the boiler wall were **kaolin** and **sewage sludge**.

Lime tends to increase the corrosion rate on the boiler wall.

At superheater conditions, **kaolin** and **sulphur** were the two additives that showed the highest reduction of corrosion on the steel samples.

Kanthal A-1 was found to have the lowest corrosion rate closely followed by 253 MA. The low alloyed 16Mo3 shows significantly higher corrosion rates amongst the three steels tested.

Observations from the analysis of elements in the deposits are listed below:

- The **lime** additive reduced concentrations of Zn and increased concentrations of Pb in the BW deposit, compared to the reference case. Lime did also, to a smaller degree, reduce the concentrations of Zn in the SH position, while the Pb concentrations remained almost unaffected.
 - Lime increased the concentrations of both Cl and S in the BW deposits. In the deposits at the SH position, the lime additive showed severely increased concentrations of Cl while the concentrations of S were reduced.
 - Lime reduced concentrations of K and increased concentrations of Ca in the SH deposits.
- The **Foundry sand** additive was found to reduce the concentrations of Zn and increase the concentrations of Pb in the BW deposits. The foundry sand increased concentrations of K and Cl on the windward side of the BW deposits. It increased the S concentrations in the deposits both at the BW- and SH-positions. Overall, this additive was found to have little effect on the SH deposits, even if the analyses show a tendency of slightly lowered concentrations of Cl.

- The **kaolin** additive gave reductions of Zn, Cl, and S in the deposits at the BW position. Some measurements of the concentrations of elements in the SH deposits failed, but the few analyses obtained indicate reduced concentrations of these elements also at the SH-position.
- The Sulphur additive reduced Zn in both the BW and the SH positions but increased
 concentrations of Pb in the SH position. The sulphur additive increased Sconcentrations in the deposits at both positions and reduced the concentration of Cl at
 the SH position. The concentration of K increased in BW position but decreased in SH
 deposits.
- The **sewage sludge** reduced the concentrations of Cl in the deposits at both BW and SH positions The sewage sludge also reduced the concentration of K in the BW deposits. On the other hand, **sewage sludge** showed the least improvement of the additives tested regarding Zn in the BW deposits and it gave increased concentrations of Pb in the deposits at the SH position. It may also be noted that the addition of sewage sludge increased concentrations of P in all deposits.
- Spiking the fuel with **PbO** resulted in increased concentrations of Pb in the deposits at both the BW and the SH positions. The addition of PbO also reduced the concentration of Zn in the BW deposits.

The influence of the additives on elemental concentrations found in the deposits are summarised in Table 1 for BW-tests and in Table 2 for SH-tests. In these tables, the symbols represent the ratios calculated from the average concentrations in deposits from a test case (3 rings) relative to the average concentrations in the deposits from the reference case as:

- ++ Concentration is more than 200 % of the reference case
- + Concentration is between 125 and 200% of reference case Concentration is between 75% and 125 % of reference case (insignificant)
- Concentration is between 50 % and 75 % of reference case
- -- Concentration is less than 50 % of reference case

The abbreviations used in the tables for the test cases of different additives are: FS) Foundry sand, Kao) Kaolin, Lime) Lime stone, SWS1) Sewage sludge case 1, S) Elemental sulphur, SWS2) Sewage sludge case 2, PbO) Fuel spiked with PbO, PbO+SWS) Fuel spiked with PbO and added sewage sludge.

Table 1. Summary of concentration deviation from reference case, BW (boiler wall).

BW	FS	Kao	Lime	SWS1	S	SWS2	PbO	PbO+SWS
Cl	++		++					
\mathbf{S}	++		++	-	++			-
P		-		++	-	++		++
K	++			-	+		-	
Pb	+		++		-		++	
Zn	-	-					-	
Ca	-		-					

Table 2. Summary of concentration deviation from reference case at SH (superheater).

SH	FS	Kao	Lime	SWS1	S	SWS2	PbO	PbO+SWS
Cl			++					
\mathbf{S}		-			+	+		+
P				++		++		++
K			-		-			
Pb		++		++	++	+	++	++
Zn	-			-	-	-		-
Ca			++					

The optical corrosion study showed that **kaolin** and **sewage sludge** were the only additives that clearly reduced the corrosion in the BW position (compared to reference case) while **sulphur** and **kaolin** showed the most improvement at the SH position.

Lime tends to increase the corrosion in the furnace region.

The lowest deposition rates (of "hardly attached" deposits) at the BW position were found for foundry sand, lime and kaolin. At the SH-position, the lowest deposition rates case from the kaolin and sulphur cases. Also the sewage sludge reduced the amount of deposits compared to the reference case.

The amount of fine fly ash was similar for all test cases except lime, which had significantly higher fly ash concentrations. The concentration of Cl in the fine fraction of the fly ash was highest for the lime case and the lowest for the sulphur case. The concentration of Cl in the fly ash was also reduced by the kaolin additive and, to a smaller extent, the sewage sludge additive.

In the bed material, remaining after the test runs, the Cl content was reduced by the additives kaolin, sulphur and foundry sand. The chlorine concentration in the bed material was almost unaffected by the sewage sludge and significantly increased by the lime.

The concentration of HCl in the flue gas increased from, on average, 213 ppm in the reference case to 348 ppm in the sulphur case, which indicates that S reacted with alkali chlorides. For the lime additive, the HCl concentration in the flue gas was reduced to 117 ppm, possibly as a consequence of the formation of calcium chlorides. Only slightly increased concentrations of HCl were observed for the other additives (sewage sludge 244 ppm, kaolin 248 ppm and foundry sand 230 ppm).

A tentative ranking of test cases based on the average concentrations of chlorine in BW deposits is, from best to worst:

- Kaolin
- Sewage sludge
- Sulphur
- Lime
- Foundry Sand

1 Background

Wide fuel mixes are of interest for many energy companies due to increasing prices and reduced availability of clean biomass. However, wide fuel mixes, including for example waste wood, contain components, for example chlorine, alkali, lead, zinc and tin, causes corrosion in the furnace and convective superheaters. Especially water-wall corrosion in the furnace is a problem in plants that today operate at conventional / commercial steam data. For the period 2010-2013, one goal for the KME program is to report a technically and commercially viable process solution for a model plant concept that will provide the basis for a demonstration plant to be commissioned in 2017/2018. Therefore, to be able to increase the steam data level in a demonstration plant using wide fuel mixes including waste wood, it must be shown that the wall corrosion can be limited to levels that allow cost-effective operation of the plant. Different ways to solve the problem of furnace wall corrosion are, for example, the use of more expensive materials, frequent change of heat transfer surfaces, wall cladding or additives or fuel blends to reduce the amount and/or corrosiveness of deposits and slag formation on the furnace walls.

The fuel additives are fed into the boiler together with the fuel or, in the case of fluidised beds, possibly also with the bed material. The additives can be co-fuels or materials containing elements or compounds that are beneficial to the ash chemistry in the furnace and the convective section of a boiler. One or more of the following effects could achieve these criteria:

- Chemical reaction binding critical inorganics into the bottom ash or bed material in a form that does not melt at typical furnace temperatures
- Creation of particles with a porous structure, to which problematic inorganics such as alkali or heavy metal compounds can adsorb
- Addition of particles to the flue gas for abrasive blasting of the heat transfer surfaces, which prevent deposits from growing
- Acting as an inert diluting agent in the fly ash or fluidised bed material

The effect of additives on deposits and corrosion on heat transfer surfaces and bed agglomeration in fluidised bed boilers has been thoroughly studied. Examples of additives tested are ammonium sulphate, elemental sulphur, de-inking sludge and digested sewage sludge. The most promising additive for reducing bed agglomeration, fouling and corrosion was found to be digested sewage sludge. In in most studies on additives, the main objective is to reduce the superheater tube corrosion, where the metal temperatures usually are too high (450 -700 °C) for Zn, Pb and Sn compounds to condense in any considerable amounts. However, these compounds (e.g. with chloride) might very well cause corrosion at the lower metal temperatures on furnace walls. There is a lack of information about the effects of additives on boiler wall corrosion. It is of great interest to find an additive, or a combination of additives, that could simultaneously reduce the problems of both furnace and superheater corrosion.

This project aims to evaluate, based on laboratory-scale combustion tests, the potential of bed/fuel additives as means to reduce furnace wall corrosion during combustion of wide fuel mixes/waste wood in CHP plants.

2 Methods

2.1 Laboratory reactor

The outline of the laboratory reactor that was used for the combustion experiments is shown in Figure 1. All tests were performed under as stationary conditions as possible, with an operating set-point listed in Table 3:

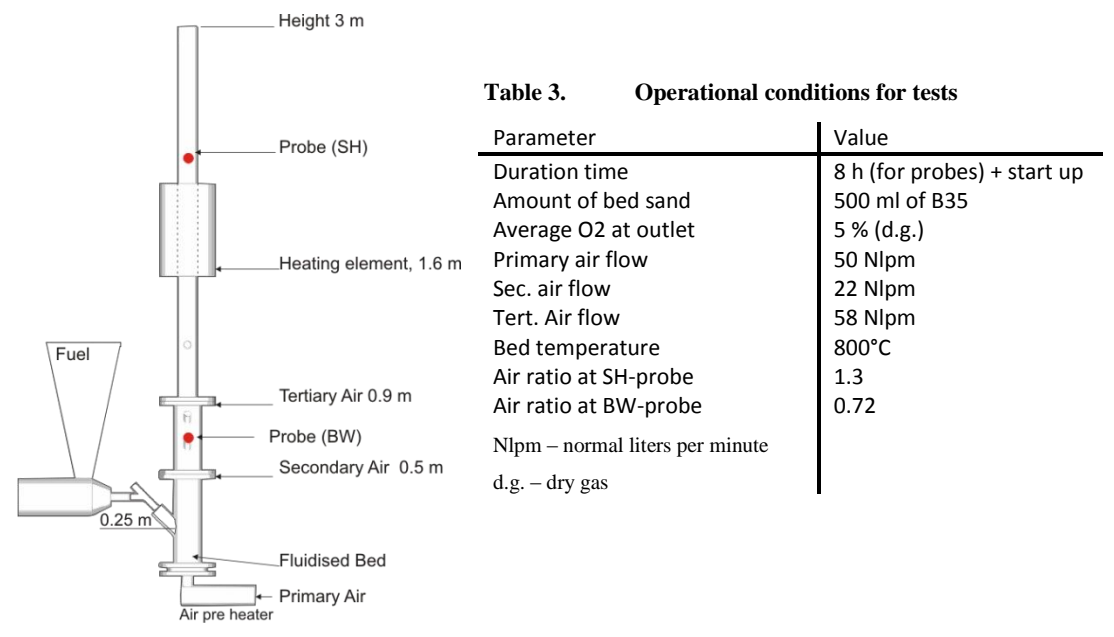


Figure 1. Outline of the laboratory reactor.

The reactor has an inner diameter of 0.10 m. The bed temperature is automatically controlled by an electrical air preheater of the primary air, which is, if needed, complemented by a manually controlled water cooled tube coil in the bed. No arrangement for flue gas recirculation exists at present. The steel tube walls are refractory lined at the inside up to a height of 0.9 meters from the air distributor. The reactor is insulated outside the steel tube along the whole reactor. An external electrical heating element surrounds the reactor at about 1.6 meter, in order to keep a sufficiently high flue gas temperature at the sampling ports on top of the reactor. The fuel is fed into the reactor by a manually controlled screw feeder at 0.25 meter above the bottom of the reactor.

An outlet oxygen concentration of 5.0 %, dry gas corresponds to an air factor of 1.3 in the reactor above the inlet of the tertiary air. At the port for the boiler wall probe, between secondary and tertiary air, the corresponding air factor is about 0.72, calculated from the ratio between the total added air and the air factor at the reactor outlet. Additional measurements of oxygen at the position of the boiler wall probe showed no oxygen above the detection limit of about 0.1 %, by volume, verifying that the gas conditions are indeed reducing at the boiler wall probe. There may be intermittent spikes of short duration of oxygen passing the position due to the "turbulent" nature of a fluidized bed, but if so, that could not be detected by the conventional gas analyser used.

2.2 Fuels

Waste wood for the experiments was provided by the Vattenfall CHP in Nyköping, Idbäcken. The fuel was milled and pressed to pellets at SP. Larger pieces of scrap metals and stones were manually removed prior to milling. The fuel has been analysed several times within the project; 1) a chemical analysis of the raw fuel, 2) a chemical analysis of a sample of pelletized fuel and 3) advanced fuel analysis of pellets by Åbo Akademi. See Appendix A for results of these analyses.

The pellets (6 mm diameter) were pressed from demolition wood for reference case as well as demolition wood with different additives as shown in Table 4. All additives were mixed with the milled demolition wood prior to being pelletized.

Table 4. List of cases with the concentrations of additives

Case	Additive
	[g dry additive/kg dry fuel]
Ref 1	-
Foundry Sand (FS)	30
Kaolin (Kao)	30
Lime	30
Sewage Sludge (SWS 1)	40
Sulphur (S)	10
Ref 2	-
Sewage Sludge (SWS 2)	80
Pb (PbO)	1
Sewage Sludge + Pb (PbO+SWS)	80 g sewage sludge + 1 g Pb

2.3 Test procedure

Prior to each test run, the reactor was cleaned and filled with 500 ml unused sand (Baskarp B35) and a weighed amount of fuel was poured into the fuel hopper. The first heating of the reactor is achieved by the air preheater on the primary air flow. Then, a gas burner was ignited on top of the bed to further increase the temperature. After one hour of gas heating, the screw feeder for the solid fuel was started. The solid fuel was fed for two hours into the reactor in order to reach stationary conditions, before the deposit probes, holding the material samples rings, were inserted at both BW and SH positions. About four hours after insertion of the deposit probes, a fly ash sampling probe was inserted at the outlet of the reactor for a sampling period of one hour. The deposit probes were removed after 8 hours, after which the solid fuel screw feeder was stopped and the reactor cooled down.

During the steady state operation of the reactor, the inlet air flows were fixed by mass flow controllers while the fuel screw feeder rate had to be manually adjusted to get an oxygen concentration of about 5 % in the flue gas. The bed temperature was controlled by the electric air preheater. From the ash content in the fuel, the amount of bed material gradually increased during the tests. To counteract this, some bed material was tapped off through a chute a few times during operation.

After each test, when the reactor had cooled down, the bed material in the reactor was collected in a plastic container. The reactor walls were swept while the removed dust was collected in a separate container. The fuel remaining in the hopper was weighed to enable calculation of the fuel consumption.

2.4 Measurement methods

2.4.1 Fly ash

Fly ash was sampled at the outlet of the reactor during one hour per test case. The sampling was started after at least 4 hours of continuous operation of the furnace, in order to take samples under as representative conditions as possible.

Flue gas was sampled by a probe with a tip facing downwards, meeting the flow, see Figure 2. To get a representative particle distribution, the suction rate through the probe was adjusted to reach isokinetic conditions at the probe tip (meaning that the gas velocity into the probe tip is the same as the gas velocity in the reactor). After the bent probe tip, there is a heated horizontal section reaching out of the reactor. The inner diameter of this horizontal section is wider than the probe tip, implying that the gas velocity in the horizontal section of the probe is reduced compared to the probe tip. Since the flue gas velocity in the lab reactor is lower than in a normal flue gas duct for which the probe is designed, the flue gas velocity in the probe was lower than the design value. This resulted in formation of more solid deposits in the horizontal part of the probe than usual. Most likely, these deposits consist predominantly of relative large particles that settled in the tube due to the relatively low gas velocity.

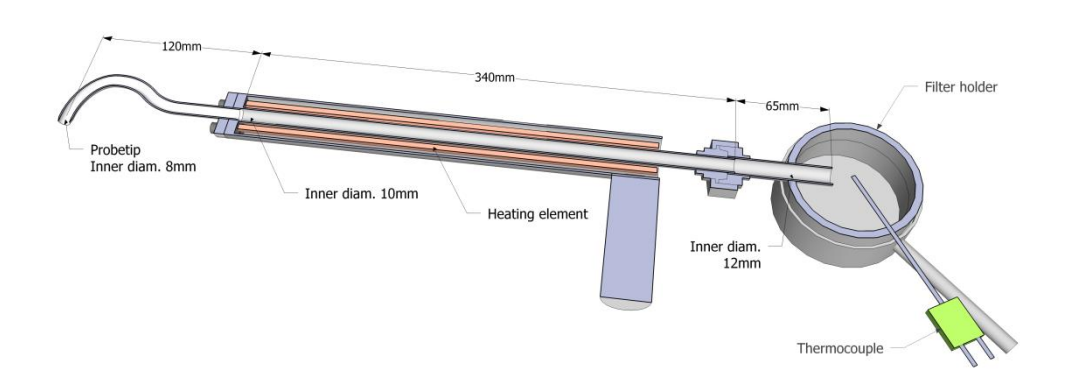


Figure 2. Sketch of the fly-ash sampling probe.

After the horizontal section of the probe, the particle laden flue gas passes two parallel Teflon filters of 90 mm diameter, in a filter holder, where remaining particles are collected. After the filters, the gas passes a silica gel dryer, a gas meter and a suction pump, which controls the sample gas flow.

After each test, the probe was rinsed with acetone to flush out the fly ash deposited. Then the acetone in the fly ash/acetone mixture was vaporized in an oven. Afterwards, the ash from the probe was weighed and analysed by handheld XRF instrument (described in 2.4.4). The filters were analysed by conventional methods, as described in 2.4.5.

2.4.2 Bottom ash

The bed material, containing a mixture of bed sand and bottom ash, was collected after each test run.

2.4.3 Deposit probe sampling

During the test runs, two temperature controlled cylindrical probes with steel samples were inserted into the reactor at the positions marked by red dots in Figure 1. One probe was located between the inlets of secondary and tertiary air, with a material temperature of 400°C simulating elevated boiler wall (BW) conditions. The local air factor at the position of the BW-probe is estimated to about 0.72 based on the flow rates of air and fuel. That is, the condition is clearly sub-stoichiometric, implying reducing conditions. The other probe was placed further downstream (at an air factor of 1.3), simulating conditions of a super heater (SH) with a material temperature of 550°C. Each probe carried three rings of different materials: 16Mo3, 253 MA and Kanthal-A1 (which was replaced by another 16Mo3 ring in the last four test runs, because only negligible corrosion was found on A1). The diameter of the rings was 25 mm. The material samples were exposed during 8 hours.

The deposit probes are heated by the flue gas and are temperature controlled by cooling air at the inside of the deposit rings. The material temperature is measured by a thermocouple in an adjacent ring with same diameter. The air distributor of the cooling air was adjusted during pretests to accomplish an even temperature distribution between the three parallel test rings, resulting in a final temperature difference less than 10°C. During these pre-tests, each ring had an individual thermocouple wielded into the material.

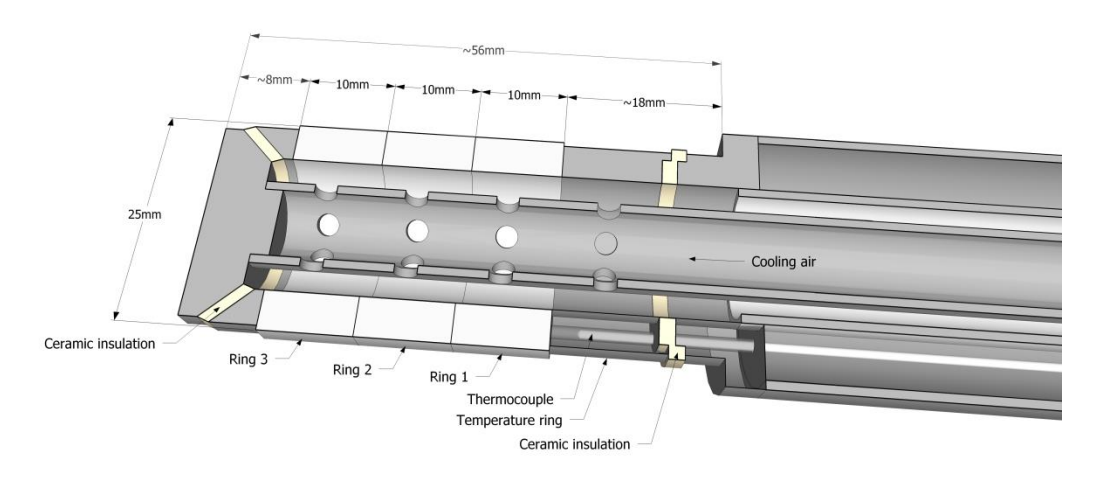


Figure 3. Cross section sketch of the deposit probe. The light-coloured parts are the deposit rings.

The procedure for the handling of deposit/corrosion samples are as follows:

- 1. The sample rings are cleaned in ultrasonic bath in isopropanol. The samples are dried and placed in a desiccator.
- 2. The sample rings are individually weighed together with a marked plastic container prior to exposure in the furnace.

- 3. The rings are mounted on the probes, three different materials on each of two probes.
- 4. The rings are exposed in the furnace. To start with, the probe is inserted with a shielding cover to be heated without being exposed directly to the flue gas. At the start of the 8-hours sampling, the shield is removed.
- 5. After exposure, the probe is cooled in a tin containing silica gel. The rings are later dismounted from the probe. Loose deposits falling off during the procedure are collected in separate plastic containers for each probe.
- 6. The rings are stored in individual plastic containers, which subsequently are placed in a desiccator.
- 7. To remove loose deposits, a ring is threaded on a fall tube where it is being held by a pin, see Figure 4. The fall tube is vertically fixed in a laboratory tripod. When the pin is removed, the ring falls 100 mm before hitting the expanded end of the fall tube. The shock of impact removes the loose deposits which are being collected in a container under the fall tube.
- 8. The loose dust and the ring with the hard deposits are individually weighed, before being stored in a desiccator for later chemical analyses.

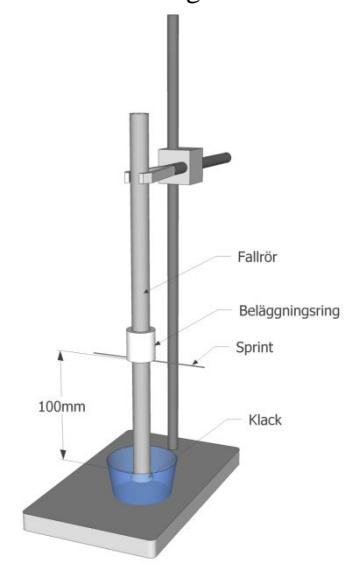


Figure 4. The set up for separating loosely attached deposits from the steel ring.

2.4.4 Handheld XRF analysis of deposits and ashes

Handheld XRFs instruments have been on the market for almost 20 years, during which technical development has improved the measurement accuracy, especially of lighter elements. At present, elements down to Mg (element 12) can be analysed by handheld XRF devices, without the use of helium or vacuum in the sample holder. The detection limits, however, is higher and the precision is lower for lighter elements compared to heavier elements. A Thermo Scientific Niton XL3t handheld x-ray fluorescence (XRF) analyser has been used within this project.

For many sample compositions, such as typical mining samples, it is necessary to measure both lighter elements that emit lower energy x-rays (that are easily absorbed) as well as heavier

elements that emit much higher energy x-rays (that penetrate comparatively long distances through the sample). In these multi-element samples, it is possible that one or more of the elements present act as critical absorbers. The effects of absorption, enhancement, and secondary fluorescence vary widely depending on the chemistry of the sample matrix; but in a sample with many elements in substantial concentrations, such effects are typically present.

Modern XRF analysers automatically adjusts for such effects, as well as various geometric effects, to determine the chemistries of samples of widely different composition, without any requirement for instrument users to input empirical sample-specific calibrations. However, there are occasional samples that require sample-specific calibrations to give accurate results. The case of the ashes and deposits analysed within present project fall in this category where sample-specific calibrations are beneficial. A study which aims to give more accurate calibrations has been implemented by SP by comparison of handheld XRF results of a limited number of ashes and fuels analysed to various conventional methods of analysis. Although this calibration has improved the accuracy of the XRF instrument, the accuracy cannot be guaranteed for all elements in all the different kind of samples obtained within this project. Therefore, the concentrations obtained by the XRF within this report should only be regarded as semi-qualitative, to be used mainly for comparison between test cases. Nevertheless, even if the concentrations measured by XRF should be less accurate for some elements, the values remain essentially proportional to actual concentrations.

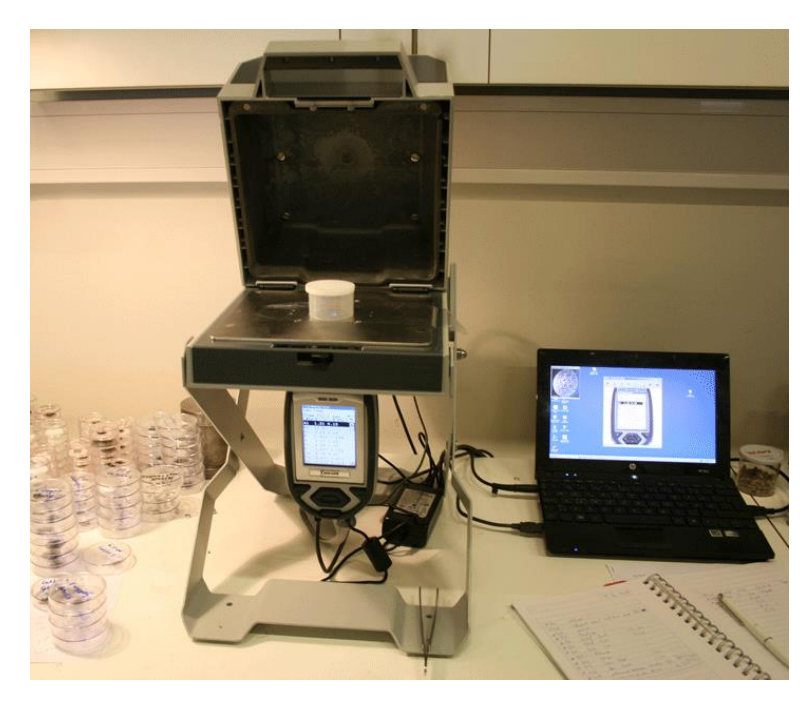


Figure 5. The shielded test stand provides a safe platform for the handheld XRF gun attached underneath the table.

It is important to note that the handheld XRF instrument does not measure C, N, O, and Na. To measure such light elements with the XRF technique, the sample should be placed in vacuum or in helium atmosphere to avoid fluorescence or absorption of gas molecules in the pathway of the photons in X-Rays and fluorescence. The handheld XRF enables fast analysis of a large number of samples that would be very costly to do with ordinary wet chemical methods.

The ash samples were analysed in a plastic cup with a 6 μ m polyethylene-foil at the bottom standing on the test stand. The deposit rings were suspended in a sample holder on the test stand while analysed, see Figure 6.

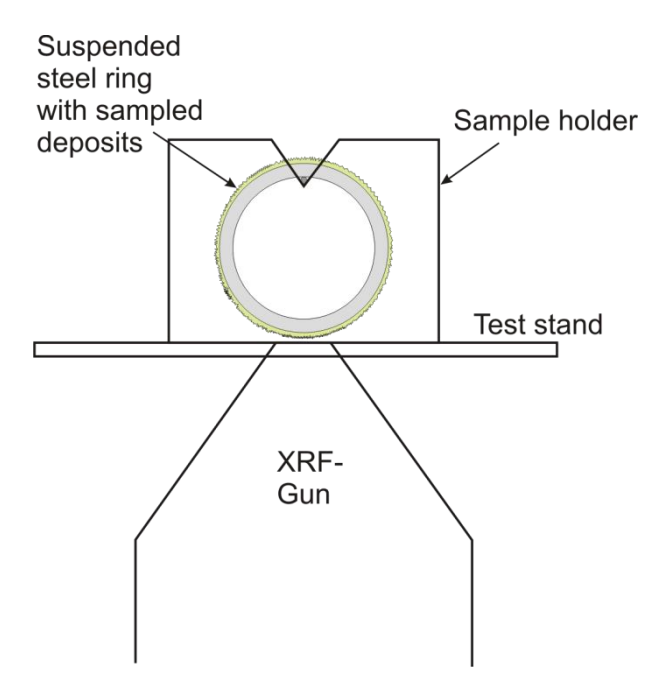


Figure 6. Sketch of set-up when analysing sample deposits by handheld XRF.

2.4.5 Chemical Analysis of fly ash on filters

The filters from the fly-ash sampling were leached in water (at 80°C for 24 h) where after the amount of leached chlorine was determined by ion chromatography with a conductivity detector. The liquid was sequentially evaporated and the rest were leached in an acid mixture of nitric acid, hydrochloric acid and hydrofluoric acid (80°C for 4 h). Leached amounts of Al, Ba, Ca, Cd, Cu, Fe, K, Mg, Mn, Na, Ni, P, Pb, S, Si, Ti and Zn were determined by inductively coupled plasma optical emission spectrometry (ICP-OES). There could be a loss of Si during the leaching in the acid mixture, implying that the given Si-concentrations may be an underestimation of the real value.

2.4.6 Optical studies of corrosion

After the exposure in the furnace, and subsequent analysis of the deposits, the sample rings were cleaned by isopropanol and brushed with a cloth in order to see the alloy surface. A more extensive mechanical cleaning could have removed corrosion products formed, in addition to eventual remaining deposits. However, doing so would have required much more effort.

Macroscopic photos were taken at the inclination angle of the flue gas stream (wind side, 0°)..

3 Results

3.1 Gas concentrations and temperatures

Gas concentrations and reactor temperatures, as average for the eight (8) hours of deposit/corrosion probe exposure, are summarized in Table 5 (without correction for occasional disturbances):

Table 5. Average values of operational parameters during deposit/corrosion probe exposure.

	Ref 1	SWS1	S	Kao	FS	Lime	Ref 2	SWS2	PbO	PbO +SWS
O ₂ [%, d.g.]	4,90	5,07	5,22	5,14	5,09	5,26	5,26	5,18	5,30	5,34
CO [ppm, d.g.]	37	19	34	36	15	16	15	30	13	10
NO [ppm, w.g.]	267	287	280	339	289	272	266	300	270	312
SO ₂ [ppm, w.g.]	11	20	284	24	19	8	4	43	5	33
HCl [ppm, w.g.]	213	244	348	248	230	117	231	227	266	281
H ₂ O [%, w.g.]	12,4	12,6	13,0	13,0	13,1	12,8	12,7	12,3	13,0	13,0
CO ₂ [%, w.g.]	13,9	14,5	14,6	14,7	14,5	14,2	14,4	14,3	14,5	14,1
T _{bed} [°C]	799	799	800	800	800	800	800	800	800	800
T_1 [°C]	907	911	903	878	875	879	873	871	875	870
T_2 [°C]	924	936	935	924	934	930	940	919	937	919
T_3 [°C]	779	779	785	784	785	786	784	782	778	780

SWS – Sewage sludge, S – elemental Sulphur, FS – Foundry Sand, w.g. – wet gas, d.g. – dry gas.

In Table 5, temperature T_{-1} refers to the boiler wall zone (here an average of two thermocouples), T_{-2} is the temperature above tertiary air and T_{-3} is the measured gas temperature close to the SH probe. All these temperatures are measured with bare thermocouples (type K) inserted into the reactor.

3.2 Fly Ash

For each test run, fly ash was collected during a one-hour sampling at the outlet of the reactor, where the gas temperature was about 400°C. The method is described in section 2.4.1. A summary of the concentrations of collected fly ashes is given in Figure 7 below.

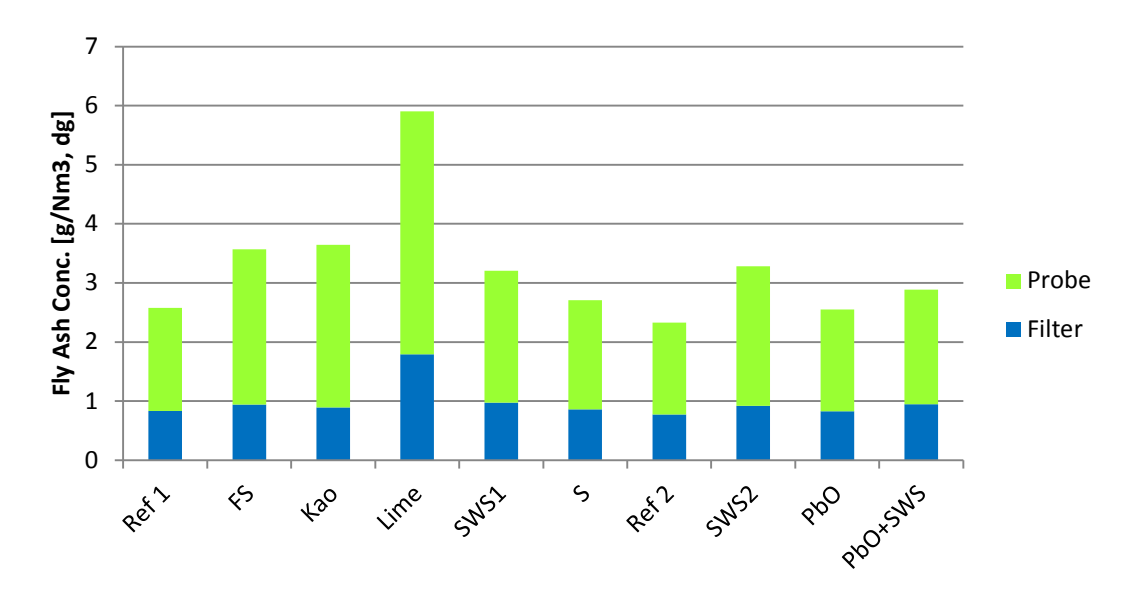


Figure 7. Measured concentrations of fly ash. The green parts of the bars represent the fly ash deposited inside the probe and the blue parts are fly ash collected on the filters.

The elemental compositions of the fly ash sampled on filters, analysed by conventional wet chemical methods, are shown in Figure 8. The top fields of the bars "Bal" (dashed boundaries with white filling) contain undetermined elements to make up for the total collected mass. A large part of this is probably oxygen. A table of concentrations of selected elements, especially those in too low concentrations to be visible in the bar plot, is given in Table 6. Solids removed from the probe after each sampling period were analysed by XRF, providing the elemental distributions presented in Figure 9 and in Table 7.

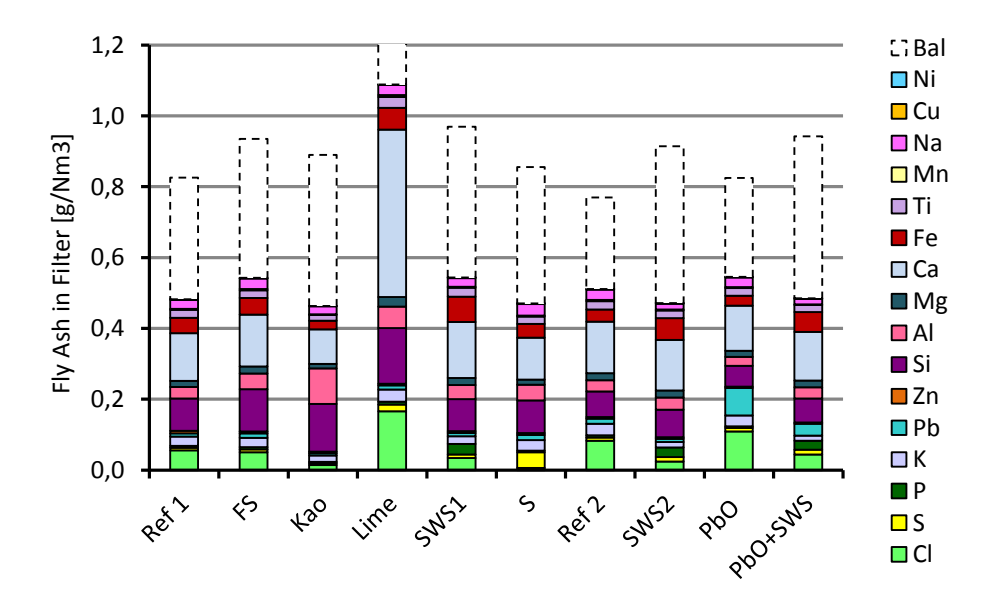


Figure 8. Elemental composition of fly ash on filters, as analysed by conventional wet chemical methods.

Table 6. Elemental concentrations in fly ash on filters, based on the same data as in Figure 8.

Element	Test Cas	se FS	Kao	Lime	SWS1	S	Ref 2	SWS2	PbO	PbO+
%, by mass	Kei I	гэ	NaU	Lille	34/31	3	Rei Z	30032	PDO	SWS
Cl	6,7	5,3	1,5	9,3	3,5	0,65	9,6	2,8	12,7	5,1
S	0,93	0,92	0,70	1,1	1,0	5,2	1,1	1,5	1,1	1,6
P	0,67	0,62	0,41	0,44	3,0	0,56	0,73	3,1	0,60	3,0
Na	3,0	3,2	2,5	1,6	2,4	3,7	3,4	1,9	3,1	1,7
K	3,1	2,8	2,0	1,9	2,3	3,4	3,8	1,8	3,5	1,6
Pb	1,1	1,4	0,8	0,7	0,9	1,7	1,7	1,1	9,1	3,9
Zn	0,87	0,53	0,45	0,29	0,50	0,56	0,46	0,45	0,42	0,38

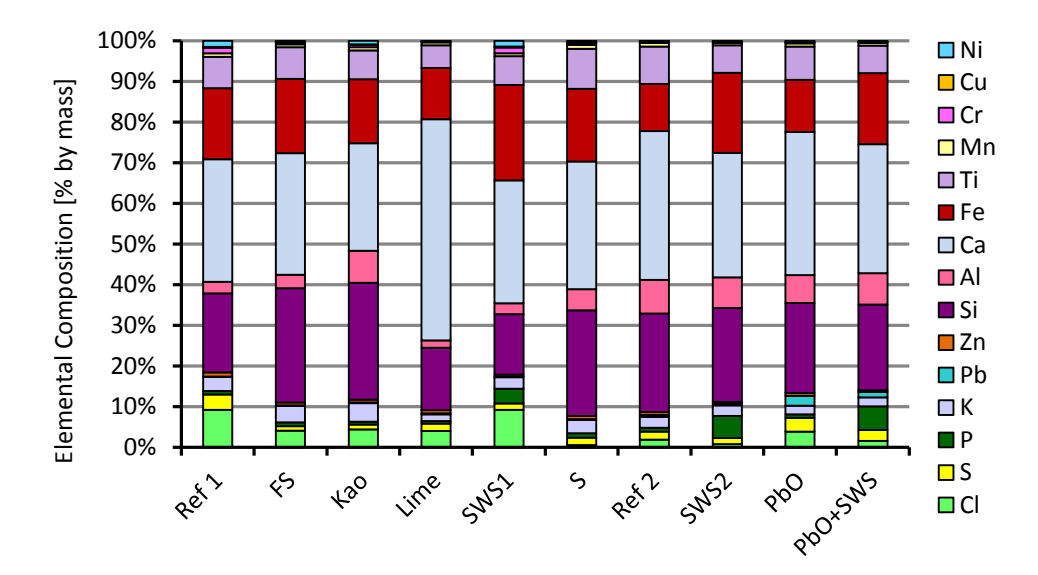


Figure 9. Elemental composition of dust deposited in probe during fly ash sampling, as analysed by XRF.

Table 7. Elemental concentrations in fly ash, deposited in probe, same data as in Figure 9.

Element	Test Case											
%	Ref 1	FS	Kao	Lime	SWS1	S	Ref 2	SWS2	PbO	PbO +		
by mass										SWS		
Cl	6,4	2,3	2,1	1,9	6,0	0,31	1,5	0,59	2,8	1,2		
S	2,7	0,60	0,55	0,88	1,0	0,98	1,7	1,1	2,4	2,0		
Р	0,60	0,52	0,35	0,31	2,4	0,60	0,76	4,2	0,59	4,3		
K	2,4	2,3	2,2	0,80	1,9	1,8	2,3	2,0	1,6	1,6		
Pb	0,08	0,09	0,09	0,10	0,07	0,10	0,38	0,31	1,8	0,97		
Zn	0,70	0,39	0,35	0,36	0,33	0,44	0,62	0,39	0,48	0,33		

3.3 Bottom Ash

The bed material was weighed before and after the test runs, both the bed material remaining inside the reactor and the bed material tapped off during operation are considered here. The difference is roughly considered to represent the amount of bottom ash. The deposits on the wall that fell down during "chimney sweep" after each test run were also collected and weighed. A

summary of the amounts of bottom ash is given in Figure 10, on a scale of the vertical axis as the fraction of the mass of the fuel (including additives) added during the test run. The elemental distributions of the bed material after the tests (bottom ash+ sand) are given in Figure 11, with additional details in Table 8. The elemental composition of the dust particles removed from the reactor walls during sweeping is given in Figure 12 and Table 9. The compositions of the wall deposits are strikingly consistent for the different test cases, even though the Lime additive gives higher concentrations of Ca, Cl and S. Other, more or less expected, observations are that the cases involving sewage sludge provide more phosphorous to the wall deposits and that the sulphur additive increases the sulphur content in the wall deposits.

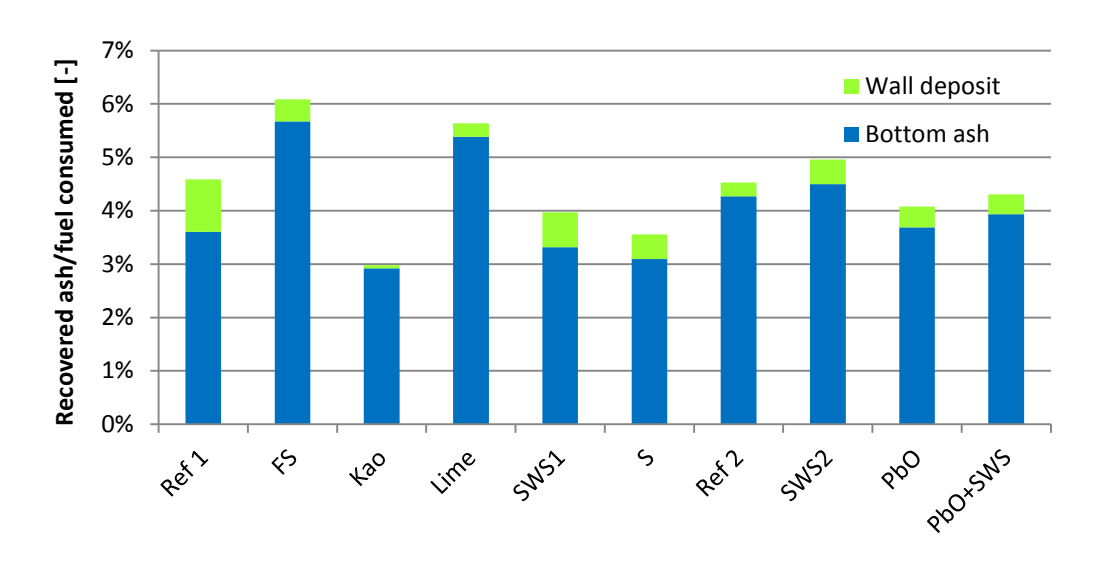


Figure 10. Fraction of fuel recovered as bottom ash.

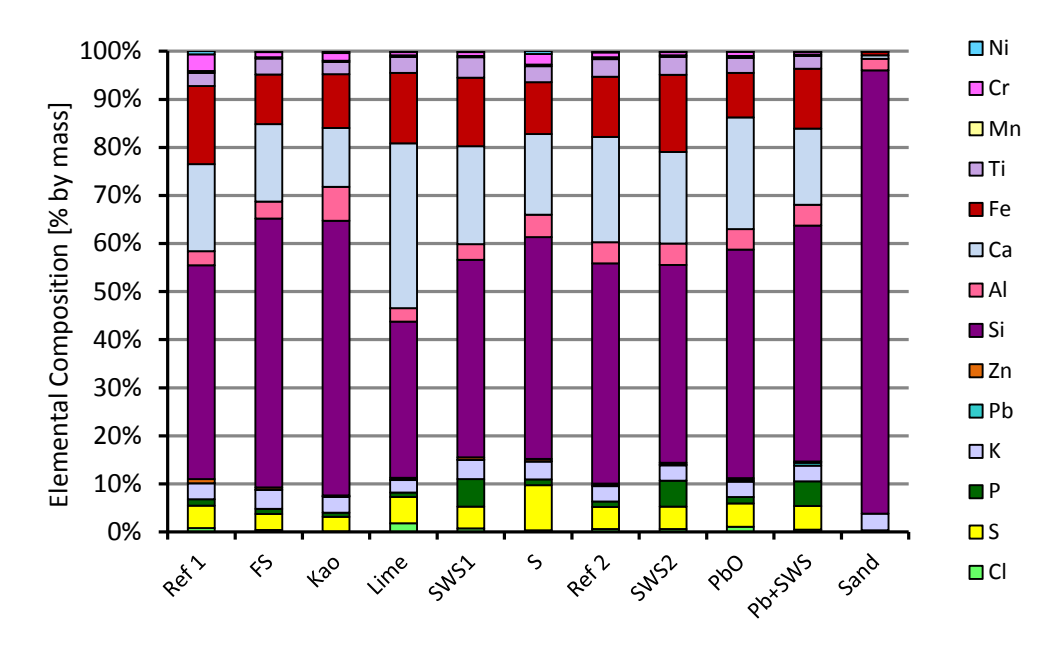


Figure 11. Elemental composition of bed material after test runs, as analysed by means of XRF. An analysis of virgin sand used as bed material is included as reference to the right.

Table 8. Concentrations of elements in bed material, same analysis as illustrated in Figure 11.

Element	Test Ca	se									
[%, mass]	Ref 1	FS	Kao	Lime	SWS1	S	Ref 2	SWS2	PbO	PbO+ SWS	Sand
Cl	0,24	0,12	0,03	0,65	0,22	0,10	0,21	0,22	0,33	0,18	0,00
S	1,4	1,0	1,0	1,9	1,4	<u>2,9</u>	1,5	1,7	1,5	1,7	0,01
Р	0,41	0,35	0,28	0,34	<u>1,8</u>	0,37	0,37	2,0	0,43	1,8	0,12
K	1,0	1,2	1,1	0,92	1,2	1,2	1,0	1,2	0,98	1,2	1,2
Pb	0,005	0,010	0,009	0,017	0,013	0,008	0,04	0,09	0,11	0,21	0,000
Zn	0,25	0,15	<u>0,06</u>	0,13	0,16	0,14	0,12	0,12	0,12	0,09	0,00

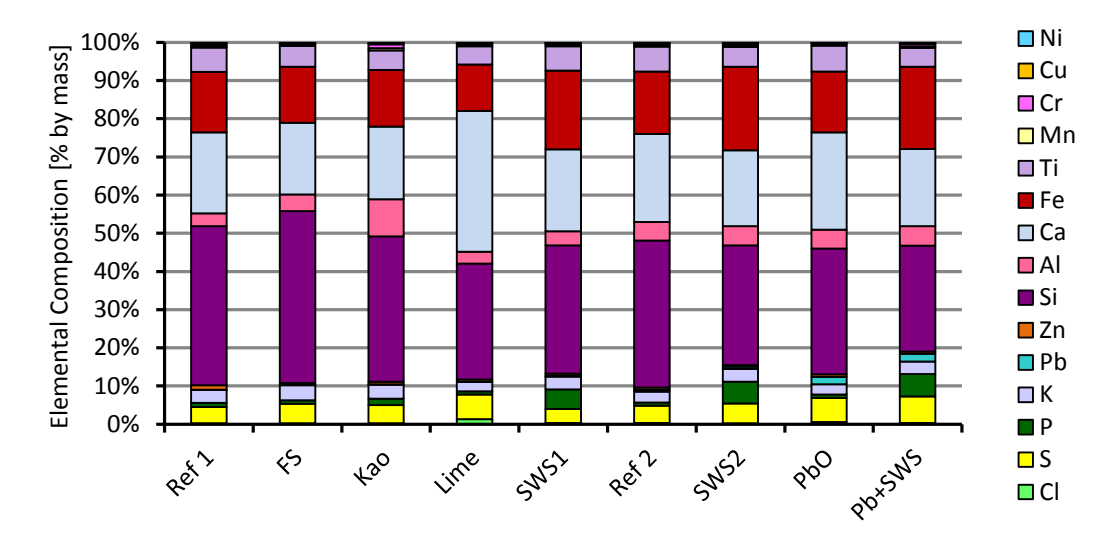


Figure 12. Elemental composition of solids removed from the vertical walls after each test, as analysed by XRF. The sample from the "Sulphur" case is omitted because the sample handling failed.

Table 9. Concentrations of some elements, same data as illustrated in Figure 12.

	Ref 1	FS	Kao	Lime	SWS1	Ref 2	SWS2	PbO	PbO+ SWS
Cl	0,09	0,11	0,08	<u>0,57</u>	0,13	0,14	0,10	0,25	0,14
S	1,7	1,9	1,9	<u>2,8</u>	1,5	1,9	2,4	2,7	3,2
Р	0,43	0,37	0,65	0,33	<u>2,1</u>	0,35	<u>2,6</u>	0,37	<u>2,7</u>
K	1,3	1,5	1,5	1,1	1,3	1,2	1,5	1,1	1,5
Pb	0,044	0,040	0,047	0,044	0,046	0,22	0,26	0,82	<u>0,93</u>
Zn	0,46	0,20	0,24	0,26	0,23	0,22	0,22	0,27	0,28

3.4 Deposits

Some of the deposits on the rings fell off during handling and another part was intentionally removed by a controlled mechanical "knock" on each ring. The collected loose deposits could not be referred back to individual rings and were consequently handled as lump samples for the three rings on each probe. In some cases, the masses of the "loose" deposits were significantly higher than the corresponding masses of the "hard" deposits. The masses of the "loose" deposits are generally fairly unreliable because some of the loose dust like particles may have fallen off inside the reactor during the withdrawal of the probe. However, the "loose" deposits are of secondary interest here as they probably would have been easily removed by ordinary soot blowing methods in full scale boilers.

3.4.1 Deposits on boiler wall (BW) probes

The deposition rates found on the BW-probes are shown in Figure 13, where the blue part of the bars represent the amount of deposits that stuck to the sample rings even after a mechanical

knock, and the red part represents the recovered loose dust that fell off during handing and knocking. For the case of "kaolin", it was observed that build-ups were formed on the walls during operation. These build-ups appeared to be of a "fluffy" structure, and occasionally, when grown large in size, they detached from the walls and fell down towards the bed. Such falling wall deposits may have removed some of the loose deposits from the BW-probe, implying that the red fraction of the bar for the kaolin case (in Figure 13) probably is unrepresentatively low. The amounts of "hard" deposits on the individual rings are compared in Figure 14. Please note that part of the mass gain can be caused by corrosion products, especially for the 16Mo3 samples. The elemental composition of the loose material (as analysed by XRF) is shown in Figure 15 and in Table 10, while averages of the analyses of the hard deposits are given in Table 11. The analyses of the hard deposits are further reported in Section 3.5 and in Appendix A .

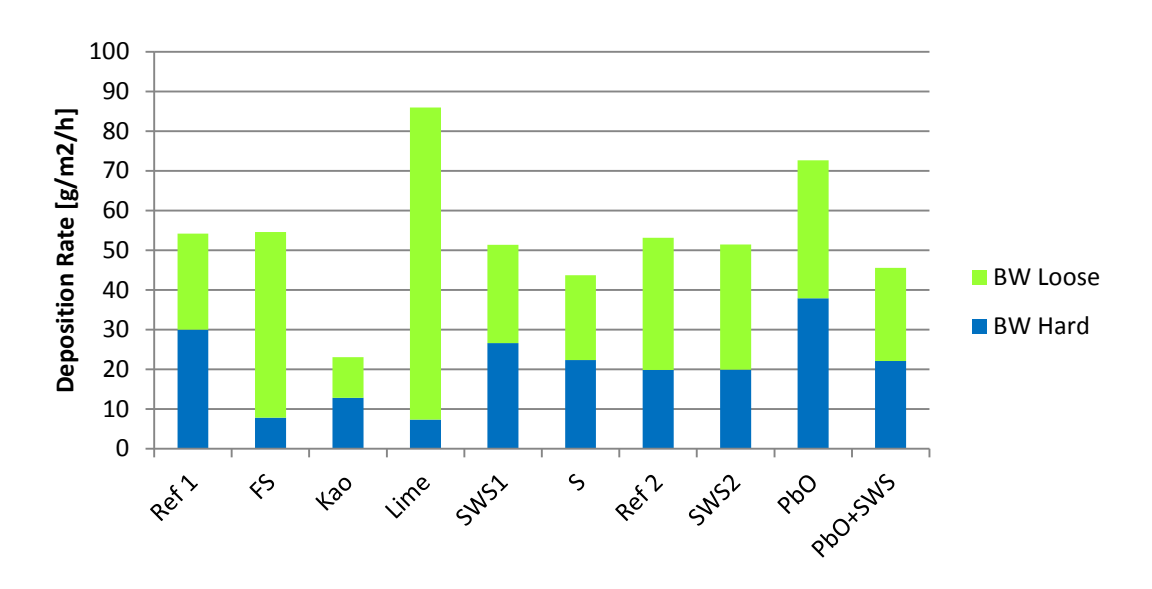


Figure 13. Deposition rate on rings at boiler wall (BW) position, as average of 3 rings.

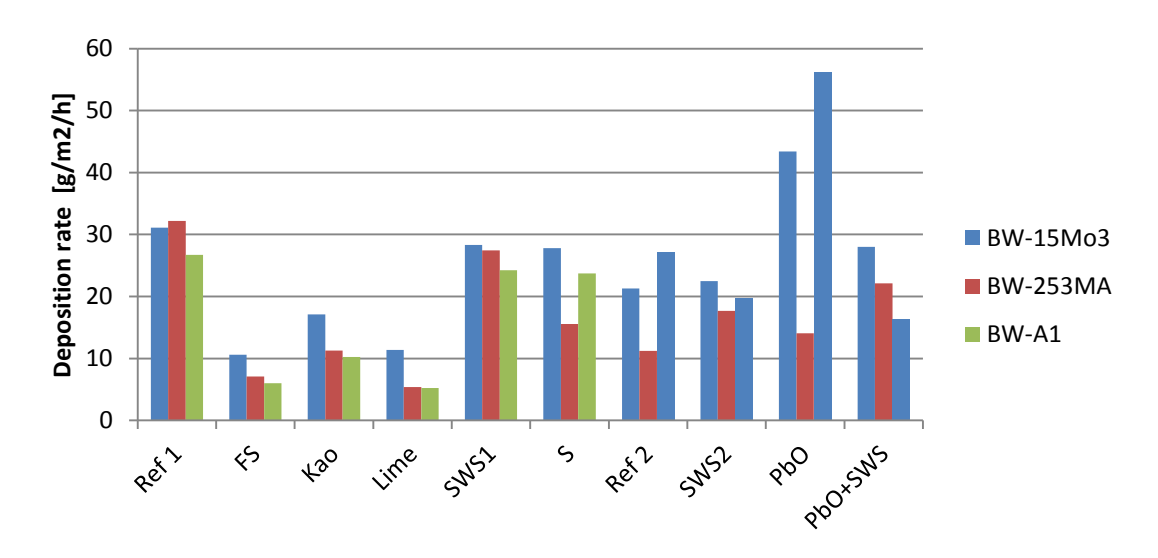


Figure 14. Deposition rate of "hard" deposits on individual rings.

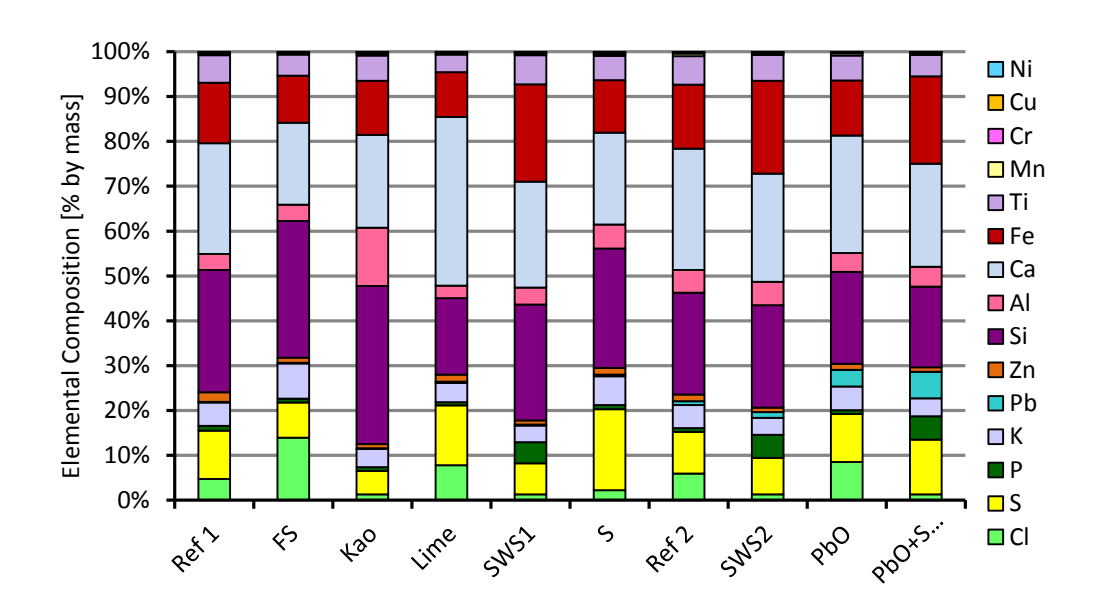


Figure 15. Elemental composition of "loose" deposits on BW probes, analysed by XRF.

Table 10.	Selected elements of low concentrations in Figure 15.
-----------	---

% mass	Ref 1	FS	Kao	Lime	SWS1	S	Ref 2	SWS2	PbO	PbO+ SWS
Cl	2,5	6,4	1,0	4,2	0,71	1,1	3,0	0,68	4,1	0,67
S	5,6	3,6	3,9	7,1	3,7	9,2	4,7	4,2	5,1	6,3
P	0,57	0,38	0,60	0,38	2,6	0,50	0,42	2,7	0,40	2,7
K	2,7	3,6	3,0	2,3	2,0	3,2	2,6	1,9	2,5	2,1
Pb	0,079	0,087	0,13	0,16	0,11	0,17	0,42	0,68	1,78	3,05
Zn	1,1	0,52	0,70	0,83	0,51	0,78	0,74	0,51	0,66	0,50

Table 11. Average of selected elements found in <u>hard</u> deposits on rings exposed at the BW position.

% mass	Ref 1	FS	Kao	Lime	SWS1	S	Ref 2	SWS2	PbO	PbO+ SWS
Cl	7,6	18,0	2,6	17,3	3,0	9,4	12,6	4,1	9,9	1,8
S	5,7	18,5	2,0	25,3	3,8	16,7	11,9	3,5	13,1	8,4
Р	1,6	1,4	1,1	1,6	7,0	1,1	1,3	5,6	1,3	5,7
K	4,9	10,7	5,6	5,5	3,0	9,7	8,5	4,2	5,6	3,8
Pb	1,4	2,6	1,3	3,2	1,7	1,0	6,4	6,9	15,5	7,6
Zn	9,2	5,5	5,7	2,5	7,1	3,6	3,7	3,5	2,1	3,4

3.4.2 Deposits on super heater (SH) probes

The average deposition rates found on the SH-probes are shown in Figure 16, where the blue part of the bars represent the amount of deposits that stuck to the sample rings after a mechanical knock, and the red part represents the loose dust that fell off during handing and knocking. The distribution of "hard" deposits between the individual rings is shown in Figure 17 and the elemental compositions of the loose material (as analysed by XRF) are shown in Figure 18 and in Table 12. Averaged concentrations of the hard deposits on the rings are given in Table 13. More detailed analyses of the hard deposits are reported in Appendix B.

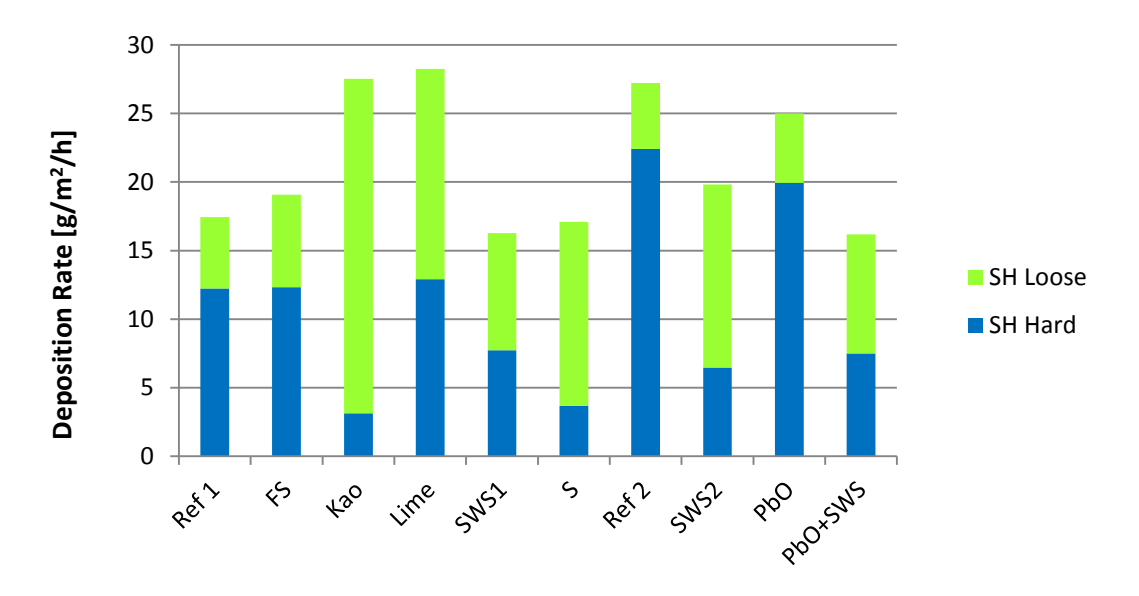


Figure 16. Deposition rate on rings at superheater position, as average of three (3) rings.

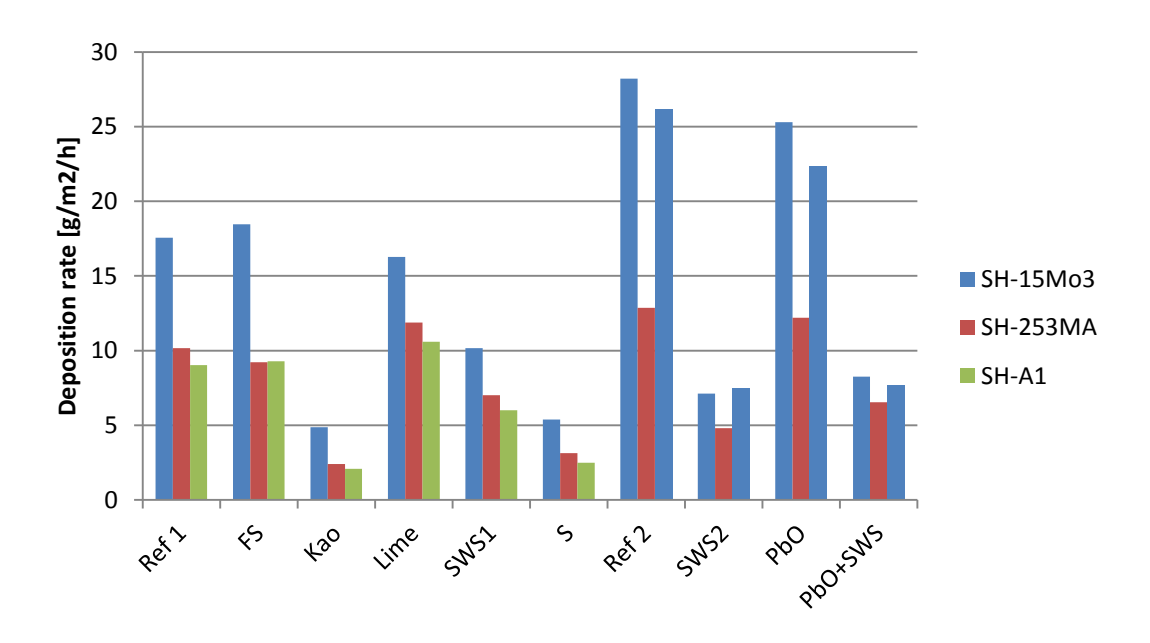


Figure 17. Deposition rate of "hard" deposits on individual rings at SH.

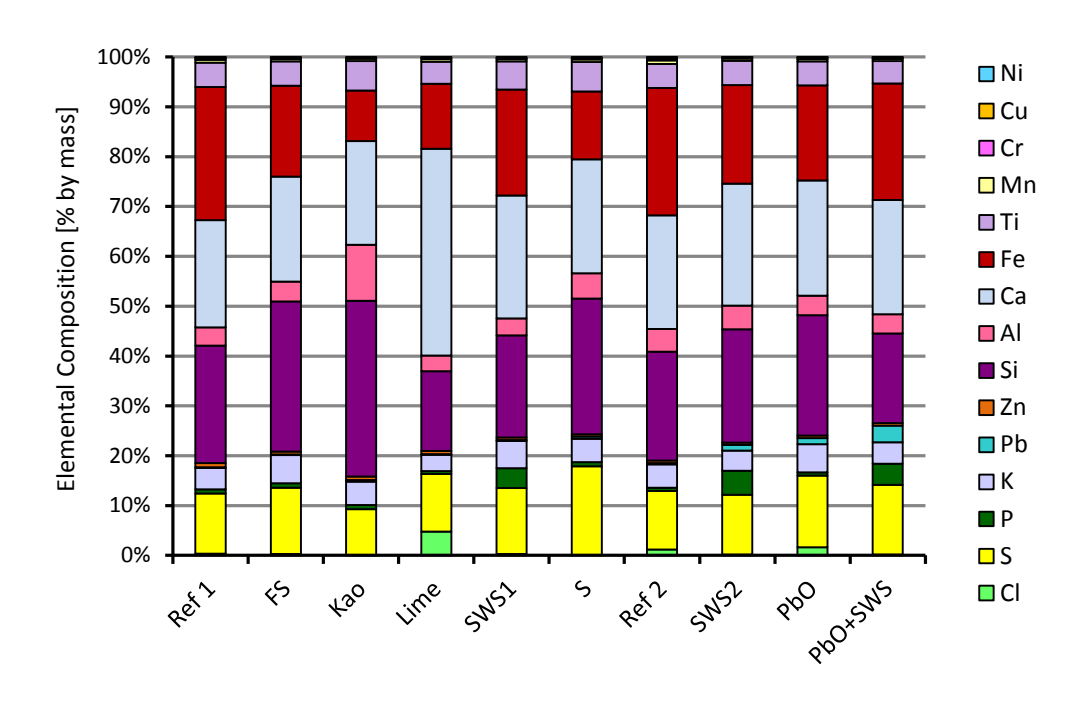


Figure 18. Elemental composition of "loose" deposits on superheater probes.

Table 12. Concentrations of selected elements of low concentrations in Figure 18.

%, mass	Ref 1	FS	Као	Lime	SWS1	S	Ref 2	SWS2	PbO	PbO+ SWS
Cl	0,22	0,15	0,022	3,3	0,16	0,034	0,61	0,08	0,62	0,09
S	7,9	6,3	4,8	8,1	7,2	10,3	6,0	5,8	5,4	6,5
P	0,53	0,42	0,44	0,43	2,15	0,45	0,31	2,3	0,23	2,0
K	2,8	2,7	2,5	2,3	2,9	2,7	2,4	2,0	2,2	2,0
Pb	0,054	0,067	0,15	0,060	0,11	0,24	0,14	0,54	0,47	1,6
Zn	0,54	0,25	0,35	0,44	0,30	0,26	0,26	0,22	0,19	0,23

Table 13. Average of selected elements found in <u>hard</u> deposits on rings exposed at the SH position..

%, mass	Ref 1	FS	Као	Lime	SWS1	S	Ref 2	SWS2	PbO	PbO+ SWS
Cl	3,8	1,4	0,1	19,3	0,5	0,2	8,1	0,2	10,8	0,4
S	34,2	31,9	20,8	13,8	32,4	48,1	19,3	30,5	22,4	33,3
Р	0,9	1,0	0,9	0,8	4,4	1,0	1,0	4,0	0,9	4,1
K	19,2	16,9	6,8	12,5	17,6	10,7	14,2	12,9	14,8	11,6
Pb	0,1	0,1	0,4	0,1	0,2	1,2	0,8	1,3	2,4	6,0
Zn	1,1	0,6	0,5	0,5	0,7	0,7	0,8	0,5	0,7	0,5

3.5 Study of selected elements in the deposits

The distributions of elements measured by the XRF on the samples of hard deposits are given in the Appendices as bar plots for different positions on all the exposed rings. It is difficult to draw generalized conclusions directly from such large number of plots. Therefore, to simplify comparisons of test cases, the data from those plots have been compiled into one plot per selected element and position in this chapter. The graphs show fractions of elements detected, excluding elements of the substrate alloy and undetermined elements ("Balance"). The averages are calculated from analyses of the three rings located in parallel on one probe, keeping the angle dependence. The horizontal axes in the plots represent the analysed position on the deposit rings with respect to the direction of the gas flow. Every ring is represented by a line of different format while the test cases are separated by colour.

3.5.1 Cl in deposits

At the BW position (Figure 19) the additives of kaolin and sewage sludge provided clearly reduced chlorine concentrations. The additive sulphur reduced the chlorine concentration on the leeward side of the probe. The additives lime and foundry sand increased the average concentrations of Cl in the BW deposits.

At the SH position (Figure 20), the lime and the PbO additives increased the chlorine contents significantly. The foundry sand reduced the chlorine concentration marginally while the other additives (sulphur, sewage sludge) clearly reduced the concentrations of Cl in the SH-deposits. It is also likely that the kaolin did reduce the chlorine concentration, although not proven by these analyses.

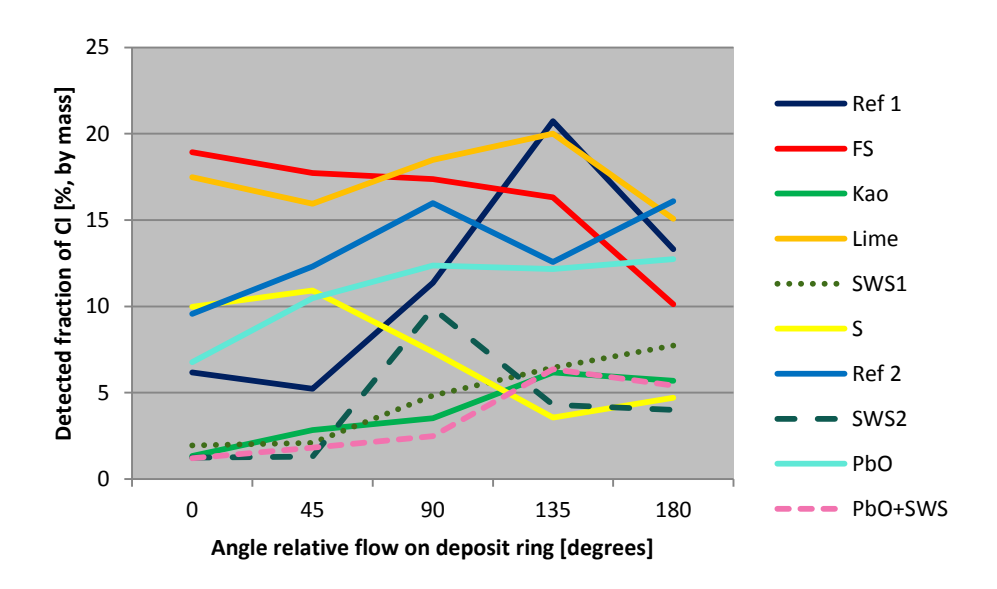


Figure 19. Detected concentrations of Cl in deposits on boiler wall (BW) probes as function of angle on the ring (0° is windward side while 180° is leeward side).

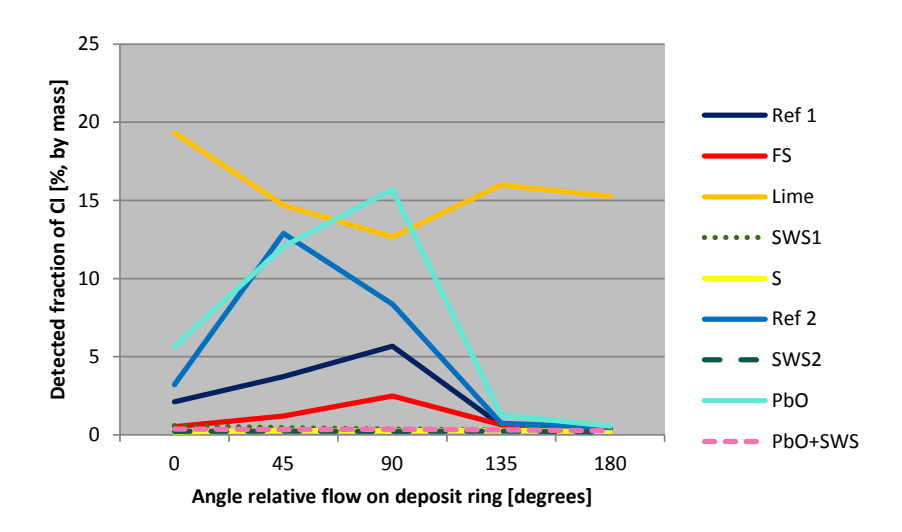


Figure 20. Detected concentrations of Cl in deposits on super heater (SH) probes as function of angle on the ring (0° is windward side while 180° is leeward side).

3.5.2 S in deposits

The sulphur concentrations increased in the BW deposits relative to the reference case when using the additives lime, foundry sand and, not surprisingly, sulphur (Figure 21). The results from sewage sludge were inconclusive; the sulphur concentration was lower than reference on the windward side while it was higher on the leeward side. The additive kaolin showed reduced sulphur concentrations at BW.

Regarding the sulphur concentrations in the deposits at the SH-position (Figure 22), it is obvious that lime reduces the sulphur concentration in the deposits. The concentrations of S in the deposits are increased by the sulphur additive. The other additives (foundry sand and sewage sludge) showed only minor effects upon the concentrations of S in the SH-deposits.

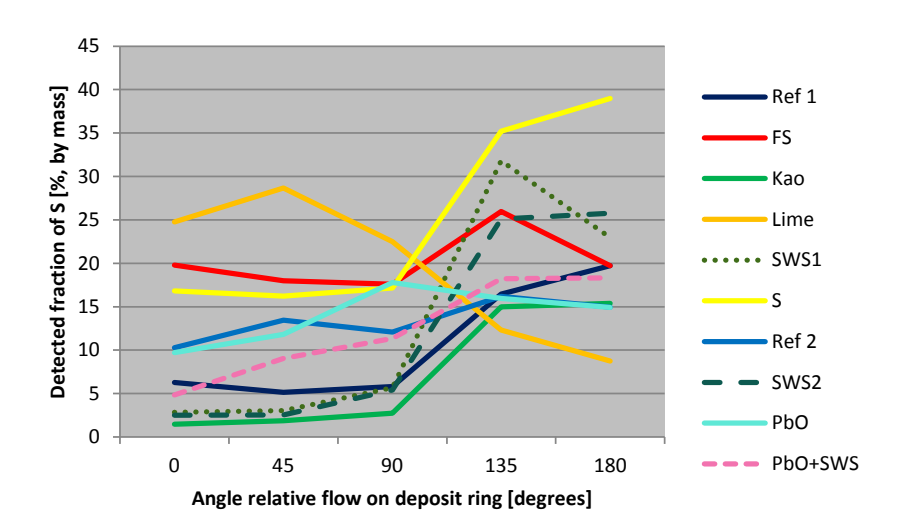


Figure 21. Detected concentrations of S in deposits on boiler wall (BW) probes as function of angle on the ring (0° is windward side while 180° is leeward side).

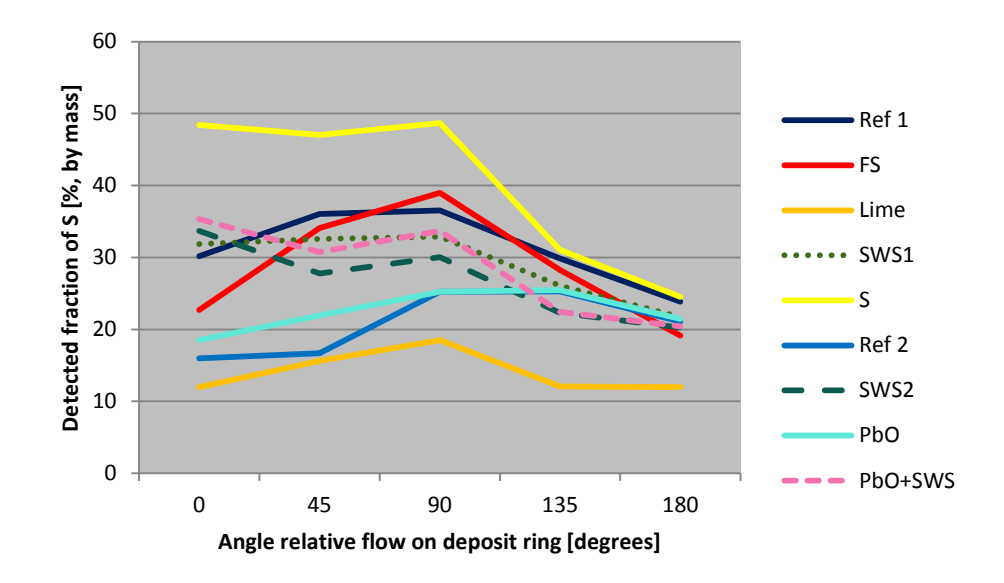


Figure 22. Detected concentrations of S in deposits on super heater (SH) probes as function of angle on the ring (0° is windward side while 180° is leeward side).

3.5.3 Zn in deposits

The concentrations of Zn measured in the deposits on the boiler wall (BW) probes are presented in Figure 23, showing that all additives reduce the concentrations of Zn compared to the reference case (Ref 1). This could be a consequence of unrepresentatively high amount of zinc supplied by the fuel of the Ref 1 case, which is highlighted by the much lower zinc concentrations found from the Ref 2 case. Most beneficial (with respect to reduction of Zn in the deposits) are the lime and sulphur additives, while the sewage sludge displays the least improvement. It also seems like additional Pb in the fuel reduces concentrations of zinc in the BW deposits.

The concentrations in the deposits on the superheater (SH) probe (Figure 24) are generally more than one order of magnitude lower than in the boiler wall position. In this position, all additives tested were found to reduce the concentration of Zn in the deposits. There is little difference between additives. Please note that the XRF-measurements for the "Kaolin" case at SH-rings were incomplete and are omitted from the figure.

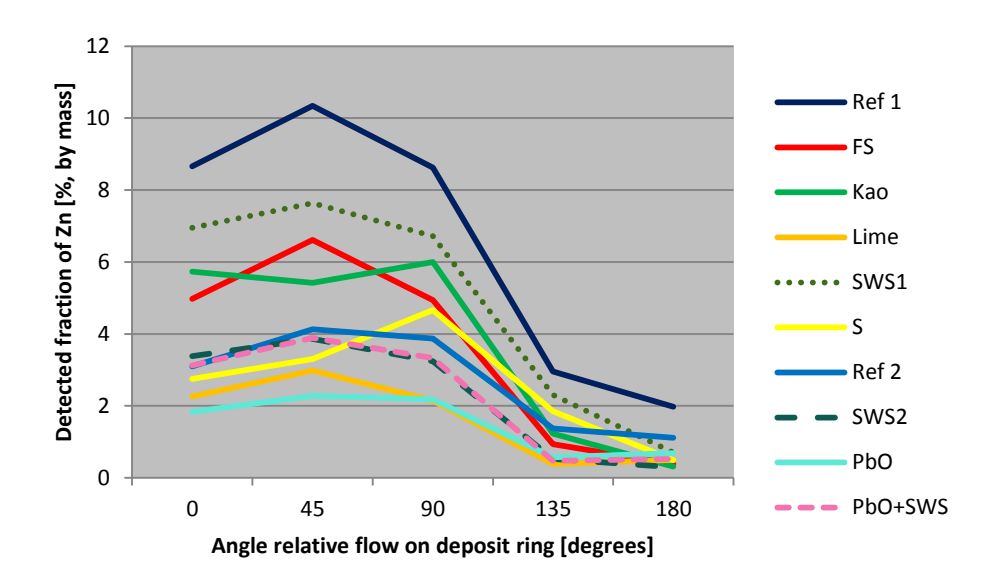


Figure 23. Detected concentrations of Zn in deposits on boiler wall (BW) probes as function of angle on the ring (0° is windward side while 180° is leeward side).

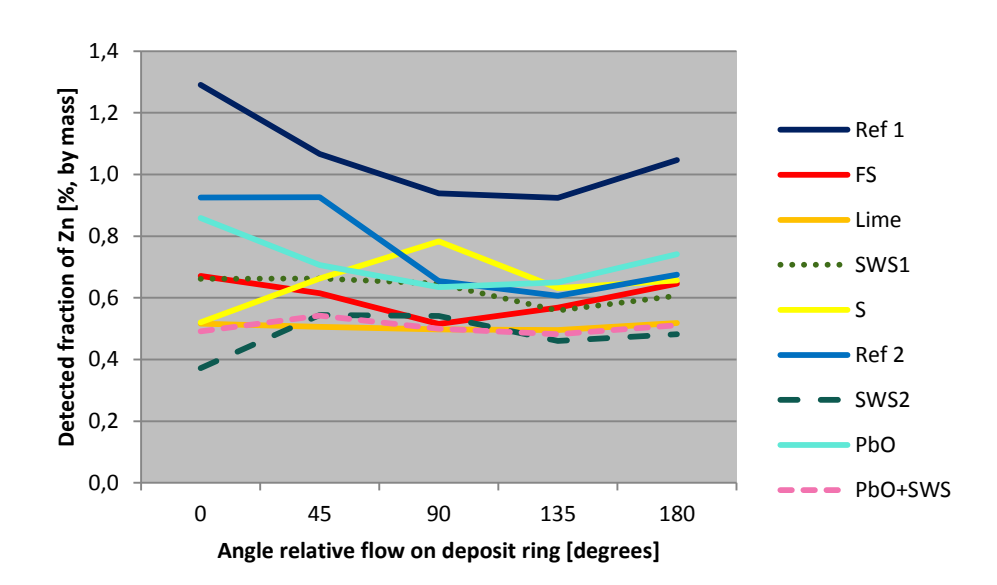


Figure 24. Detected concentrations of Zn in deposits on super heater (SH) probes as function of angle on the ring (0° is windward side while 180° is leeward side).

3.5.4 Pb in deposits

Regarding the analyses of Pb in the deposits, the XRF instrument was upgraded between first and second set of tests. For some reason, this upgrade resulted in generally higher detected lead concentrations in the second set of tests (Cases: Ref 2, SWS2, PbO and PbO+SWS). Because of this, lead concentrations from first and second set of tests should not be directly compared.

The detected concentrations of Pb in the deposits on the boiler wall (BW) probes are presented in Figure 25. In contrary to Zn, none of the additives shows a clear reduction of Pb concentrations compared to the reference case. Only sulphur, and maybe kaolin, reduced the Pb concentrations in the deposits at BW to some degree. The additives of lime and foundry sand showed increased concentrations of Pb. From the second set of tests, it is obvious that PbO added to the fuel increased the lead content of the BW deposits, but the effect is counteracted by the addition of sewage sludge in the PbO+SWS case. Comparing Ref 1 to SWS1 and Ref 2 to SWS2 show no significant effect of the sewage sludge on lead content in BW deposits.

Figure 26 shows detected concentrations of Pb in the deposits on the super heater probe (SH). Here it is interesting to note that both sewage sludge and PbO give increased lead concentrations in SH-deposits. Clearly most Pb is found in the SH deposits when both PbO and sewage sludge are added to the fuel.

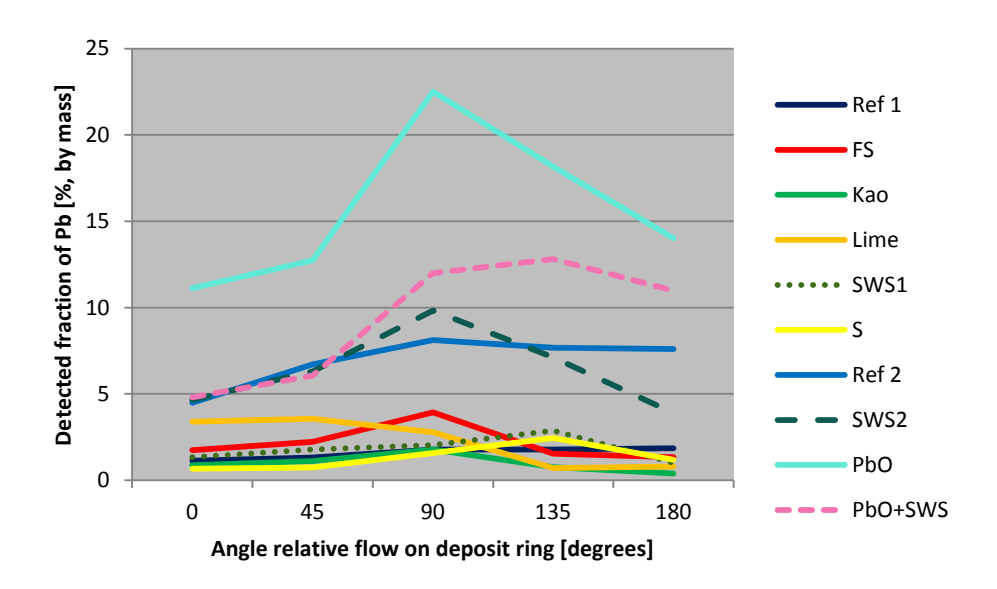


Figure 25. Detected concentrations of Pb in deposits on boiler wall (BW) probes as function of angle on the ring (0° is windward side while 180° is leeward side).

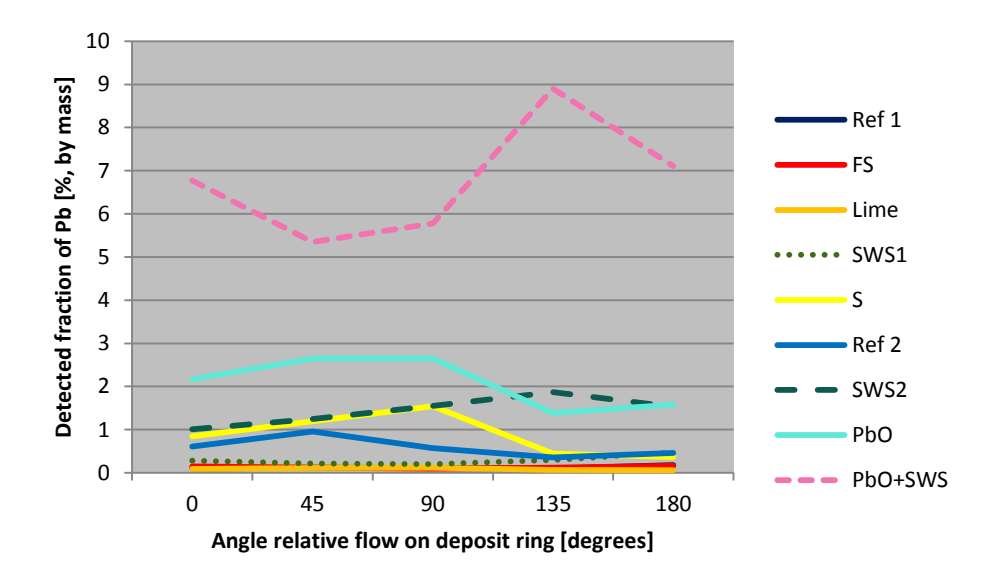


Figure 26. Detected concentrations of Pb in deposits on super heater (SH) probes as function of angle on the ring (0° is windward side while 180° is leeward side).

3.5.5 K in deposits

Regarding the measured concentrations of K, at both positions, in Figure 27 and Figure 28, it is hard to draw many conclusions because the variations on individual rings are often larger than the difference between test cases. One observation is that the additive sulphur reduced the concentrations of K at SH but increased it at BW. The sewage sludge showed, at average, reduced concentrations of K at both BW and SH. The lime additive reduced the concentration of K at SH and on the leeward side on the BW deposits.

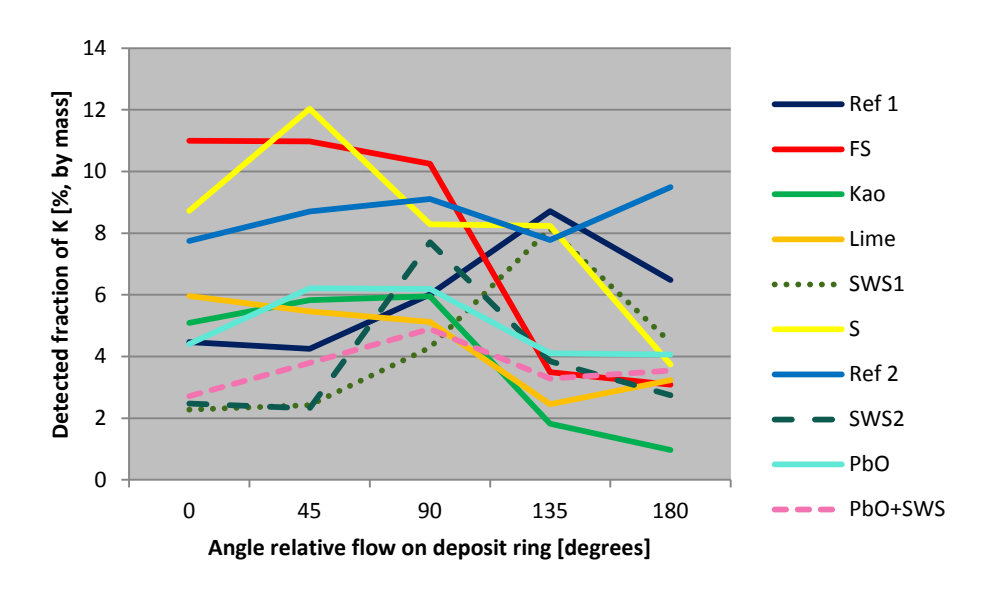


Figure 27. Detected concentrations of K in deposits on boiler wall (BW) probes as function of angle on the ring (0° is windward side while 180° is leeward side).

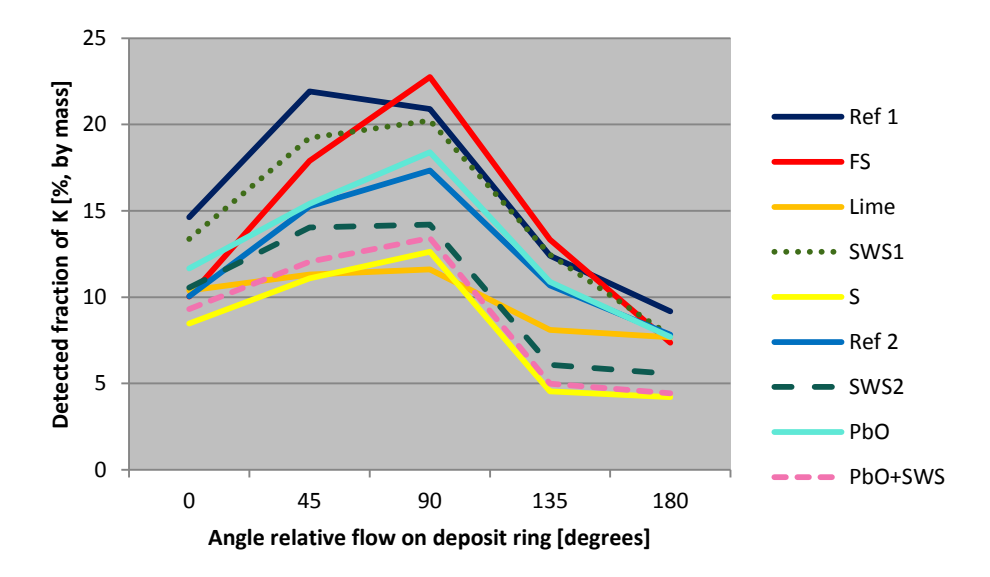


Figure 28. Detected concentrations of K on superheater (SH) proves as function of angle on the ring deposits on boiler wall (BW) probes as function of angle on the ring (0° is windward side while 180° is leeward side).

3.5.6 Ca in deposits

At BW, the concentrations of Ca were decreasing from the windward side towards the leeward side for all test cases except the Lime case, see Figure 29. All additives except Sewage sludge showed lower Ca concentrations than the reference case at the windward side.

At the SH, the Ca-concentration profiles were more even as shown in Figure 30, with increased concentrations towards the leeward side. The lime case showed clearly higher concentrations of Ca than the other cases. The additive sewage sludge increased the Ca concentrations slightly compared to the reference case, while the other additives showed no significant difference from the reference case.

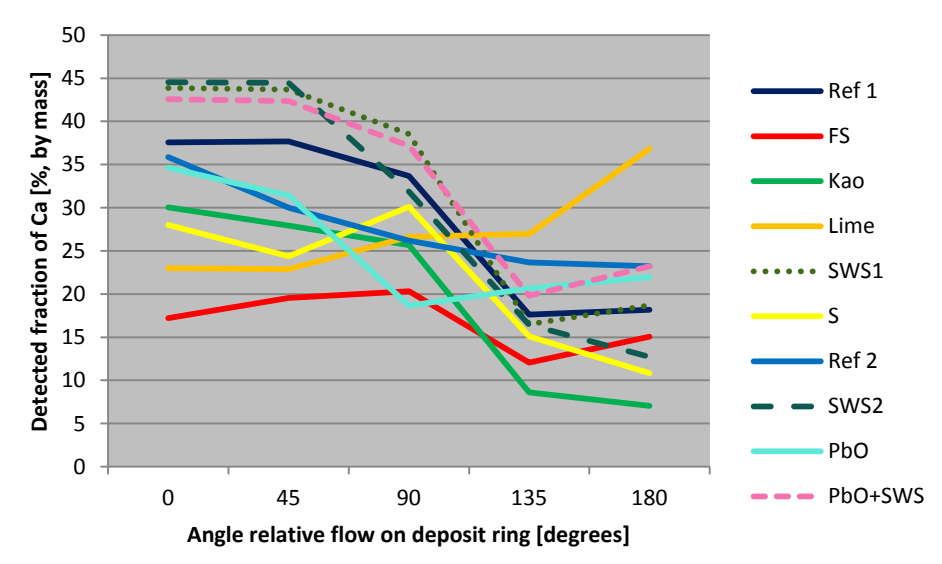


Figure 29. Detected concentrations of Ca in deposits on boiler wall (BW) probes as function of angle on the ring (0° is windward side while 180° is leeward side).

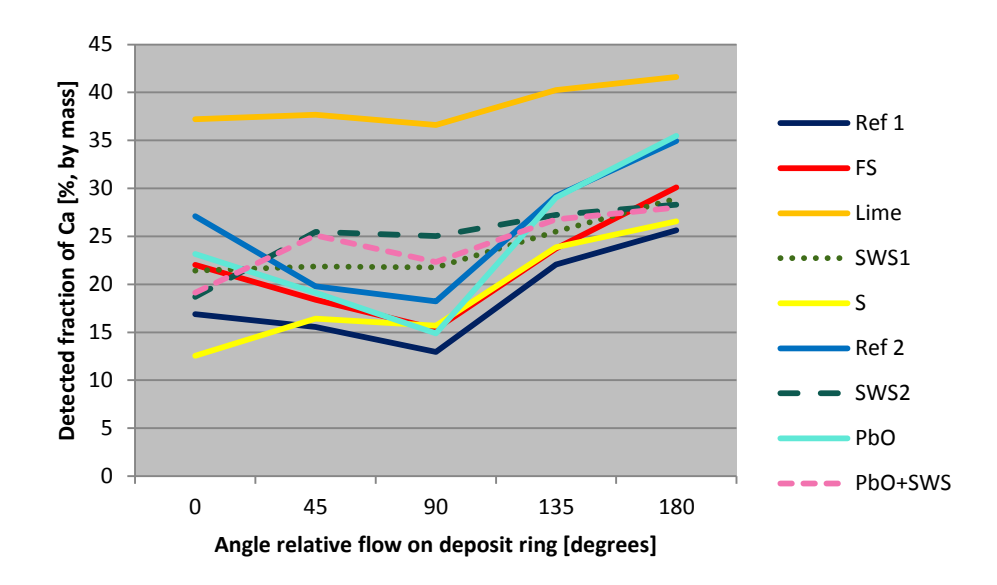


Figure 30. Detected concentrations of Ca in deposits on superheater (SH) prove as function of angle on the ring (0° is windward side while 180° is leeward side).

3.6 XRD Analyses

A number of deposit samples from the BW-probes were analysed by XRD (X-Ray Diffraction) at Gävle Högskola. The relatively small amount of deposits collected made the measurements difficult, and only five samples were successfully analysed. They were:

- 1. Loose deposits from BW-probe, Case Ref 2
- 2. Loose deposits from BW-probe, Case SWS 2
- 3. Loose deposits from BW-probe, Case PbO
- 4. Loose deposits from BW-probe, Case PbO+SWS
- 5. Hard deposits from BW-probe, Case PbO+SWS

The large number of chemical compounds present in the samples made identifications difficult for the compounds present in low concentrations. For instance, Pb₂O, PbO, ZnS, FeS and FeS₂ shows overlapping peaks with each other as well as with NaCl and KCl, which prevented positive identification of these compounds.

A semi-qualitative estimation of the distribution of identified compounds in the samples is given in Table 14. The diffraction intensity (counts) for the different compounds are divided into strong intensity denoted "S", medium intensity – "M" and weak intensity – "W".

Table 14. A qualitative estimation of the distribution of identified compounds in the samples by XRD

Compound	Loose Deposit Ref 1	Loose Deposit SWS2	Loose Deposit PbO	Loose Deposit PbO+SWS	Hard Deposit PbO
SiO ₂	S	S	S	S	W
NaCl	M		M		S
Ca(SO ₄)	M	M	M	M	W
KCI	W		M		M
TiO ₂	W	W	W	W	
Fe ₂ O ₃	W		W	M	M
CaAl ₂ Si ₂ O ₈	W	W	W	W	
Fe ₃ O ₄		М		W	

^{*)} Fe₃O₄ may be difficult to distinguish from Fe₂O₃ by this method

From the Table 14, it is notable that the XRD failed to detect neither NaCl nor KCl for the two cases when sewage sludge was added to the fuel (SWS2 and PbO+SWS). In the reference case, the fraction of alkali chlorides was 21 %, which was increased to 28 % when PbO was added to the fuel. The loose deposits did contain a high fraction of SiO_2 and a substantial amount of $CaSO_4$. When sewage sludge was added to the fuel, the iron was detected as Fe_3O_4 instead of Fe_2O_3 , but this is uncertain because it is hard to differentiate between these two compounds with this measurement technique.

In the hard deposit, closer to the tube surface, the fraction of alkali chlorides increases, as indicated by the last column of Table 14. The results comes from the PbO case, which was the worst case regarding the corrosion rate and the XRD analysis reveals an alkali fraction of 86%! Even though the figures come from a basically qualitative method it gives an idea of the situation.

The XRD results show that for most cases, the fraction of NaCl is higher than the fraction of KCl; it is four times more NaCl than KCl in the loose deposits in the Ref 2 case and almost three times more in the hard deposits of the PbO. On the other hand, the fractions of NaCl and KCl are quite evenly matched in the loose deposit of the PbO case. The comparison between NaCl and KCl is of interest here because the XRF analyser used detects the concentrations of K but not Na. Since the fuel contains roughly the same quantities of these alkali metals, it could have been assumed that they would show up at roughly equal concentrations in the deposits as well. However, these XRD analyses show that such an assumption may be incorrect.

3.7 Distribution of selected elements in ash, deposit and flue gas

The distributions of some elements between different ashes, deposits and in gas phase (for Cl and S) are calculated from measured amounts of ash and the concentrations of elements. There are of course uncertainties in these numbers; for example the fly ashes were sampled for 60 minutes and it has to be assumed that the fly ash concentrations were constant for the 8 hours of a testing period. It is possible that wall build-ups occasionally detached from the walls and caused irregular fly ash concentrations. Nevertheless, the balances shown below may indicate trends of different additives. The studied elements are Cl, S, Zn, Pb and K.

For the test case of the Sulphur additive, the wall deposits could not be properly analysed due to a sample handling mistake. Instead an average concentration from the other test cases is used in the figures below as it is probably closer to the truth than disregarding it completely. Anyway, the wall deposits constitute only a minor fraction of the distribution for most elements.

3.7.1 Distribution of Cl

The distribution of chlorine between bottom ashes, fly ashes, HCl in gas phase, and the deposits on the probes are shown in Figure 31. Most of the Cl is apparently leaving the furnace in the gas phase as HCl, except when using the lime additive. For the lime additive, a substantially increased fraction of Cl was found in the ashes, in the fly ash as well as the bottom ash. The additives minimizing the Cl in ashes are sulphur and kaolin followed by sewage sludge (SWS2). For these cases, the fraction of Cl as HCl increased instead. The additives of kaolin and sewage sludge reduce the fraction of Cl in deposits, both at BW and SH. The sulphur additive reduces the Cl fraction at SH but not so at BW.

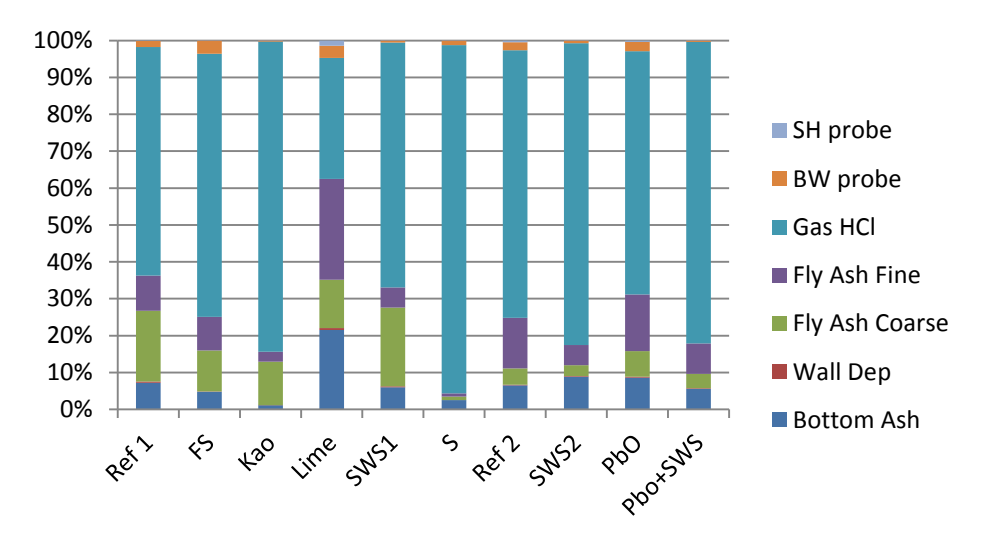


Figure 31. The distribution of CI recovered in ashes, flue gas and deposits.

3.7.2 Distribution of S

Most of the S supplied by the fuel is recovered in the bottom ash, except when S is used as an additive which causes a high fraction of S leaving the reactor in the flue gas as SO2. The additive Lime increases the fractions of S in the bottom bed, fine fly ash and in the deposits at the BW. The additives reducing the fraction of S in the BW deposits are kaolin, sulphur and sewage sludge.

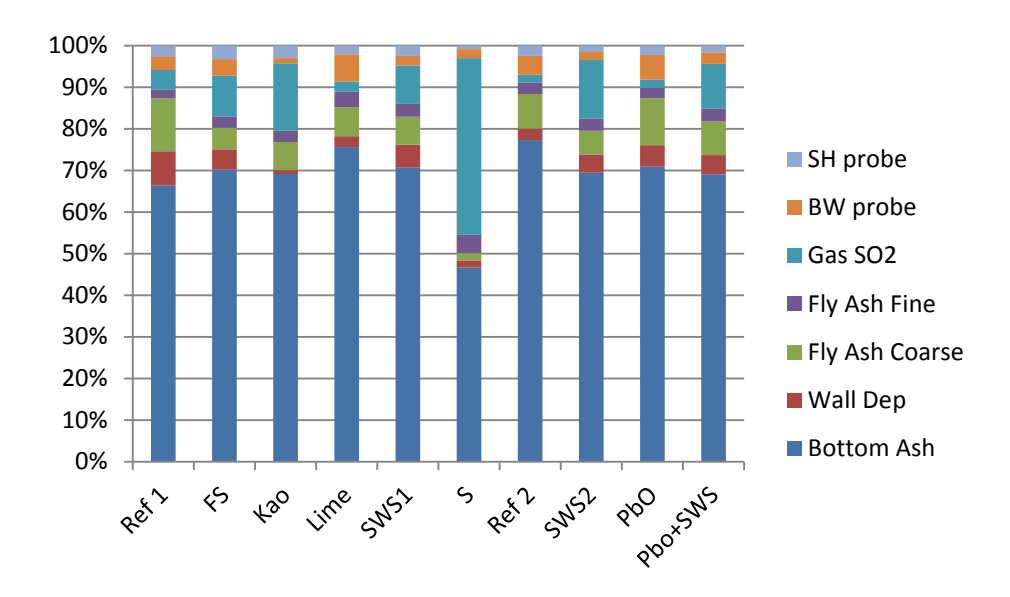


Figure 32. The distribution of S recovered in ashes, flue gas and deposits.

3.7.3 Distribution of Zn

For Zn, shown in Figure 33, between 50 and 60 % is found in the bottom ash, except for the case of kaolin additive, which instead shows increased amounts of Zn in the fly ashes. The two additives with the least fractions of Zn in the BW deposits were foundry sand and lime. These two additives were, however, the two least efficient with respect to reducing the corrosion on the 16Mo3 samples in the furnace (see Figure 33). It is not obvious in Figure 33 that Lime captures Zn, but it does increase the fraction of the Zn recovered in the coarse fly ash, maybe as a consequence of that the amount of fly ash was increased by the lime.

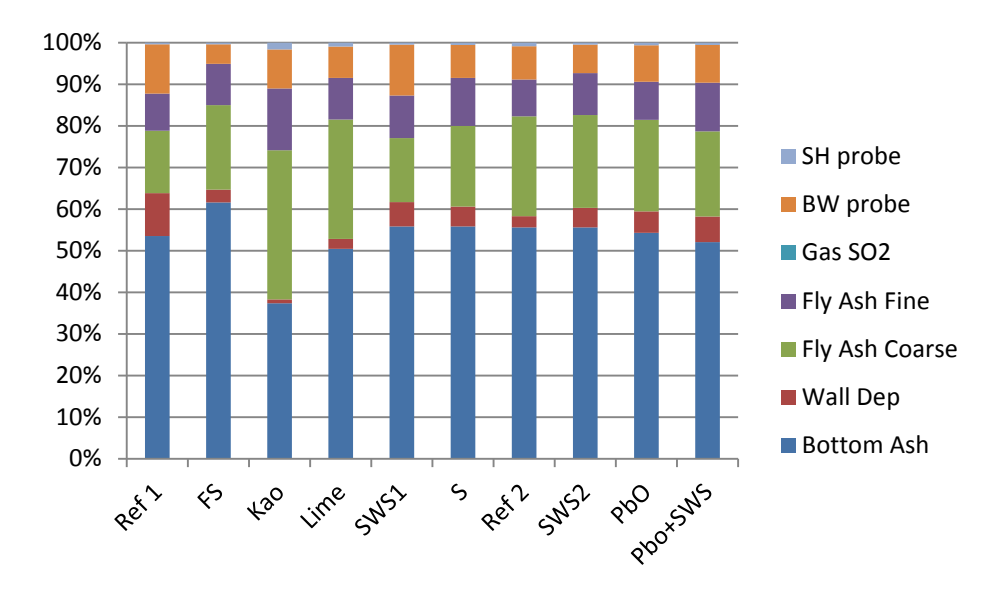


Figure 33. The distribution of recovered Zn in ashes, flue gas and deposits.

3.7.4 Distribution of Pb

The distribution of Pb in Figure 34 is quite different from Zn (in Figure 33), with relatively low fractions of the Pb in the bottom ash, but instead rather high in the fine fraction of the fly ash. Here, it seems that lime and also sewage sludge capture some of the Pb in the bottom ash and in the coarse fraction of the fly ash. Consequently, these additives reduce the fraction of Pb found in the fine fly ash. Adding kaolin increased the amount of Pb in the coarse fraction and reduced it in the fine fraction of the fly ash. On the other hand, sulphur, gives increased fraction of Pb in the fine fly ash and reduced fraction in the coarse fly ash.

The two cases of clearly visible (in Figure 34) fractions of Pb in SH deposits are kaolin and sulphur, which coincidentally were the two additives showing the least corrosion on the SH samples (see next section). This may be explained by the Pb here being present in another form than the highly corrosive PbCl2. At the BW, the additives reducing the fraction of Pb were foundry sand, sulphur and kaolin.

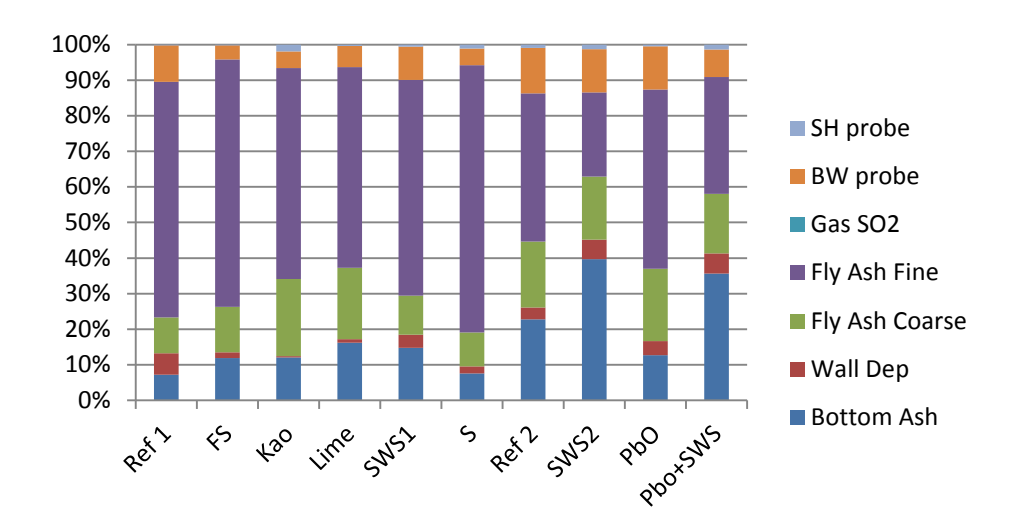


Figure 34. The distribution of recovered Pb in ashes, flue gas and deposits.

3.7.5 Distribution of K

As can be seen in Figure 35, most of the K found was in the bottom ash. It should be noted, however, that most of this K was already present in the fresh sand used as bed material. Nevertheless, the sewage sludge tends to increase the fraction of K in the bottom ash, while the fraction is reduced somewhat by kaolin.

The fractions of the K recovered in the fine fly ashes were reduced by kaolin, foundry sand and sewage sludge, while it was increased by the additives lime and sulphur.

Another observation is that the additives of sewage sludge and kaolin minimizes the fractions of K in the deposits on the probes (both SH and BW). Sulphur reduces the fraction of K captured at SH but increases the fraction at BW. Lime increases the fractions of the K in both BW and SH.

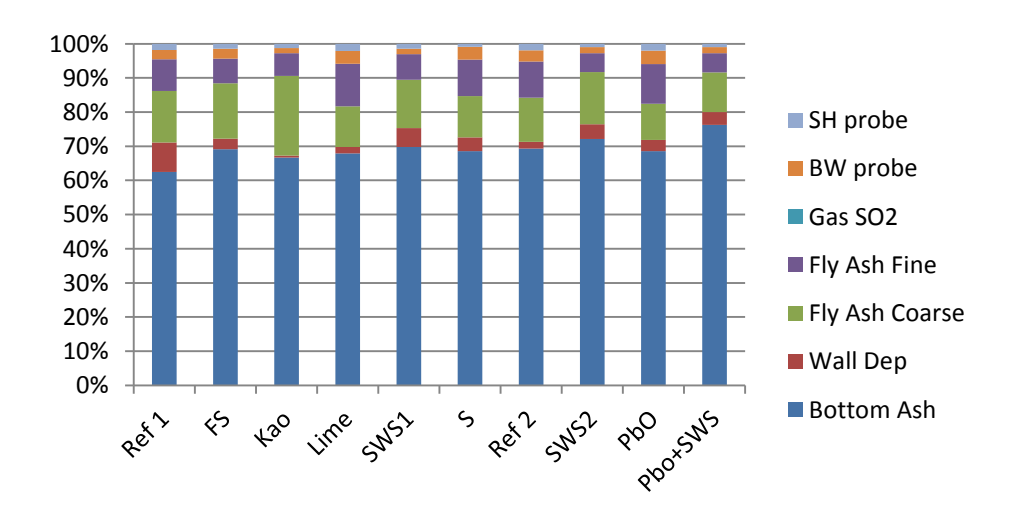


Figure 35. The distribution of recovered K in ashes, flue gas and deposits

4 Corrosion analysis

After the exposure in the laboratory reactor, the corrosion test rings were cleaned by isopropanol and lightly brushed with a cloth. A more extensive mechanical cleaning would also have removed the corrosion product formed. However, it required much more effort in doing so.

Macroscopic photos were taken at the inclination angle of the gas flow (wind side). The corrosion attack was in general limited to the wind side.

4.1 BW comparison (first set of tests)

The first set of tests performed is the first six cases listed in Table 4: Ref 1, FS, Kaolin, Lime, SWS1 and Sulphur. The corrosion of the test rings was not analysed in detail for this first set of tests. Instead, the overall corrosion was evaluated by optical evaluation, which was sufficient to provide a tentative ranking of additives tested.

4.1.1 BW 16Mo3 rings

Macroscopic photos of the 16Mo3 rings after exposure, in the boiler wall (BW) position of the furnace and consequent removal of deposits are shown in Figure 36. These photos of corrosion attacks on the substrate can be compared to the XRF analyses of selected elements in the deposits, prior to its removal, in Figure 37.

The two rings in Figure 36 that obviously are least attacked by corrosion are C and E (Kaolin and SWS1), on which the grinding marks from the sample preparation are still visible. In the case of Ref 1 (A), corrosion products have scaled off between -100° to $+100^{\circ}$. The ring from the case of foundry sand (Figure 36 B) has corroded spots between -90° and +90°. This deposit has higher concentrations of S, Cl and K than the reference case, at least on the windward side (Figure 37 B). For the kaolin case (C), the ring is somewhat discoloured after the exposure, whereas the XRF analysis shows that it contains less S and Cl than the reference case (Figure 37 A and C). The K concentration, however, is less affected by the additive. The ring from the lime case (D) is visibly corroded. The XRF analysis of the deposit shows that the S and Cl concentrations increase, while the K concentration is slightly reduced (perhaps replaced by Ca). The 16Mo3 ring from the sewage sludge case (Figure 36 E) shows only minor spots of onset of corrosion. The XRF analysis reveals that the concentration of Cl is reduced, compared to Ref 1, while the sulphur concentration has increased on the leeward side. The K concentration is lower on the windward side but higher on the leeward side. The P content in the deposit increase by the sewage sludge additive. The ring from the sulphur case (F) is corroded between -40° and +40°. This deposit contains more S and K than reference, while the Cl content is only marginally affected by the sulphur additive.

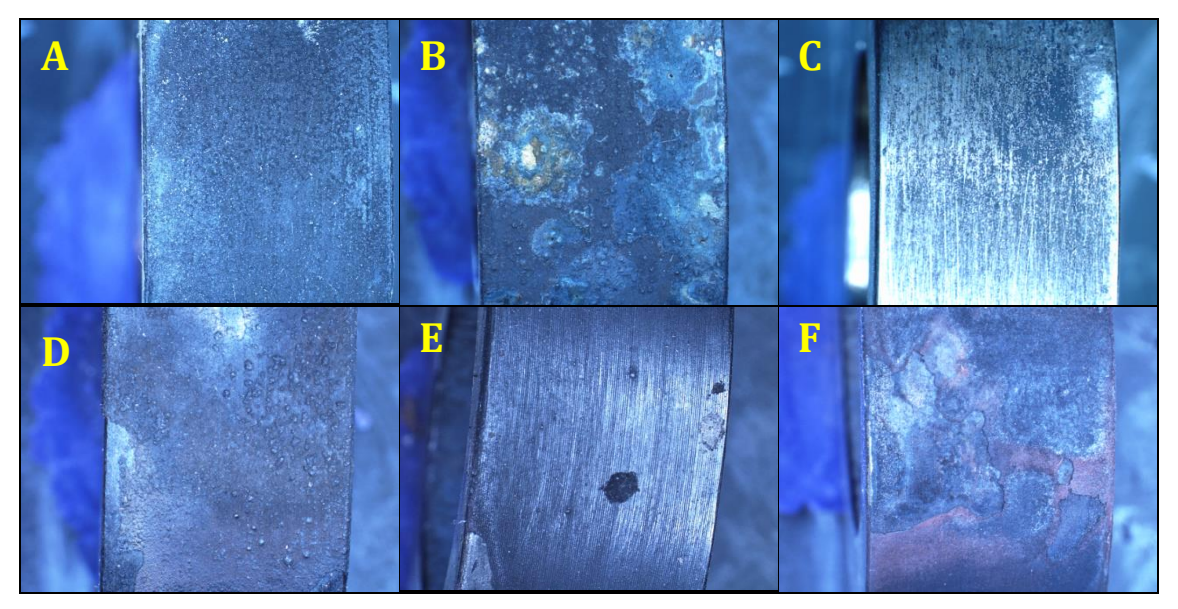


Figure 36. 16Mo3 rings from BW position, after cleaning. A) Ref 1, B) FS, C) Kaolin, D) Lime, E) SWS1 F) S.

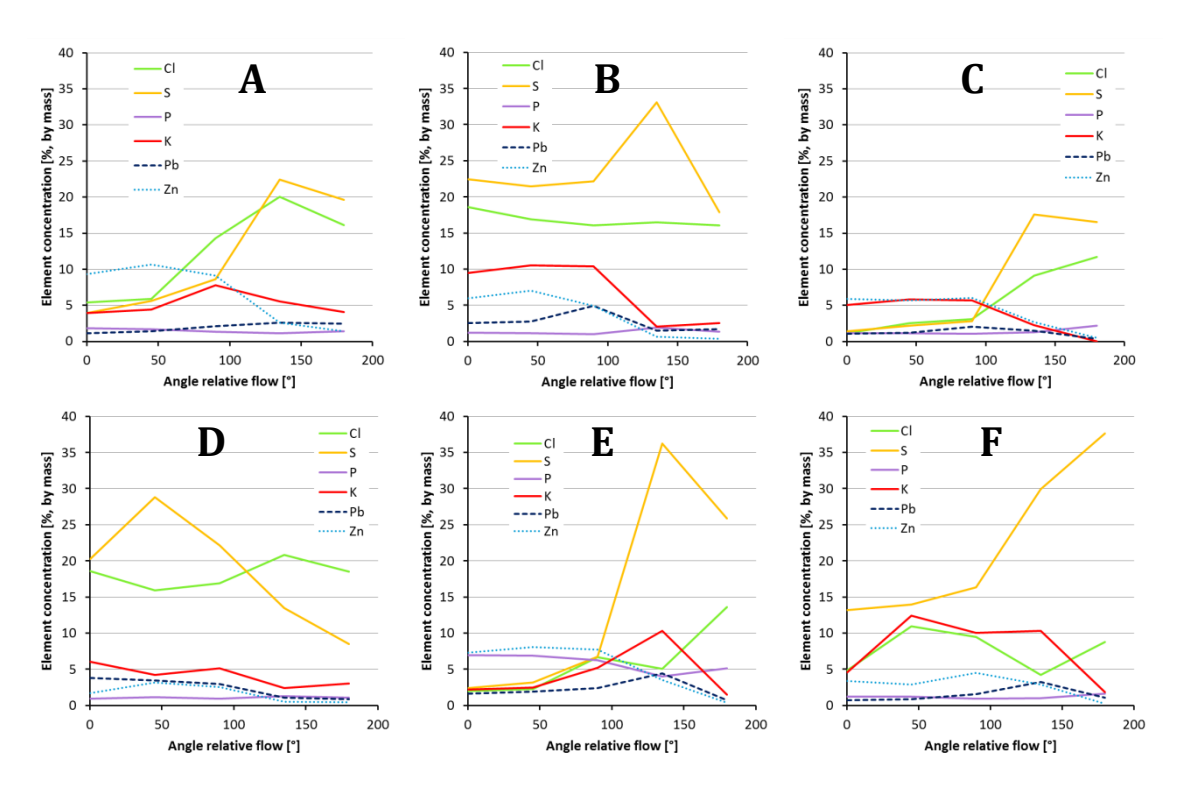


Figure 37. Elemental concentrations in deposits on the BW 16Mo3 rings, measured by XRF-instrument on the surface at varied angles relative to the windward side. A) Ref 1, B) FS, C) Kaolin, D) Lime, E) SWS1, F) S.

4.1.2 **BW 253 MA rings**

Macroscopic photos of the 253 MA rings after exposure in the boiler wall (BW) position of the furnace and subsequent removal of deposits are shown in Figure 38. These photos of the substrate can be compared to the XRF analyses of selected elements in the deposits, prior to its removal, in Figure 39.

The 253 MA ring from the **reference** case, in Figure 38A, is only somewhat discoloured at the windward side (-90° to $+90^{\circ}$). The concentrations of Cl and S (Figure 39A) are similar to each other, while there is a relatively high concentration of zinc.

In the case of **foundry sand additive** (B in Figure 38 and Figure 39), there is still only visual discolouration of the 253 MA steel, although the XRF analyses reveal increased concentrations of Cl, S and K in the deposit. Also when using the **kaolin** additive (C), the alloy is found to be slightly discoloured under the deposit. In this case, the deposit contains substantially lower concentrations of Cl and S, while the K is reduced at the leeward side of the ring. The only 253 MA ring that suffered apparent corrosion (in the first set of tests) is from the of **lime** case, in Figure 38D. In the deposit on this ring, the concentrations of Cl and S are higher than in the reference case. Furthermore, the concentrations are reduced for Zn and increased for Pb. For the **SWS1** case (E), the ring material is discoloured but not corroded. The concentration of Cl is significantly lower than reference case; it is comparable to the kaolin case. The S concentration is higher than for the kaolin case but lower than the reference case, apart from an exceptional peak at 135°. The ring from the **sulphur** case (F) has spot-wise discoloration, which may be signs of onset of corrosion attacks. The XRF analyses of the deposit on this ring show ominously high concentrations of S, Cl and K, with a strong emphasis towards the windward side.

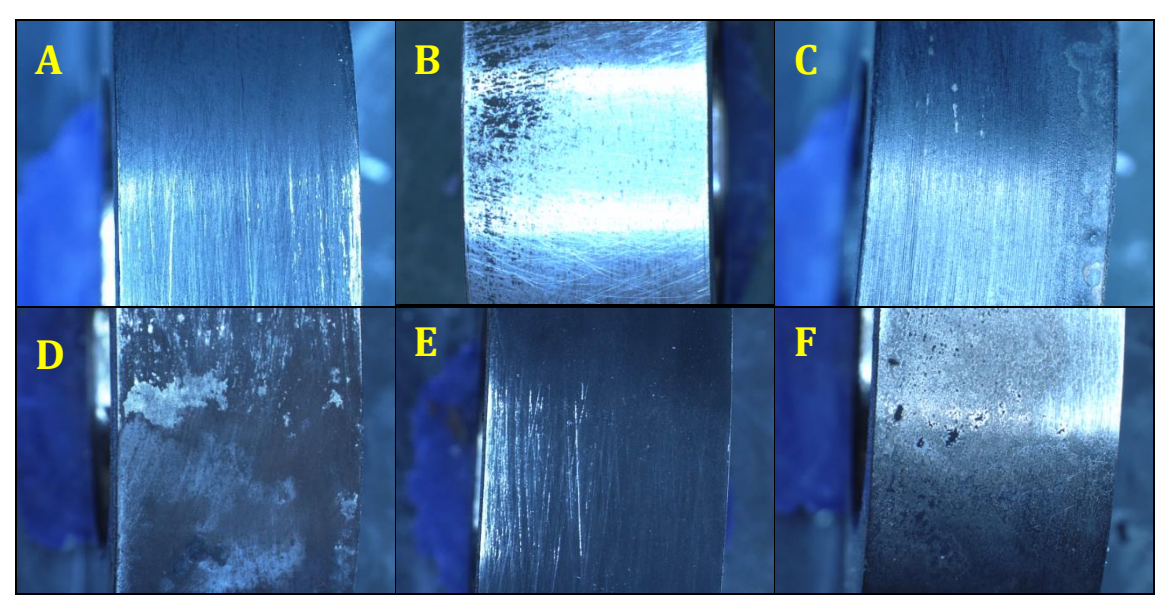


Figure 38. 253 MA rings from BW position, after cleaning. A) Ref 1, B) FS, C) Kaolin, D) Lime, E) SWS1, F) S.

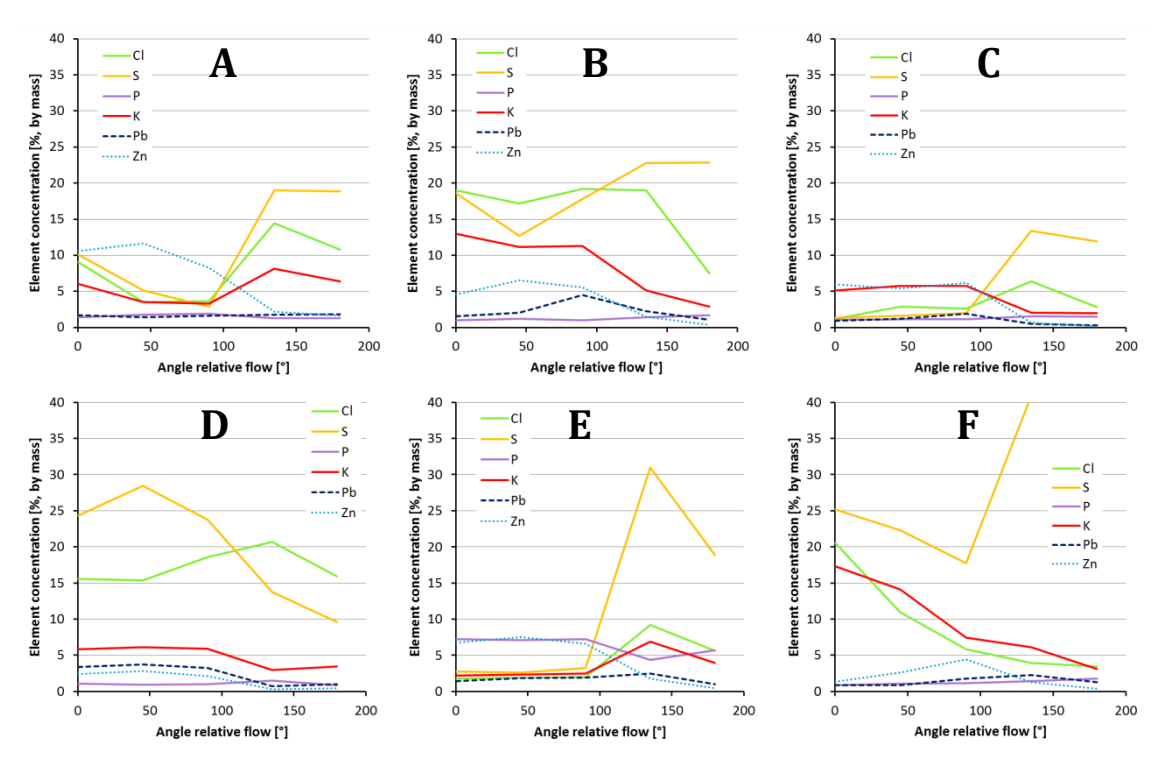


Figure 39. Elemental concentrations in deposits of the BW 253 MA rings, measured by XRF on the surface at varied angles relative to the windward side. A) Ref 1, B) FS, C) Kaolin, D) Lime, E) SWS1, F) S.

4.1.3 BW Kanthal-A1 rings

The rings of Kanthal-A1 are shown in Figure 40. The ring from the case Ref 1 (A) is discoloured to about half its width for some (unknown) reason. The XRF analysis, in Figure 41A, shows high concentrations of Cl peaking at 135°. The concentrations of S and Cl were increasing towards the leeward side. The ring from the foundry sand case (B) has some slightly discoloured spots. The analysis of its deposit shows higher concentrations of Cl, K and S than the reference ring on the windward side. The ring from the kaolin case (C) is virtually clean, and its deposit has much lower concentrations of Cl and S compared to the reference case. For the lime case (D), the Kanthal-A1 ring is faintly corroded in some spots. The XRF analysis of the deposit reveals that Cl and especially S concentrations are high at the windward side, compared to reference. Meanwhile, the content of K is somewhat lower than reference, maybe replaced by Ca to some extent. The lime additive also reduces the content of Zn in the deposit. As for the reference case, the A1 ring from the sewage sludge case (E) was partly discoloured. The analyses of the deposit shows reduced Cl concentrations, while the S concentration increases towards the leeward side. The ring from the sulphur case (F) shows sporadic corrosion although the average Cl concentration in the deposit is found to be lower than for the reference case. On the other hand, the S concentration is substantially higher and the K concentration is higher than for the reference case on the windward side.

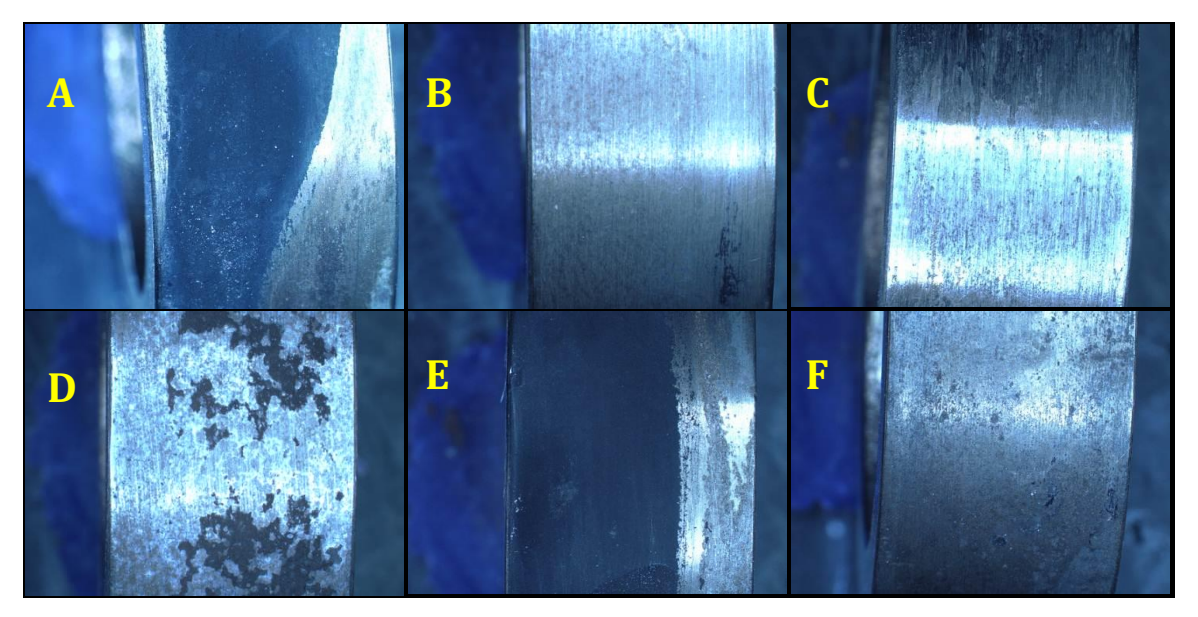


Figure 40. Kanthal-A1 rings from BW position, after cleaning. A) Ref 1, B) FS, C) Kaolin, D) Lime, E) SWS1, F) S.

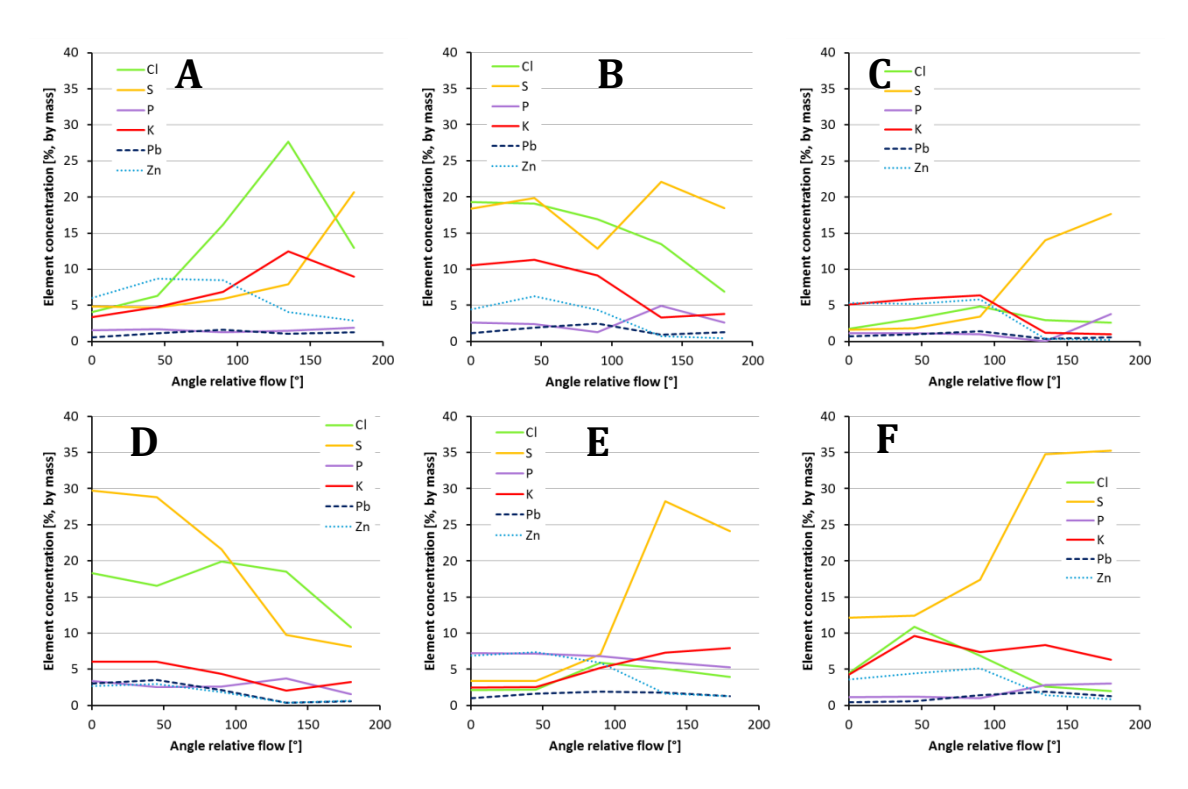


Figure 41. Elemental concentrations in deposits on the BW Kanthal-A1 rings, measured by XRF on the surface at varied angles relative to the windward side. A) Ref 1, B) FS, C) Kaolin, D) Lime, E) SWS1, F) S.

4.2 BW comparison between Ref 2 and SWS2 (second set of tests)

The exposed test rings from a case of sewage sludge additive (SWS2) are compared to a reference case (Ref 2) in order to highlight observed effects of the additive on the deposits and signs of initial corrosion.

4.2.1 BW 16Mo3 rings

4.2.1.1 Deposits

Figure 42 shows the wind sides of the 16Mo3-test rings after the exposure at the boiler wall (BW) position. The left ring has been exposed during case Ref 2 and the right ring during case SWS2. The ring from Ref 2 is only partly covered with greyish/dark deposit as the rest has fallen off after removal from the furnace. It can be seen that the surface is significantly corroded beneath the deposit where the deposit has scaled off. The ring from SWS2 is almost fully covered with dark grey/greyish deposit. The deposit has only spalled off at some minor areas.





Figure 42. Photos of the windward sides of the 16Mo3 rings after exposure at the boiler wall position. Left) Ref 2, Right) SWS2.

The leeward sides of the same rings as in Figure 42 are shown in Figure 43. The ring from Ref 2 has a greyish deposit with dispersed darker spots over the whole surface. The darker spots are corrosion products formed from the substrate alloy. The ring from SWS2 shows only a thin deposit layer. The metallic surface can be seen and the grinding grooves are still visible. The upper part of this ring is somewhat corroded.





Figure 43. Photos of the leeward sides of the 16Mo3 rings after exposure at the boiler wall position. Left) Ref 2, Right) SWS2.

The graphs in Figure 44 show the concentrations of selected key elements (measured by XRF) as a function of the circumference. 0° and 180° corresponds to the wind side and leeward side, respectively. The concentrations are given in mass percentage. The major alloying elements of the test rings, i.e. Fe, Cr and Ni are normally detected but are not accounted for in the shown concentrations. The left hand graphs show the results from Ref 2 and the right hand graphs from SWS2.

Figure 44 shows that the Cl-and S-concentrations in the deposits are reduced when sewage sludge is added to the fuel. The maximal value of the Cl-concentration found at 90° is significantly reduced from about 17 mass-% to about 13 mass-%, and the Cl-reduction is even higher elsewhere around the ring. The average S-concentration is also significantly reduced, even though the thin deposits towards the leeward sides shows high concentrations. The Zn-concentrations are similar between the cases. The K- and Pb-concentrations are found to be in similar ranges for the two test cases. The P-concentration increases when sewage sludge is added, due to the chemical composition of the additive.

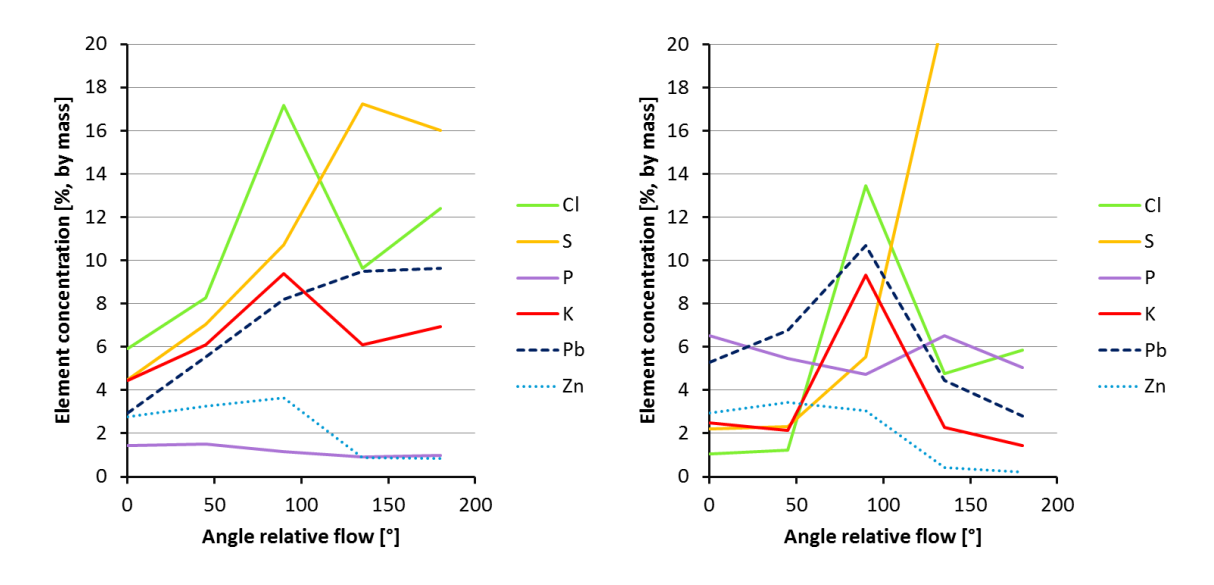


Figure 44. Elemental concentrations in BW deposits on 16Mo3 rings by XRF analyses. Left) Ref 2. Right) SWS2.

4.2.1.2 Ring surfaces after cleaning

After the exposure and subsequent examination of the deposit layer, the corrosion test rings were cleaned by isopropanol and brushed with a coarse cloth in order to remove the deposit scale. Figure 45 shows the windward ring surfaces beneath the scale. For the ring from case Ref 2 (left), the corrosion product spalled of during the cleaning process revealing a severely corroded surface. The surface of the ring from case SWS2 is also corroded, but the metallic lustre and grinding grooves remain visible (right).





Figure 45. Photos of the windward sides of the 16Mo3 rings after deposit removal (BW position). Left) Ref 2, Right) SWS2.

The leeward sides (in Figure 46) are, of course, less corroded than the wind sides. The left hand photo taken of the Ref 2 ring shows a corroded surface. However, less corrosion products was removed during the cleansing compared to the wind side. The surface of the SWS2 ring (to the right in Figure 46) is slightly corroded, but a metallic lustre is evident and the grinding grooves are visible.

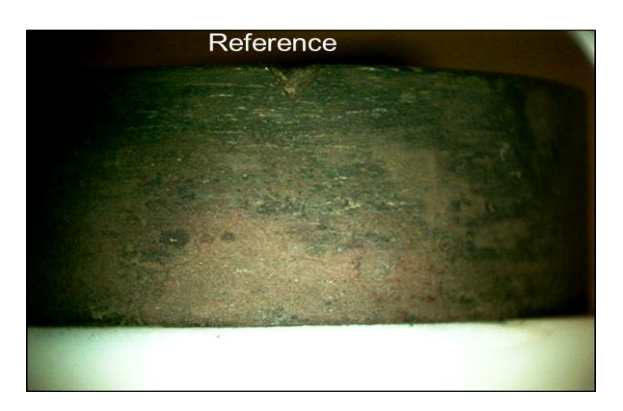




Figure 46. Photos of the leeward sides of the 16Mo3 rings after deposit removal (BW position). Left) Ref 2, Right) SWS2.

4.2.1.3 Optical microscope images

The micrographs in this section are captured by optical microscopy. The cross-sections had been ground with emery paper and polished with diamond paste. The upper dark areas in the micrographs are the mount resin material. The images are captured under polarized light, colorizing different areas, and a slight side-view embosses the relief structure. In order to strengthen the colour difference, some cross-sections were etched with water. The magnification is between 200x - 350x.

Figure 47 shows cross sections of 16Mo3 rings exposed in the BW-position from the test cases of Ref 2 (top figure) and SWS2 (bottom figure). The top figure (case Ref 2) consists of the etched yellow/grey steel substrate topped by a 40-50 μ m thick etched corrosion layer outside. A thicker dark greyish layer is observed between the corrosion layer and the resin. The cross-

section of the ring from case SWS2 (Figure 47, bottom) shows an etched reddish steel substrate with a $20\text{-}30~\mu m$ thick etched corrosion layer outside. An outer dark layer can also be seen between the corrosion layer and the resin.

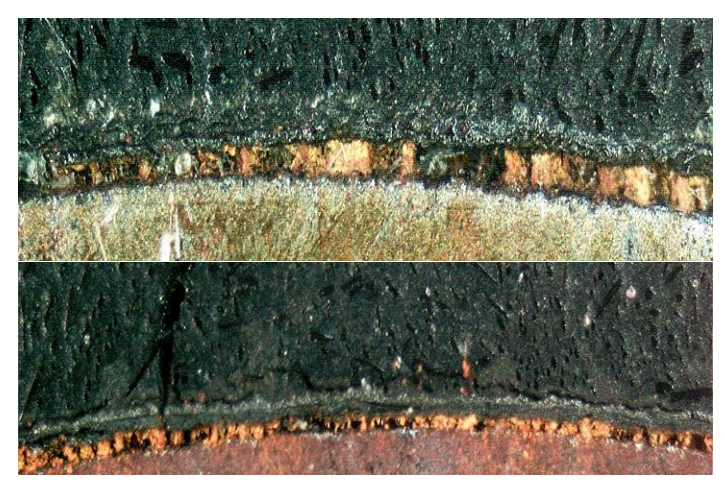


Figure 47. Micrographs cross-sections of windward sides of 16Mo3 rings exposed in the BW-position. Top) Ref 2. Below) SWS2.

Figure 48 shows the cross-sections of the leeward sides of the 16Mo3 test rings. The scratches on the substrates may originate from the sample preparation when some corrosion scales came loose and the particles caused groves in the steel. A very thin brown-reddish scale can be seen between the scratched ring substrate and the resin but some of the scale might have fallen off during sample preparations, as mentioned above. The leeward side of the 16Mo3 ring from case SWS2 is shown to the right in Figure 48. Some scratches of the steel substrate are visible, but no scale between the test ring the resin is found.





Figure 48. Micrographs cross-sections of leeward sides of 16Mo3 rings exposed in the BW-position. Left) Ref 2. Right) SWS2.

4.2.1.4 SEM/EDX-analysis of windward side – Ref 2

The figures in this section show cross-sections analysed by means of SEM (Scanning Electron Microscope) and EDX (Energy Dispersive X-Ray). The BSE-option (Backscatter Electrons) was used when the aim was to identify heavier elements, e.g. Pb. The samples have been mounted in resin, grinded with emery paper and polished with 1.5 μ m diamond paste. The analyses were made at several positions round the circumference of the sample ring.

The top image in Figure 49 is taken by means of BSE-SEM-imaging on the windward side of the 16Mo3 ring from case Ref 2. The steel substrate is seen at the lower and left part of the image. The layered $75-80~\mu m$ thick corrosion scale, which appears dark grey, is on top of the steel substrate. At the rightmost upper part, the black resin with bright areas is seen. At the outermost part of the corrosion scale Pb is present, represented by the bright areas. Lead is also dispersed within the corrosion scale.

The element EDX-mappings shown in the matrix-figure of smaller images show the lateral distribution of selected elements over the area shown in the BSE-SEM image. Chlorine is present in the corrosion front at locally high concentrations. On the other hand, S is not detected at the corrosion front. Instead, the highest S-concentrations are found at the outer part of the scale. The alkali metals are also found at the outer part of the scale. Lead is, as already shown, mainly present at the outer part of the scale but some Pb can also be found dispersed in the scale. The map of Pb does show some noise which should not be taken for the presence of Pb. Zinc is also present in higher concentrations at the outer part of the scale. Calcium is mainly present in the resin. Oxygen can be found through the whole scale.

The chemical analysis of a point in the outer part of the corrosion layer denoted "Spectrum 1" in the top SEM-image Figure 49 is displayed in Table 15. The S-, and Pb-concentrations are relatively high, 22 and 17 atomic-%, respectively. The Cl-concentration is close to zero. Oxygen and Fe are also present. The corrosion product may consist of a Fe–O–Pb compound, with a different composition compared to the point in Figure 50 which is closer to the corrosion front.

Table 15. Elemental composition of the point marked "Spectrum 1" in Figure 49.

Element	Weight%	Atomic-%
0	12.71	46.17
Si	0.15	0.31
S	12.32	22.33
Cl	0.22	0.37
Ca	0.16	0.23
Fe	12.17	12.66
Zn	0.35	0.31
Pb	61.69	17.30

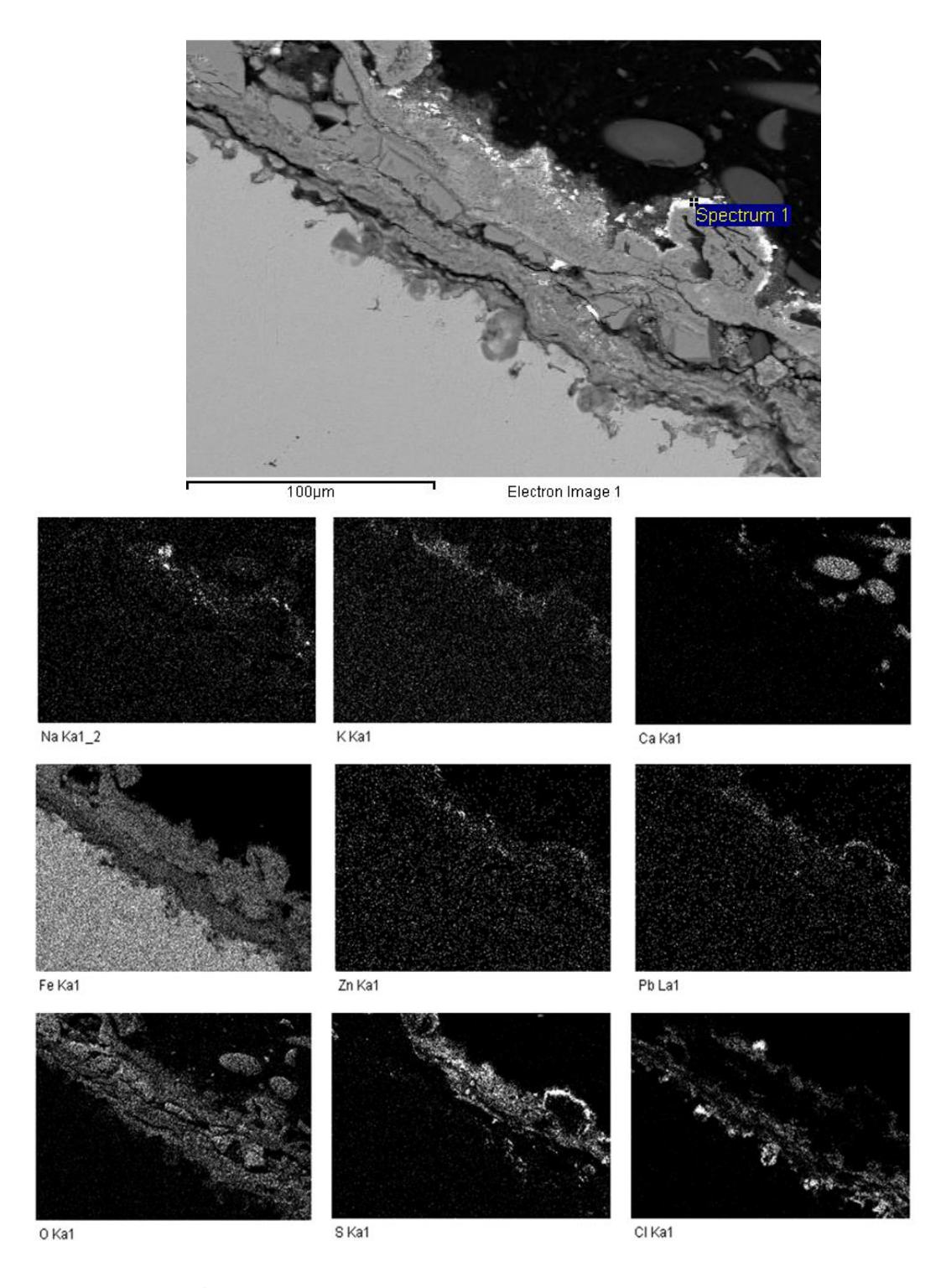


Figure 49. SEM/EDX image of the corrosion layer at the windward of a 16Mo3 ring from case Ref 2. Top photo by BSE-SEM, below a matrix of element mapping. Elemental composition of point "Spectrum 1" is given in Table 15.

Figure 50 is also captured at the windward side, from the same ring as in Figure 49, showing the presence of Pb as bright spots. The chemical analysis made in the bright spot, relatively close to but not at the corrosion front, denoted "Spectrum 1" are shown in Table 16. About 14 atomic-% of Pb was found, Chlorine is present at 10 atomic-%. Sodium, K and Zn are also present at relatively low concentrations, below 1 atomic-%. It is worth to notice that no S was detected. Iron and oxygen are also present. It can be speculated if the corrosion product includes Pb – O – Cl compounds.

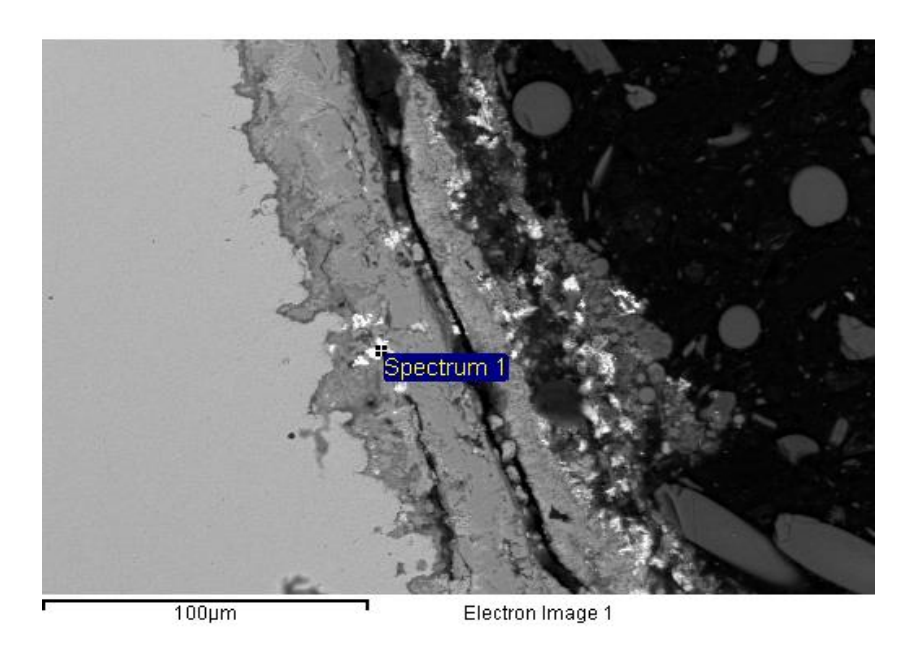


Figure 50. SEM image of the corrosion layer at the windward of a 16Mo3 ring from case Ref 2.The bright areas consist of Pb, O and S. Elemental composition of point "Spectrum 1" is given in Table 16.

Table 16. Elemental composition of point marked in Figure 50.

Element	Weight%	Atomic%
0	20.80	63.48
Na	0.48	1.01
S	0.00	0.00
CI	7.20	9.92
K	0.20	0.24
Fe	11.64	10.17
Zn	0.58	0.44
Pb	58.47	13.78

4.2.1.5 SEM/EDX-analysis of leeward side - Ref 2

The SEM-image in Figure 51 is captured at the leeward side of the same ring as above (16Mo3, BW-position, case Ref 2). The corrosion scale thicknesses here vary in the range between 5 and 15 μ m. The chemical composition in "Spectrum 1" is shown in Table 17. The Cl-concentration is relatively high, 12.7 atomic-%. Only minor amounts of Pb, K, Ca, Mn and Na are detected, less than 0.5 atomic %. No sulphur is detected. Iron and oxygen are present. Nitrogen is present at relatively high concentration; 12.2 atomic %. It is not clear if this concentration is an artefact or if N actually is present.

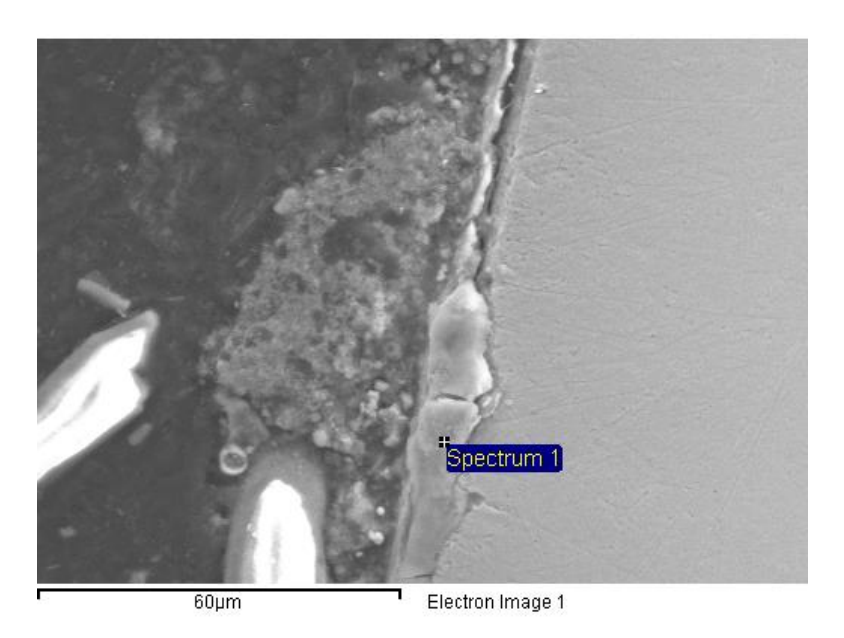


Figure 51. SEM image of the corrosion layer at the leeward side of a 16Mo3 ring from case Ref 2. Elemental composition of point "Spectrum 1" is given in Table 17.

Table 17. Elemental composition of the point marked in Figure 51.

Element	Weight%	Atomic%
N	5.68	12.17
0	24.07	45.13
Na	0.33	0.43
Si	0.14	0.15
Cl	15.04	12.73
K	0.49	0.37
Ca	0.13	0.09
Mn	0.37	0.20
Fe	53.38	28.68
Pb	0.38	0.05

4.2.1.6 SEM/EDX-analysis of windward side – SWS2

Figure 52 below is captured at the windward side of a 16Mo3 sample ring exposed during test case SWS2. The metal substrate is at the top of this picture and the scale thickness is about $70-80~\mu m$. The correlating element maps show that Cl is present in the corrosion front but also elsewhere in scale in connection with the structures in the layer.

Some S is present a relatively low concentration at the corrosion front but S is present at higher concentrations elsewhere in the scale. No alkali metals are detected in the corrosion front, but can be found in the outer part of the scale. Lead is detected in the outer parts of the scale and some is also dispersed in the scale, but no lead is detected at the corrosion front. Phosphorous originating from the sewage sludge is found in the outer part of the scale.

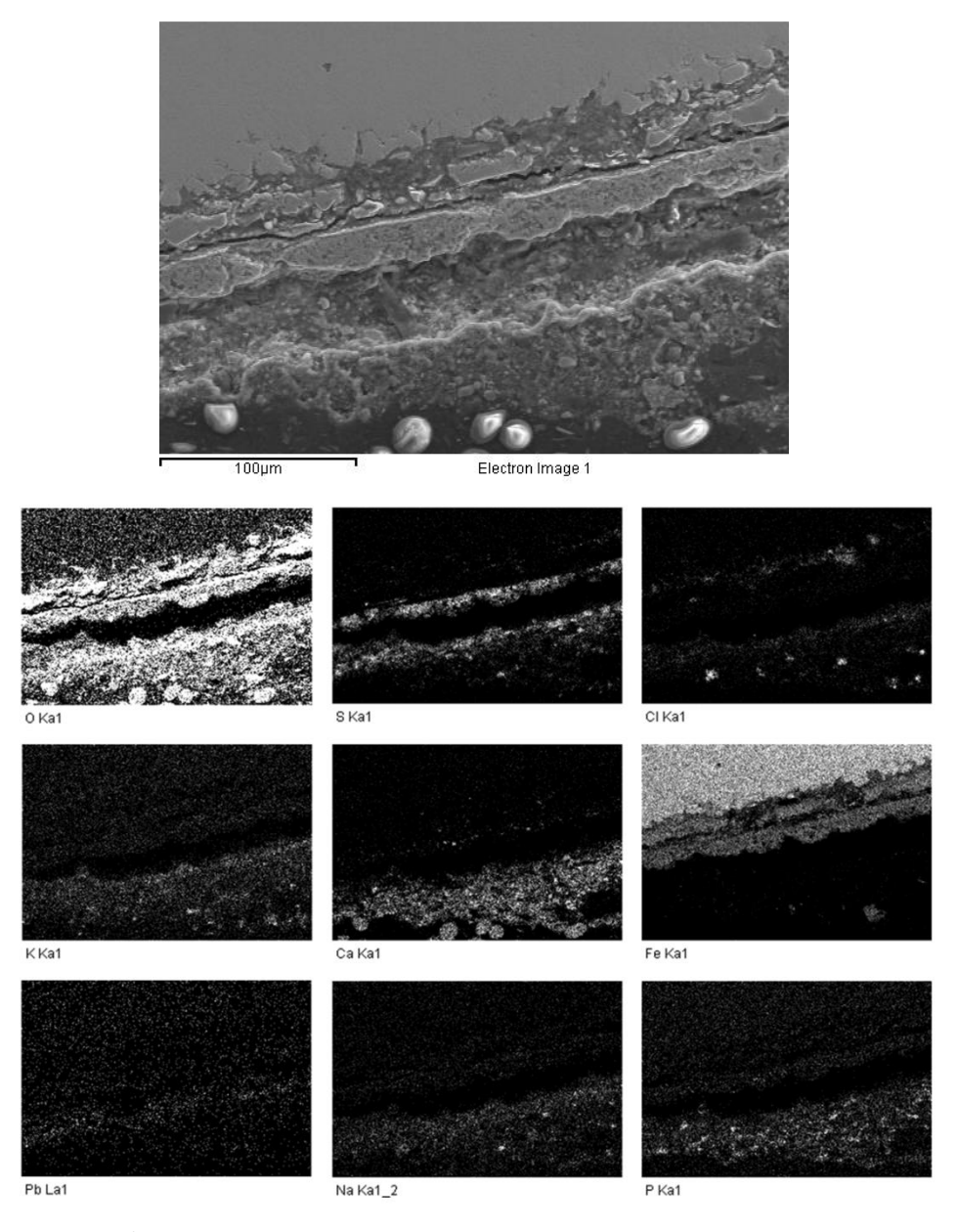


Figure 52. SEM/EDX image of the corrosion layer at the windward of a 16Mo3 ring from case SWS2. Top photo by BSE-SEM, below a matrix of element mapping.

4.2.1.7 SEM/EDX-analysis of leeward side – SWS2

The Figure 53 below is taken at the leeward side of the same sample ring as above. The oxide thickness is thin, only some μm thick. The chemical analysis at the point denoted "Spectrum 3" consists mainly of Fe and O. Several other elements are present at low concentrations, see Table 3.

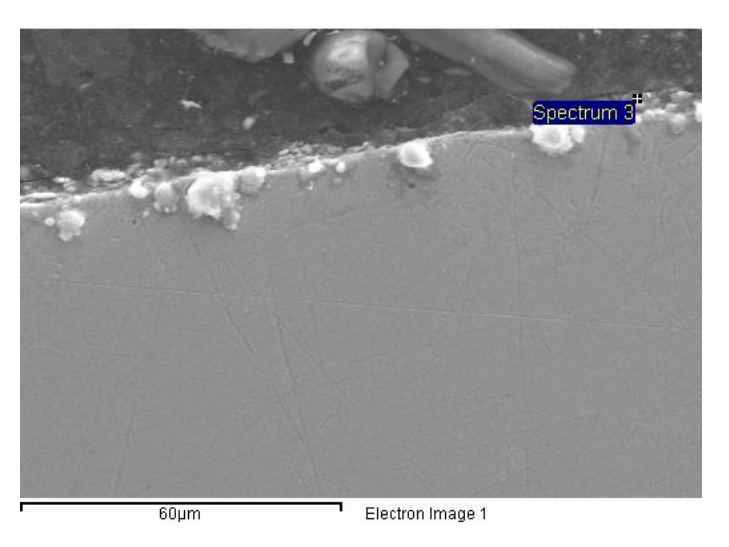


Figure 53. SEM image of the thin corrosion layer at the leeward of a 16Mo3 ring from case SWS2. Elemental composition of "Spectrum 3" is reported in Table 18.

Table 18. Elemental composition of the point marked in Figure 53.

Element	Weight%	Atomic%
0	33.53	60.67
Na	1.54	1.94
Mg	1.55	1.85
Al	0.96	1.03
Si	1.47	1.52
P	0.50	0.47
S	0.41	0.37
Cl	2.21	1.81
K	0.48	0.35
Ca	2.12	1.53
Cr	0.24	0.13
Mn	0.35	0.19
Fe	54.21	28.10
Pb	0.43	0.06

4.2.2 BW 253 MA rings

4.2.2.1 Deposits

Figure 54 shows the windward sides of the 253 MA-test rings after their exposures to boiler wall (BW) conditions. The left ring has been exposed during case Ref 2 and the right ring during case SWS2. (The exposure conditions are the same as in previous trials; the metal temperature was 400°C and the exposure time was 8h.)

The wind side of the ring from case Ref 2 is covered with greyish/yellow deposit with dispersed smaller darker areas. The dark areas may be sign of corrosion. The right hand image showing the case from the sewage sludge case is slightly discoloured in order to enhance the appearance of the deposit. The ring exposed is covered by a greyish deposit but the deposit is thinner at the upper part of the figure.





Figure 54. Photos of the windward sides of the 253 MA rings after exposure at the BW position. Left) Ref 2. The wind side is covered with greyish yellow deposit with dispersion of smaller darker areas. Right) SWS2. A greyish deposit covers the wind side surface.

The leeward sides of the sample rings above are shown in Figure 55. The left photo shows the 253 MA test ring from case Ref 2 and the right photo the ring from case SWS2. The deposit on the Ref 2 ring appears to be thin. The colour of the deposit is greyish deposit with dispersed darker smaller spots. The deposit covers almost the whole surface.

The image to the right shows the test ring after exposure from case SWS2. The image is slightly discoloured in order to minimise reflexions from the sample. The deposit became thinner when sewage sludge was added. The metallic surface can be seen be at different locations.





Figure 55. Photos of the leeward sides of the 253 MA rings after exposure at the BW position. Left) Ref 2. The deposit is still attached on the lee side and has a greyish appearance with dispersed darker spots, maybe from the corroded substrate. Right) SWS2. A thinner deposit layer has formed on the leeward side. The bare metal surface can be seen at some areas.

The graphs of Figure 56 show the results from the chemical analyses made by means of handheld-XRF on the deposits on the 253 MA rings. Case Ref 2 is shown to the left and the case SWS2 to the right. A comparison of the diagrams in Figure 56 gives that the Cl-, S- and K-concentrations are reduced when sewage sludge is added to the fuel. The Cl-concentration is significantly reduced from the range of 12 to 21 mass % to the range of 1 to 11 mass %. The maximum concentrations were found at the windward side for the reference case and at 90° for the sewage sludge case. The S-concentration is also significantly reduced by the sewage sludge. The highest S-concentration is found at the windward side for the case of Ref 2, while the concentrations are higher in the very thin deposits on the leeward side of the ring for the case of SWS2. The K content in the deposit was also reduced by the sewage sludge. It seem like the distribution of K follows the distribution of Cl. The Pb is somewhat reduced while the Zn-concentrations are similar between the cases. The P-concentration inceases when sewage sludge is added.

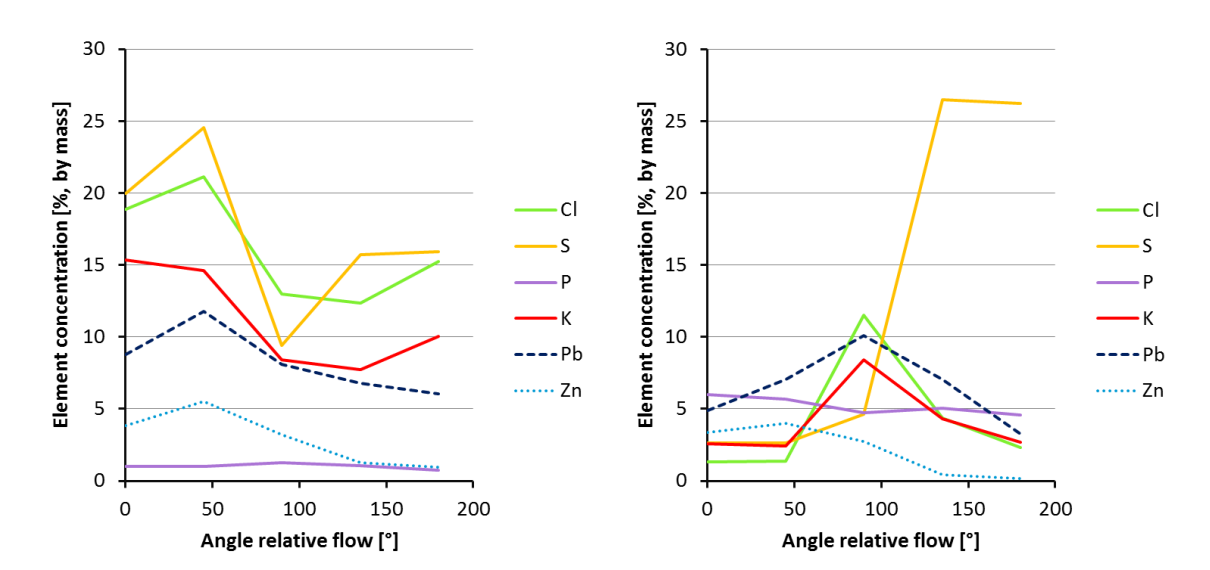


Figure 56. Elemental concentrations in BW deposits on 253 MA rings measured by XRF. Left) Ref 2. Right) SWS2.

4.2.2.2 Ring surfaces after cleaning

The 253 MA sample ring from case Ref 2, BW position, was used for SEM/EDX-analyses and therefore there are no images of this ring by the optical microscope.

Figure 57 below shows the 253 MA steel from case SWS2, after cleaning. The left image shows the wind side and the right the leeward side. The dark areas are hard sticking deposit and may develop further to corrosion. The surface of the leeward side does not show any signs of corrosion. The somewhat dark appearance is due to the reduction of the incoming light in order to reduce reflexes.

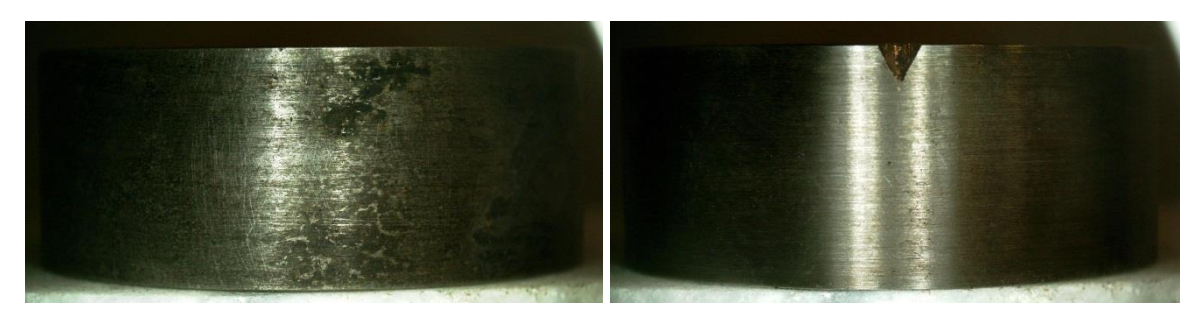


Figure 57. Photos of a 253 MA steel ring after exposure and removal of deposits. Test case SWS2 at BW position. Left) Windward side. Right) Leeward side.

4.2.2.3 SEM/EDX-analysis of windward side – Ref 2

Figure 58 shows a cross-section from the wind side of the 253 MA sample ring from case Ref 2. The elongated bright area is from resin constituents. The corrosion scale thickness is $10\text{-}20\mu\text{m}$. Table 19 shows the chemical composition in point "Spectrum 3". In addition to the alloying elements, with the exception of Ni, several elements are present. Oxygen is present at high concentration; 45 at-%. Other potentially corrosive elements such as Cl, S, Na, K, Pb, Zn are present in the corrosion scale.

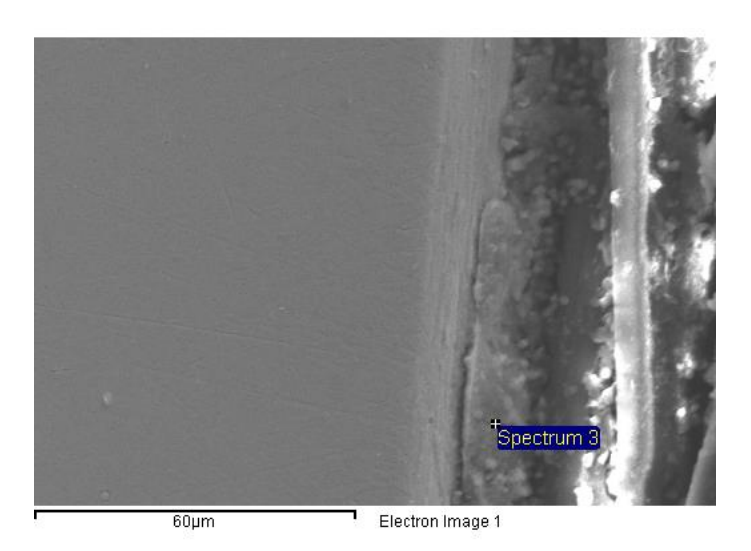


Figure 58. SEM image of the thin windward corrosion layer of a 253 MA ring from case Ref 2. Elemental composition of "Spectrum 3" is reported in Table 19.

Table 19. Elemental composition of the point marked in Figure 58.

Element	Weight%	Atomic%
0	20.11	45.15
Na	2.37	3.70
Mg	0.00	0.00
Al	1.20	1.60
Si	0.75	0.96
P	0.00	0.00
S	4.41	4.94
Cl	7.76	7.86
K	5.06	4.65
Са	2.14	1.91
Cr	5.77	3.99
Fe	30.39	19.54
Cu	1.43	0.81
Zn	4.43	2.43
Pb	14.18	2.46

4.2.2.4 SEM/EDX-analysis of leeward side – Ref 2

Figure 59 is captured on the leeward side of the 253 MA sample ring from case Ref 2. Scratches from the grinding and polishing procedures are visible. The outer part of the sample which appears as a layer is actually only a chamfering of the sample. The chemical composition in the point "Spectrum 1" is shown in Table 20. The composition corresponds to the nominal composition of the steel and the C originates from the resin. No corrosion scale is detected.

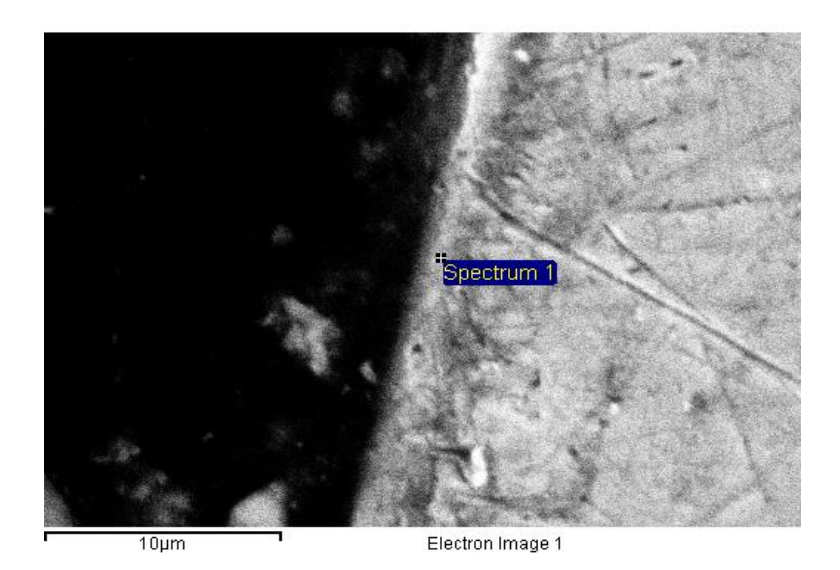


Figure 59. SEM image of the leeward outer boundary of a 253 MA ring from case Ref 2. Elemental composition of "Spectrum 1" is reported in Table 20.

Table 20. Elemental composition of the point marked in Figure 59.

Element	Weight%	Atomic%
С	16.88	46.18
0	2.21	4.54
Si	1.97	2.31
Cr	17.36	10.97
Mn	0.68	0.41
Fe	52.76	31.04
Ni	8.13	4.55

4.3 BW comparison between: PbO and PbO+SWS (second set of tests)

This section gives a comparison between the two test cases of demolition wood spiked with PbO (1g Pb per kg dry fuel) and PbO + SWS (1 g Pb + 80 g sewage sludge per kg dry fuel). The purpose of the additional PbO is to study the influence of Pb on water-wall corrosion and the comparison here is to see if the corrosive attacks of lead can be mitigated by sewage sludge.

4.3.1 BW 16Mo3 rings

4.3.1.1 Deposits

Figure 60 show the wind sides of the 16Mo3-test rings after the exposure in the BW position of the reactor. The left ring in Figure 60 has been exposed during the case of PbO and the right ring during the case of PbO+SWS. The ring from case PbO is covered with grey/yellow deposit where it has not scaled off. The surface is significantly corroded beneath the deposit. The ring from case PbO+SWS is almost fully covered with grey/yellowish deposit. This deposit has only spalled off at minor areas.

Figure 61 shows the same rings as in Figure 60 but here seen from the leeward side. The deposits are greyish/yellow with some dark spots. The deposit from the PbO case has spalled off at some areas at which the corroded surface of the 16Mo3 ring is visible.





Figure 60. Photos of the 16Mo3 rings after exposure at the BW position. Left) PbO, as seen from 60° relative to the windward side (windward side to the right). Right) PbO+SWS. Windward side.

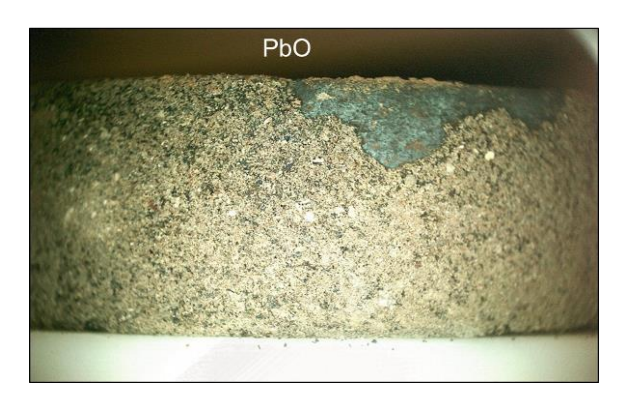




Figure 61. Photos of the leeward sides of the 16Mo3 rings after exposure in the boiler wall position. Left) PbO. Right) PbO+SWS.

Figure 62 show the concentrations of selected key elements as a function of the circumference (0° and 180° corresponds to the windward side and leeward side, respectively). The left hand graphs show the results from case PbO and the right hand graphs show case PbO+SWS. The concentrations of Cl and Pb are reduced when sewage sludge is added to the fuel. The S-concentrations appears to be insignificantly affected by the additive. The Zn-concentration is slightly increased by the sewage sludge additive while K may be somewhat reduced. The P-concentration is increased when sewage sludge is added due to the chemical composition of the additive.

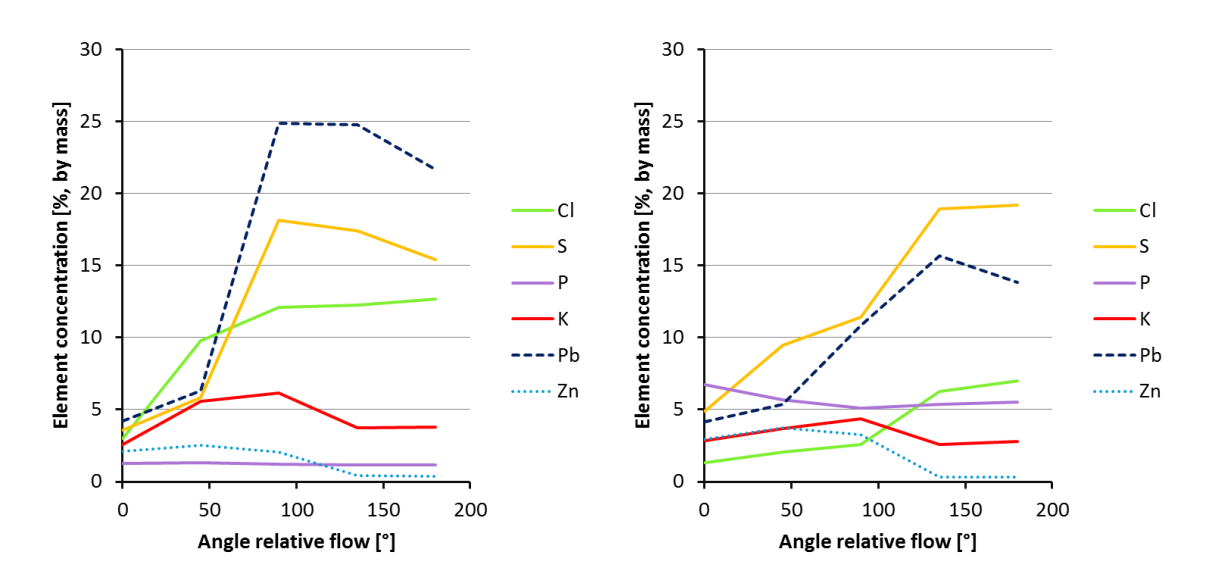


Figure 62. Elemental concentrations in the deposits on 16Mo3 rings from BW position. Left) PbO. Right) PbO+SWS.

4.3.1.2 Ring surfaces after cleaning

Figure 63 shows the wind side of the ring surface, after cleaning by isopropanol and brushed with a coarse cloth. The corrosion product on the PbO ring spalled off repeatedly during the cleaning process, revealing a severely corroded surface. The surface of the ring from case PbO+SWS is also corroded, but spalled only on limited areas. The difference between the rings is not really made clear by the photos in Figure 63.

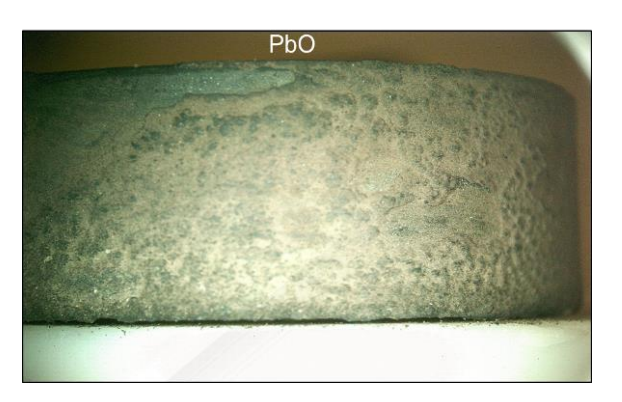




Figure 63. Photos of the windward sides of the 16Mo3 rings after deposit removal, BW position. Left) PbO. The corrosion products have spalled off repeatedly. Right) PbO+SWS. The corrosion layer has spalled off at some areas.

The leeward sides, shown in Figure 64, are somewhat less corroded than the wind sides. The left photo taken of the ring from case PbO shows a severely corroded surface that has spalled. The surface of the ring from case PbO+SWS is slightly corroded, but a metallic lustre is evident at the centre.



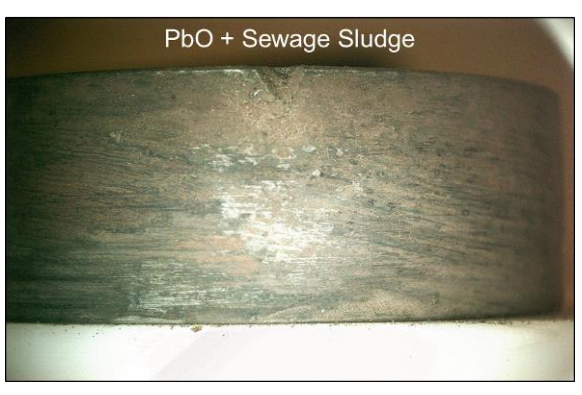


Figure 64. Photos of the leeward sides of the 16Mo3 rings after deposit removal, BW position. Left) PbO. Right) PbO+SWS.

4.3.1.3 Optical microscope images

The micrographs in Figure 65 are captured by optical microscopy on the wind side of the sample rings of 16Mo3. The upper dark areas in the micrographs are the mount resin material and the red areas at the bottom are the steel substrates. The top photo in Figure 65 shows the etched reddish 16Mo3 steel substrate and with a 1 mm thick etched corrosion layer outside from case PbO. The figure below, from case PbO+SWS, shows the etched reddish steel substrate with a 300-500 µm etched corrosion layer on the outside.

Corresponding pictures from the leeward side of the sample rings are presented in Figure 66. At this side of the rings, the corrosion layers are considerably thinner, about 100 μ m for case PbO and considerably less for case PbO+SWS.

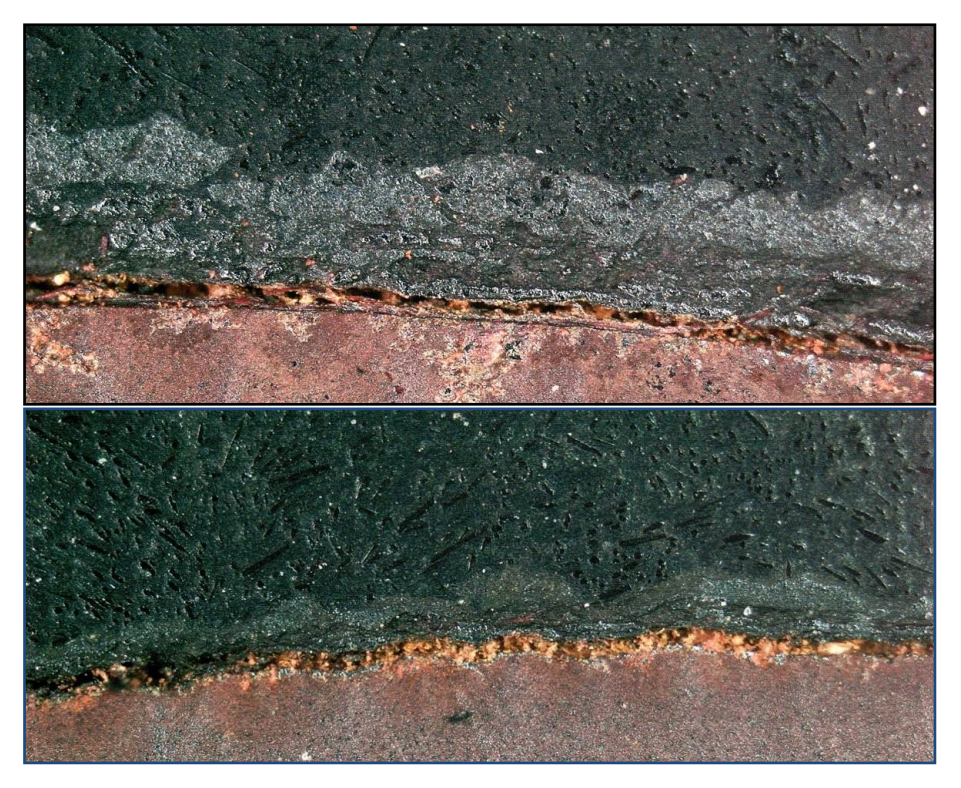


Figure 65. Micrographs cross-sections of windward sides of 16Mo3 rings exposed in the BW-position. Top) PbO. Scale thickness: 1mm. "Water etched". Bottom) PbO+SWS. Corrosion layer: 300-500μm. "Water etched". Magnification: different.

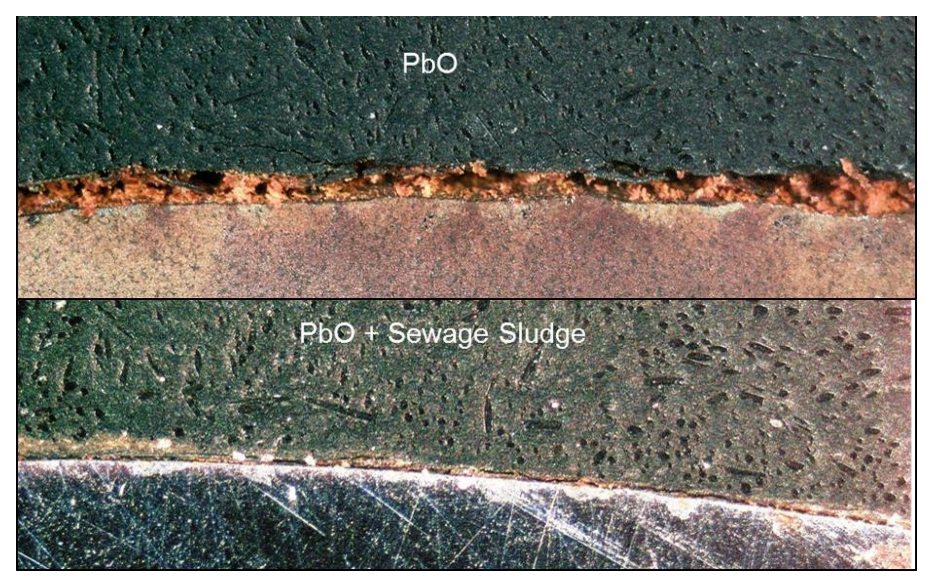


Figure 66. Micrographs cross-sections of leeward sides of 16Mo3 rings exposed in the BW-position. Top) PbO. Corrosion layer about 100 μm. "Water etched". Bottom) PbO+SWS.

4.3.1.4 SEM/EDX-analysis of windward side - PbO

A SEM/EDX picture of the cross section of the 16Mo3 sample exposed in the BW position during case PbO is shown in Figure 67, with the steel substrate is to the left. The corrosion product is here thicker than 500 μ m. The correlating element maps in Figure 67 show that Cl is concentrated in the corrosion front but also elsewhere in the structures of the layer. No visual evidence of S being present anywhere in the corrosion layer. No alkali metals are present in the corrosion front, but they can be found dispersed in the outer part of the scale. The maps for lead and zinc show many small dots that may be noise, perhaps these concentrations are below the detection limit.

The corrosion front was scanned further in search of for lead, using the SEM, because it was unexpected that no clear lead mapping appeared in Figure 67, considering that the fuel had been spiked with PbO and high concentrations of Pb were detected by XRF in Figure 62. An EDX analysis of an area where Pb was found is given in Table 21, with corresponding SEM image in Figure 68. Only lower Pb concentrations were found elsewhere, perhaps the Pb was diluted rather evenly throughout the larger scales?

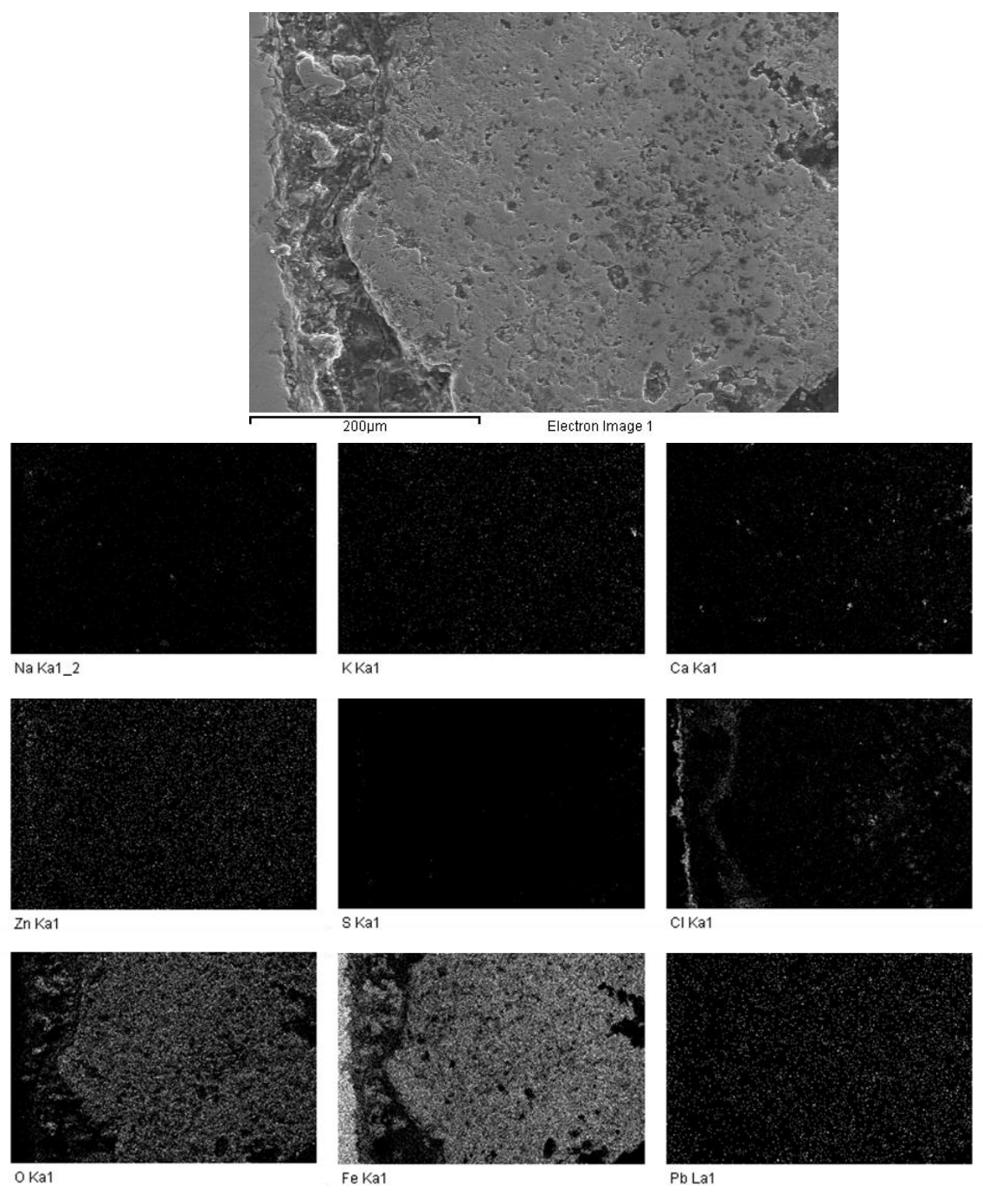


Figure 67. SEM/EDX image of the corrosion layer at the windward side of a 16Mo3 ring from case PbO. Top photo by BSE-SEM, below a matrix of element mapping

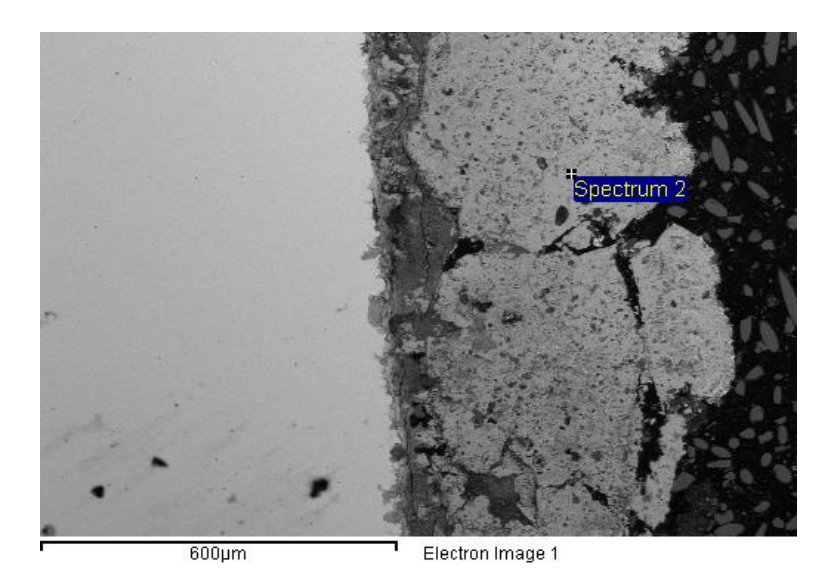


Figure 68. SEM image from cross-section of a 16Mo3 ring exposed in the BW position during case PbO. Elemental composition in point "Spectrum 2" given in Table 21.

Table 21. Selected elements of EDX analysis of the marked area in Figure 68.

Element	Weight%	Atomic%
0	31.93	62.83
Na	0.12	0.17
Al	0.07	0.08
Si	0.18	0.20
Cl	4.58	4.06
K	1.09	0.88
Ca	0.26	0.21
Mn	0.96	0.55
Fe	52.33	29.50
Zn	0.71	0.34
Pb	7.77	1.18

4.3.1.5 SEM/EDX-analysis of windward side - PbO+SWS

A SEM/EDX picture of the cross section of the 16Mo3 sample exposed in the BW position during case PbO+SWS is shown in Figure 69, in which the steel substrate is to the upper right. The thickness of the corrosion product is here about 150 μ m. The correlating element maps in Figure 69 show that Cl is concentrated mainly to the corrosion front but it is also present in an outer layer interface. S is present in boundaries at the outer corrosion layer. Some alkali metals are detected in the outer part of the scale but not at the corrosion front. Also the P detected is in the outer scale. The maps for Pb and Zn are a bit prickled by noise; perhaps the concentrations are below the detection limit, but there is a faint line of Pb at the outer corrosion layer.

An example of SEM/EDX-analysis of a spot in the inner corrosion layer is Figure 69 and Table 22, composed mainly of oxygen, iron and chlorine, with some alkali metals, Zn and a little Pb.

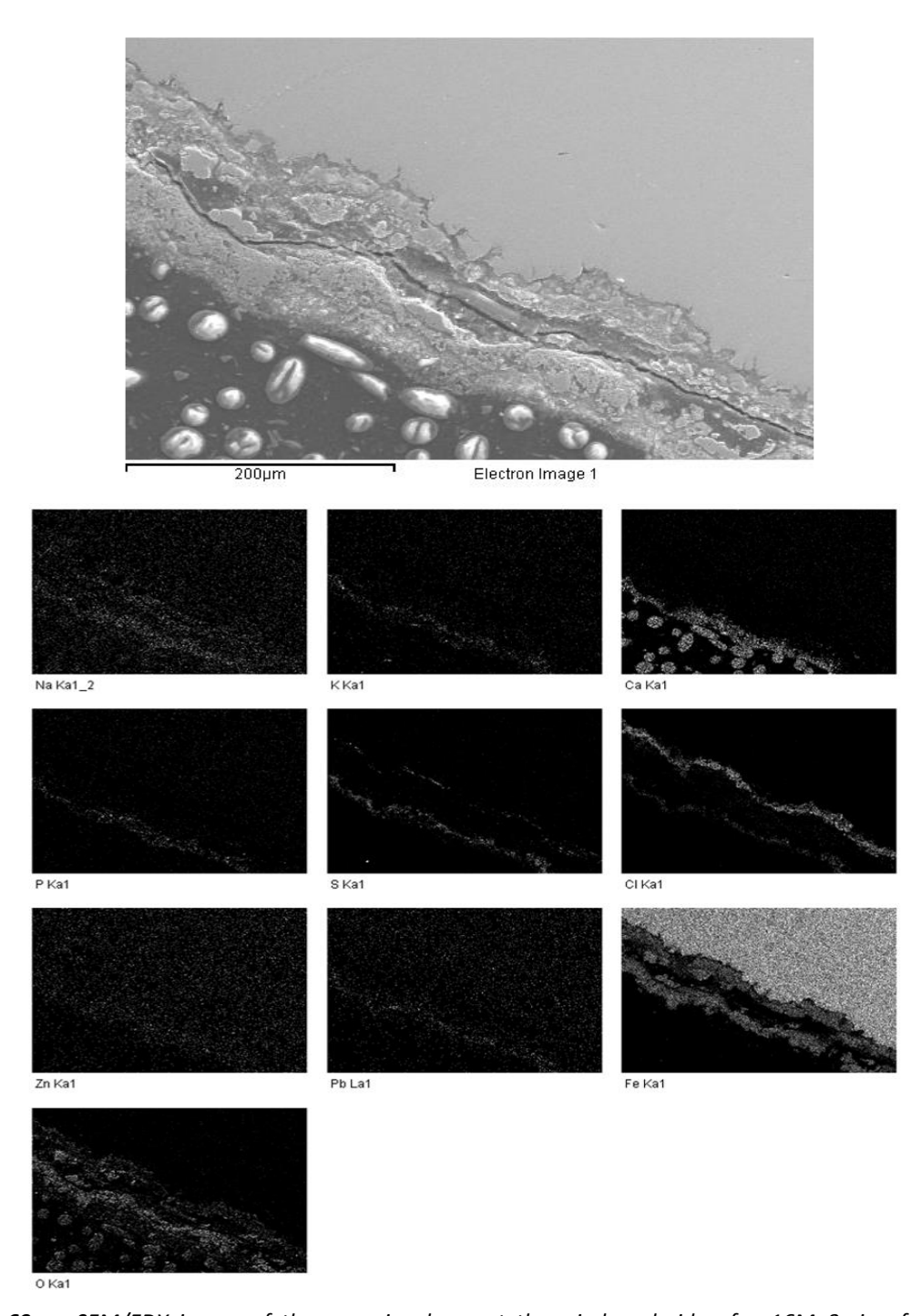


Figure 69. SEM/EDX image of the corrosion layer at the windward side of a 16Mo3 ring from case PbO+SWS. Top photo by BSE-SEM, below a matrix of element mapping.

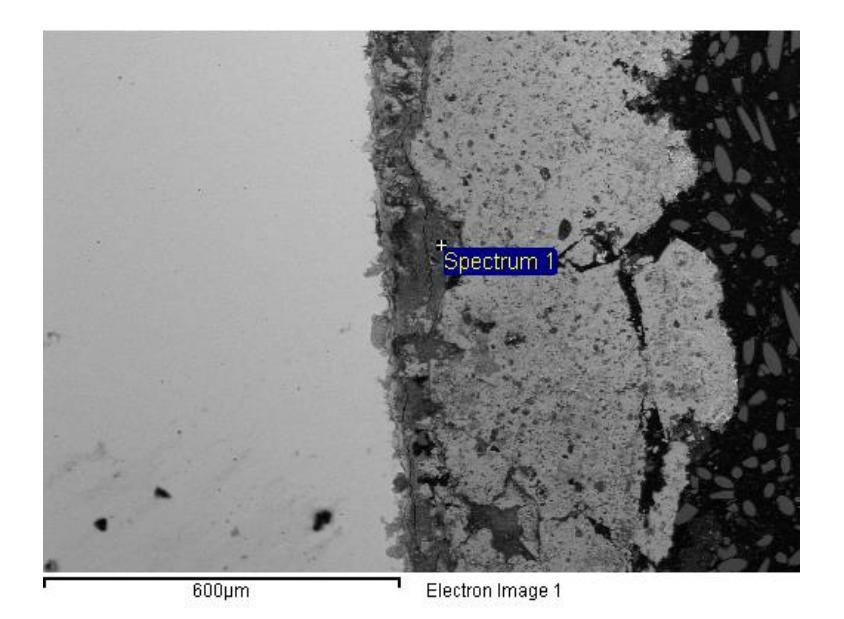


Figure 70. SEM image from windward cross-section of a 16Mo3 ring exposed in the BW position during case PbO+SWS. Elemental composition in point "Spectrum 1" given in Table 22.

Table 22. Elemental composition in the point marked in Figure 70.

Element	Weight%	Atomic%
0	47.54	73.22
Na	0.96	1.03
Mg	0.00	0.00
Al	0.46	0.42
Si	0.31	0.27
S	0.00	0.00
Cl	11.58	8.05
K	0.89	0.56
Са	0.27	0.17
Cr	0.37	0.17
Mn	0.25	0.11
Fe	34.31	15.14
Ni	0.21	0.09
Zn	1.67	0.63
Pb	1.19	0.14

4.3.1.6 SEM/EDX-analysis of leeward side – PbO+SWS

A SEM picture from the leeward side of the 16Mo3 sample from case PbO+SWS in Figure 71 displays a corrosion layer of about 20 μm . The EDX analysis of the spot marked in the figure is given in Table 23.

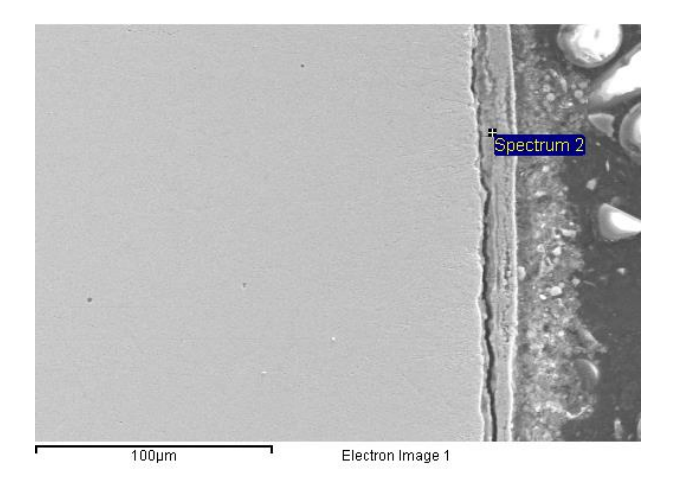


Figure 71. SEM image from leeward cross-section of a 16Mo3 ring exposed in the BW position during case PbO+SWS. Elemental composition in point "Spectrum 2" given in Table 23. The corrosion layer is here about 20 μm thick.

Table 23. EDX analysis of the spot marked in Figure 71.

Element	Weight%	Atomic%
0	31.98	60.07
Na	0.15	0.20
Al	0.24	0.26
Si	0.24	0.26
S	0.14	0.13
Cl	10.72	9.08
Mn	0.29	0.16
Fe	54.65	29.40
Pb	1.22	0.18

4.3.2 **BW 253 MA rings**

4.3.2.1 Deposits

The wind sides of the 253 MA sample rings from the BW position are shown in Figure 72. The left image shows from case PbO and the right from case PbO+SWS. The ring from case PbO, to the left, is greyish with obvious corroded spots penetrating the deposit layer. The deposit on the 253 MA ring from case PbO+SWS has flaked off locally at the inclination angle, revealing a corroded surface beneath. The deposit is greyish.

Images from the leeward side are shown in Figure 73. The ring from case PbO is covered by a greyish deposit with dispersed darker areas. The appearance is similar for the sample from case PbO+SWS.

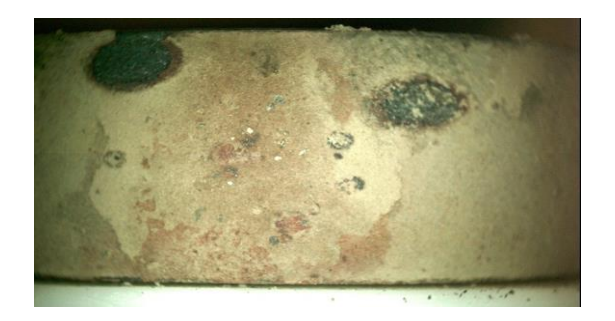




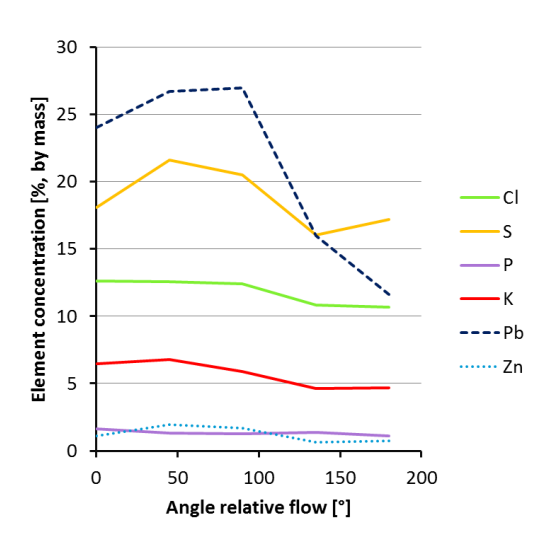
Figure 72. Photos of deposits on the windward side of the 253 MA-steel rings from the BW position. Left) PbO. Deposit is greyish with corroded areas. Right) PbO+SWS. The corroded surface is visible where deposits have scaled off.





Figure 73. Photos of deposits on the leeward side of the 253 MA-steel rings from the BW position. Left) PbO. Deposit is greyish with darker areas. Right) PbO+SWS. The appearances are similar to the case of PbO.

Figure 74 shows the elemental composition of some selected key elements from the inclination angle (0°) to 180° for the test cases of PbO (left plot) and PbO+SWS (right hand plot). The Cl-concentration is reduced from 10-13 wt% to 1-7 wt% when sewage sludge is added. Sulphur and Pb are also reduced while Zinc increases somewhat. Potassium is reduced with a few per cent units. Phosphorus is supplied by the sludge in the case of PbO+SWS.



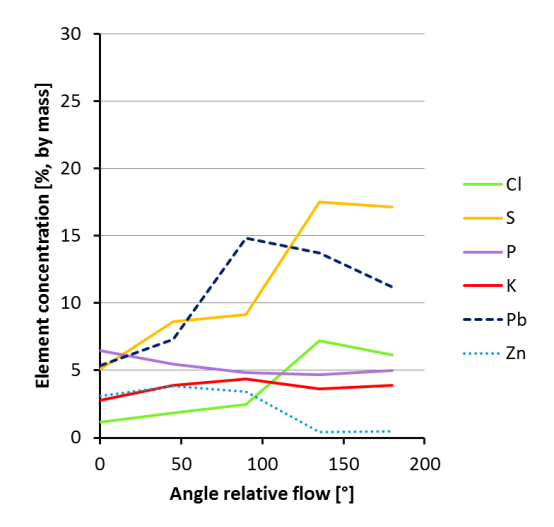


Figure 74. Elemental concentrations in the boiler wall deposits collected on 253 MA rings made by means of XRF analysis. Left) PbO. Right) PbO+SWS.

4.3.2.2 Ring surfaces after cleaning

Figure 75 shows the windward surfaces of the rings after the deposits have been removed. The surfaces have been cleaned with a coarse cloth. The left image shows the case PbO and the right image the case PbO+SWS. Oval corroded areas are obvious in the case of PbO. Some corrosion can also be seen elsewhere on the surface. The surface in the right hand image (PbO+SWS) is not noticeably corroded.



Figure 75. Photos of 253 MA-steel rings from the BW position, windward side, after deposit removal. Left) PbO. Right) PbO+SWS.

Figure 76 shows the leeward sides of the 253 MA-sample rings from cases PbO and PbO+SWS, respectively. Parts of the surface on the sample ring to the left (PbO) is corroded, while other areas are not. The image to the right (PbO+SWS) shows no corroded areas. However, some spots are miscoloured.

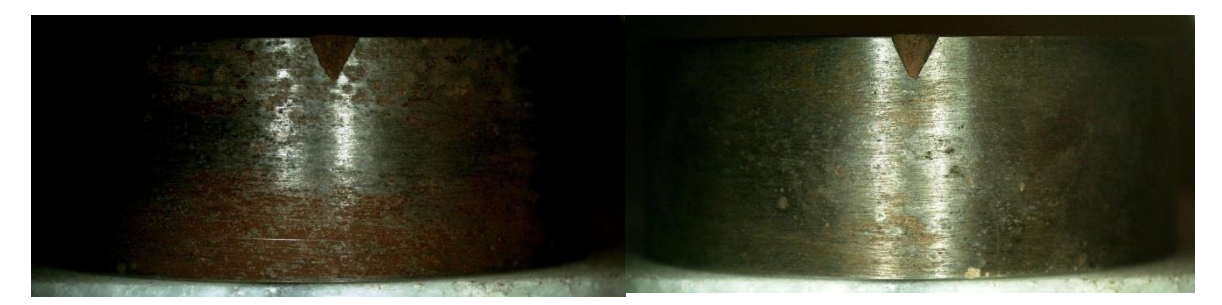


Figure 76. Photos of 253 MA-steel rings from the BW position, leeward side, after deposit removal. Left) PbO. Right) PbO+SWS.

4.4 BW Comparisons between Ref 1 and Ref 2 (second set of tests)

To check how the reference trial of the first set of tests relates to the reference trial in the second set of tests, the analyses of their deposits and the observations from the two tests are compared to each other below.

4.4.1 BW 16Mo3 rings

4.4.1.1 Ring surface after cleaning

The surfaces of the 16Mo3 rings exposed in the BW position of the reactor for cases Ref 1 and Ref 2 are compared in Figure 77. Different devices were used to capture these pictures, which makes a comparison difficult. Anyway, both samples were strongly corroded underneath the deposits. The XRF analyses of the deposits are given in Figure 78, showing similar concentrations of Cl, S and K. However, the concentration of Zn was higher in case Ref 1, while the concentration of Pb was higher in case Ref 2. The difference in Zn is probably caused by higher Zn content in the fuel for Ref 1, while the difference between lead concentrations mainly is a measurement deviation caused by an upgrade of the XRF analyser between the measurements.





Figure 77. Photos from the windward sides of 16Mo3 substrates, after deposits have been removed. Samples were exposed at the BW position. Left) Ref 1. The sample is corroded underneath the deposit. Right) Ref 2. Severe spallation of corrosion product

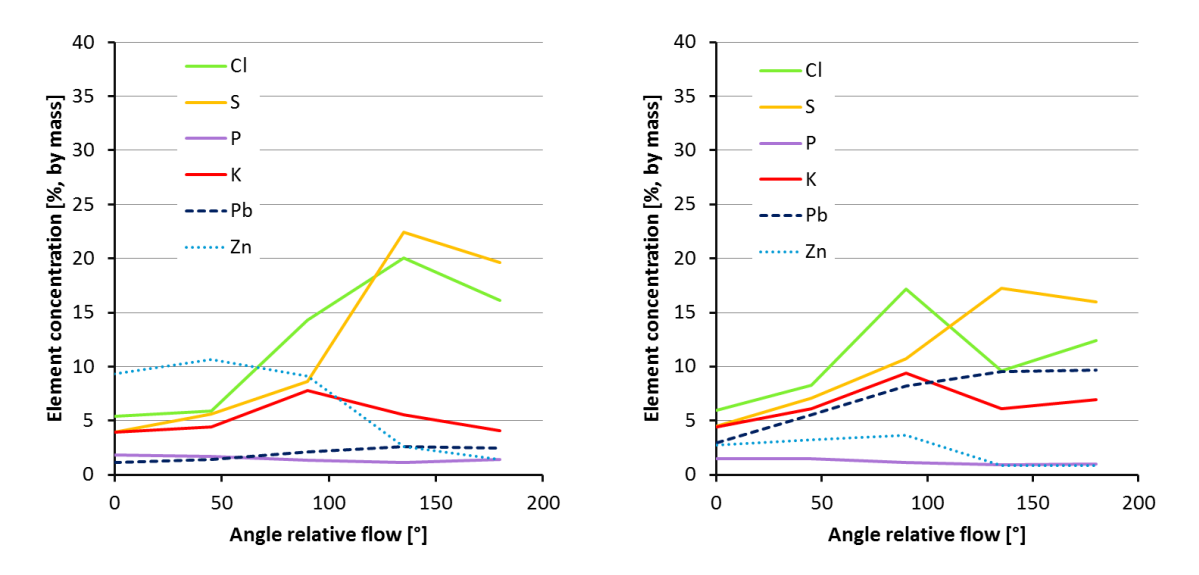


Figure 78. Elemental concentrations in BW deposits on 16Mo3 samples. Left) Ref 1 Right) Ref 2

4.5 BW comparison between SWS1 and SWS2 (second set of tests)

4.5.1 BW 16Mo3 rings

4.5.1.1 Ring surface after cleaning

Ring surfaces of 16Mo3 samples from the BW position, after deposit removal, are shown in Figure 79 for the cases of SWS1 and SWS2. The ring in the left image is not severely corroded as the grinding groves still are visible. The photo to the right is more corroded but the image exaggerates the corrosion product. The XRF analyses of the deposits are given in Figure 80. Both rings have lowest Cl concentrations at the windward sides. The S and Zn concentrations are higher for case SWS1 than case SWS2, while Pb is higher for SWS2 (probably mostly due to analytical error). The S concentrations increased towards the leeward sides for both rings.

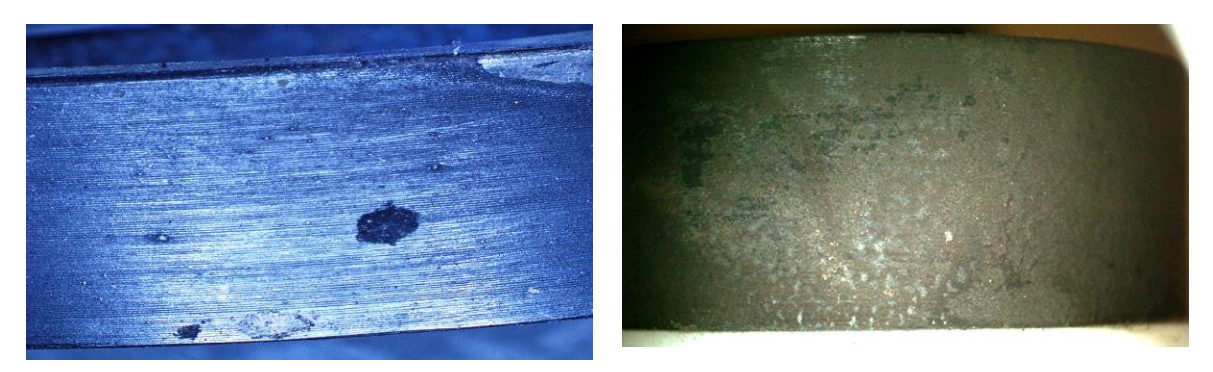


Figure 79. Photos of the 16Mo3 rings after exposure in the boiler wall position. Left) SWS1. Right) SWS2. The surface is covered with a brownish layer. The grinding grooves can be seen. The photo does not reflect the reality perfectly.

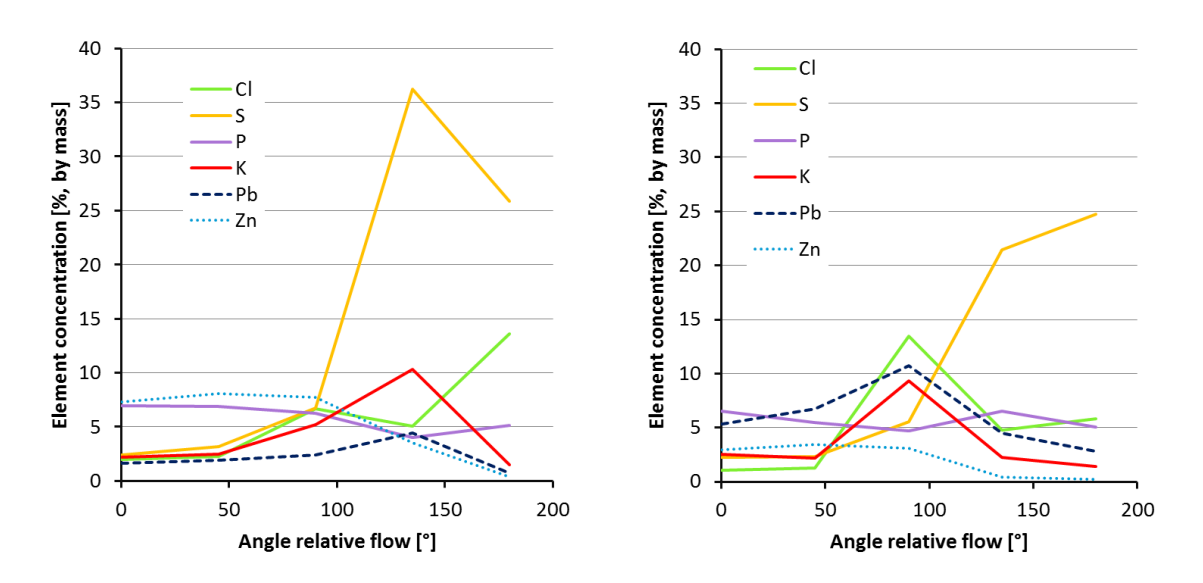


Figure 80. Elemental concentrations in BW deposits on 16Mo3 samples. Left) SWS1, Right) SWS2.

4.6 SH comparison (first set of tests)

4.6.1 SH 16Mo3 rings

Macroscopic photos of the 16Mo3 rings after exposure in the superheater (SH) position of the furnace and subsequent removal of deposits are shown in Figure 81. These photos of corrosion attacks on the substrate can be compared to the XRF analyses of selected elements in the deposits, prior to its removal, in Figure 82.

The SH positioned 16Mo3 ring from the case of Ref 1 (A in Figure 81) is scaled in the region between -90° and 90°. The corresponding XRF analysis of its deposit (in Figure 82A) shows that the deposit contains fairly high concentrations of S and K and up to 10 % Cl. The ring from the case of foundry sand (B in Figure 81) is corroded in the region between -20° and 20°, and discoloured elsewhere. That is, it suffered somewhat less from corrosion than the ring from the reference case. The analysis of its deposit (in Figure 82B) reveals that the Cl content is reduced from the reference case, while the S and K concentrations are less affected by the additive. The grinding marks from the preparation of the 16Mo3 ring remained intact for the kaolin case (C in Figure 81), indicating that the corrosion is not severe in this case, although traces of light corrosion could be found all around the ring. Unfortunately, the XRF analysis of this deposit failed. The ring from the lime case (D in Figure 81) fare a lot worse and is corroded between -20° and 20°. The analysis of the deposit (in Figure 82D) shows significantly higher Cl and lower S concentrations than the reference case. The additive of sewage sludge (SWS1, Figure 81E) results in corroded spots all around the ring. The corresponding analysis of the deposit reveals relative low chlorine content, but both S and K are higher than in the reference case. The phosphorous from the additive is rather evenly distributed around the ring. The 16Mo3 ring from the case of sulphur additive is only lightly corroded in the region between -90° and 90°. The analysis of the deposit on this ring shows Cl and K at significantly lower levels than in the reference case. On the other hand, the content of S is higher.

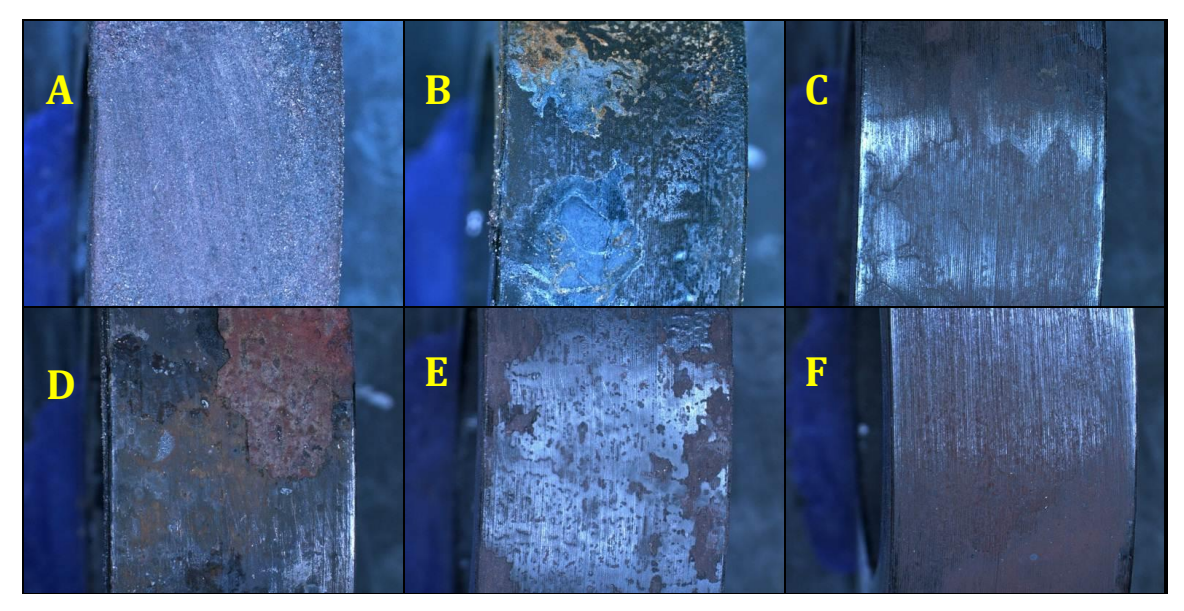


Figure 81. 16Mo3 rings from SH position, after cleaning. A) Ref 1, B) FS, C) Kaolin, D) Lime, E) SWS1, F) S.

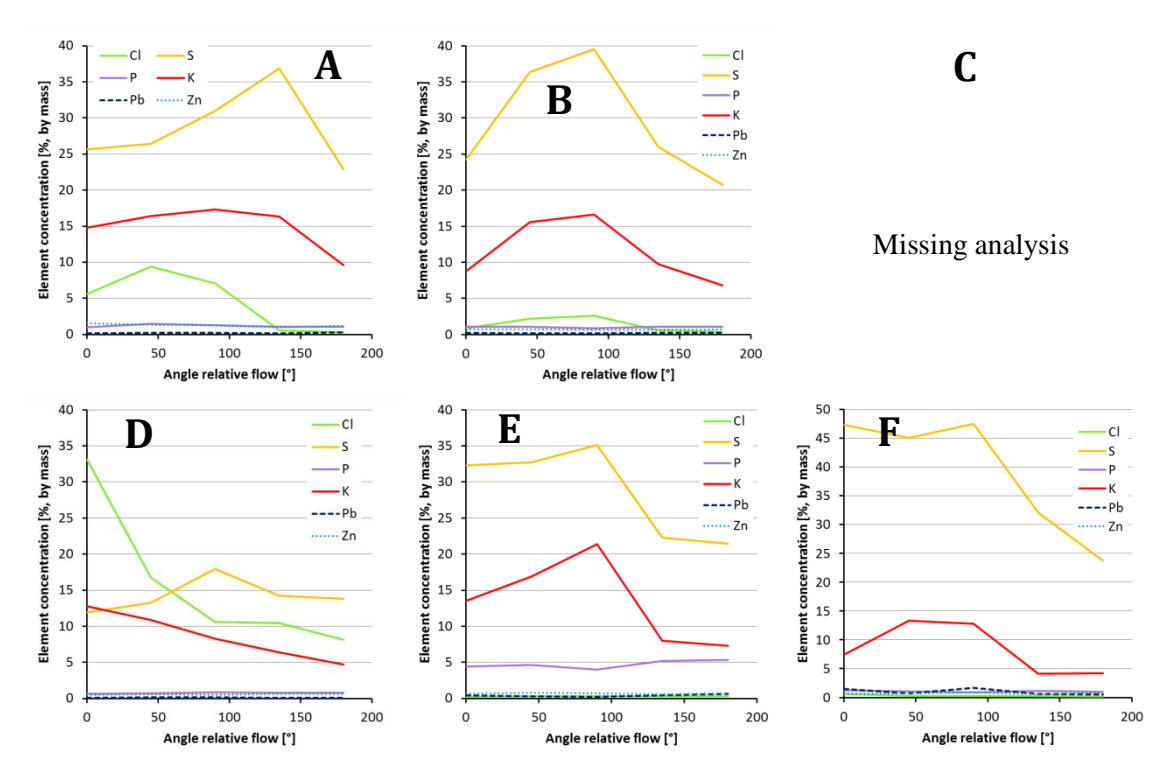


Figure 82. Elemental concentrations in deposits on the SH 16Mo3 rings, measured by XRF on the surface at varied angles relative to the windward side. A) Ref 1, B) FS, C) Kaolin, D) Lime, E) SWS1, F) S.

4.6.2 SH 253 MA rings

The 253 MA ring from the Ref 1 case, in SH position, is shown in Figure 83A. It is somewhat discoloured in the region between -70° and 70°. The corresponding XRF analysis of its deposit (in Figure 84A) shows that the deposit contains a high amount of S, considerable amounts of K and less Cl. The ring from the case of **foundry sand** (missing in Figure 83) is dispersedly corroded. Its deposit contains similar contents of Cl, S and K as the reference ring. The ring from the **kaolin** case has some discoloured spots around the circumference. The XRF analysis failed in most positions except towards the leeward side, where the trend points towards reduced concentrations of Cl, K and S. The ring from the **lime** case has some evident corrosion on the windward side (in Figure 83D). This may be a consequence of a much higher chlorine content in the deposit than for the other test cases (Figure 84D). The ring from the **sewage sludge** case has some spots of corrosion at 0° and some pitting at 90° (in Figure 83E). The deposit on this ring shows a bit lower concentrations of S and K than the reference case. The Cl content is relatively low. The 253 MA ring from the **sulphur** case is only lightly discoloured (maybe by heat) on the windward side. The analysis of the deposit shows reduced Cl and K concentrations while the concentration of S is similar to the reference case.

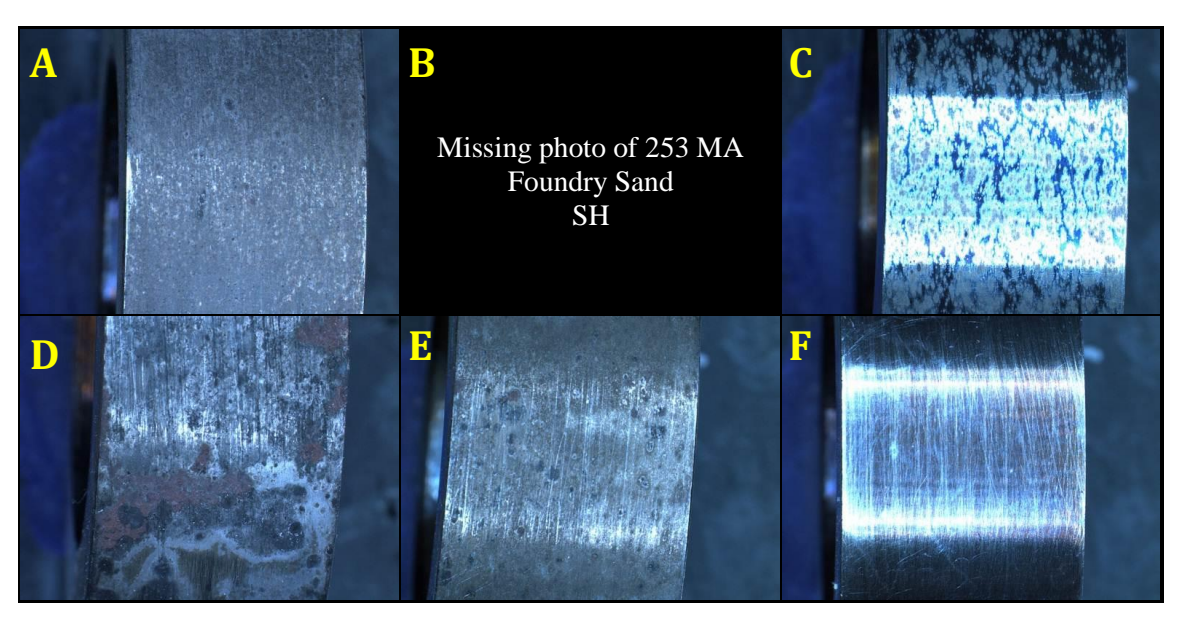


Figure 83. 253 MA rings from SH position, after cleaning. A) Ref 1, B) FS, C) Kaolin, D) Lime, E) SWS1, F) S.

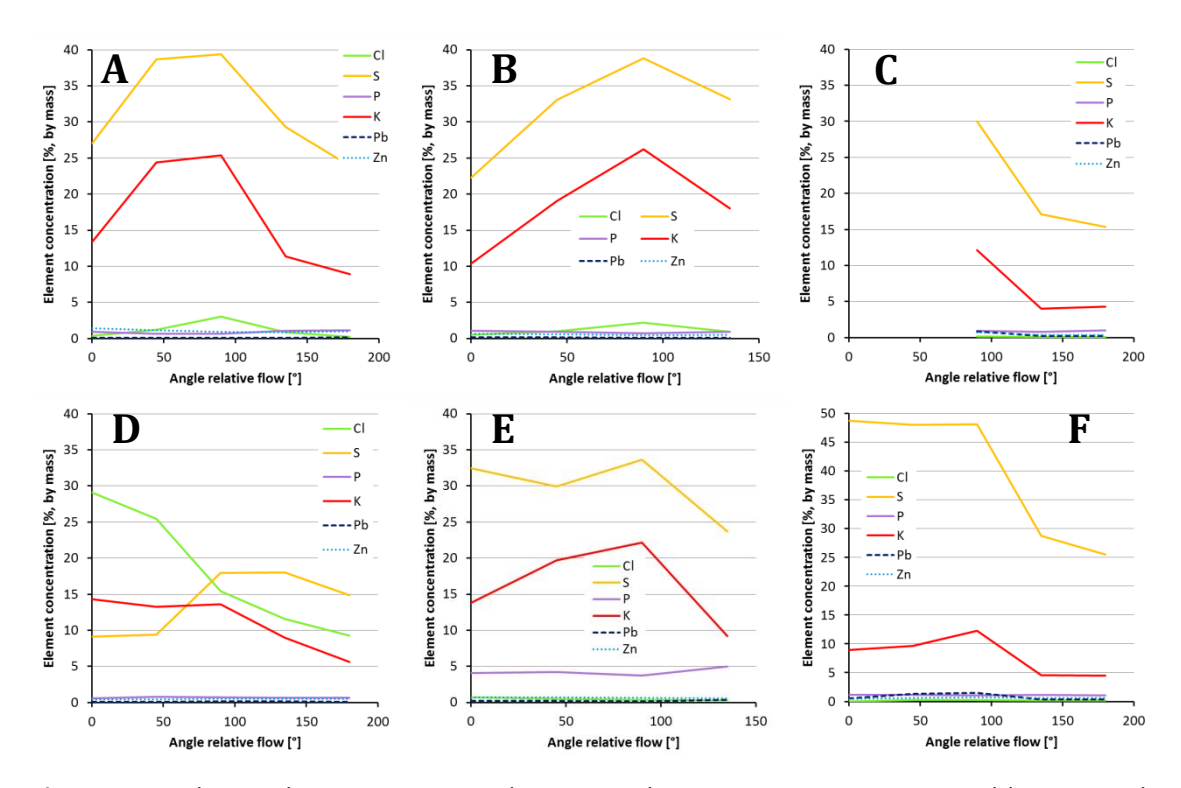


Figure 84. Elemental concentrations in deposits on the SH 253 MA rings, measured by XRF on the surface at varied angles relative to the windward side. A) Ref 1, B) FS, C) Kaolin, D) Lime, E) SWS1, F) S.

4.6.3 SH Kanthal-A1 rings

The Kanthal-A1 rings sustain the 8 hours exposure at SH-conditions well, as can be seen in the macroscopic photos of Figure 85. The rings from the reference and sewage sludge cases are only lightly discoloured. The rings from the cases of foundry sand, kaolin and sulphur are almost clean. Only the ring from the case with the lime additive shows some dispersed stains, that may be signs of initiating corrosion, on the windward side. The analyses of the deposits, in Figure 86, follow the same trend as those for 253 MA in Figure 84, which are discussed above.

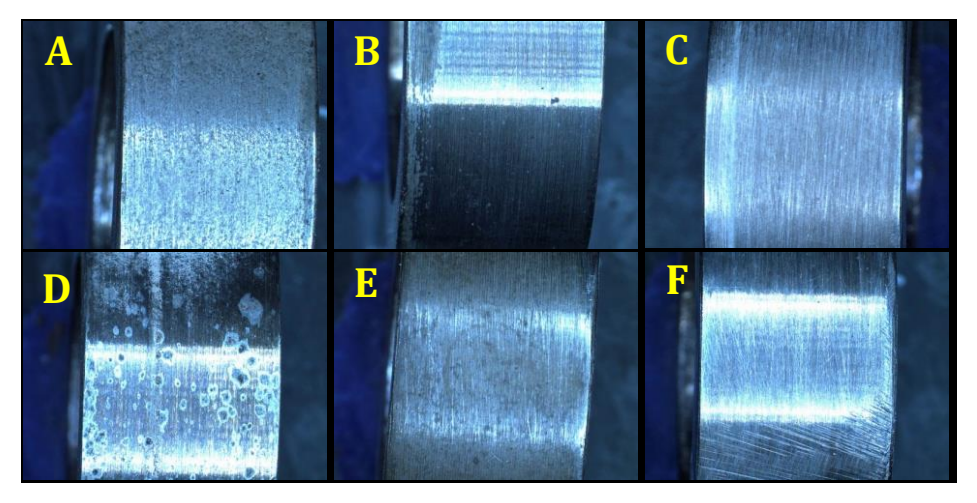


Figure 85. Kanthal-A1 rings from SH position, after cleaning. A) Ref 1, B) FS, C) Kaolin, D) Lime, E) SWS1, F) S.

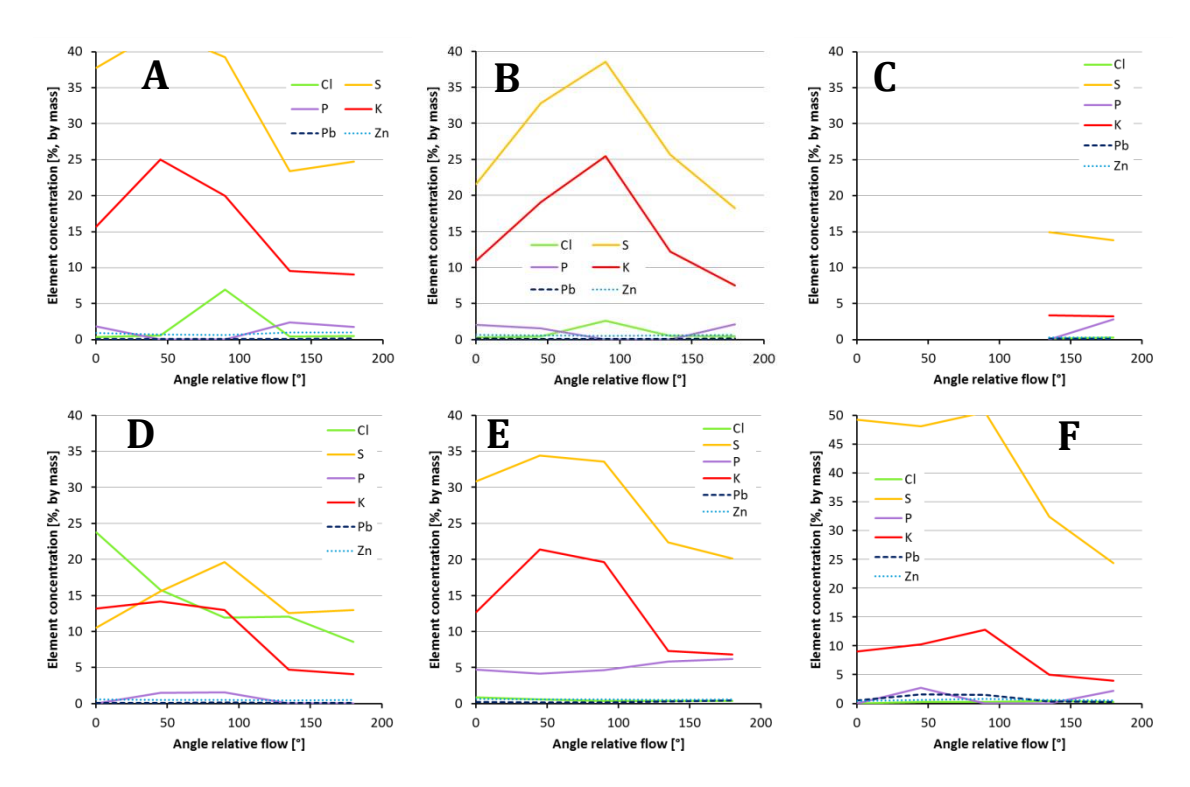


Figure 86. Elemental concentrations in deposits on the SH Kanthal-A1 rings, measured by XRF on the surface at varied angles relative to the windward side. A) Ref 1, B) FS, C) Kaolin, D) Lime, E) SWS1, F) S.

4.7 SH comparison between Ref 2 and SWS2 (second set of tests)

4.7.1 SH 16Mo3 rings

4.7.1.1 Deposits

Photos of the windward side of the deposits on the 16Mo3 rings from the superheater position are shown in Figure 87, with case Ref 2 to the left and the case SWS2 to the right. The ring from case Ref 2 is covered by a grey deposit with darker dispersed spots, indicating corrosion. The deposit from case SWS 2 is more yellowish with some small darker spots. On the leeward sides of these rings, shown in Figure 88, the rings are covered by deposits of a somewhat smoother surface than on the windward side.





Figure 87. Photos of the windward sides of the 16Mo3 rings after exposure in the superheater position. Left) Ref 2. Covered with a grey deposit dispersion of darker spots, indicating corrosion Right) SWS2. Covered with a yellow/grey deposit with darker spots.





Figure 88. Photos of the leeward sides of the 16Mo3 steel after exposure in the superheater position. Left) Ref 2, covered with a grey deposit. Right) SWS2, covered with a yellow/grey deposit.

The XRF analyses of these superheater deposits are shown in Figure 89, revealing that that the additive of sewage sludge reduces the Cl content in the deposits while increasing the concentrations of S and P. The content of Pb is also increased by the sewage sludge, whereas concentrations of K and Zn are less affected.

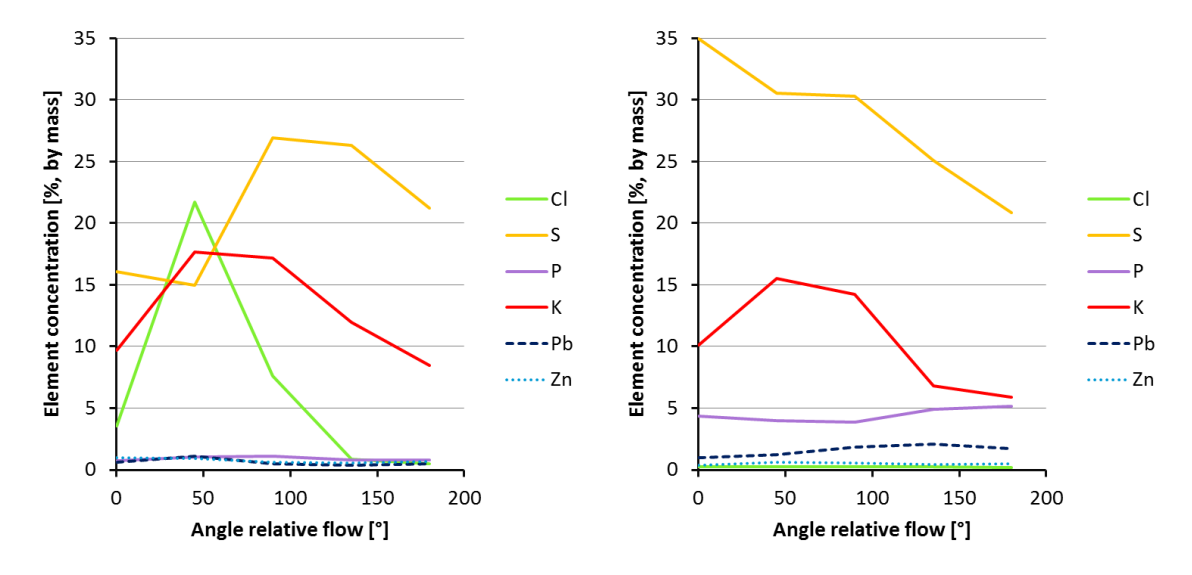


Figure 89. Elemental concentrations in SH deposits on 16Mo3-steel. Left) Ref 2. Right) SWS2.

4.7.1.2 Sample ring surfaces after cleaning

The metal surfaces of the wind sides of the 16Mo3 deposit rings from the SH position, after removal of the deposits, are shown in Figure 90. The surface is severely corroded for case Ref 2 and much lesser corroded in the case of SWS2, where still some grinding marks remain. On the leeward sides of these rings, Figure 91, less signs of corrosion are found. The ring from case Ref 2 has some brown areas indicating moderate corrosion (grinding grooves remain visible). The ring from case SWS2 is less affected but has areas that are discoloured (bronze).

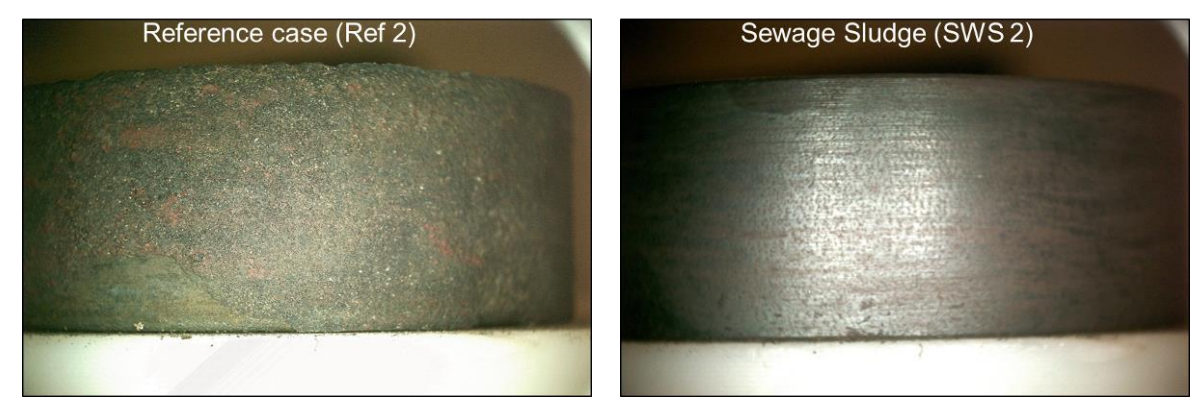


Figure 90. Photos of the windward sides of the 16Mo3 rings after deposit removal, from the SH position. Left) Ref 2. Severely corroded. Right) SWS2. Brownish but no obvious corrosion products.





Figure 91. Photos of the leeward sides of 16Mo3 rings after deposit removal, from the SH position. Left) Ref 2. Only few signs of corrosion (brown areas). Right) SWS2. Partly covered with a thin dark layer and some areas have been discoloured (bronze).

4.7.2 SH 253 MA rings

4.7.2.1 Deposits

The deposits of the windward side of the 253 MA SH-deposit rings are photographed in Figure 92. The ring from case Ref 2 is covered by a brown/grey deposit which is darker towards the inclination angle, while the ring from case SWS2 is of a more yellow/grey tone, stained by some darker dots. On the leeward sides of these rings, the deposits are thinner and the cases exhibits similar deposits, perhaps with a somewhat more yellowish tone for the SWS2 case.





Figure 92. Photos of the windward sides of the 253 MA rings after exposure in the SH position. Left) Ref 2, Right) SWS2.

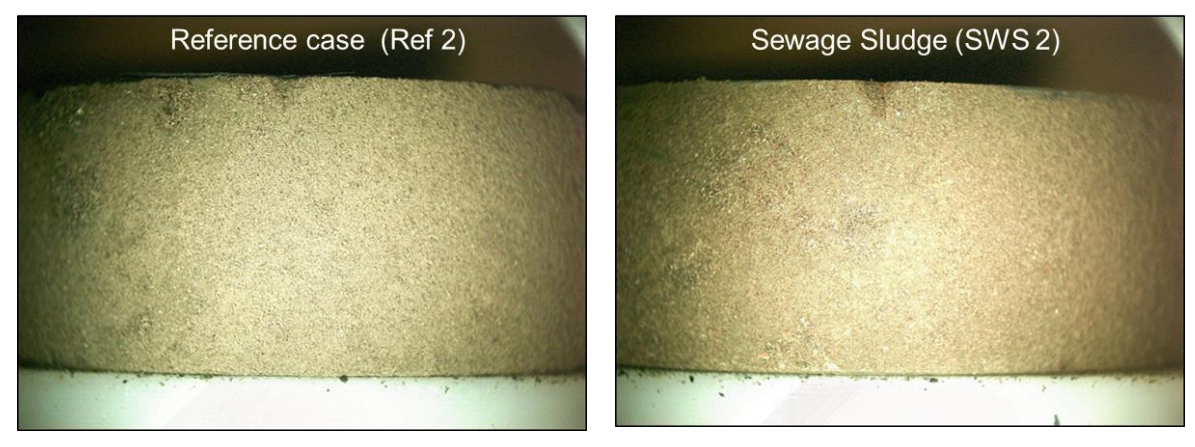


Figure 93. Photos of the leeward sides of the 253 MA rings after exposure in the superheater position. Left) Ref 2, Right) SWS2.

The elemental analyses of the deposits on the 253 MA rings from the SH-position are illustrated in Figure 94. The concentration of Cl is clearly reduced by the addition of sewage sludge, while the concentrations of P, S and Pb increase. The effects of the additive on K and Zn are too small to be judged as conclusive.

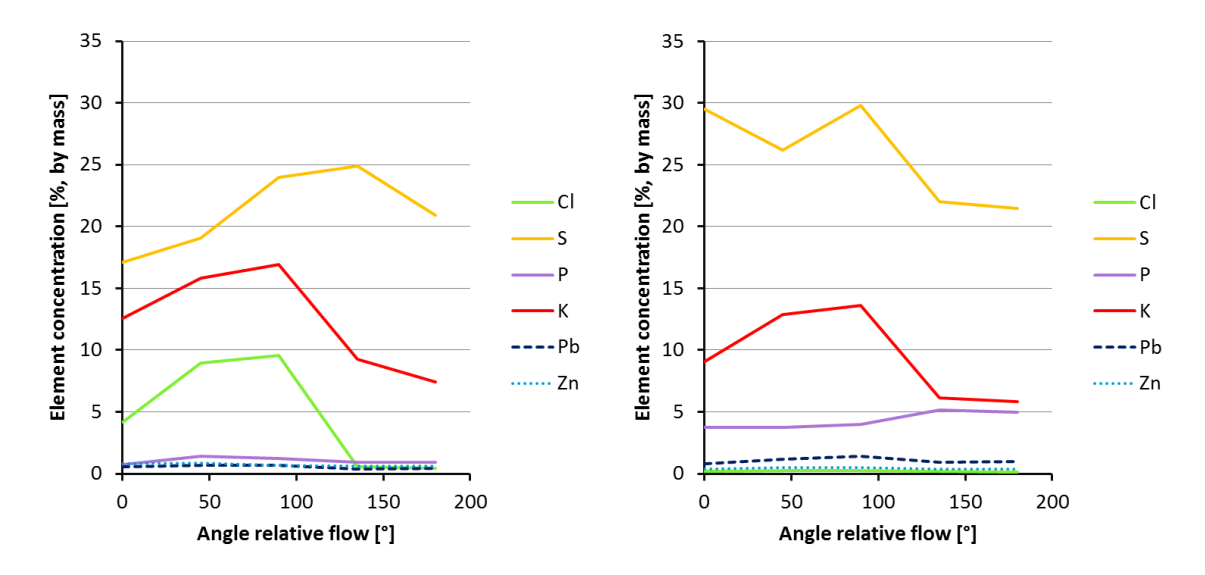


Figure 94. Elemental concentrations in SH deposits on 253 MA rings by XRF analysis. Left) Ref 2. Right) SWS2.

4.7.2.2 Ring surfaces after cleaning

The 253 MA surfaces beneath the deposits are revealed in Figure 95 and in Figure 96, showing the windward and leeward sides, respectively. The ring from case Ref 2 is partly corroded on the windward side, where some corrosion products may have spalled off, while it showed a metallic surface with some darker spots on the leeward side. The ring from case SWS2 still has a metallic lustre with some dark stains on the windward side and a virtually unaffected surface on the leeward side.





Figure 95. Photos of the windward sides of the 253 MA rings after deposit removal, from the superheater position. Left) Ref 2, Right) SWS2.

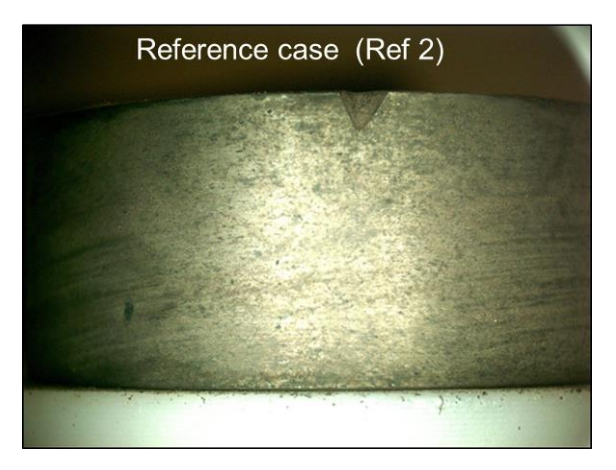




Figure 96. Photos of the leeward sides of the 253 MA rings after deposit removal, from the superheater position. Left) Ref 2, Right) SWS2.

4.8 SH comparison between: PbO and PbO+SWS (second set of tests)

4.8.1 SH 16Mo3 rings

4.8.1.1 Deposits

The deposits on the 16Mo3 rings from the SH position during the cases of PbO and PbO+SWS are compared in Figure 97 (windward side) and Figure 98 (leeward side). On the windward side, the deposit from case PbO is dark grey with brown corrosion products visible through the deposit layer, while the deposit from case PbO+SWS has a yellow/grey hue covered by darker spots. On the leeward sides, the deposits were quite similar, with a slight shift in hue and the deposits had spalled off somewhat more from the PbO case.



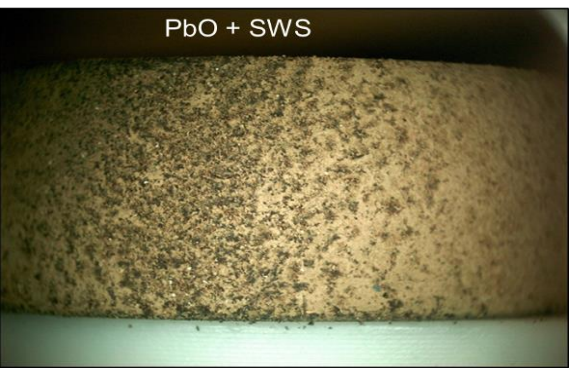


Figure 97. Photos of deposits on the windward side of the 16Mo3-steel rings from the SH position. Left) PbO. A dark and a grey deposit with brown corrosion products visible through the deposit. Right) PbO + SWS. A yellow/grey deposit with darker spots.





Figure 98. Photos of deposits on the leeward side of the 16Mo3-steel rings from the SH position.

A) PbO. The deposit has spalled off some areas revealing corrosion products underneath.

B) PbO+SWS. Covered with a yellow/grey deposit, which has spalled off locally. Some corrosion can be seen.

The elemental analyses of the deposits, in Figure 99, show that the sewage sludge in the case of PbO+SWS drastically reduces the chlorine content in the deposits. On the other hand, the contents of S, P and Pb increase by the addition of sewage sludge to the fuel. The content of K is somewhat reduced by the sewage sludge.

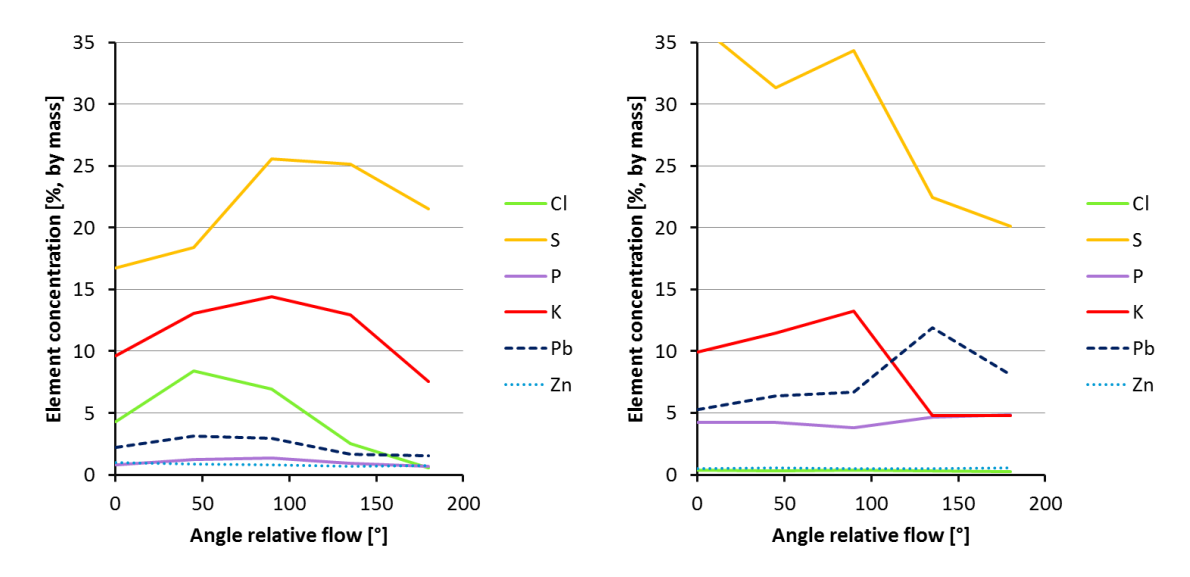


Figure 99. Elemental concentrations in SH deposits on 16Mo3 rings, by XRF analysis. Left) PbO. Right) PbO+SWS.

4.8.1.2 Ring surface after cleaning

After removal of the deposits (shown in Figure 100 for the windward side and in Figure 101 for the leeward side), it is obvious that the 16Mo3 steel is severely corroded on the windward side of the ring from case PbO while the leeward side fared better with only partial corrosion. For case PbO+SWS, the surfaces are less corroded than for the PbO case, but corrosion products still have spalled.

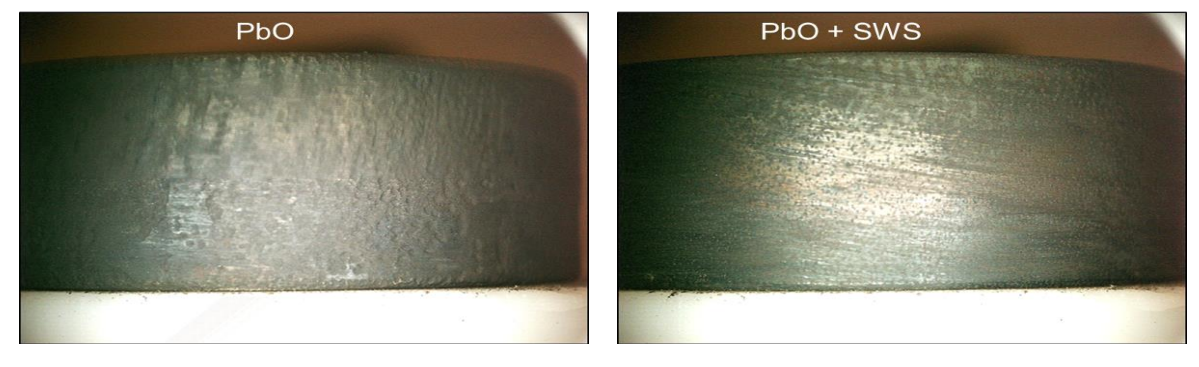


Figure 100. Photos of 16Mo3-steel rings from the SH position, windward side after deposit removal Left) PbO. Severely corroded. The corrosion products have spalled. Right) PbO+ SWS. The surface has spalled.





Figure 101. Photos of 16Mo3-steel rings from the super heater position, leeward side after deposit removal Left) PbO. The lee side is partly corroded and the corrosion product has spalled at some areas. Right) PbO + SWS. The surface has spalled off.

4.8.2 SH 253 MA rings

4.8.2.1 Deposits

The deposits on the 253 MA rings, shown in Figure 102 and Figure 103, are similar to the ones described above on the 16Mo3 rings. The difference is mainly that no corrosion products are visible through the deposit layer on the 253 MA ring from case PbO. There are also no spalled deposits on the 253 MA rings on the leeward sides.





Figure 102. Photos of deposits on the windward side of the 253 MA-steel rings from the SH position. Left) PbO. The wind side is covered with a brown/grey deposit with darker spots. Right) PbO + SWS. The wind side is covered with a yellow/grey deposit with darker spots.

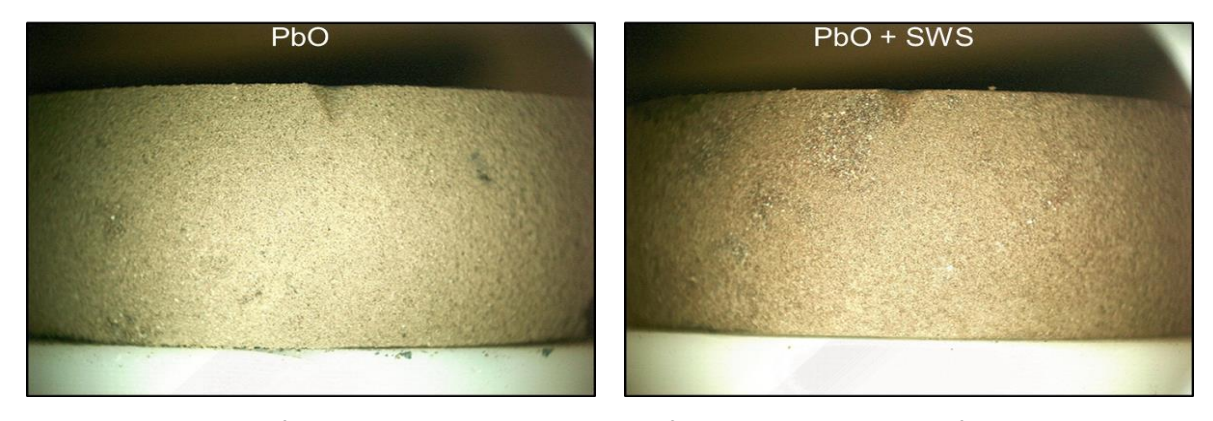


Figure 103. Photos of deposits on the windward side of the 253 MA steel rings from the SH position. Left) PbO. A yellow/grey deposit. Right) PbO+SWS. A yellow/grey deposit.

The comparison of elemental analyses of the deposits on the 253 MA rings in Figure 104 shows less chlorine in the deposit from the case of PbO+SWS compared to the case of PbO. There is also a trend of reduced K concentrations. Meanwhile, the concentrations of S, P and Pb increase by the sewage sludge additive. The analysis of the deposit on the 253 MA ring from case PbO (Figure 104) differs from the analysis of the 16Mo3 ring from the same case (Figure 99). This difference may be connected to observed corrosion products penetrating the deposit layer on the windward side of the 16Mo3 ring but not on the 253 MAsubstrate, i.e. more corrosion products may be included in the analysis of the former.

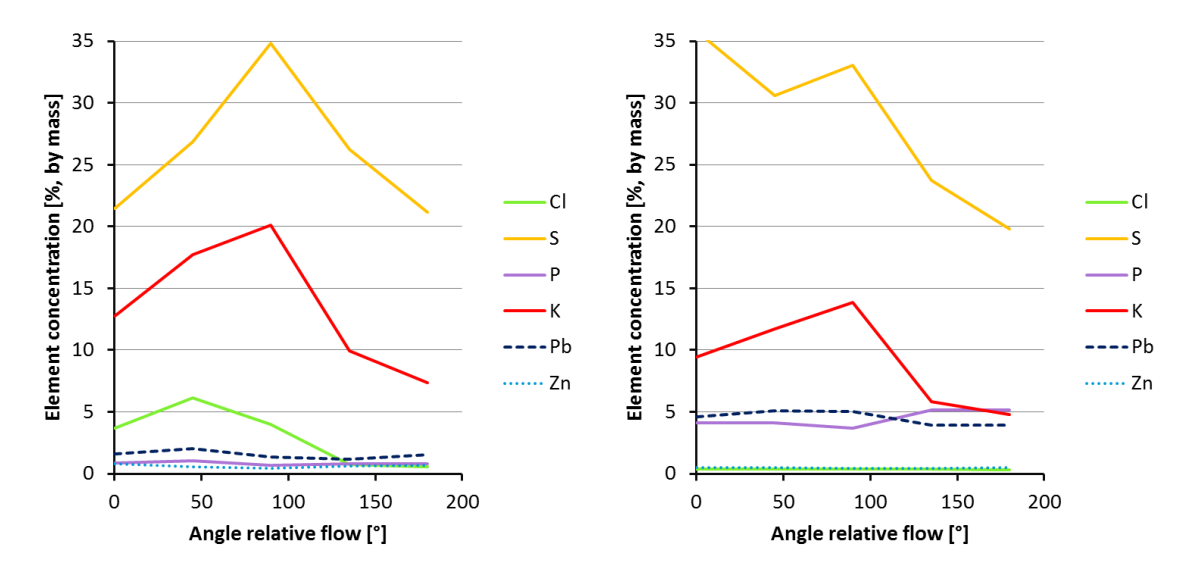


Figure 104. Elemental concentrations in SH deposits on 253 MA rings, by XRF analysis. Left) PbO. Right) PbO+SWS.

4.8.2.2 Ring surfaces after cleaning

After removal of the deposits on the 253 MA rings, the steel surfaces are shown in Figure 105 (windward side) and Figure 106 (leeward side). On the windward side of the ring from case PbO, there is a dark layer covering the surface on which corrosion is obvious in some minor areas. The windward side of the ring from case PbO+SWS has a metallic appearance with a few dark stains on it.

The surface of the 253 MA ring from case PbO exhibits a distinguished transition from a dark to a bright layer at about 90° (perpendicular to the direction of the gas flow), as can be seen in Figure 106A. The ring from case PbO+SWS shows a slight discolouration towards the leeward side of the ring (starts at about 15° from the inclination angle).



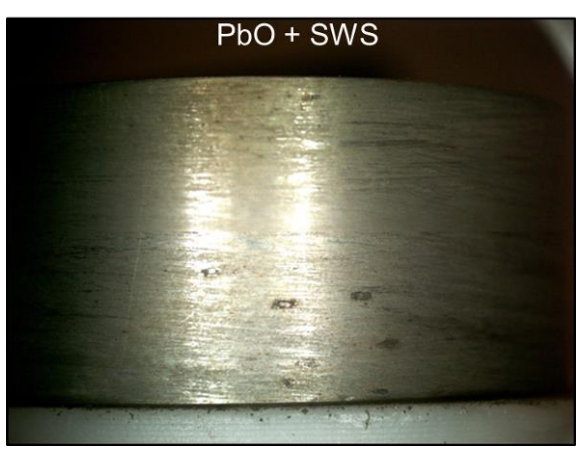
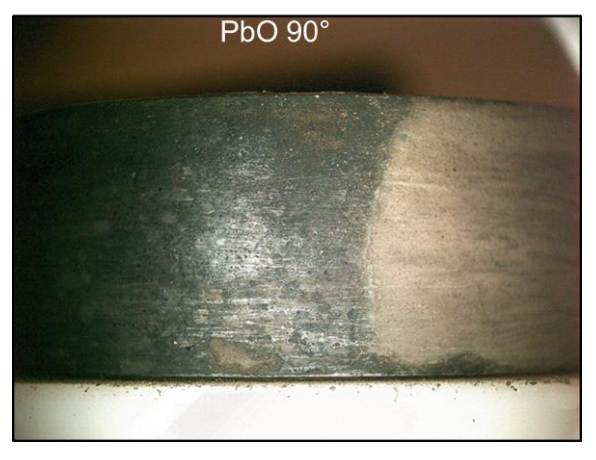


Figure 105. Photos of substrate, after deposits are removed, on the windward side of the 253 MA steel rings from the SH position. Left) PbO. Some minor areas are corroded and a dark layer has formed on the surface. Right) PbO+SWS. A metallic appearance with a few dark stains.



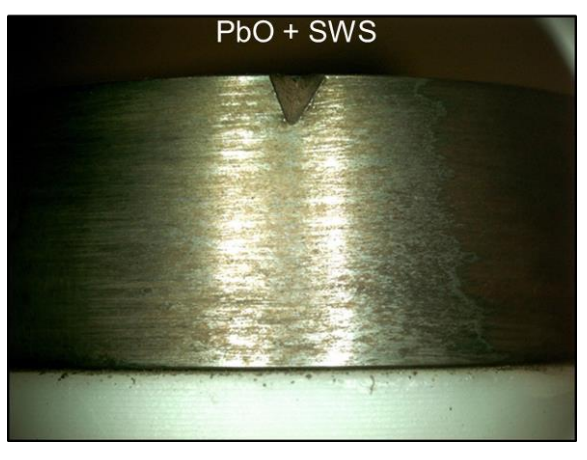


Figure 106. Photos of substrate, after deposits are removed, from the 253 MA steel rings exposed at the SH position. A) PbO, picture from 90° where a sharp transition from a darker layer to a bright layer can be seen. B) PbO+SWS, picture from leeward side. A metallic appearance of the alloy (a discolouration starts at 15°).

4.9 SH Comparisons between Ref 1 and Ref 2

4.9.1 SH 16Mo3 rings

4.9.1.1 Ring surface after cleaning

The 16Mo3 rings, from the SH position, from the cases of Ref 1 and Ref 2 are shown after removal of their deposits in Figure 107. Corrosion products have scaled off both of the rings and they are heavily corroded. The XRF analyses of the deposits are given in Figure 107, where it can be observed that there are higher concentrations of Cl in the deposit from case Ref 1 compared to case Ref 2, while S and K are detected in similar concentrations.

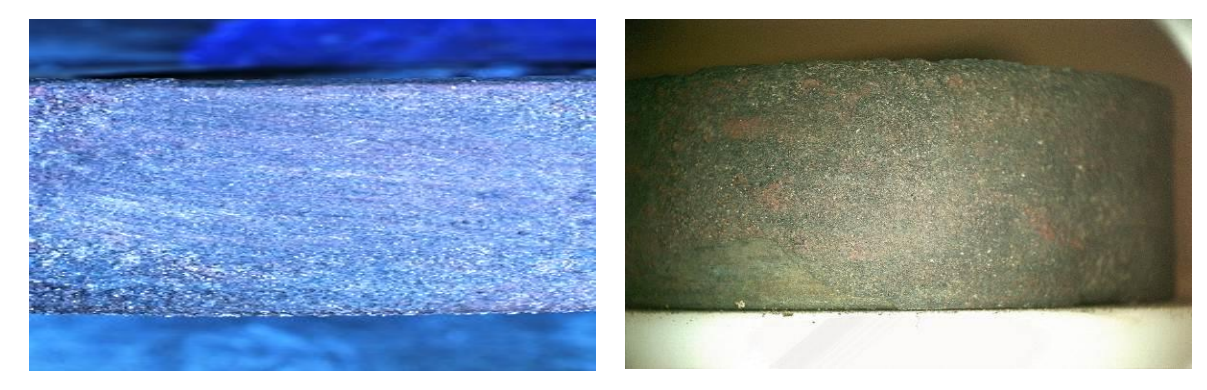


Figure 107. Photos from the windward sides of 16Mo3 substrates, after deposits have been removed. Samples were exposed at the SH position. Left) Ref 1. Scaled. Right) Ref 2. Severely corroded. Parts of the corrosion product have felled off.

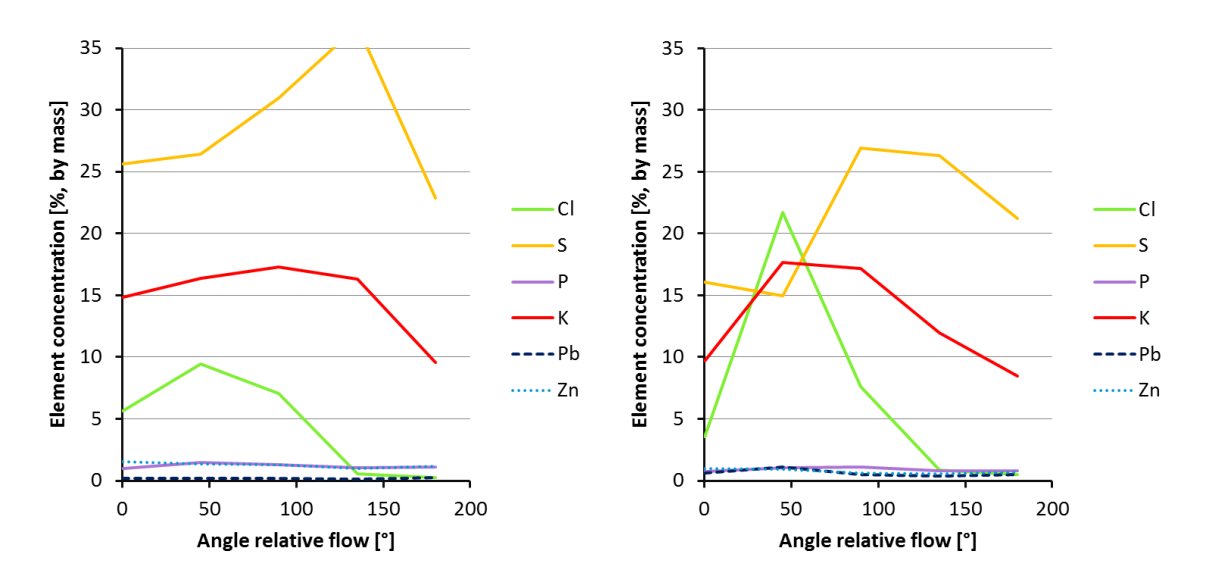


Figure 108. Elemental concentrations in deposits collected at the SH position on 16Mo3 rings. Left) Ref 1 Right) Ref 2

4.9.2 SH 253 MA rings

4.9.2.1 Rings after cleaning

A comparison between SH rings of 253 MA from the cases of Ref 1 and Ref 2 shows that the ring from case Ref 2 is more corroded than the one from case Ref 1 (Figure 109). Also the elemental analyses of the deposits on these rings indicate that the case Ref 2 is more severe than case Ref 1, because the deposits of Ref 2 contains more Cl and less S.

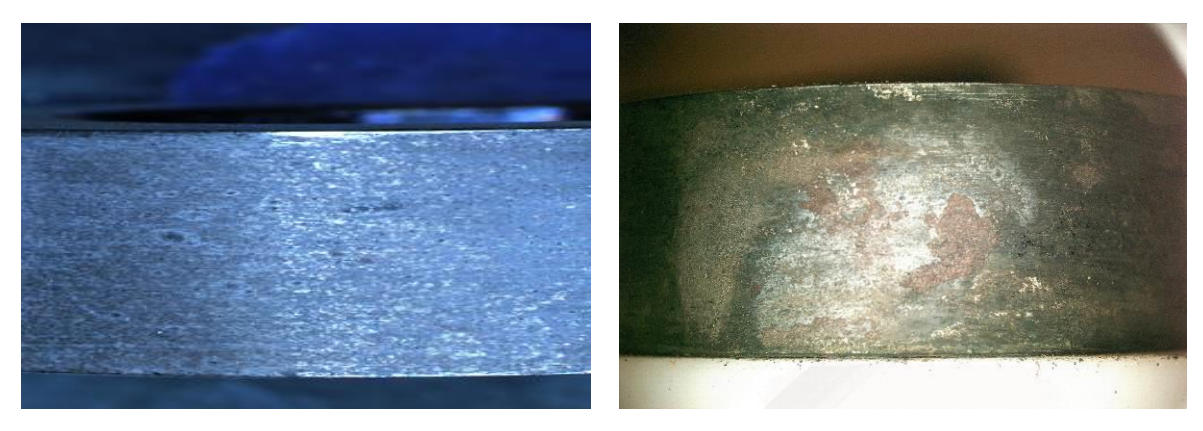


Figure 109. Photos from the windward sides of 253 MA substrates, after deposits have been removed. Samples were exposed at the SH position. Left) Ref 1. Surface slightly discoloured. Right) Ref 2. Corrosion products may have spalled off.

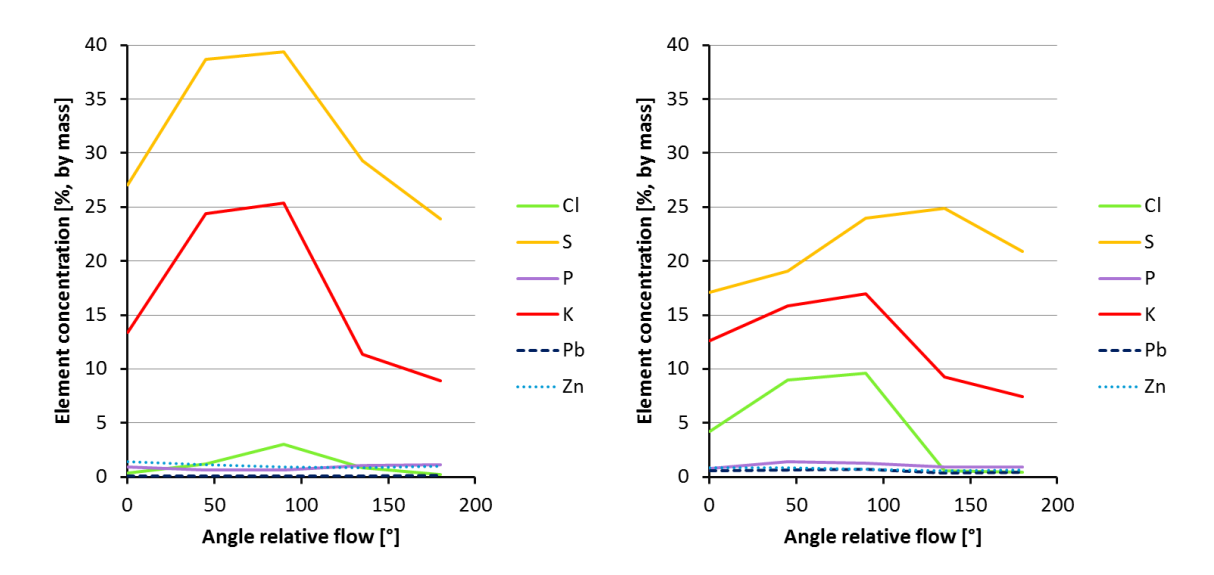


Figure 110. Elemental concentrations in deposits collected in the SH position on 253 MA sample rings. Left) Ref 1 Right) Ref 2

4.10 SH comparison between SWS1 and SWS2

4.10.1 SH 16Mo3 rings

4.10.1.1 Ring surface after cleaning

The 16Mo3 rings from the SH position, for both cases SWS1 and SWS2, are shown in Figure 111 after the deposits have been removed. The ring from case SWS1 has corroded spots all around the ring, while the ring from case SWS2 is brownish with less obvious corrosion products. The XRF analyses of the corresponding deposits, given in Figure 112, have minor differences: slightly higher S and K for case SWS1 and higher Pb for case SWS2.



Figure 111. Images of the 16Mo3 rings after exposure in the SH position from the two sewage sludge cases. A) Corroded spots around the ring, discoloured. B) The surface is brown but no obvious corrosion product is seen. Some of the grinding marks are still visible.

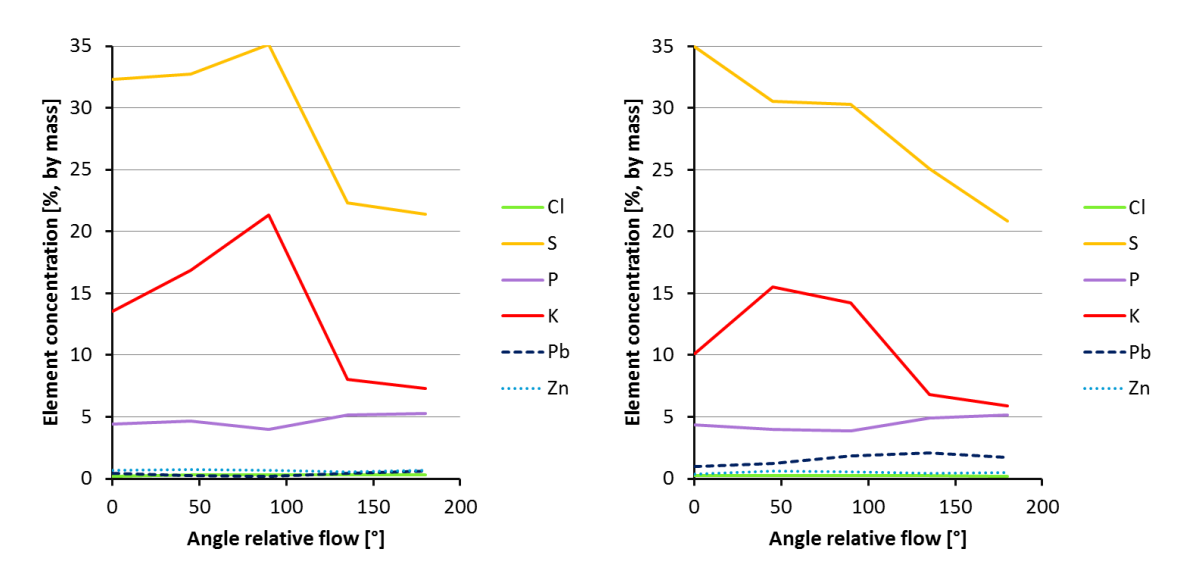


Figure 112. Elemental concentrations in SH deposits on 16Mo3 samples. Left) SWS1, Right) SWS2.

4.10.2 SH 253 MA rings

4.10.2.1 Ring surface after cleaning: Wind side

The 253 MA rings from the SH position are shown in Figure 113 after the deposits have been removed, for the test cases of SWS1 and SWS2. The rings from both cases exhibit dark stains, and some pitting is present for the case SWS1 at 90°. The corresponding XRF analyses of the deposits are plotted in Figure 114. The plots show low chlorine concentrations and high sulphur concentrations in both cases. The concentration of K is higher for case SWS1.

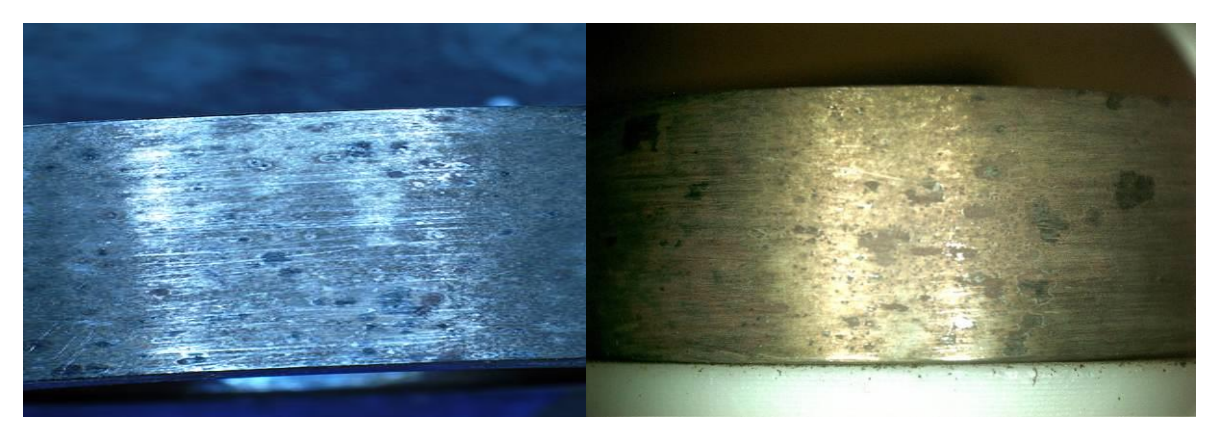


Figure 113. Photos of the windward side of the 253 MA rings after exposure in the super heater position. Left) SWS1, Spots at 0°, "pitting" at 90° Right) SWS2, The metallic appearance of the alloy is visible. Dark stains cover parts of the surface.

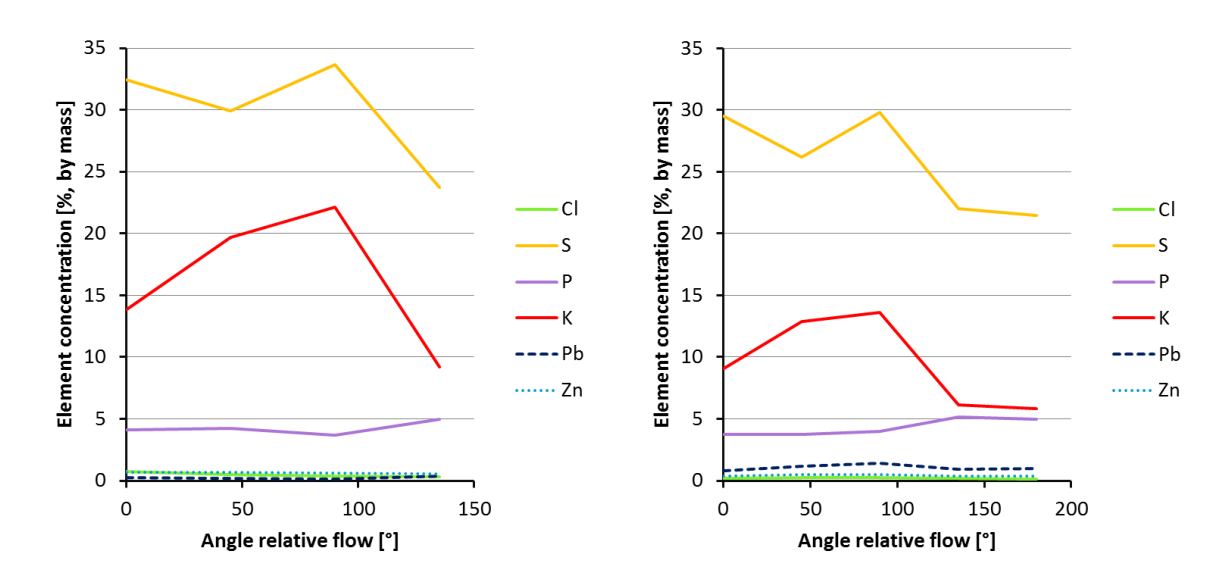


Figure 114. Elemental concentrations of the deposits collected in SH position on 253 MA samples. Left) SWS1 Right) SWS2.

4.11 Summary of corrosion analysis of second set of tests

Ref 2 and SWS2

Optical microscopy on the windward sides of 16Mo3 samples exposed at the boiler wall position (BW) showed a reduction of corrosion scale from about $50~\mu m$ for test case Ref 2 to about $30~\mu m$ for test case SWS2. The additive of sewage sludge reduced concentrations of Cl and S but increased concentrations of Pb and P in the deposits on the 16Mo3 samples. The 253~MA rings were less affected by corrosion and the analyses of their deposits showed that the sewage sludge reduced concentrations of Cl, S and K but increased concentrations of P.

SEM/EDX analyses of the corrosion layers on the 16Mo3 samples reveal that the compositions are different near the corrosion front compared to the outer corrosion layers. In general, there are higher concentrations of Cl at the corrosion front than anywhere else in the layers, while S and P are present mostly in outer corrosion scales. There are also tendencies that K, Na and Pb are mostly present in outer corrosion scales, and at least not in the corrosion front. The distribution of elements throughout the corrosion layer may be explained by the continuous movement of the corrosion front, , in this case about 75 μm . On the other hand, in the case of 253 MA steel, under the same test conditions, the corrosion layer was only about 15 μm , implying a less pronounced elemental separation. A spot analysis in this corrosion layer revealed a composition of 8 % Cl, 5 % S, 8 % alkali, 2.4 % Zn and 2.5 % Pb. That is, the most critical elements are mixed. This composition is probably a closer representation of the deposit conditions under the initial corrosion attacks on the boiler steel tubes.

At the superheater (SH) position, the additive of sewage sludge did visually reduce the corrosion on both the 16Mo3 and 253 MA steels. Most corrosion occurred on the windward side. The additive reduced the Cl concentrations on the windward side (it was low on the leeward side for both test cases), meanwhile concentrations of S increased on the windward side and P concentrations increased all around the ring.

PbO andPbO+SWS

Optical microscopy on the windward side of the 16Mo3 samples from the boiler wall position (BW) showed a corrosion scale thickness of almost 1 mm for the test case PbO, which can be compared to $50~\mu m$ for the reference case. Thus, the addition of PbO to the fuel do significantly increase the corrosiveness of the deposits. When also sewage sludge was added to the fuel (case PbO+SWS) the resulting corrosion layer on the windward side was found to be about $400~\mu m$. That is a clear reduction compared to the PbO case, but still far worse than the reference case. A comparison of the XRF analyses of the BW deposits between the test cases of PbO and PbO+SWS shows that the additive of sewage sludge reduces concentrations of Pb and Cl as well as increases concentrations of P and Zn. There is also a weak tendency of reduced concentrations of S and K on the 253~MA test rings.

The SEM/EDX analyses reveal the same distribution of elements in the corrosion scales as described above for the 16Mo3 steel in the reference case. However, even though the deposits consist of a large amount of Pb according to the XRF analysis, it was difficult to find any areas of high Pb concentrations by the SEM/EDX instrument. Instead, it is possible that the Pb is dispersed throughout the corrosion layers, which were thick in this case.

It is visually obvious that the corrosion on the rings exposed at the superheater position is reduced by the sewage sludge. The XRF analyses of the deposits reveal that the sewage sludge reduces the concentration of Cl significantly, meanwhile concentrations of S, Pb and P increase.

4.12 Ranking of additives based on observations

After the exposure the corrosion test rings were cleaned by isopropanol and lightly brushed with a cloth. Macroscopic photos were taken at the wind side and the lee side. The corrosion attacks were in general limited to the wind side.

Tentative rankings of additives and materials tested are presented below in figures. The rankings are based on the 8 hours of exposure. However, any estimates of long-term corrosion rates from such a short exposure are purely speculations.

The test cases are colour coded: reference: cyan, kaolin: green, sewage sludge: grey, sulphur: yellow, foundry sand: red, lime: orange for the first set of trials. For the second set of trials: reference: cyan, sewage sludge: violet, PbO: magenta, sewage sludge + PbO: green.

Since the two set of tests were performed at different occasions the results are presented in different graphs. The reason is that the waste and demolition wood fuel is heterogenetic and the chemical compositions of the fuel may vary significantly.

The graphs are vertically divided by the three different test materials, when applicable. The wind side of each test ring was compared to the other test rings by comparing the optical appearance, the cross-sections and the chemical analyses, each method contributing with different impact of the overall results.

No or only minor corrosion products were observed for the test samples located to the left of the label "Break" in the figures. This indicates that the corrosion rate may be acceptable for use in boiler. Samples showing corrosion products are located on the right side of "Break" label and it is an indication that the corrosion rate is too high for use in boiler.

4.12.1 Ranking of samples at boiler wall (BW) conditions

Figure 115 below shows a ranking of all additives and materials tested in the furnace (i.e. boiler wall position, BW) during the first set of tests. A similar ranking for the second set of tests is presented in Figure 116. For the samples exposed to BW conditions, generally, the Kanthal A-1 material performs slightly better than 253 MA, which in turn is far better than 16Mo3. The stainless steels do not show clear evidence of corrosion with the exception of 253 MA from the lime case. The 16Mo3 steel did not show any corrosion when kaolin or sewage sludge were used as additives but did corrode during the exposures with sulphur-, lime- and foundry sand-additives in addition to the reference. In general, kaolin and sewage sludge showed the highest reduction of the corrosion rate. A-1 do not show any corrosion attacks for any the additives.

It should be noted that lime seems to enhance the corrosion rate compared to the reference case. A conclusion from the visual comparison may be that the results originating from the 16Mo3 steels may be more significant for the ranking of the additives than the results from the high alloyed steels, since no real corrosion have started.

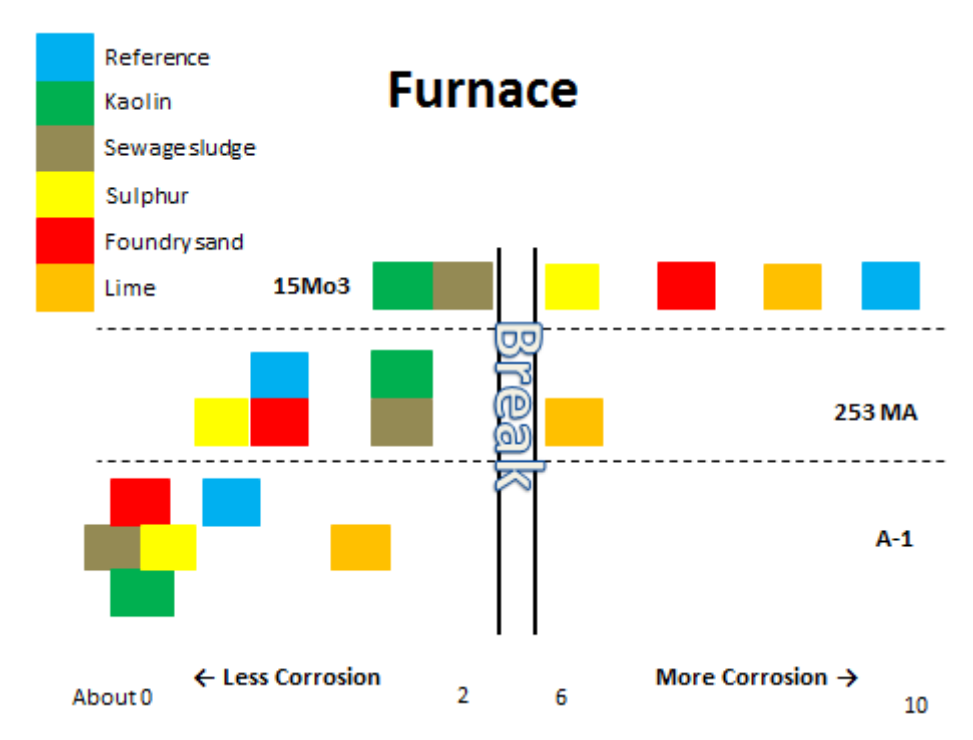


Figure 115. Ranking of additives and materials located in the furnace (BW) in 1st set of tests.

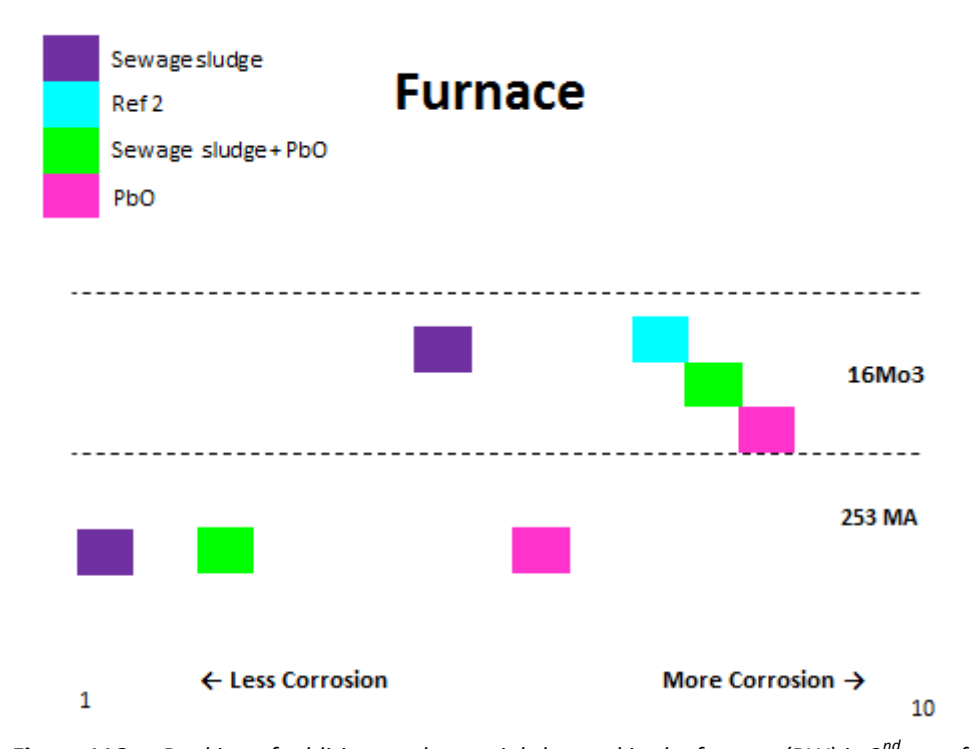


Figure 116. Ranking of additives and materials located in the furnace (BW) in 2^{nd} set of tests.

4.12.2 Ranking of samples at superheater (SH) conditions

Figure 117 is showing the corresponding ranking of the rings from the 1st set of tests at superheater conditions. The same ranking of the tests in the 2nd set of tests is given in Figure 118. The corrosion rates for the rings to the right of the "Break" label shows signs of corrosion. And if a sample is located to the right of the vertical black line the corrosion have been severe.

The ranking of the material is the same as for the furnace; A -1 is slightly better than 253 MA, which in turn is far better than 16Mo3.

The 16Mo3 steel corroded no matter which additive that was tested. The best results were coming from the additives of kaolin and sulphur. The test cases of sewage sludge, lime, and foundry sand, and also the reference case clearly showed higher corrosion. Neither the A-1- nor the 253 MA steel did corrode.

In general all additives did reduce the corrosion compared to the reference with the exception of the 253 MA steel when lime was tested. Kaolin, sulphur, and perhaps sewage sludge did show the highest reduction of the corrosion rates. The addition of PbO increased the corrosion.

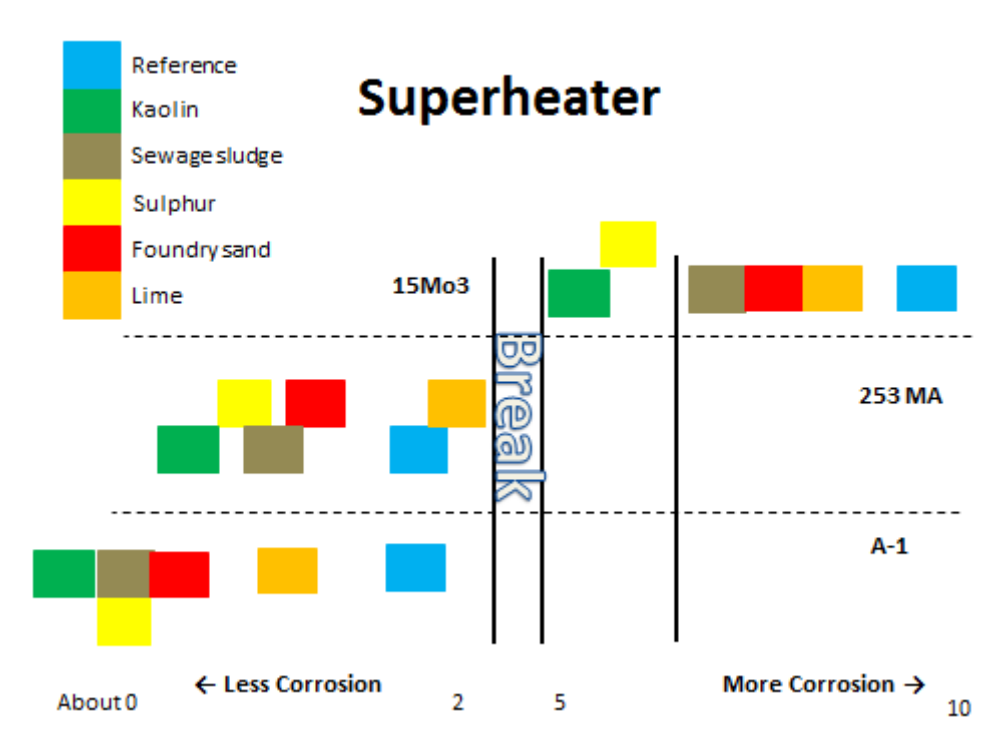


Figure 117. Ranking of additives and materials at SH from comparison study of 1st set of tests.

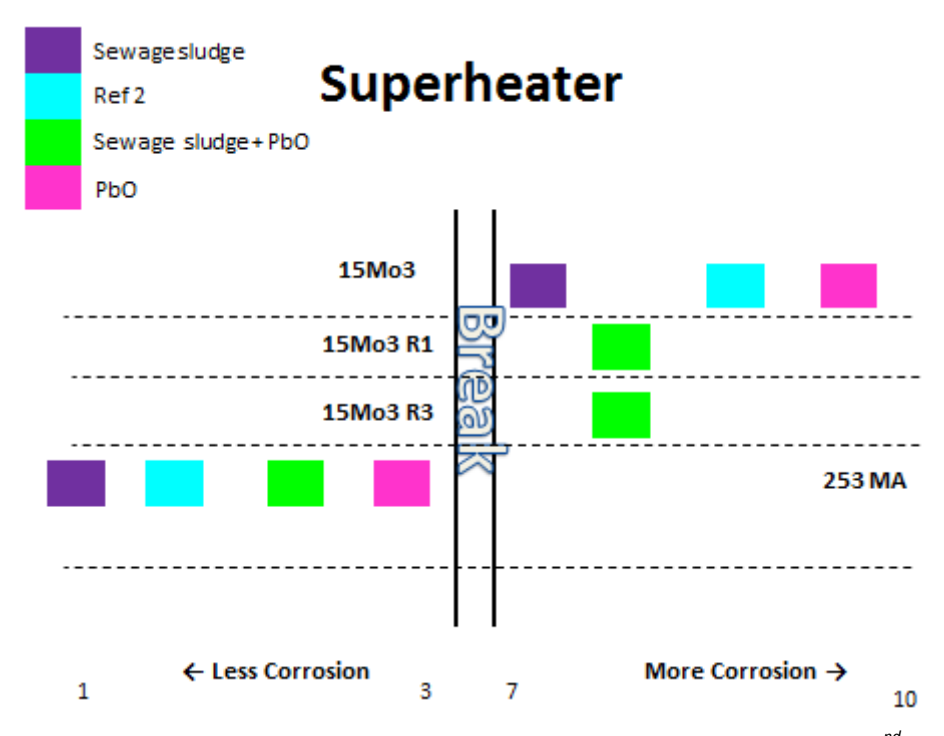


Figure 118. Ranking of additives and materials at SH from comparison study of 2^{nd} set of tests.

Appendix A Chemical composition of deposits on BW probe

The deposits were analysed by an XRF instrument at varied locations on the surfaces of the sample rings. In the figures below, the given angles refers to the direction of the flow. That is, 0° is the windward side while 180° is the leeward side of the probe.

An example of concentrations, as measured, is shown in Figure 119 below. This example is from a ring of 16Mo3. Towards the leeward side of the ring, (135 and 180°) the concentration of Fe is apparently increasing. However, this is an effect of a thinning deposit layer, implying that the XRF detects the metals in the substrate on top of the elements in the deposit. Therefore, to give a better representation of the actual composition of the deposit, metals present in the substrate (Fe, Cr and Ni) have been subtracted from the original analyses, while the concentrations of remaining elements have been scaled to sum up to 100%. This method results in the elemental distribution shown in Figure 120 from the same analysis as in Figure 119. The calculated elemental distribution can occasionally appear unbalanced with respect to an-ions and cat-ions, e.g. in the case of a thin deposit layer combined with the presence of corrosion products on the substrate surface (e.g. Fe-Cl). Even so, this method is considered to provide a better representation of the elemental distribution in the deposit layer than the raw concentrations.

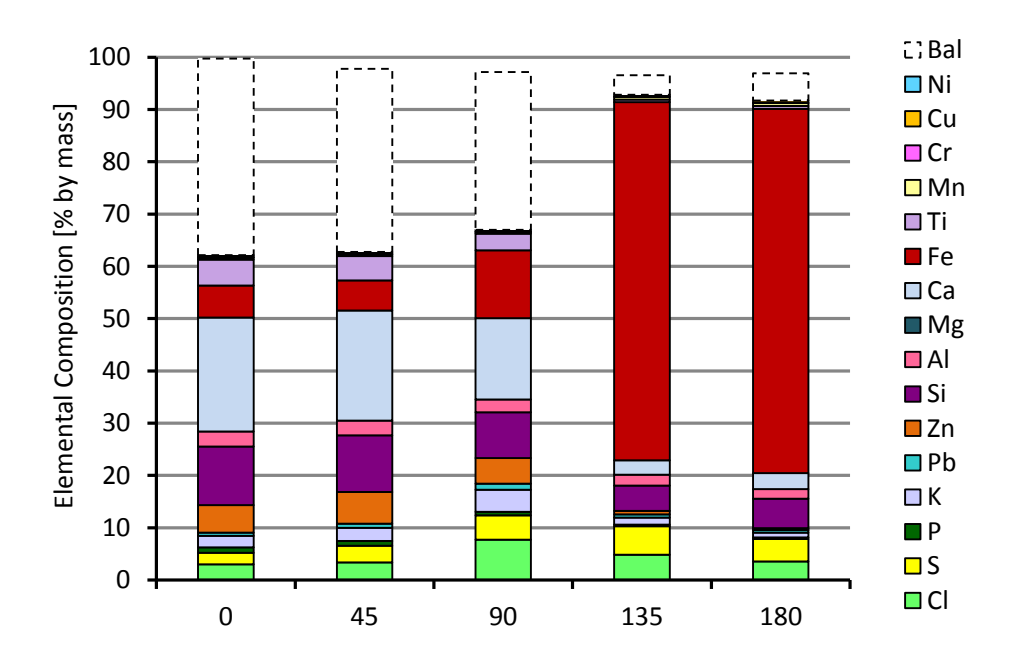


Figure 119. Example of representation of XRF analyses on the surface of a deposit ring, raw concentrations. The high Fe concentrations at 135° and 180° are caused by detection of the ring alloy (here 16Mo3) through a locally thin deposit layer.

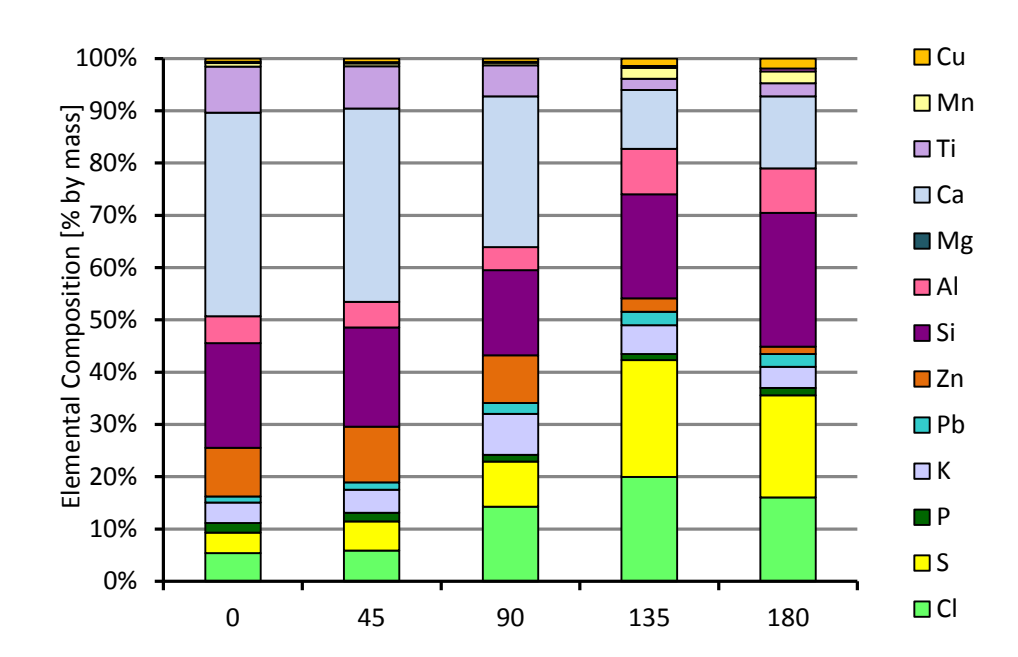


Figure 120. Example of representation of XRF analyses on the surface of a deposit ring as a distribution of listed elements, based on same analyses as in Figure 119. Here, the metals of the alloys have been subtracted (Fe, Cr and Ni) to provide a better picture of the elemental distribution in the deposit

1. Compositions of Deposits on BW-Reference

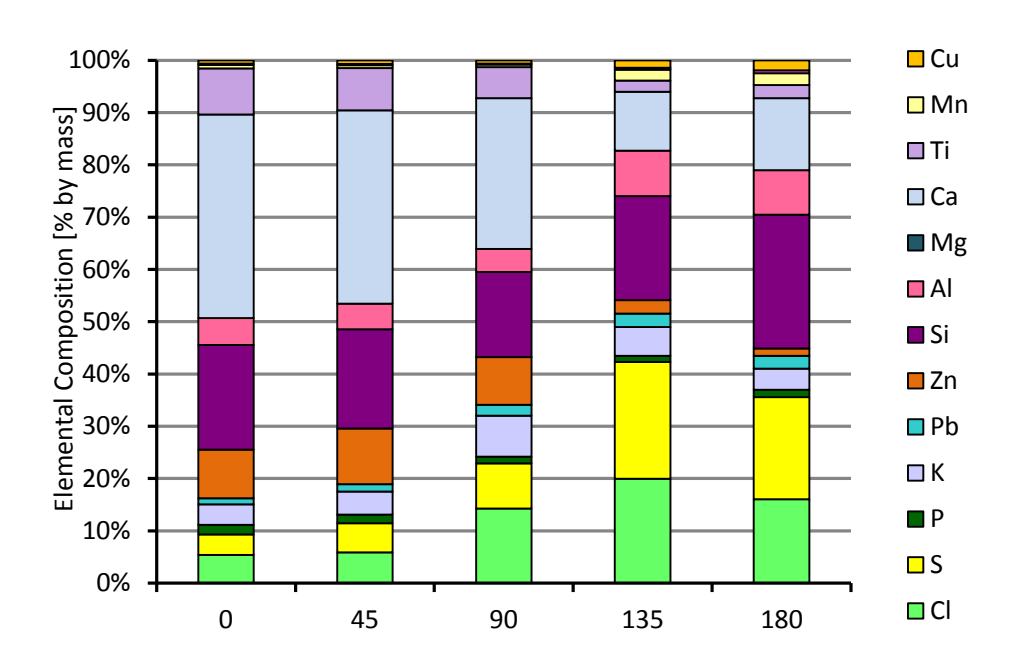


Figure 121. Elemental composition on 16Mo3 sample.

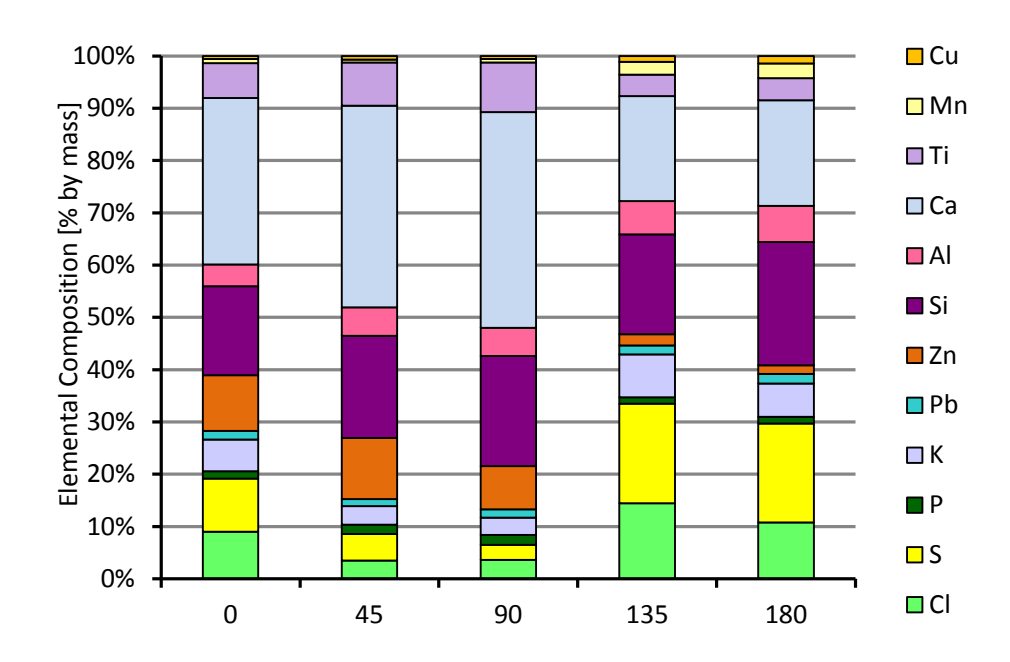


Figure 122. Elemental distribution on 253 MA sample.

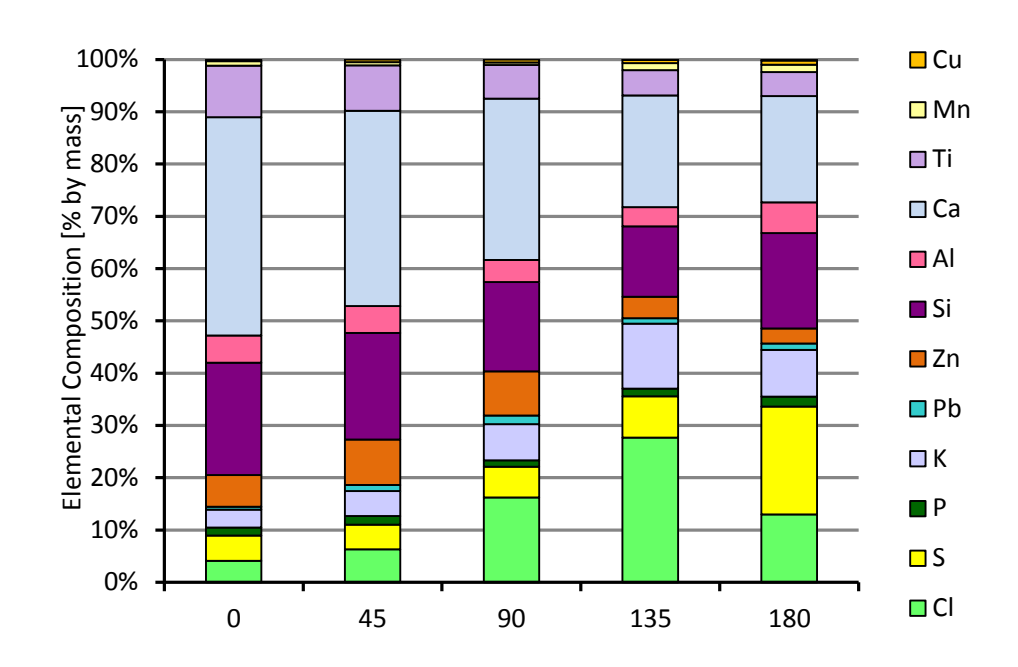


Figure 123. Elemental distribution on A1 sample.

2. Compositions of Deposits on BW-Foundry sand

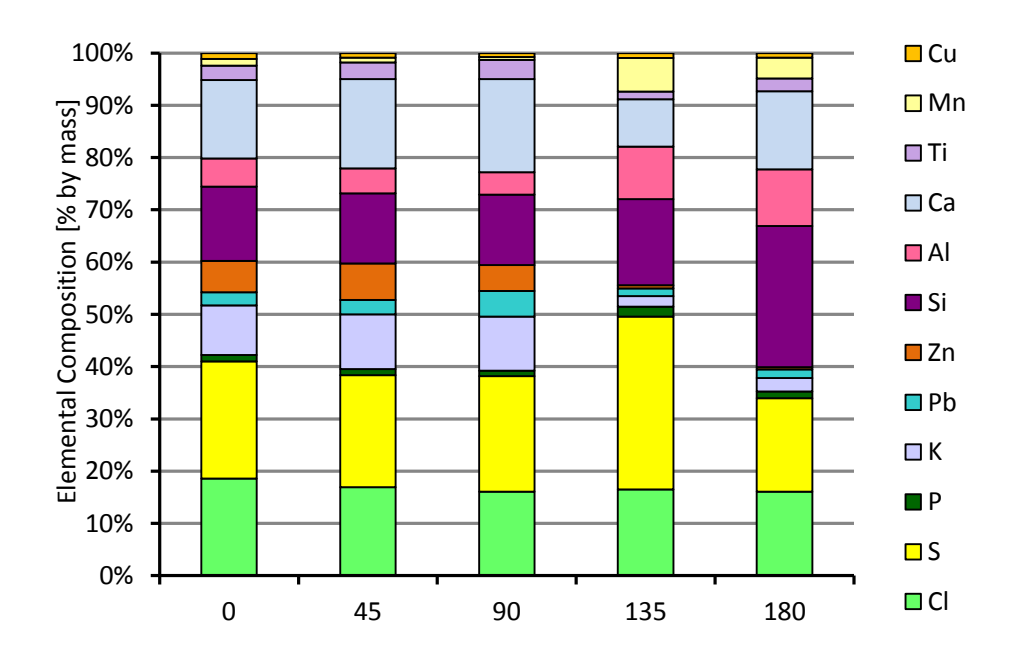


Figure 124. Elemental distribution on 16Mo3 sample.

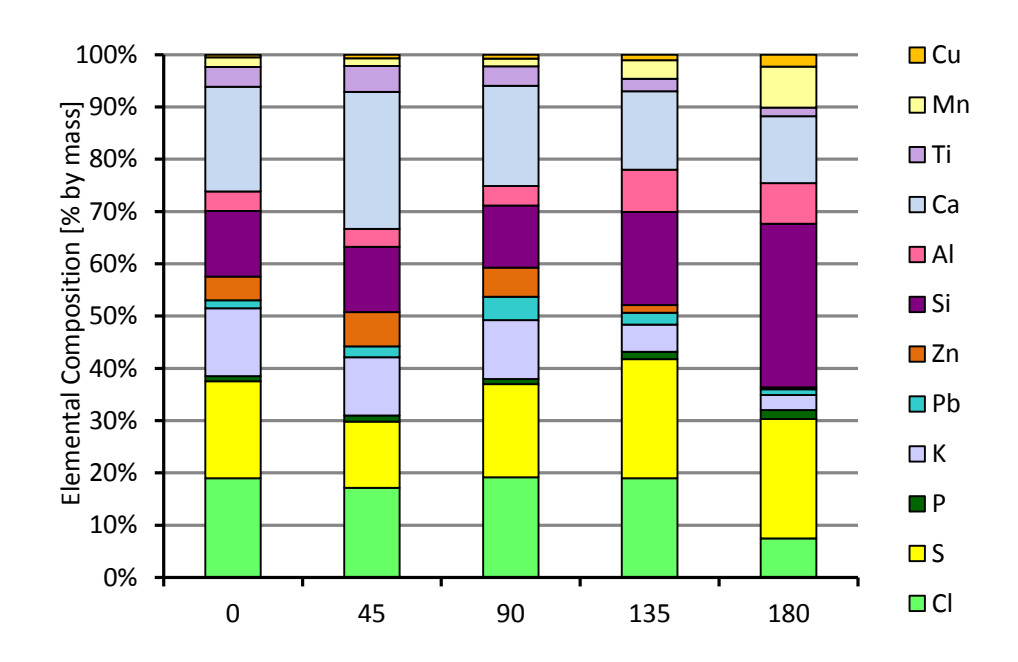


Figure 125. Elemental distribution on 253 MA sample.

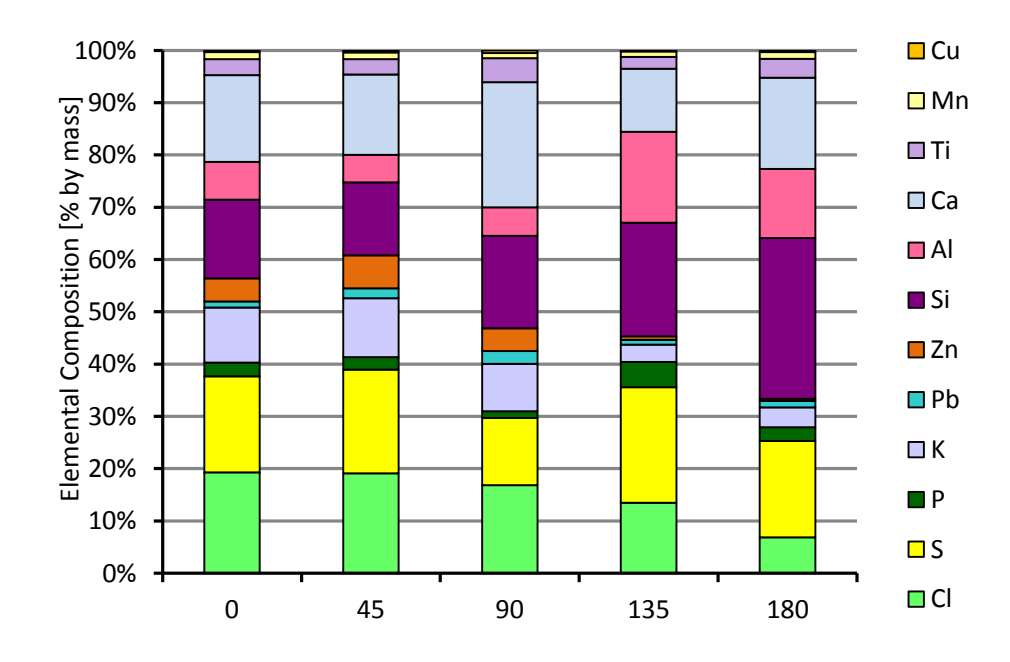


Figure 126. Elemental distribution on A1 sample.

3. Compositions of Deposits on BW-Kaolin

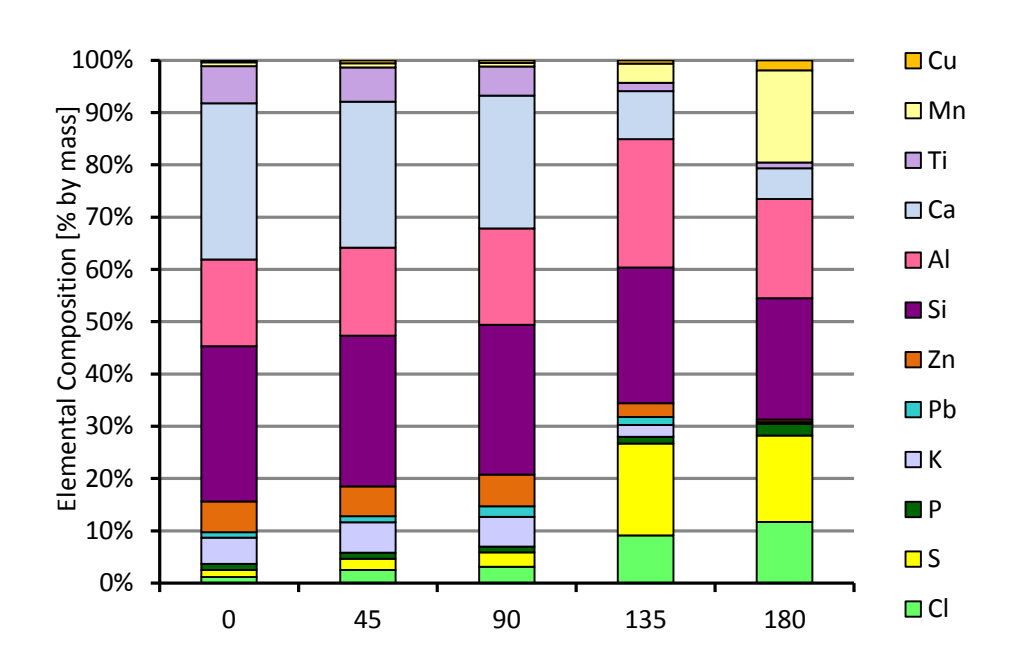


Figure 127. Elemental distribution on 16Mo3 sample.

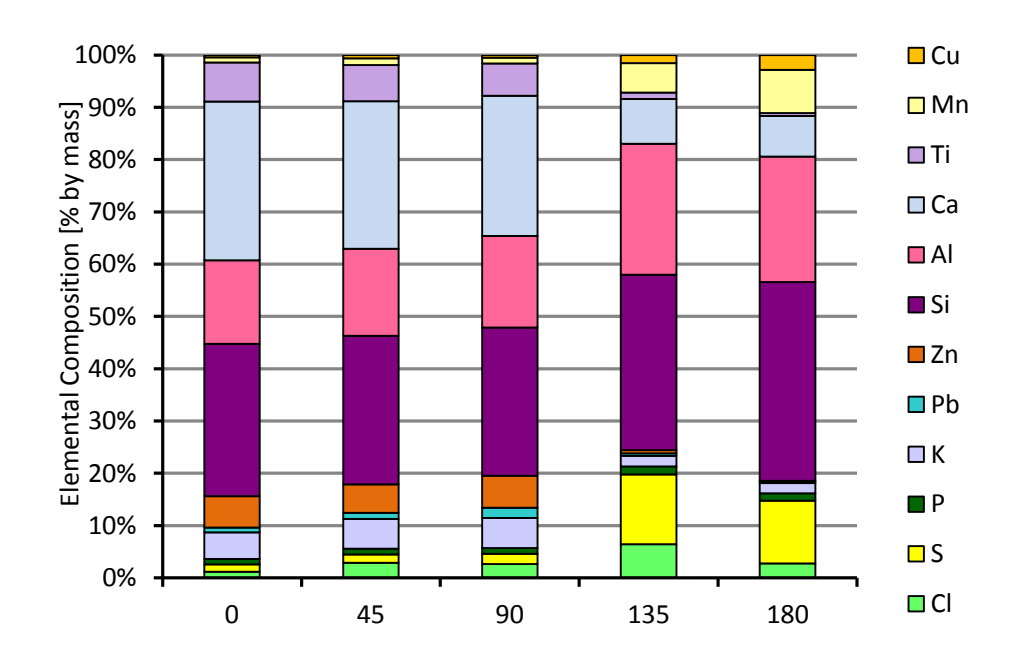


Figure 128. Elemental distribution on 253 MA sample.

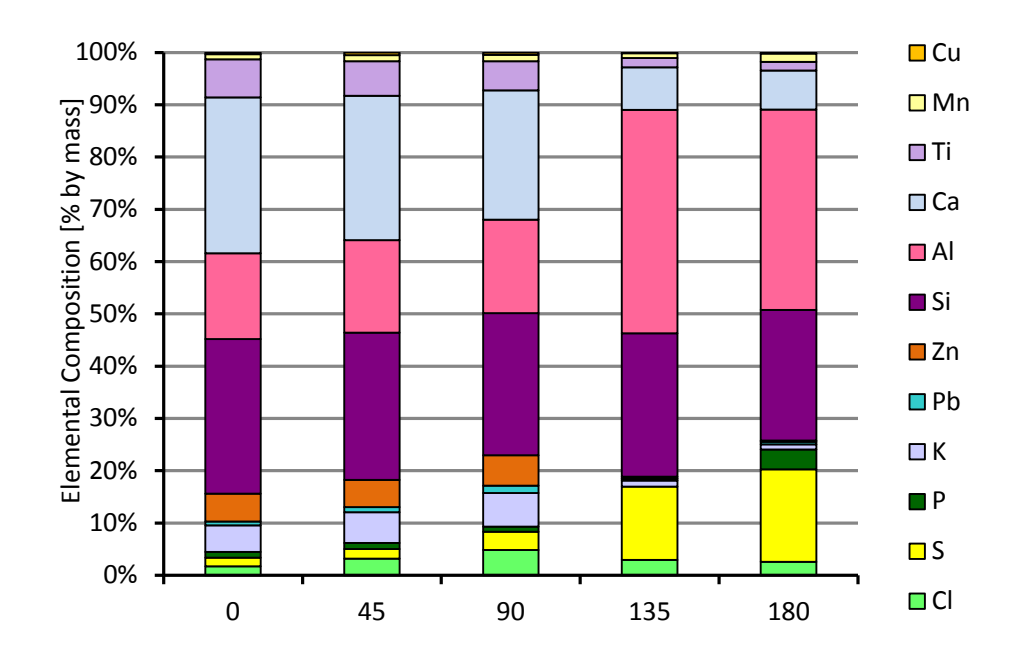


Figure 129. Elemental distribution on A1 sample.

4. Compositions of Deposits on BW-Lime

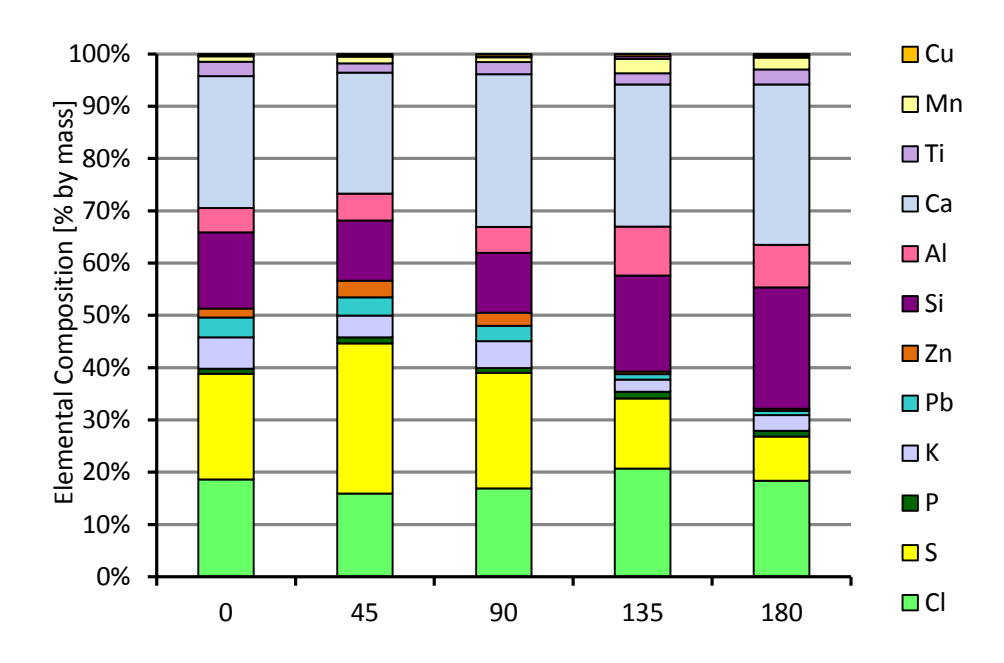


Figure 130. Elemental distribution on 16Mo3 sample.

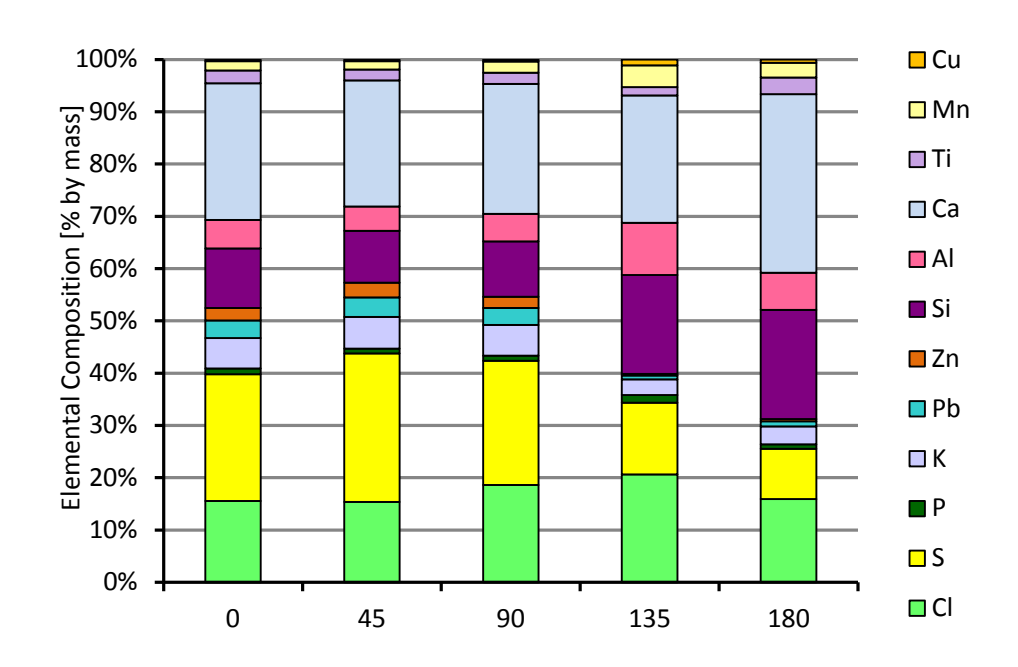


Figure 131. Elemental distribution on 253 MA sample.

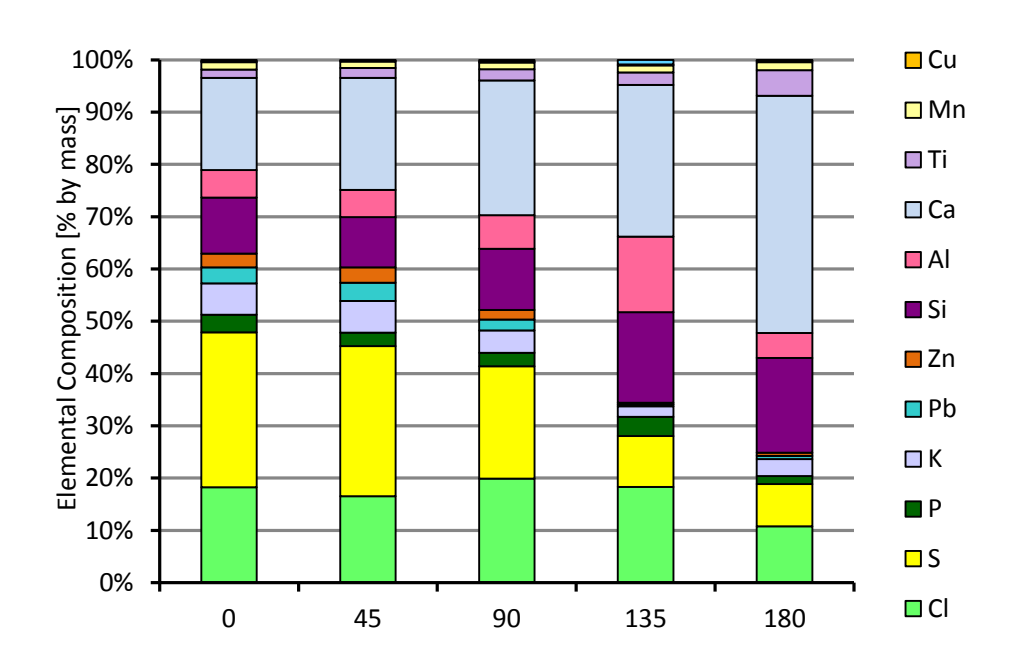


Figure 132. Elemental distribution on A1 sample.

5. Compositions of Deposits on BW-Sludge

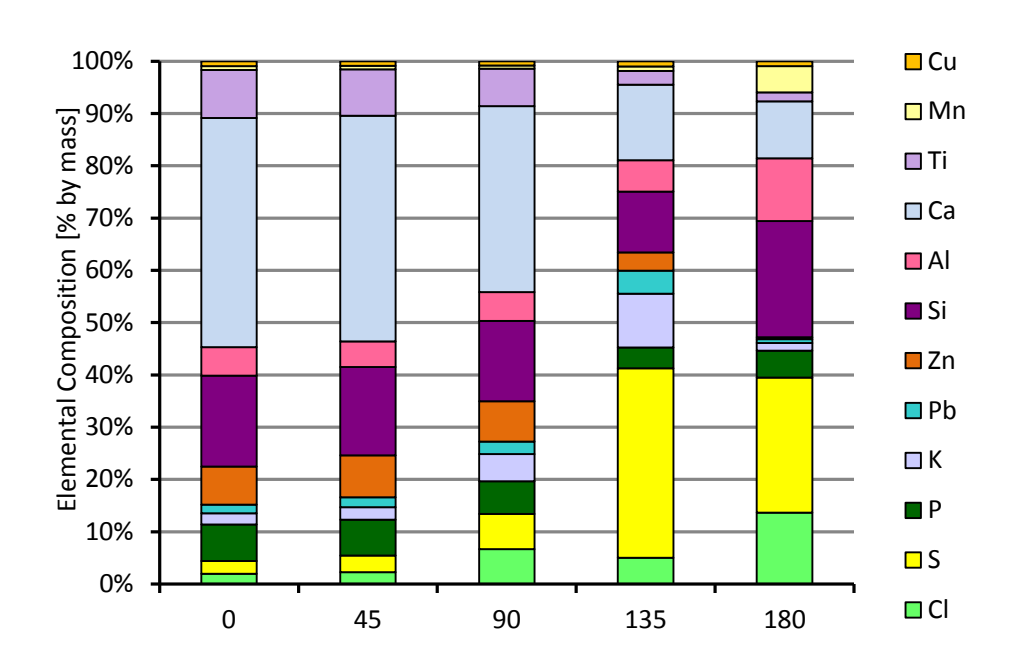


Figure 133. Elemental distribution on 16Mo3 sample.

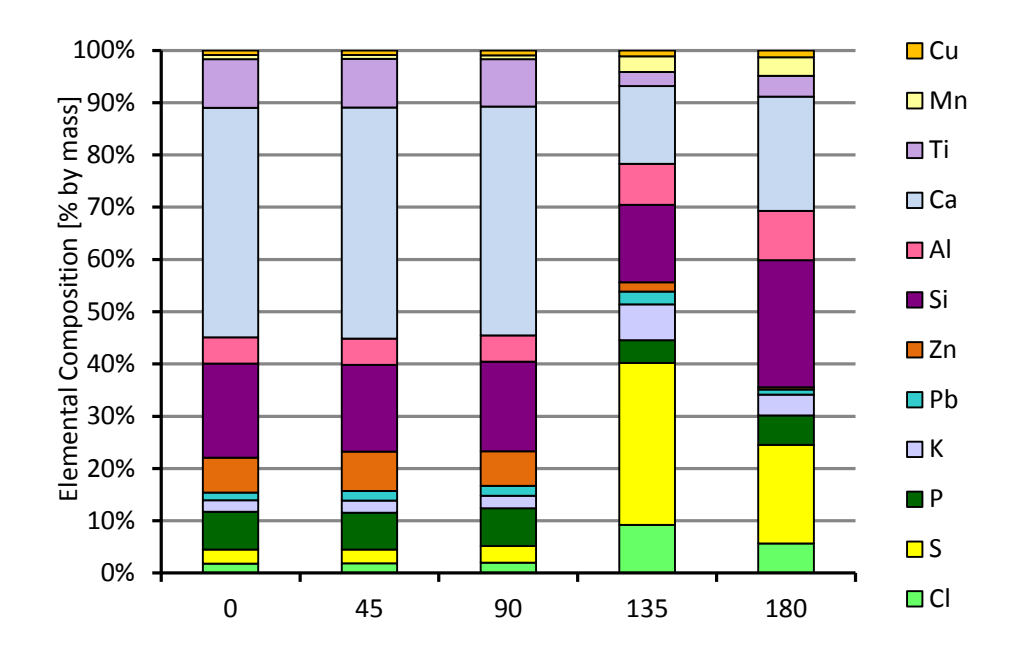


Figure 134. Elemental distribution on 253 MA sample.

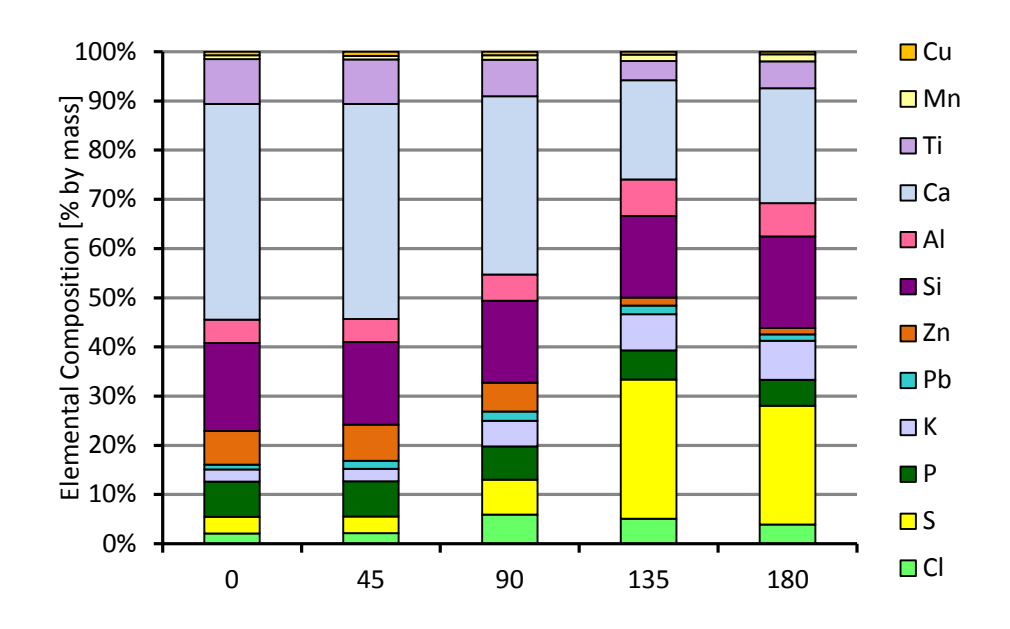


Figure 135. Elemental distribution on A1 sample.

6. Compositions of Deposits on BW-Sulphur

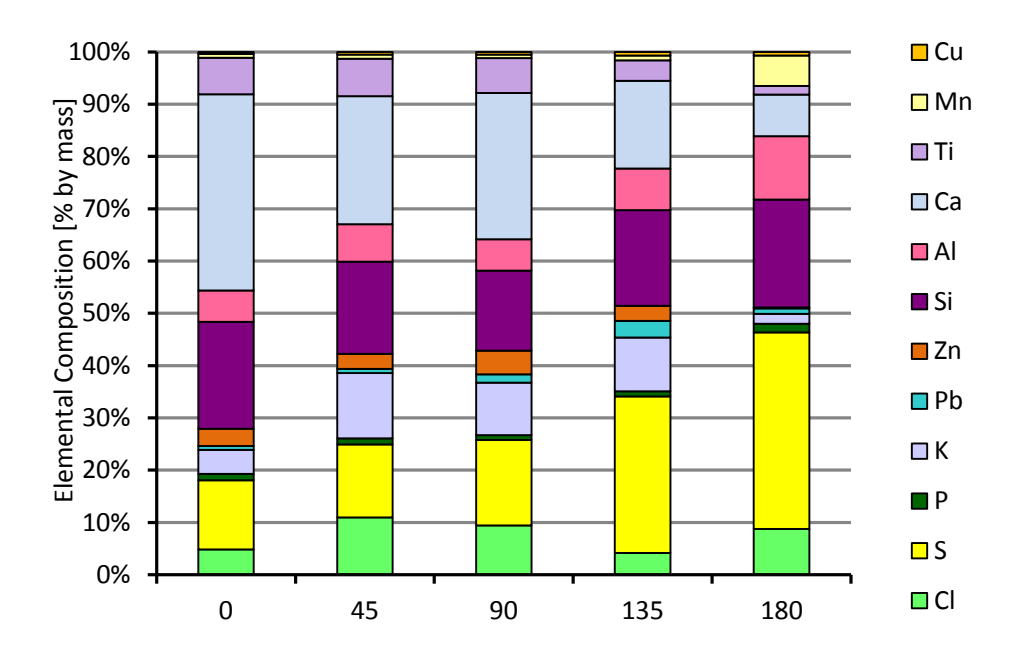


Figure 136. Elemental distribution on 16Mo3 sample.

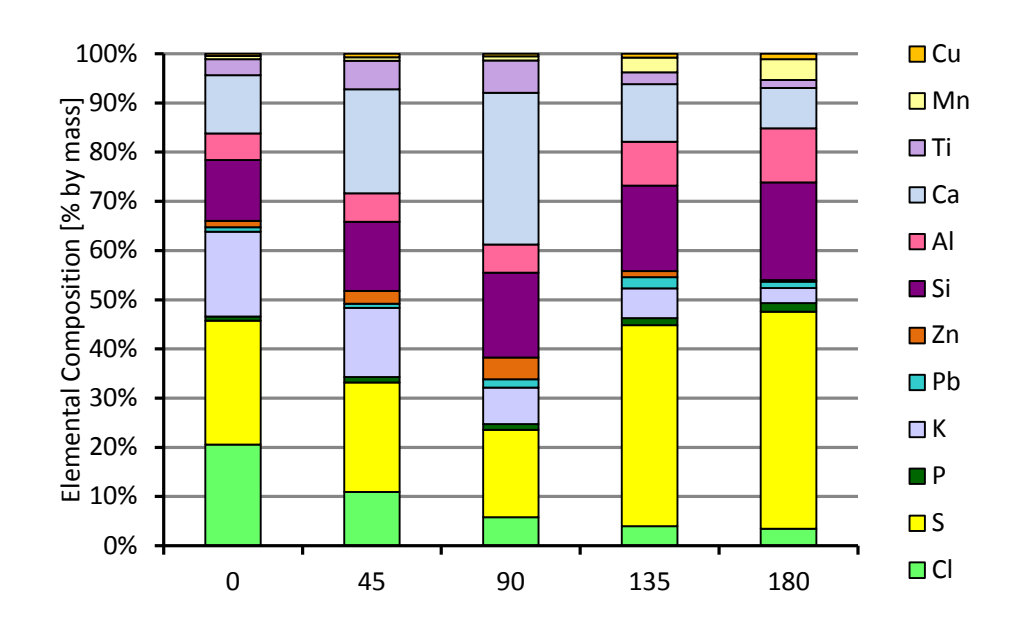


Figure 137. Elemental distribution on 253 MA sample.

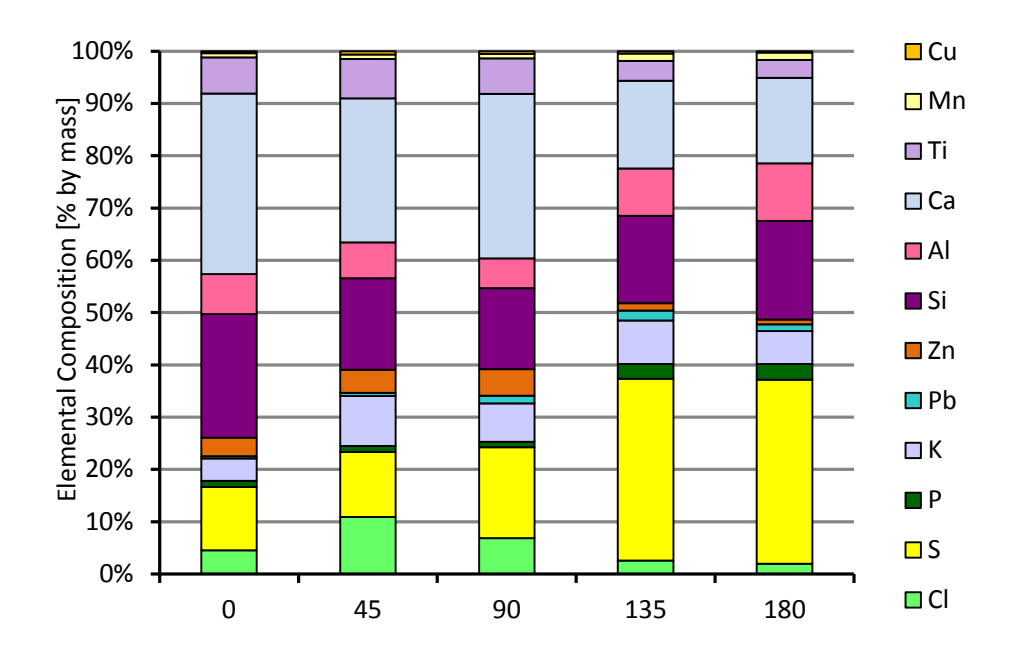


Figure 138. Elemental distribution on A1 sample.

7. Compositions of Deposits on BW-Ref 2

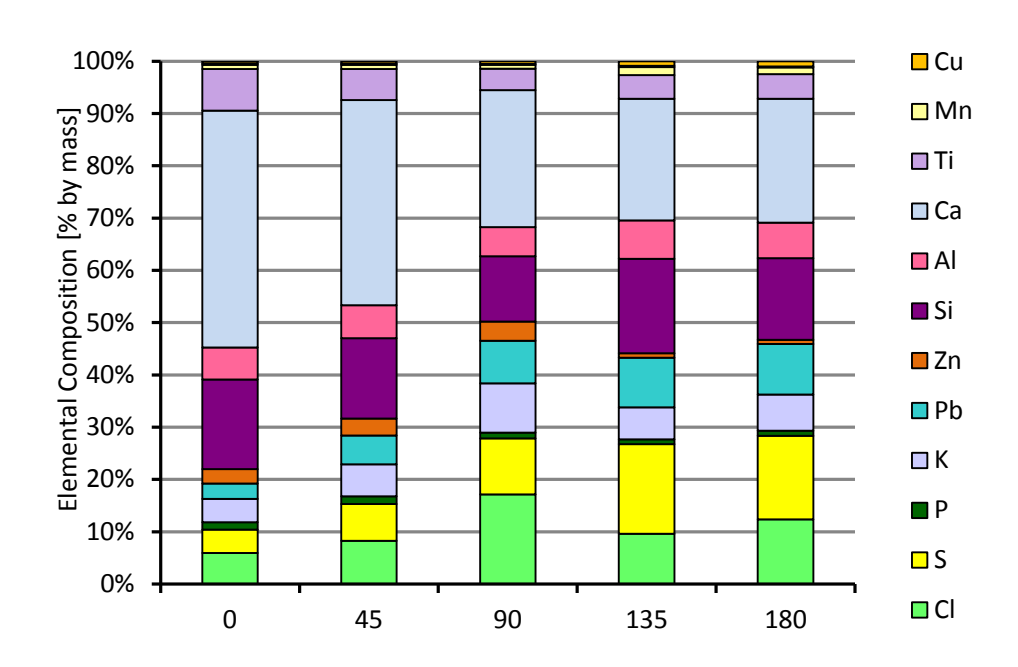


Figure 139. Elemental distribution on 16Mo3 sample (ring #1)

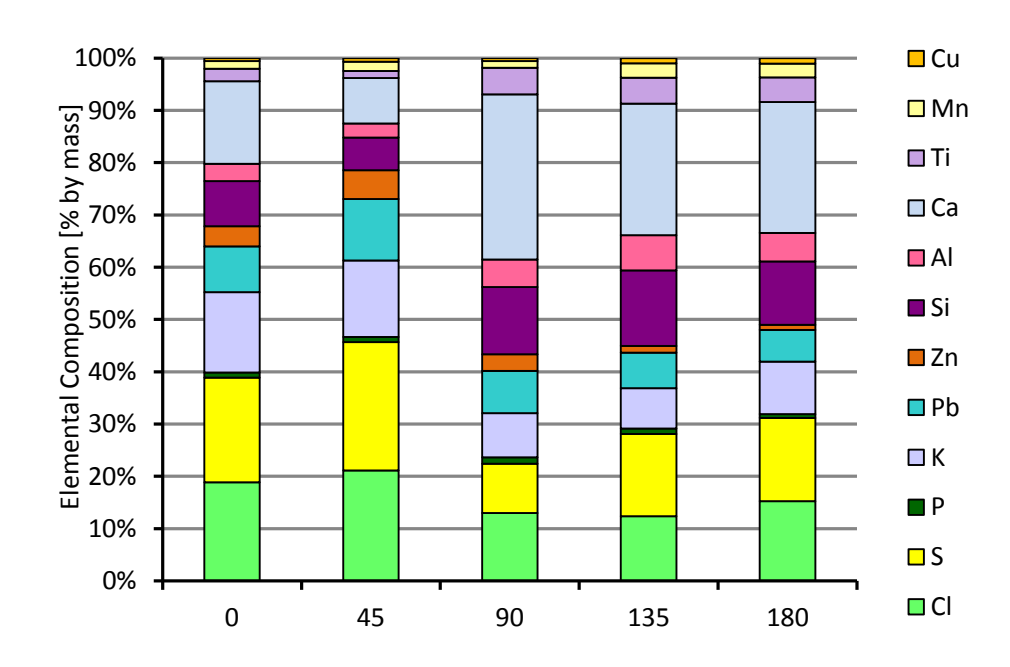


Figure 140. Elemental distribution on 253 MA sample.

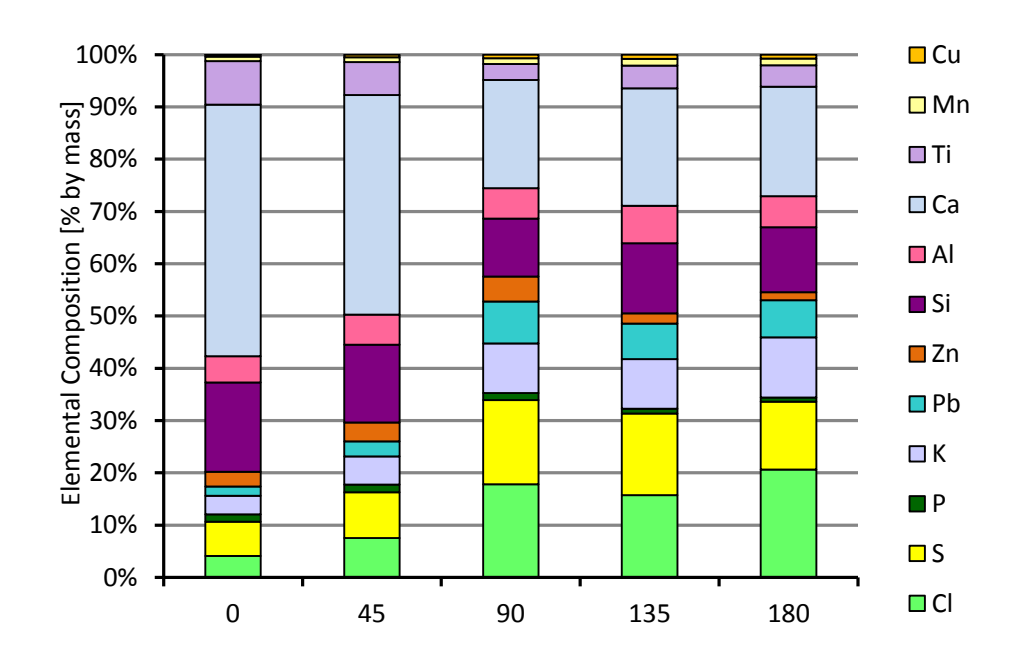


Figure 141. Elemental distribution on 16Mo3 sample (ring #3).

8. Compositions of Deposits on BW-SWS2

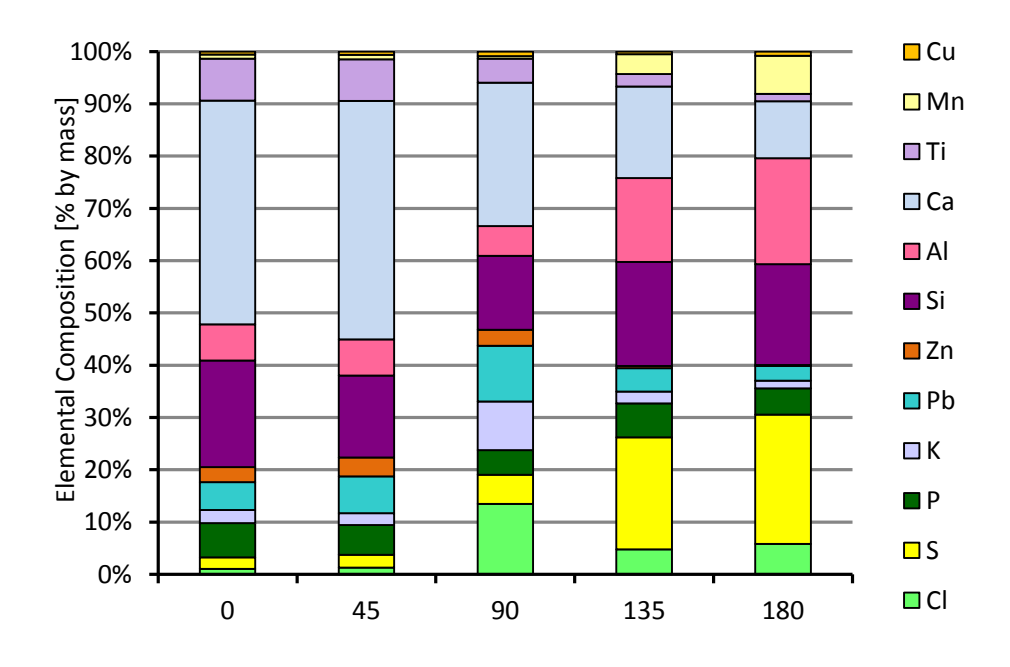


Figure 142. Elemental distribution on 16Mo3 sample (ring #1).

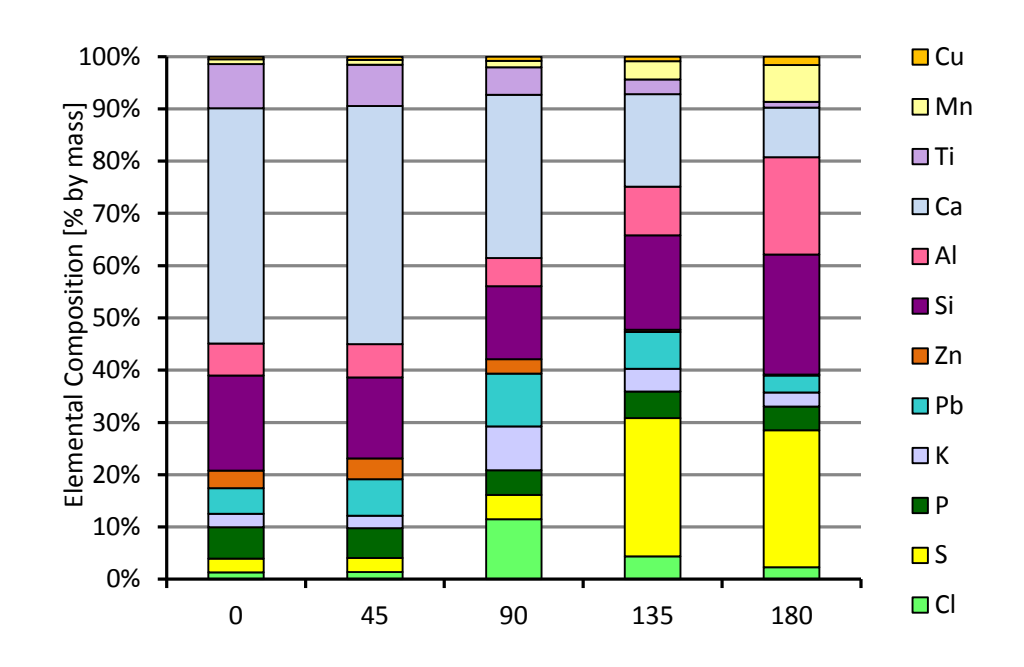


Figure 143. Elemental distribution on 253 MA sample (ring #2).

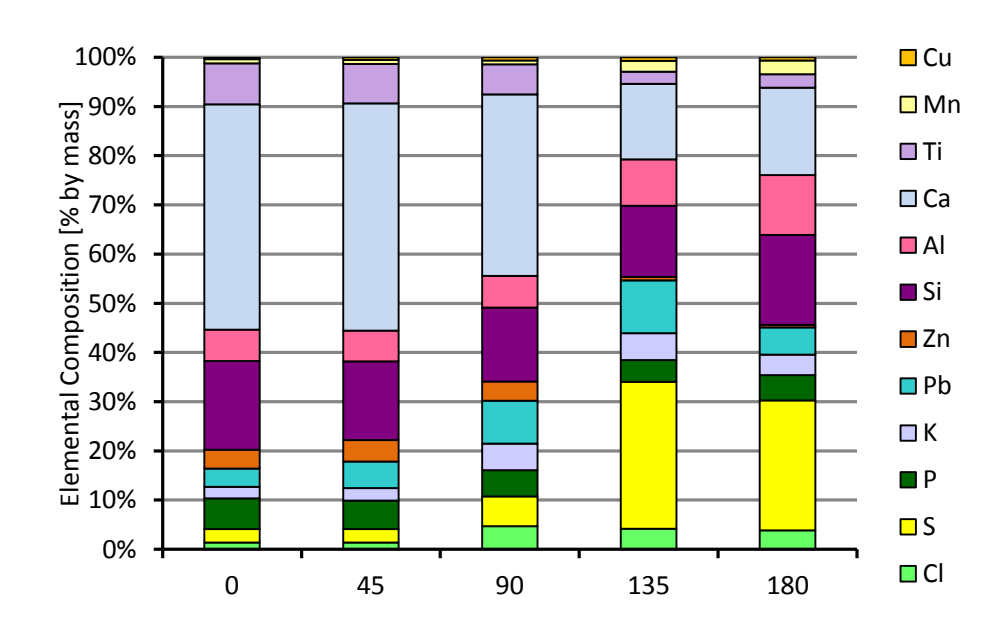


Figure 144. Elemental distribution on 16Mo3 (ring #3).

9. Compositions of Deposits on BW-PbO

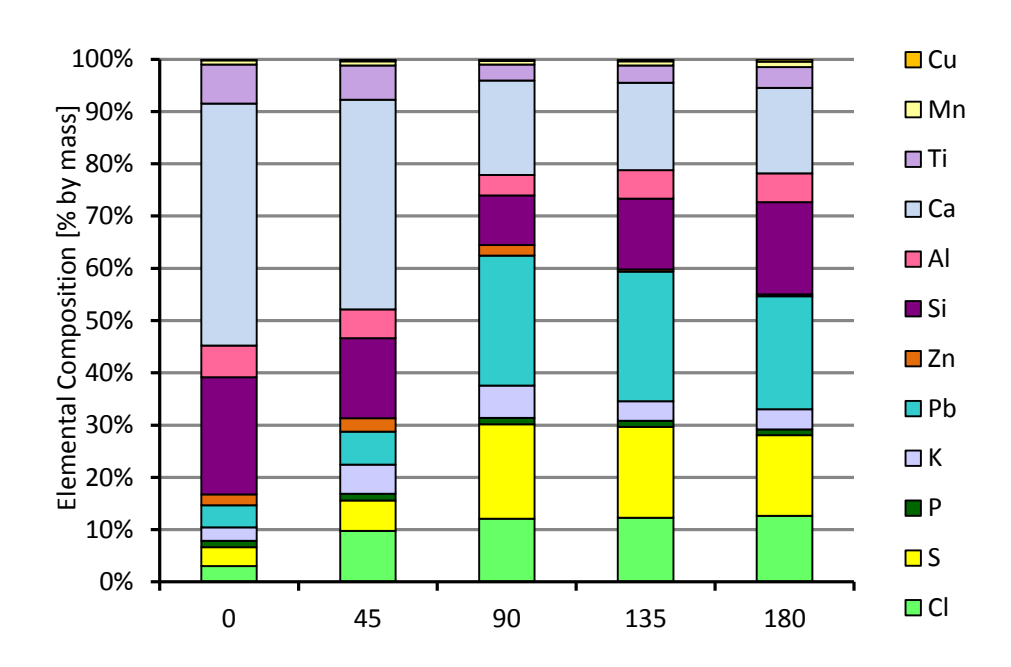


Figure 145. Elemental distribution on 16Mo3 (ring #1).

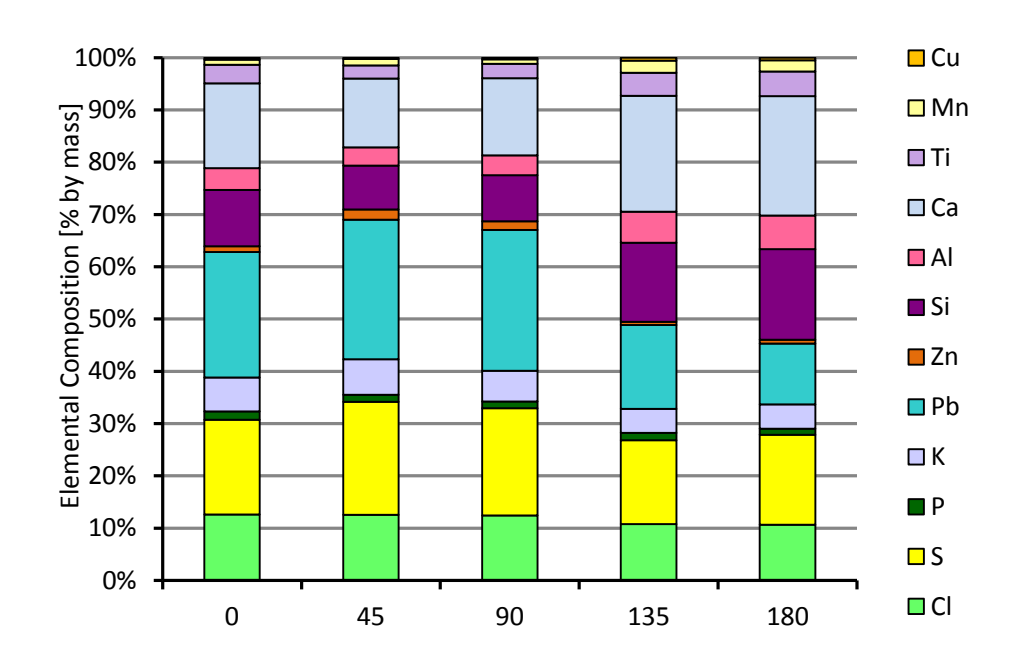


Figure 146. Elemental distribution on 253 MA sample (ring #2).

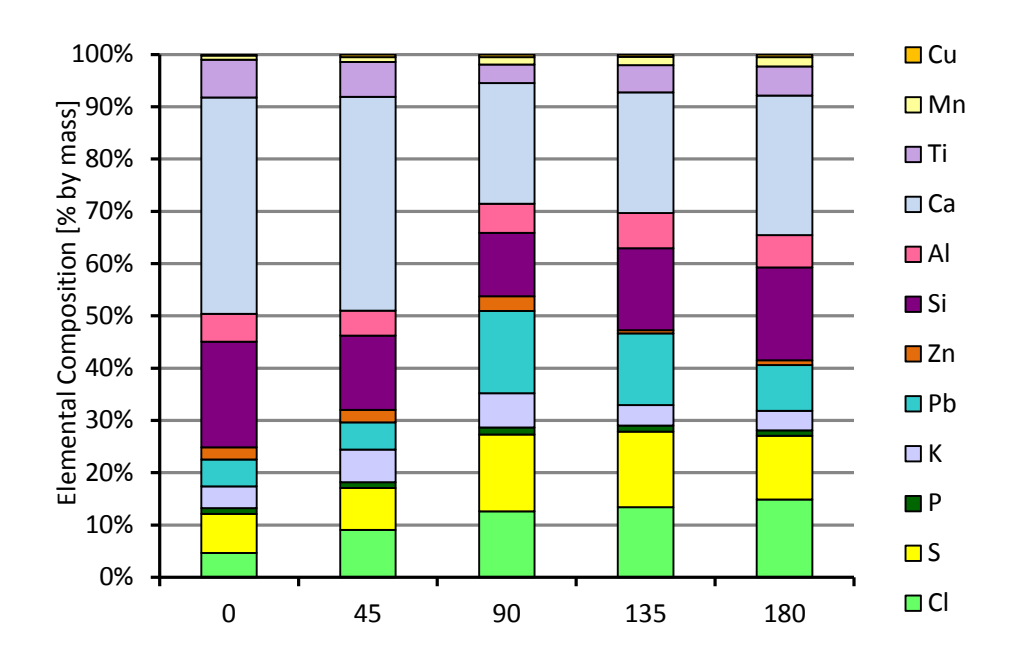


Figure 147. Elemental distribution on 16Mo3 sample (ring #3).

10. Compositions of Deposits on BW- PbO+SWS

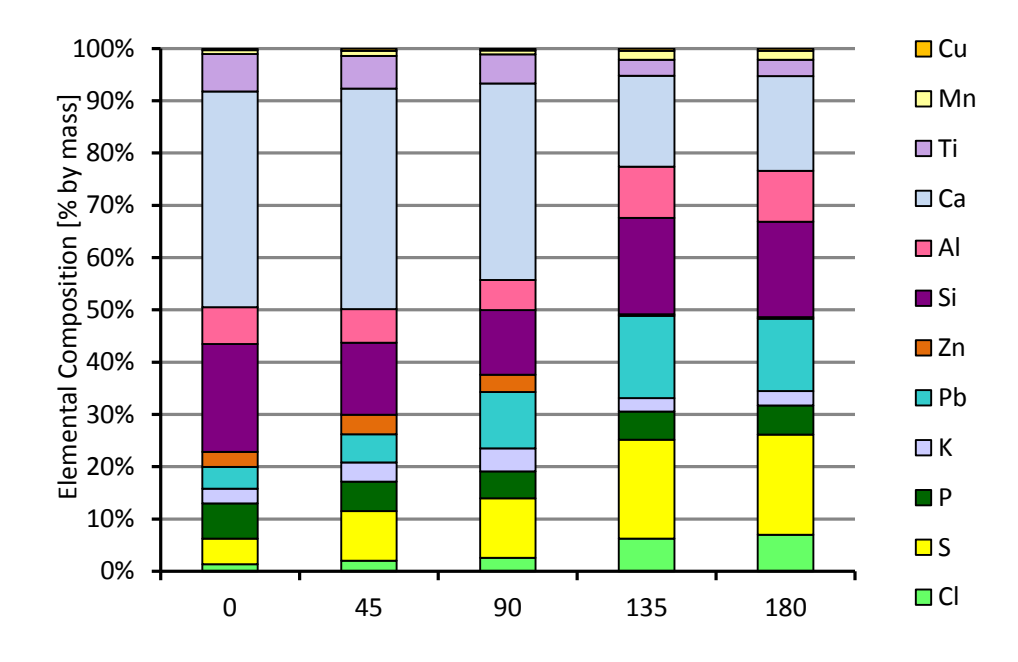


Figure 148. Elemental distribution on 16Mo3 sample (ring #1).

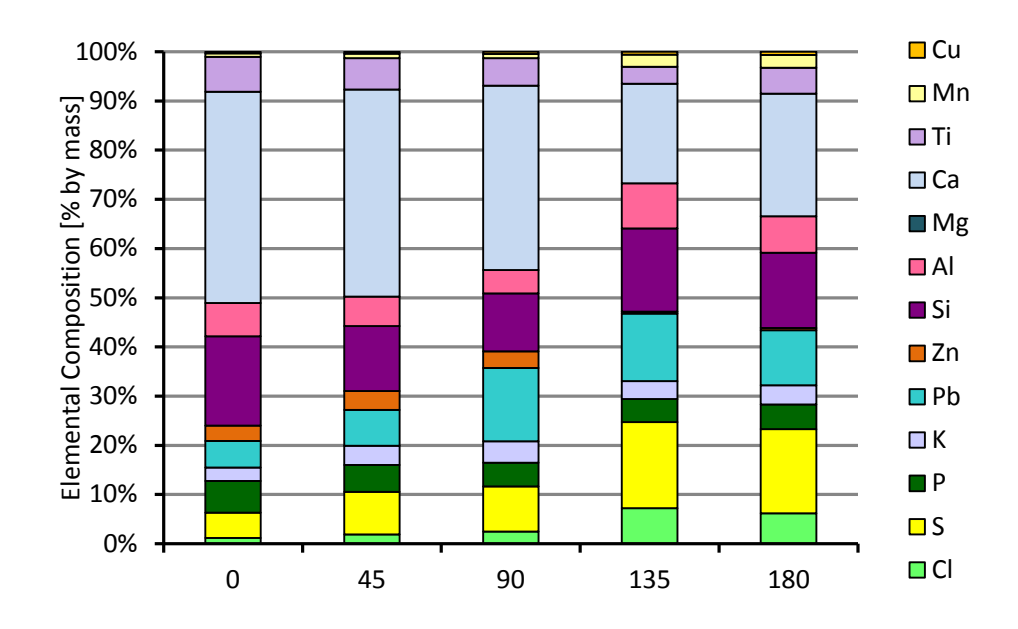


Figure 149. Elemental distribution on 253 MA sample (ring #2).

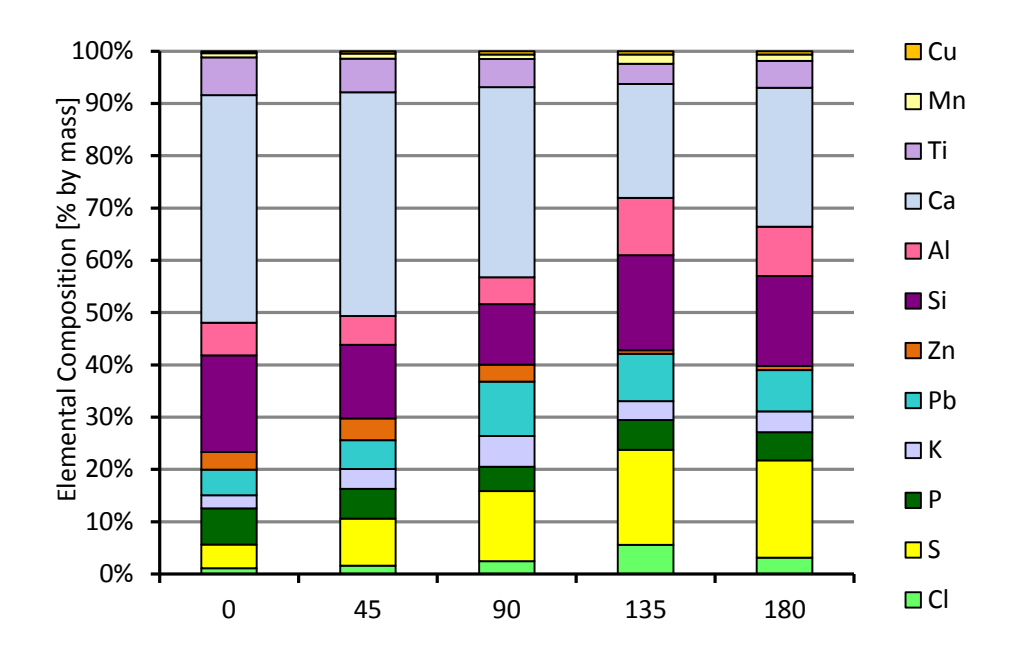


Figure 150. Elemental distribution on 16Mo3 sample (ring #3).

Appendix B Chemical composition of deposits on SH probe

1. Compositions of Deposits on SH-Reference

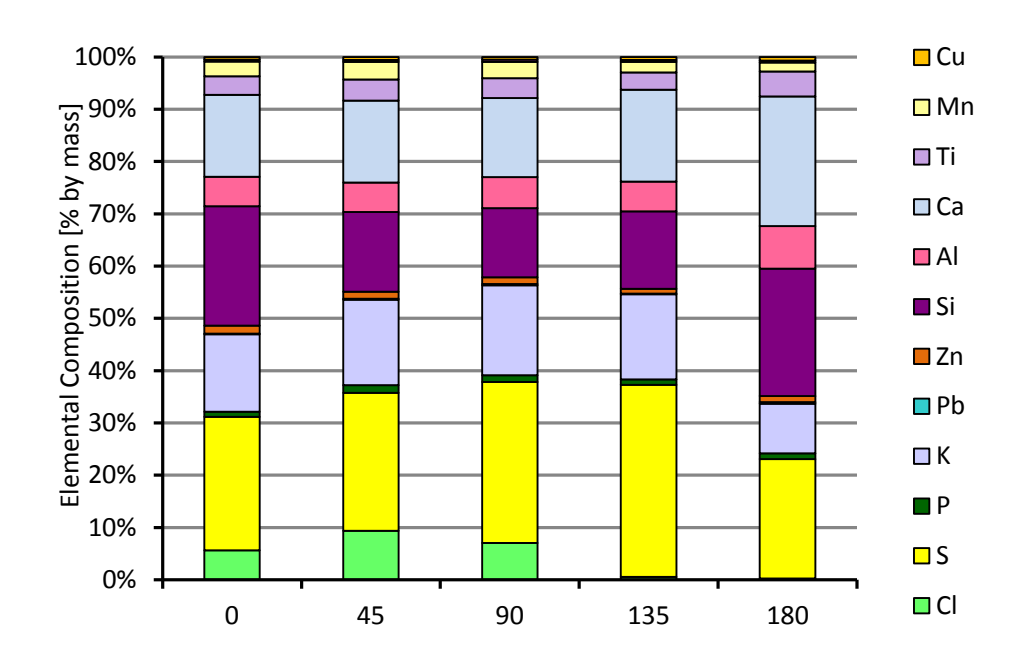


Figure 151. Elemental distribution on 16Mo3 sample.

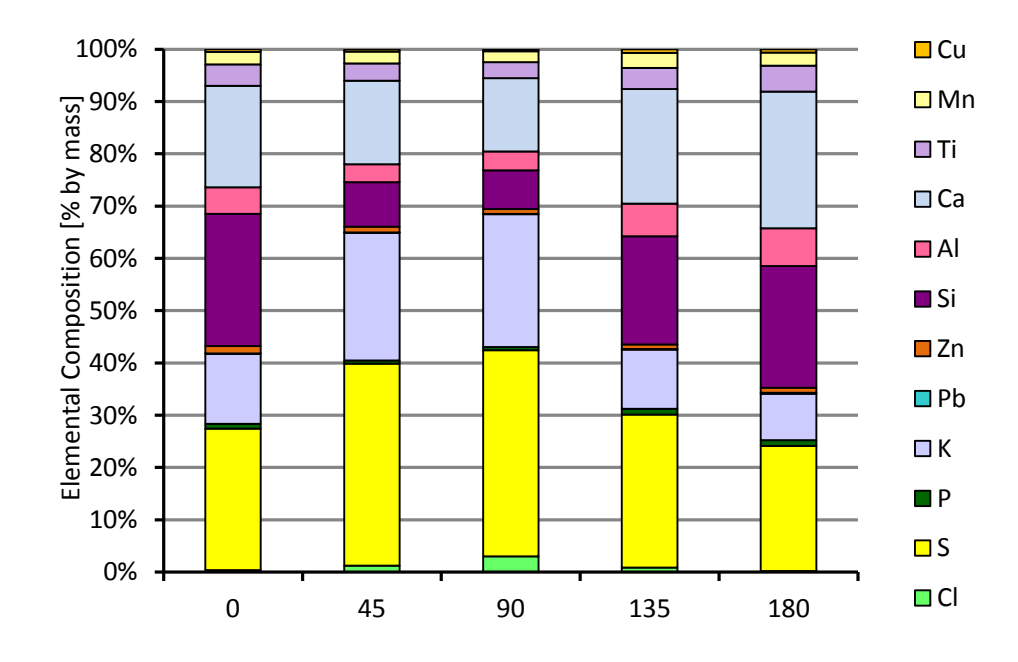


Figure 152. Elemental distribution on 253 MA sample.

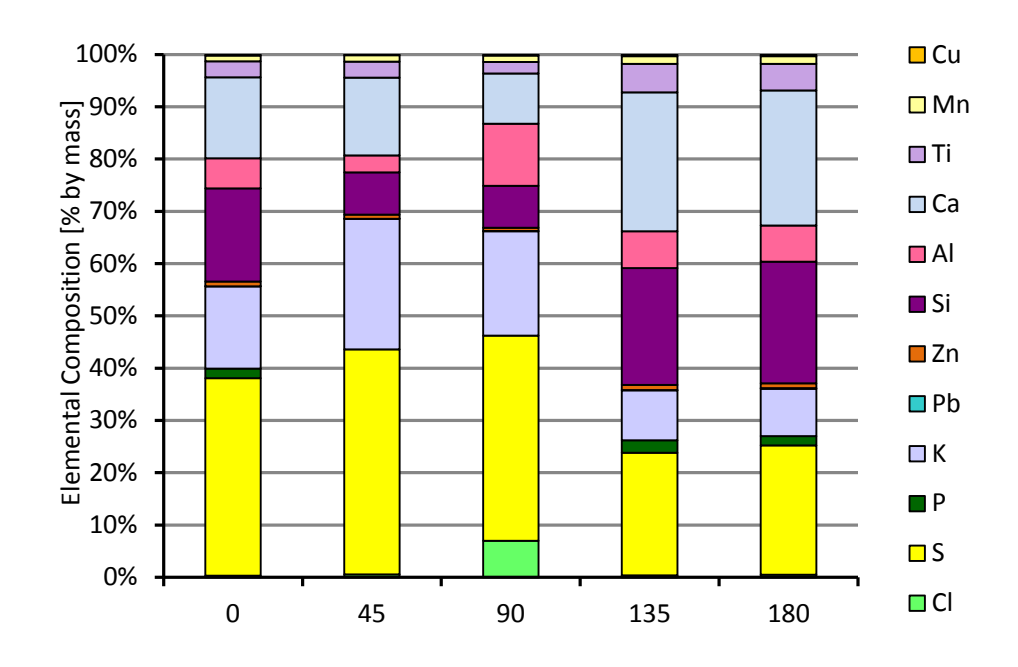


Figure 153. Elemental distribution on A1 sample.

2. Compositions of Deposits on SH-Foundry sand

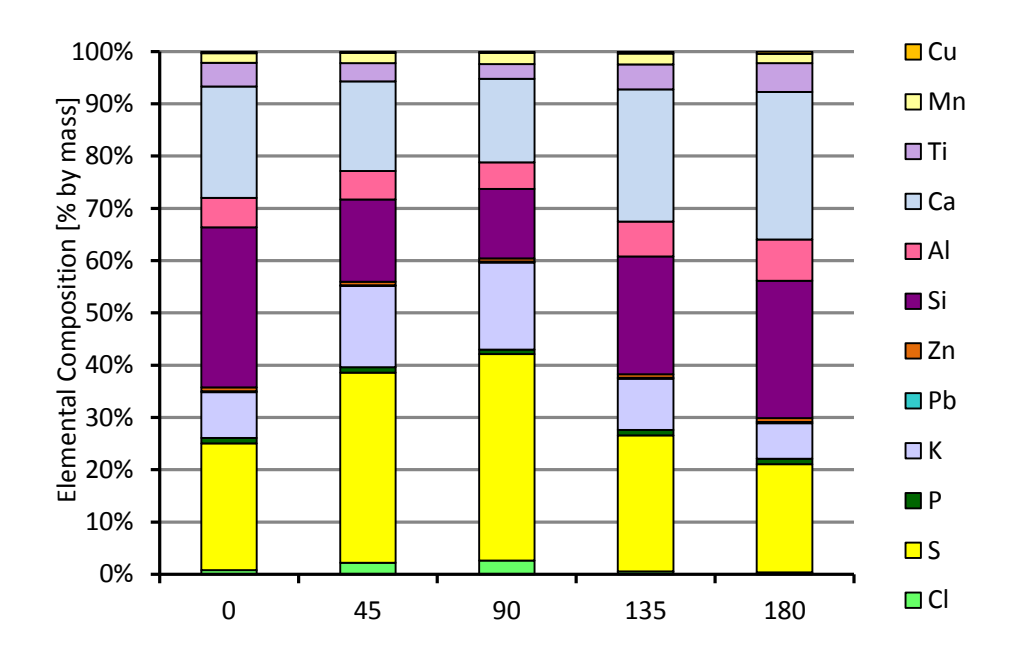


Figure 154. Elemental distribution on 16Mo3 sample.

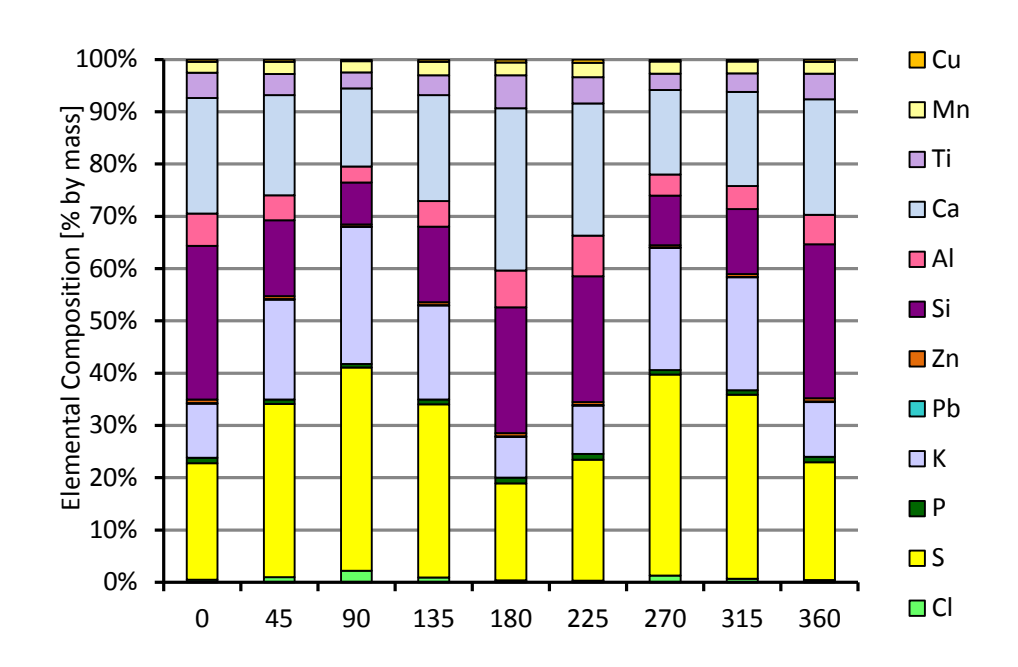


Figure 155. Elemental distribution on 253 MA sample.

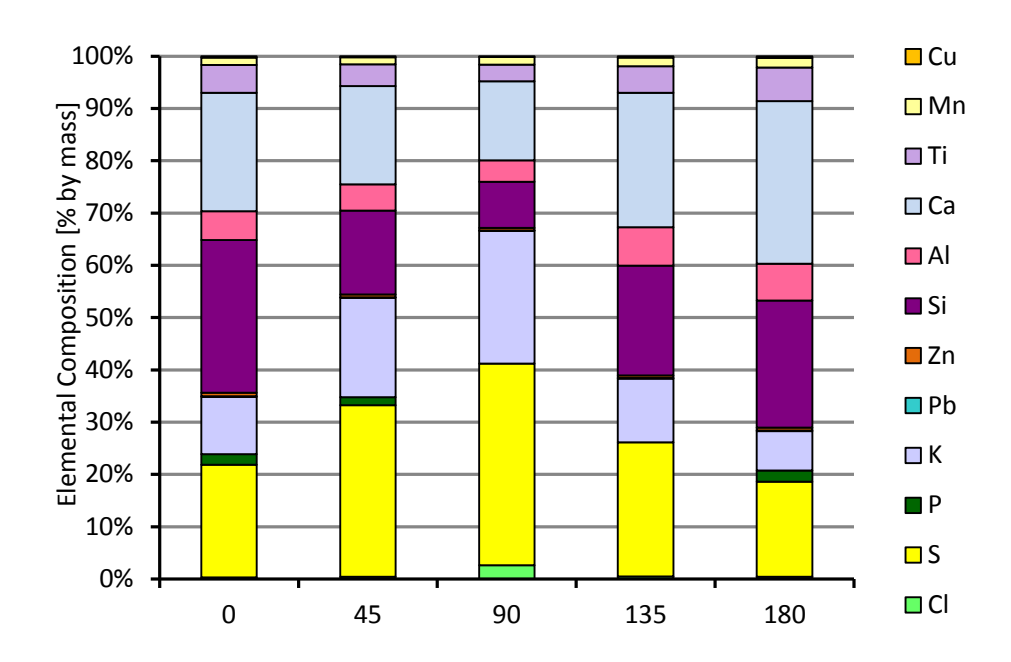


Figure 156. Elemental distribution on A1 sample.

3. Compositions of Deposits on SH-Kaolin

In this case, the XRF failed to provide a distribution of the deposits at all positions for the 16Mo3 deposits and at some positions for the other two materials.

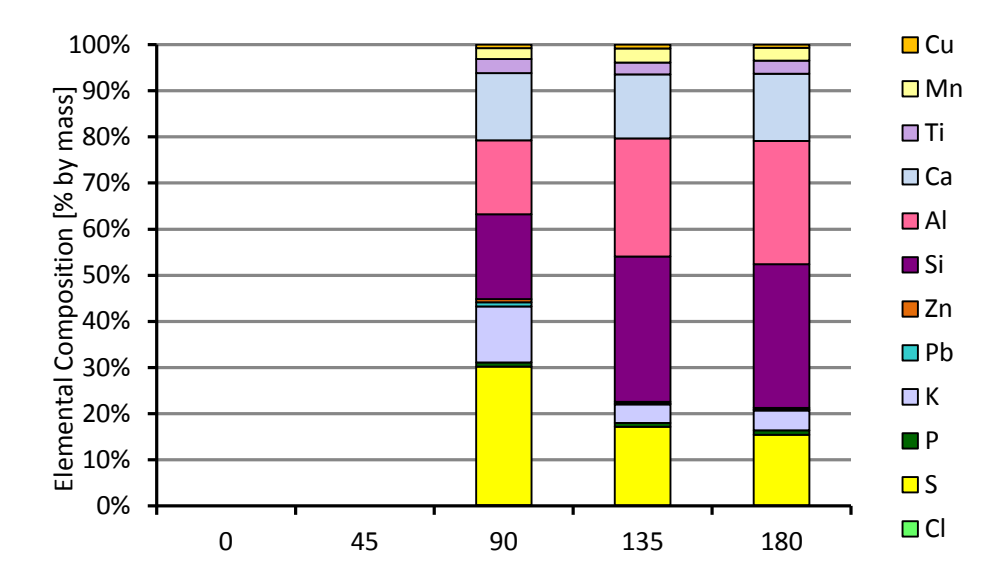


Figure 157. Elemental distribution on 253 MA sample.

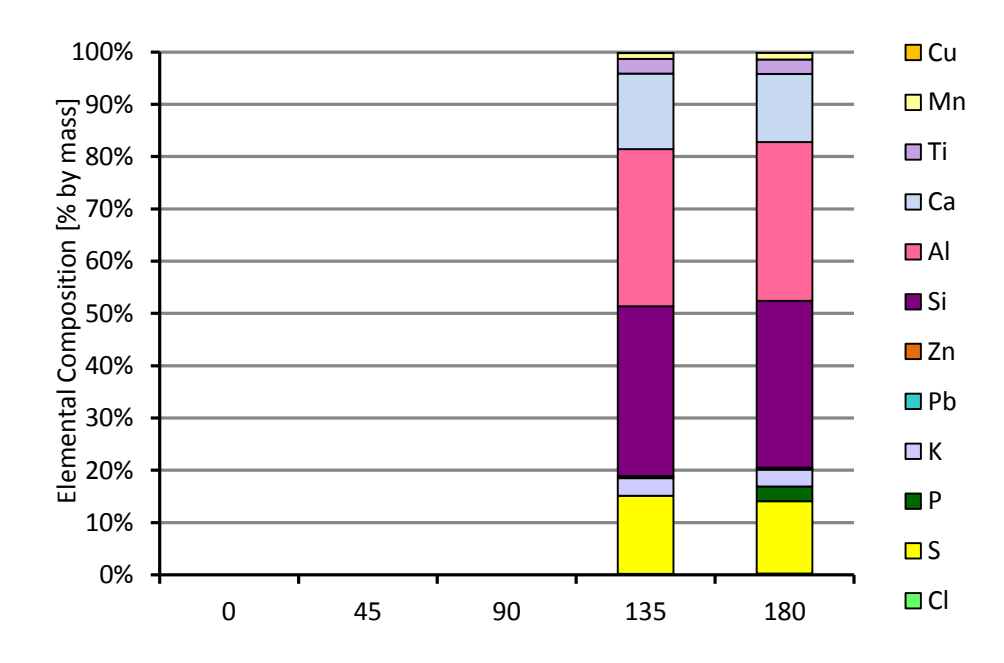


Figure 158. Elemental distribution on A1 sample.

4. Compositions of Deposits on SH-Lime

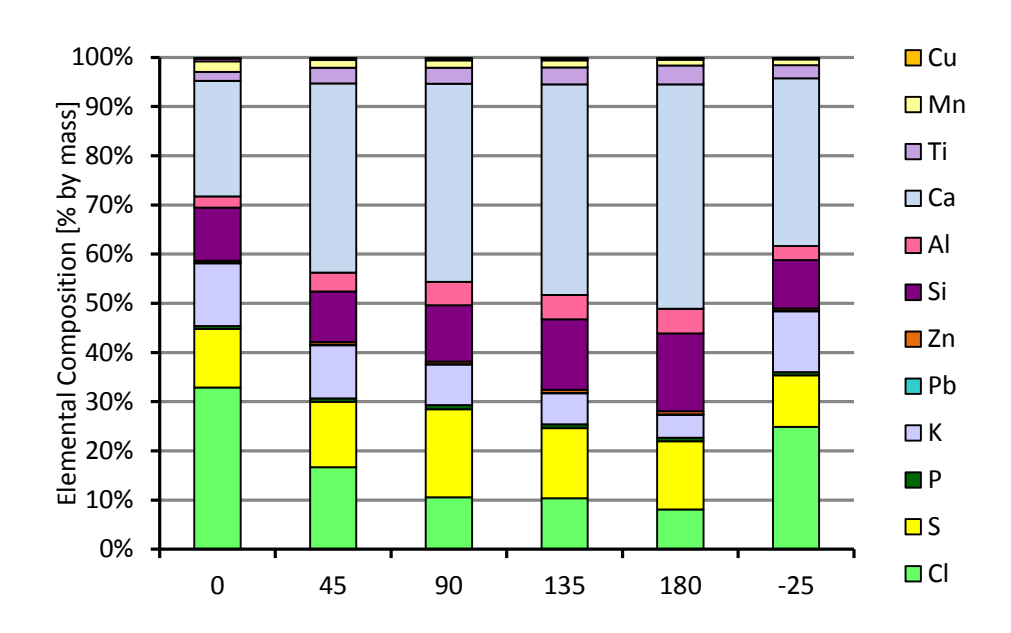


Figure 159. Elemental distribution on 16Mo3 sample. There was a large flake of deposits missing at 0°, a more representable distribution may be found at -25°.

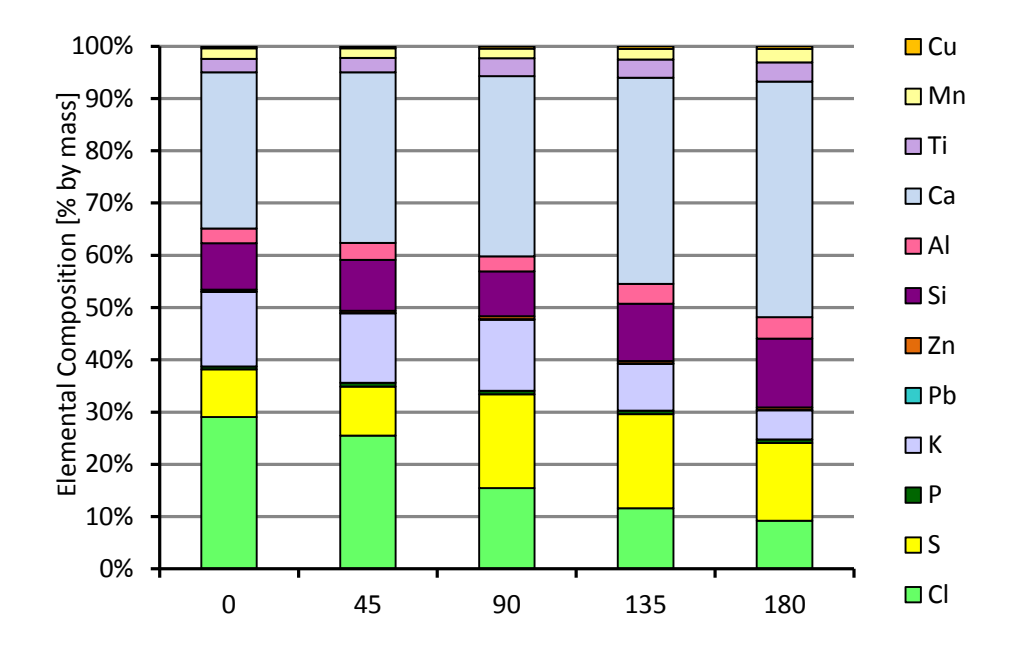


Figure 160. Elemental distribution on 253 MA sample.

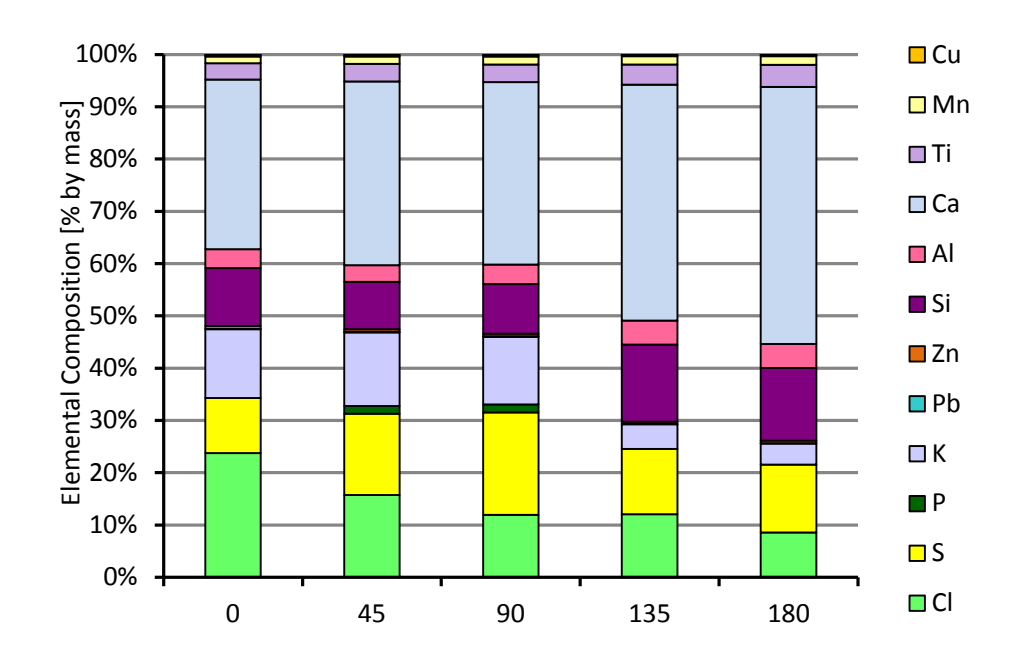


Figure 161. Elemental distribution on A1 sample.

5. Compositions of Deposits on SH-Sludge

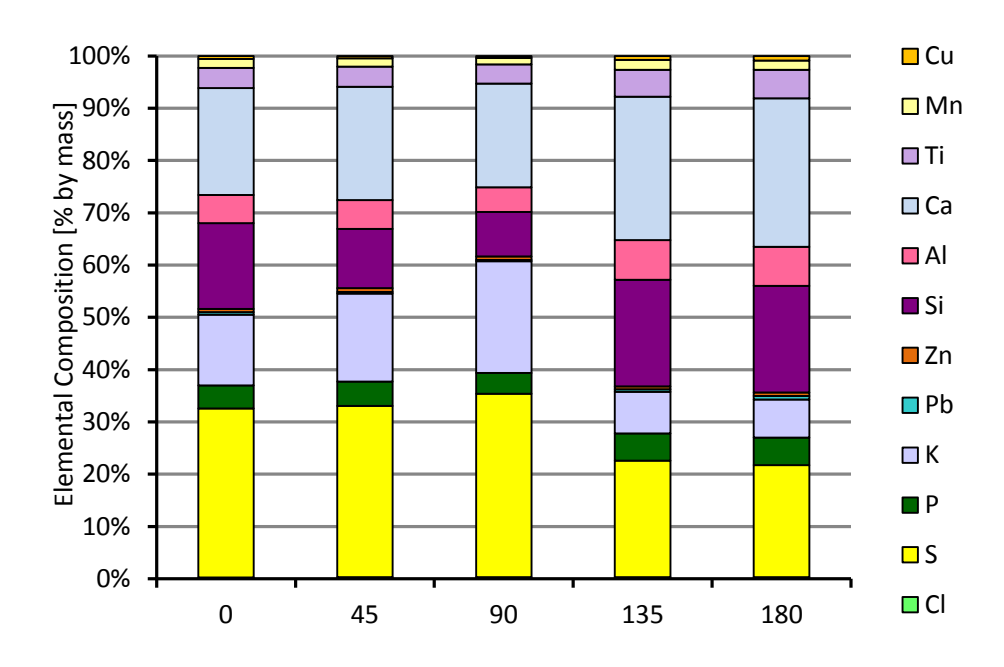


Figure 162. Elemental distribution on 16Mo3 sample.

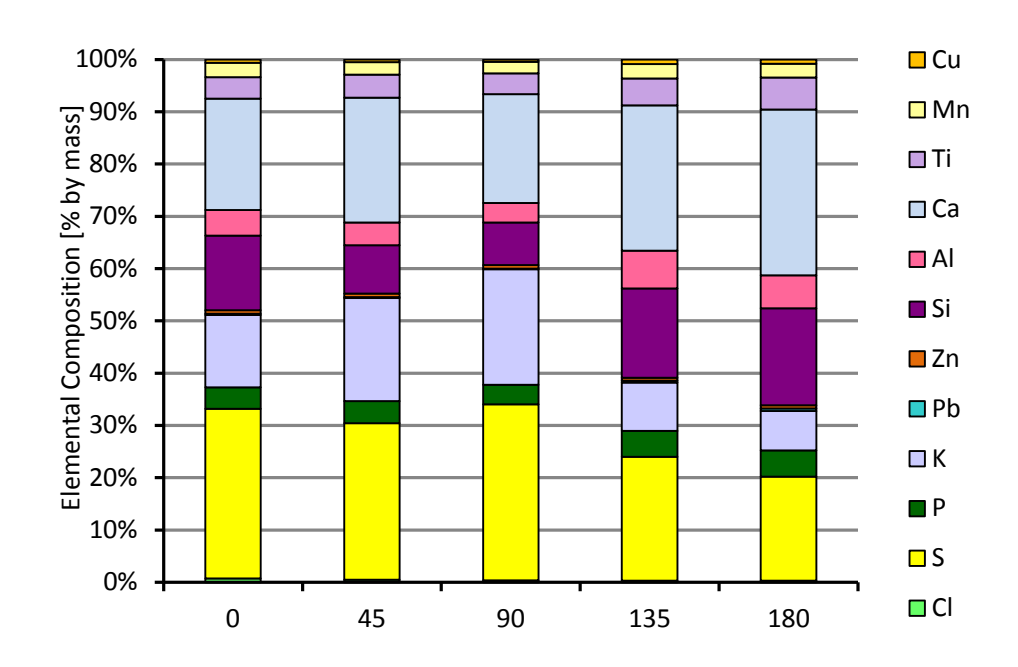


Figure 163. Elemental distribution on 253 MA sample.

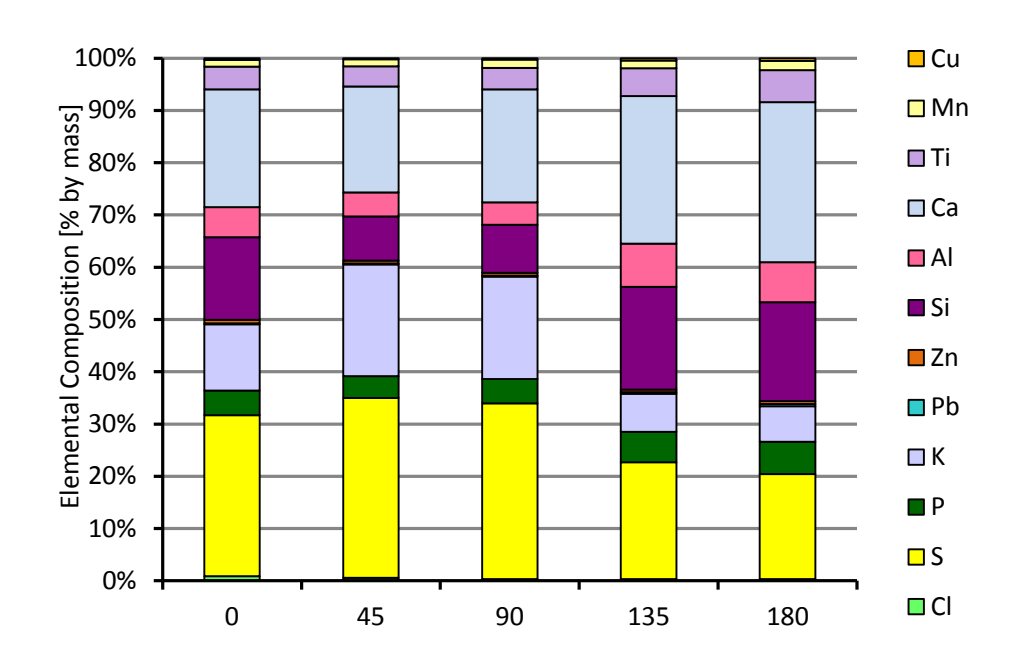


Figure 164. Elemental distribution on A1 sample.

6. Compositions of Deposits on SH-Sulphur

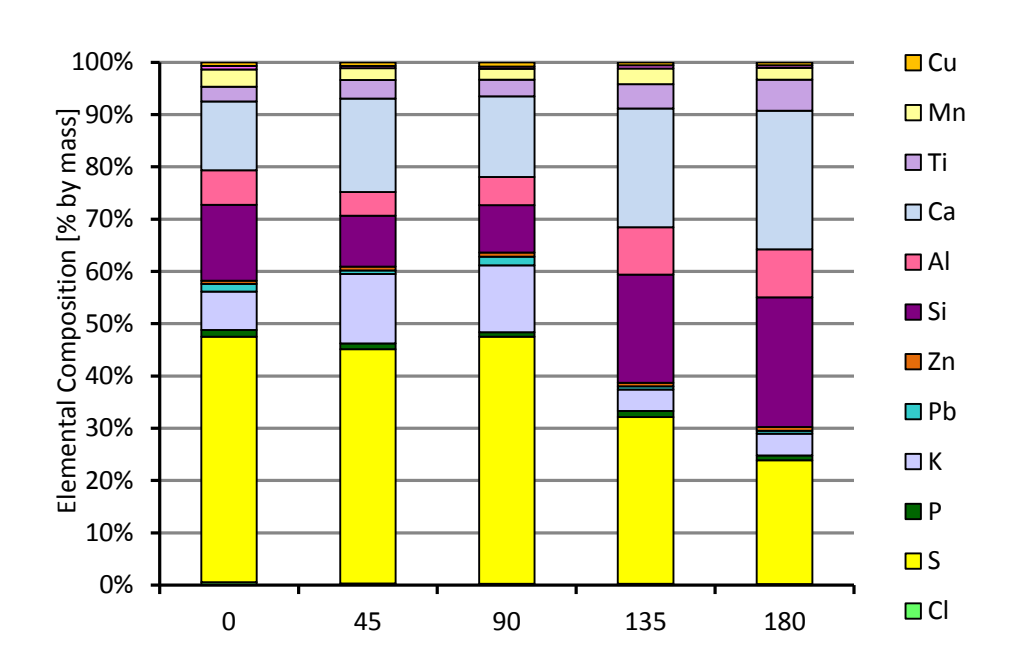


Figure 165. Elemental distribution on 16Mo3 sample.

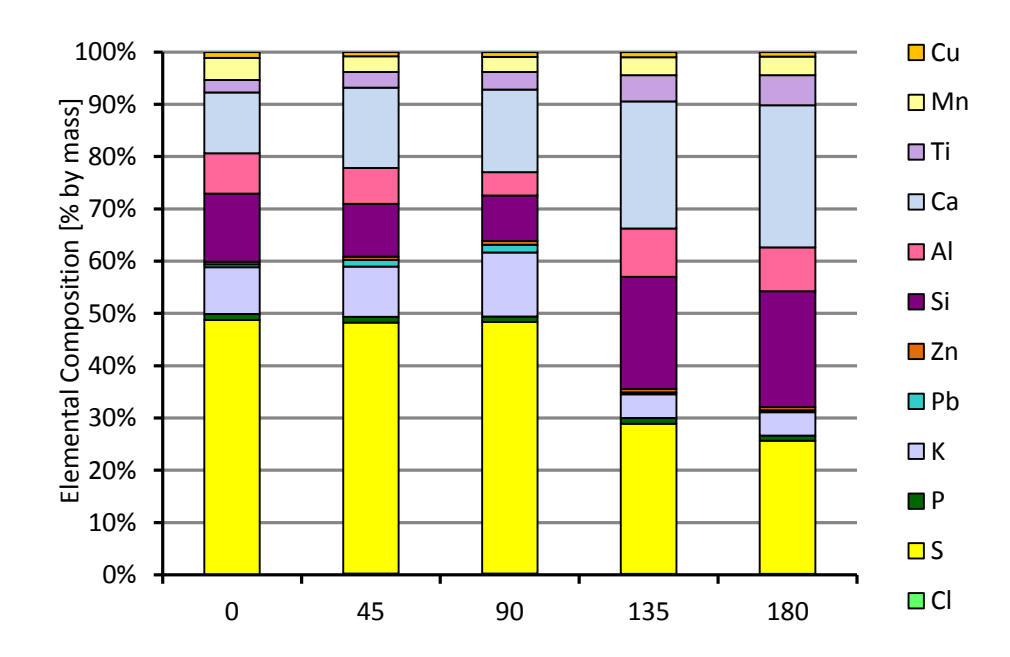


Figure 166. Elemental distribution on 253 MA sample.

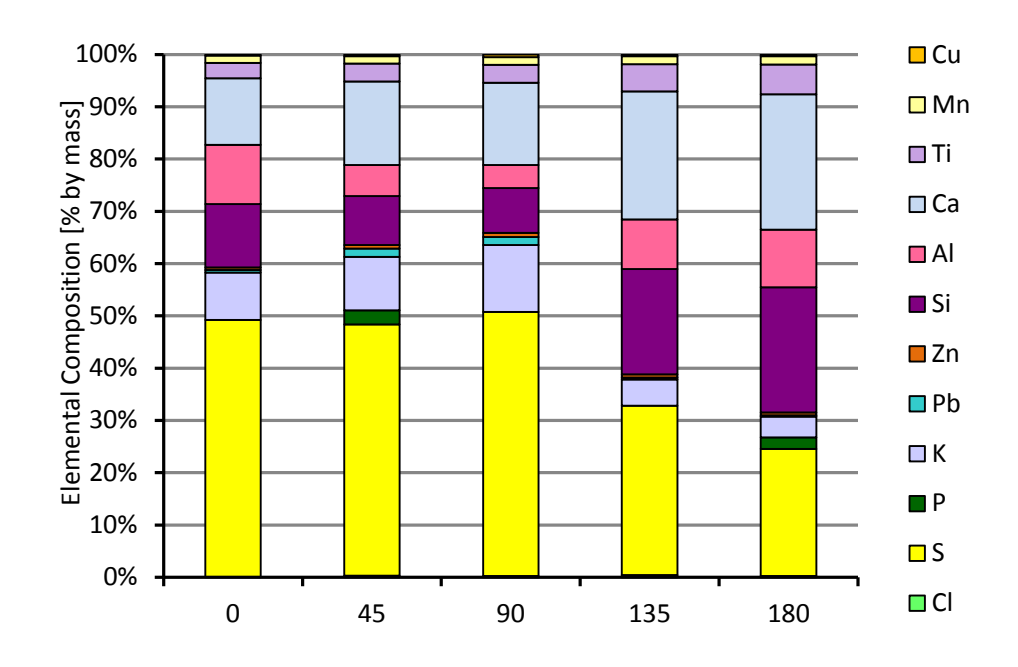


Figure 167. Elemental distribution on A1 sample.

7. Compositions of Deposits on SH-Ref 2

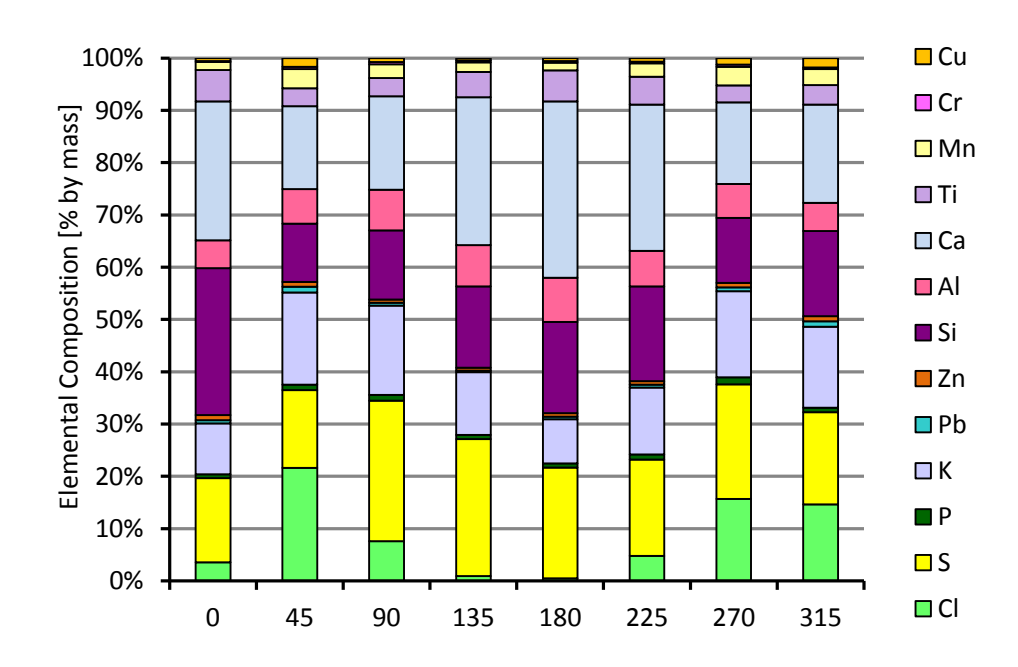


Figure 168. Elemental distribution on 16Mo3 sample (ring #1).

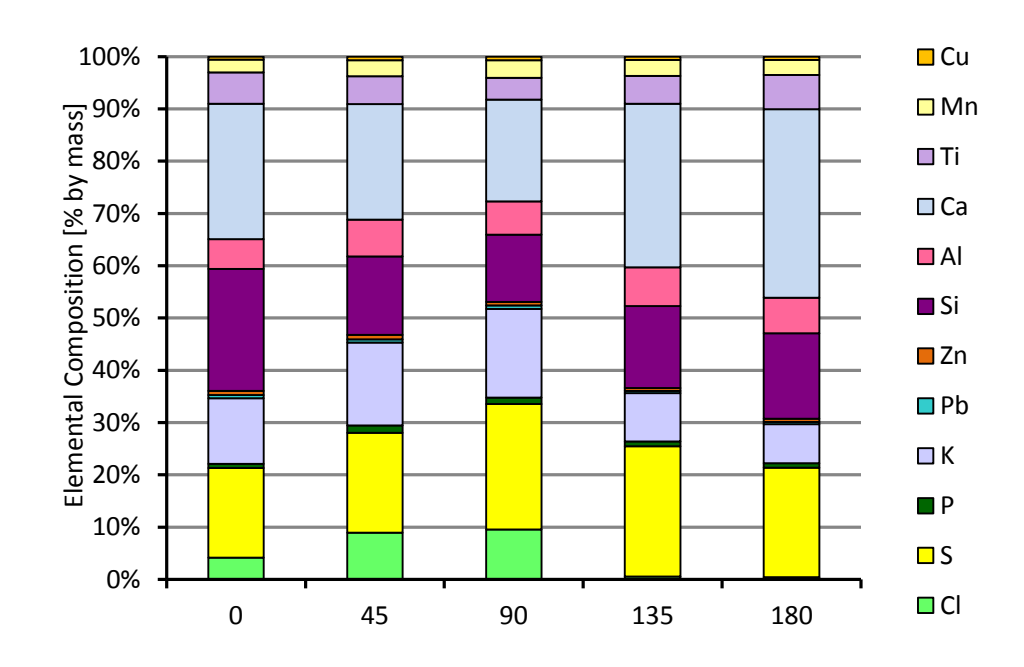


Figure 169. Elemental distribution on 253 MA sample (ring #2).

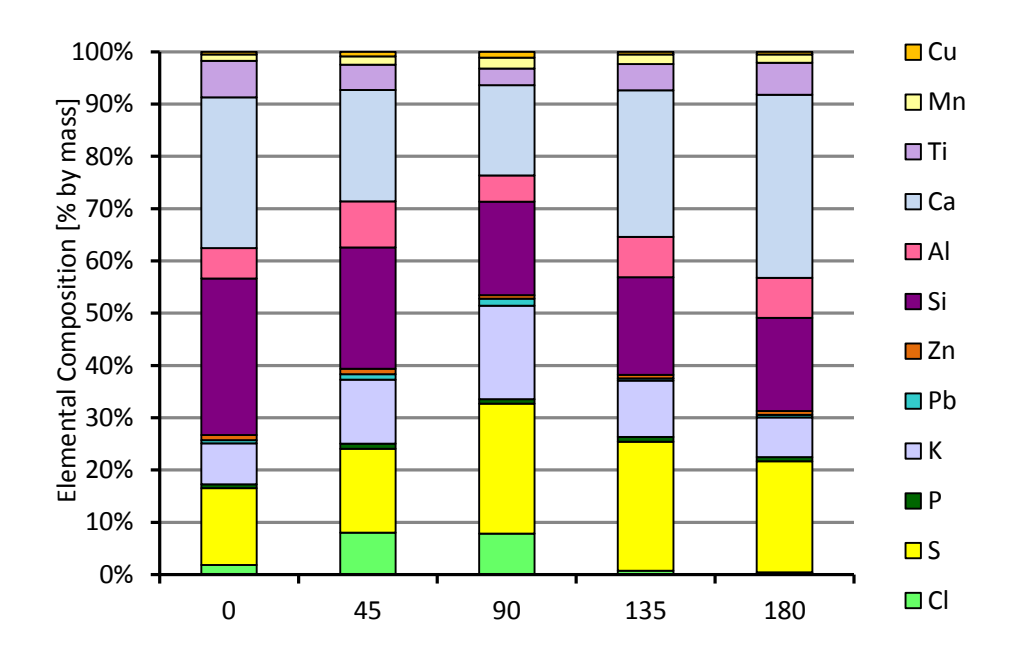


Figure 170. Elemental distribution on 16Mo3 sample (ring #3).

8. Compositions of Deposits on SH-SWS2

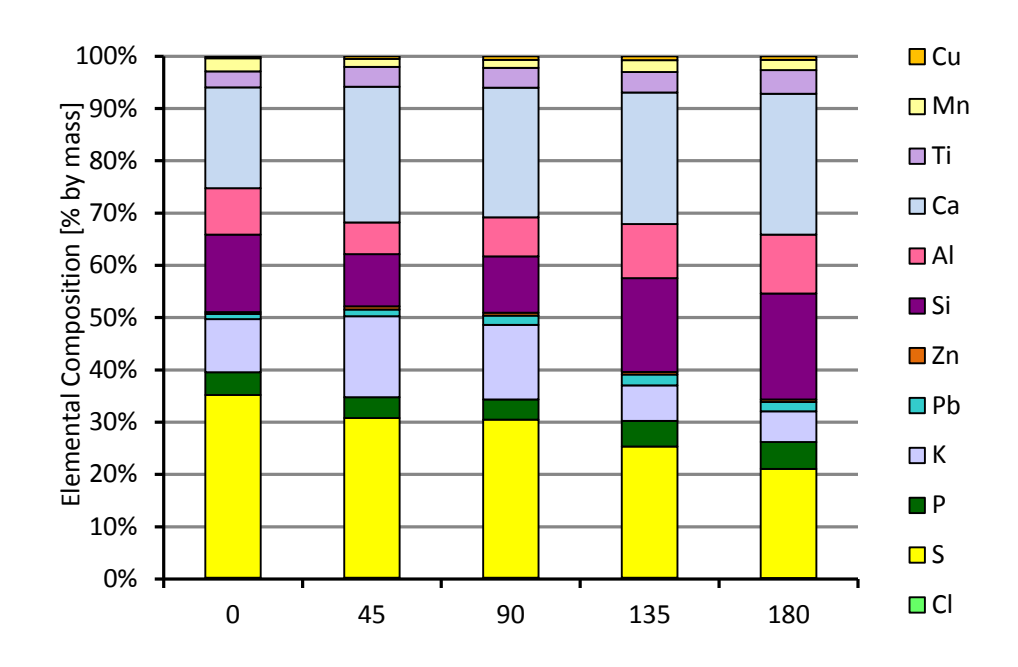


Figure 171. Elemental distribution on 16Mo3 sample (ring #1).

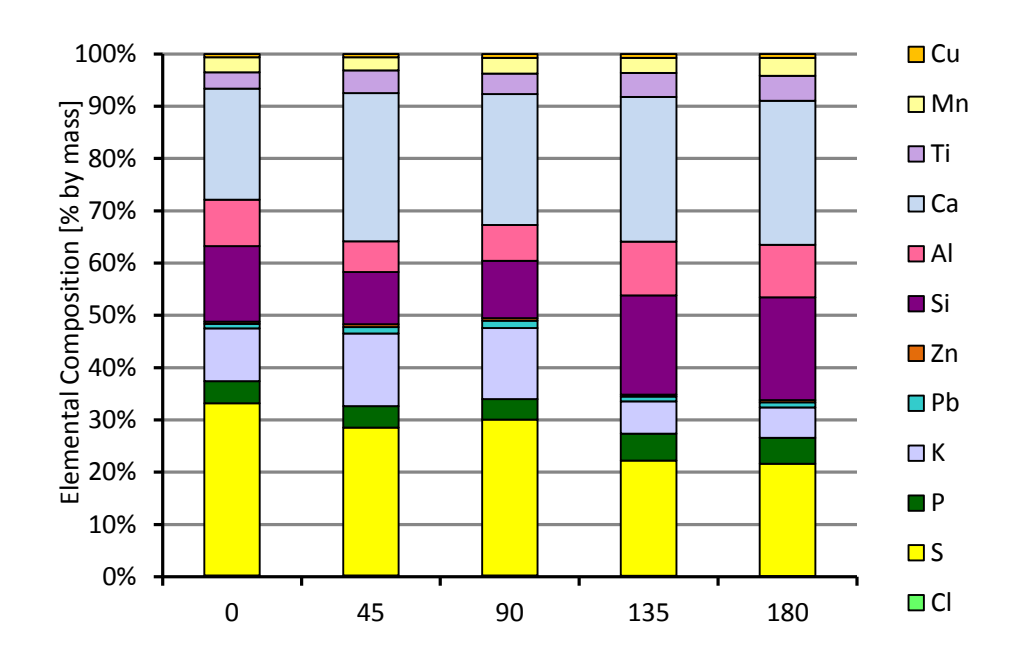


Figure 172. Elemental distribution on 253 MA sample (ring #2).

Figure 173.

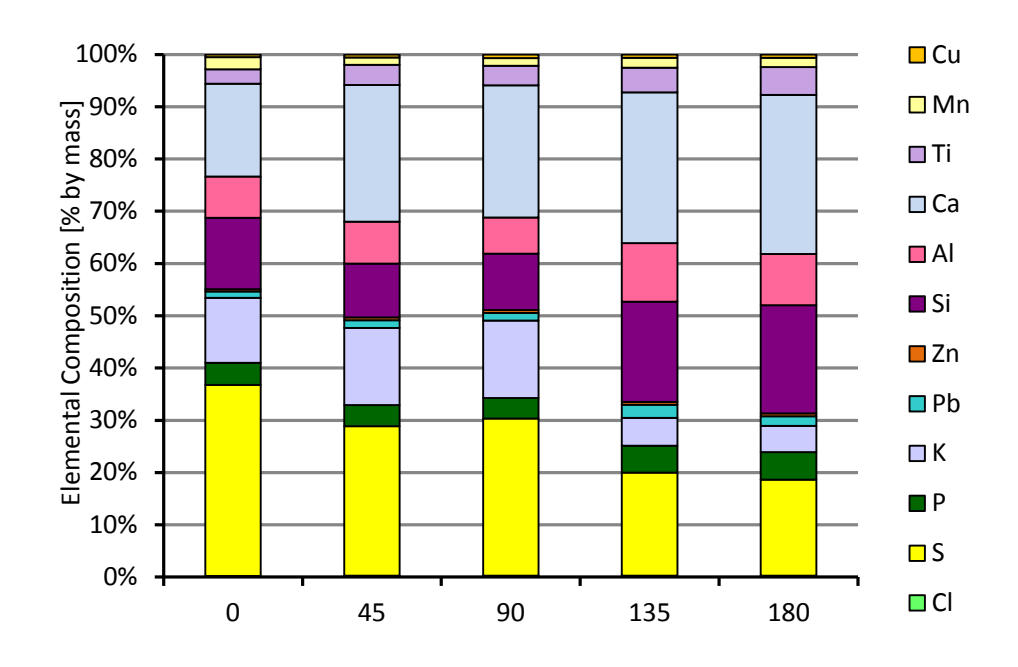


Figure 174. Elemental distribution on 16Mo3 sample (ring #3).

9. Compositions of Deposits on SH-PbO

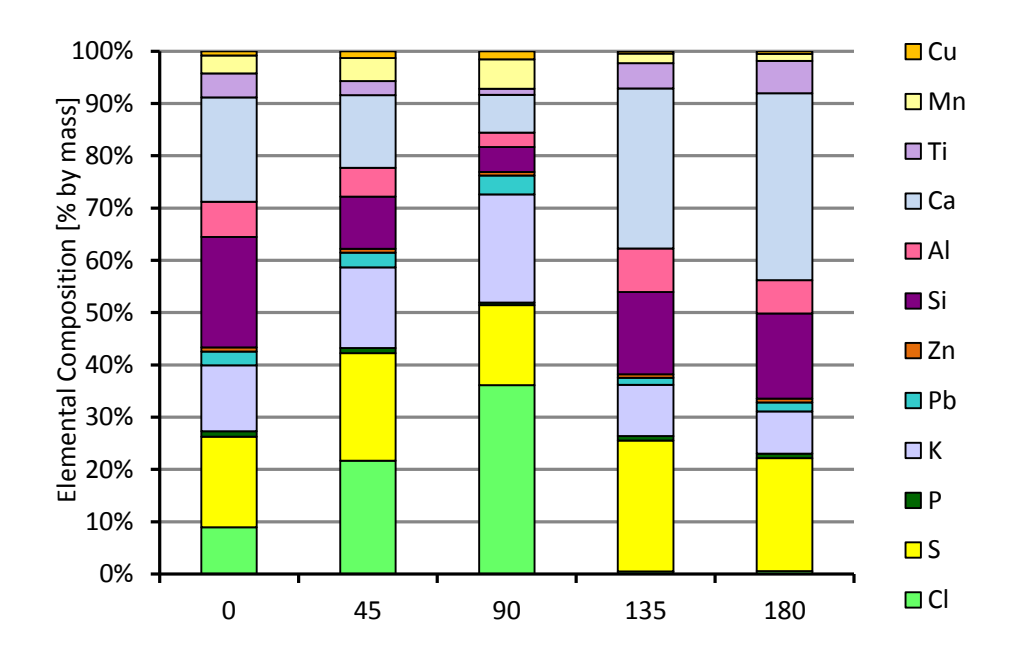


Figure 175. Elemental distribution on 16Mo3 sample (ring #1).

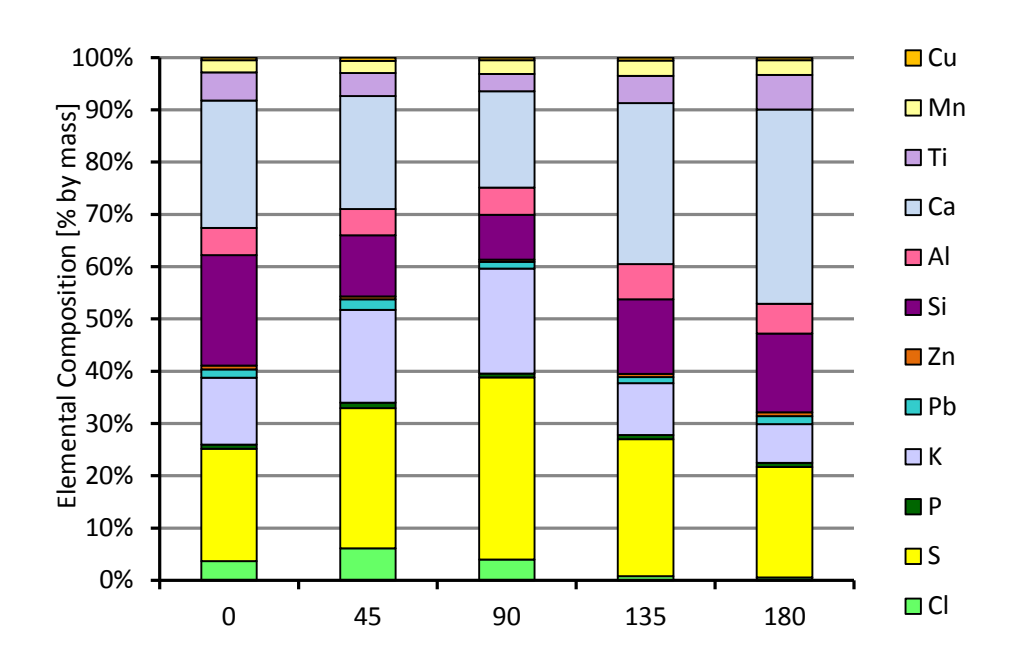


Figure 176. Elemental distribution on 253 MA sample (ring #2).

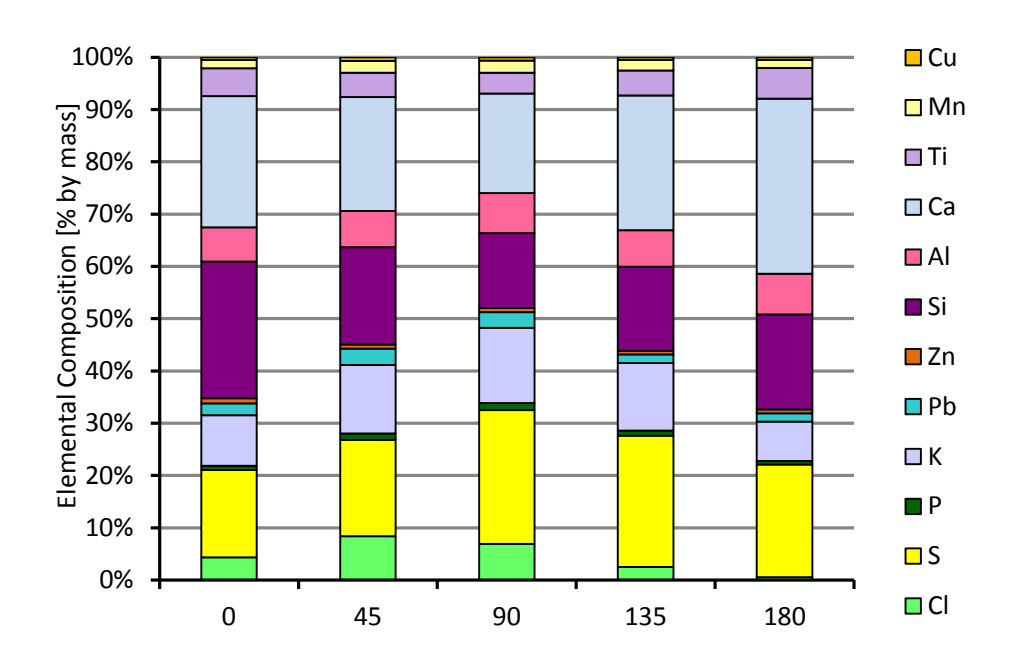


Figure 177. Elemental distribution on 16Mo3 sample (ring #3).

10. Compositions of Deposits on SH-PbO+SWS

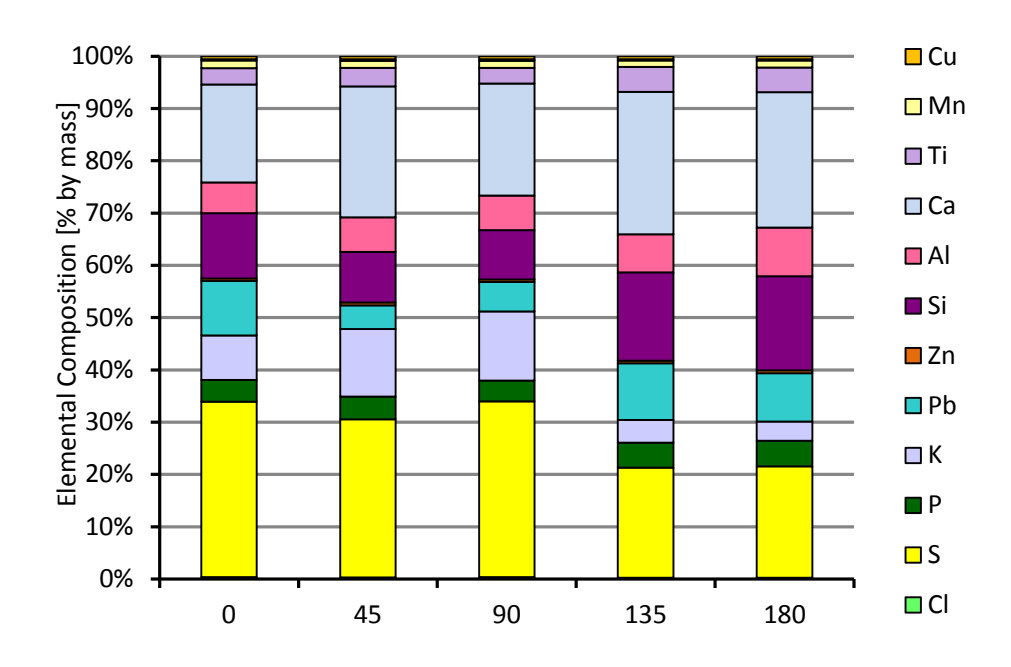


Figure 178. Elemental distribution on 16Mo3 sample (ring #1).

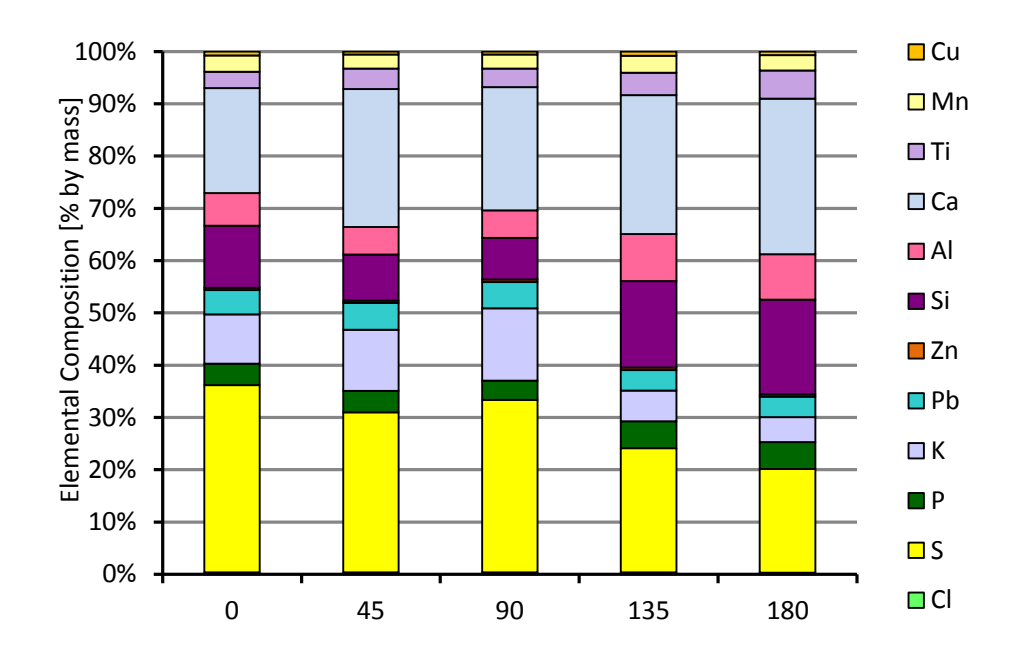


Figure 179. Elemental distribution on 253 MA sample (ring #2).

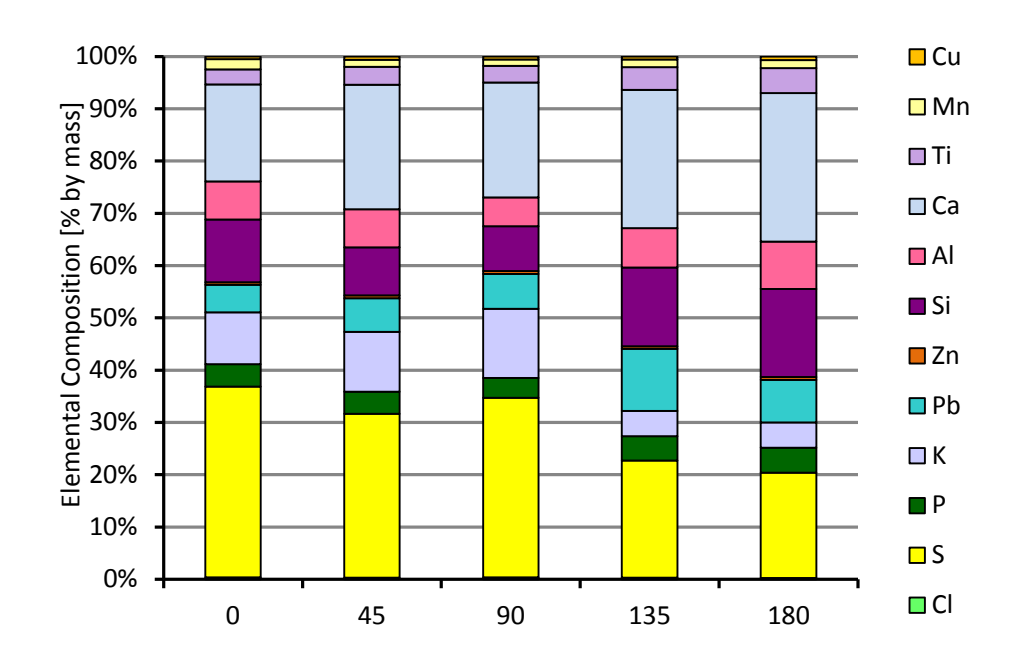


Figure 180. Elemental distribution on 16Mo3 sample (ring #3).

Appendix C Fuel analyses

Table 24. Fuel analyses

	Fuel after pelletisation	Original fuel sample	Sewage Sludge
Moisture %, a.r.	9,3	23,5	8,1
Ash %, d.f.	8,6	8,2	33,8
Cl %, d.f.	0,26	0,18	0,07
S %, d.f.	0,1	0,12	1,3
C %, d.f.	45,9	46,6	36,5
H %, d.f.	5,6	5,6	5,1
N %, d.f.	1,8	1,84	5,0
O %, d.f.	38	37,4	18,3
LHV MJ/kg, d.f.	18,54	17,3	15,1
Ash analysis			
Al %, of dry fuel	0,28	0,27	1,55
Si %, of dry fuel	2,31	2,5	3,59
Fe %, of dry fuel	0,40	0,37	5,23
Ti %, of dry fuel	0,16	0,20	0,51
Mn %, of dry fuel	0,01	0,02	0,02
Mg %, of dry fuel	0,10	0,12	0,40
Ca %, of dry fuel	0,72	0,81	2,29
Ba %, of dry fuel	0,03	0,06	
Na %, of dry fuel	0,22	0,28	0,19
K %, of dry fuel	0,17	0,16	0,35
P %, of dry fuel	0,02	0,02	2,67
Cu mg/kg dry fuel	44	38	254
V mg/kg dry fuel	6	7	16
Cr mg/kg dry fuel	39	46	29
Co mg/kg dry fuel	4	3	4
Ni mg/kg dry fuel	9	3	15
Zn mg/kg dry fuel	620	315	451
Pb mg/kg dry fuel	370	344	12
Cd mg/kg dry fuel	1	0,4	0,6
Mo mg/kg dry fuel	0,8	0,4	7
As mg/kg dry fuel	13	12	2

Table 25. Additives, as analyzed by handheld XRF

The sulphur used in the teste was sulphur flower of technical quality (min. 99% purity) provided by VWR.

Туре		Kaolin	Lime	Foundry Sand	Sludge
Pb	%, by mass a.r.	0	0	0	0
Zn	%, by mass a.r.	0	0	0,001	0,051
Cu	%, by mass a.r.	0	0	0	0,026
Ni	%, by mass a.r.	0	0	0	0
Fe	%, by mass a.r.	0,33	0,93	1,7	6,6
Mn	%, by mass a.r.	0	0,16	0	0
Cr	%, by mass a.r.	0,007	0,006	0,004	0,012
Ti	%, by mass a.r.	0,30	0,15	0,24	0,60
Са	%, by mass a.r.	0,00	38	1,3	3,1
K	%, by mass a.r.	0,00	0,65	0,93	0,34
Al	%, by mass a.r.	5,0	0,85	2,0	0,42
P	%, by mass a.r.	0,10	0,07	0,13	2,9
Si	%, by mass a.r.	13,2	4,5	20,7	2,5
Cl	%, by mass a.r.	0	0	0,04	0,08
S	%, by mass a.r.	0,05	0,18	0,51	3,3
Mg	%, by mass a.r.	0,00	0,48	0,10	0,00

Table 26. Fuel pellets as analyzed by handheld XRF.

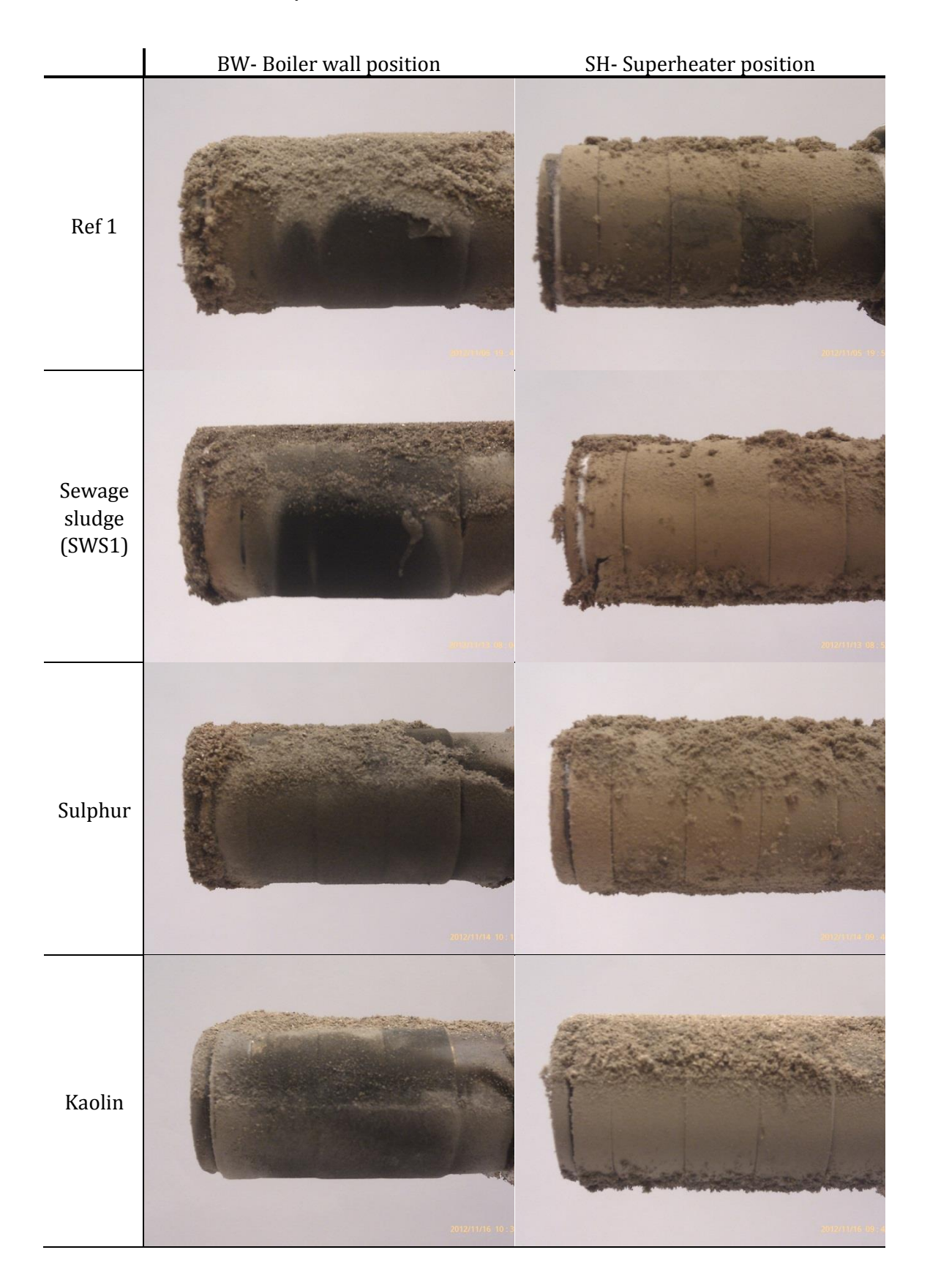
		Ref 1	FS	Као	Lime	SWS1	s	Ref 2	SWS2	PbO	PbO+ SWS
Pb	%, by mass a.r.	0,036	0,046	0,044	0,055	0,041	0,034	0,039	0,041	0,168	0,130
Zn	%, by mass a.r.	0,06	0,03	0,03	0,03	0,04	0,03	0,03	0,05	0,04	0,03
Cu	%, by mass a.r.	0,006	0,006	0,006	0,006	0,007	0,009	0,007	0,010	0,006	0,010
Fe	%, by mass a.r.	0,56	0,61	0,45	0,50	0,95	0,45	0,47	1,13	0,57	1,00
Cr	%, by mass a.r.	0,01	0,01	0,01	0,01	0,01	0,01	0,01	0,01	0,01	0,01
Ti	%, by mass a.r.	0,20	0,24	0,22	0,23	0,27	0,19	0,23	0,26	0,28	0,26
Ca	%, by mass a.r.	1,4	1,4	1,2	3,0	1,4	1,1	1,6	1,6	1,7	1,7
K	%, by mass a.r.	0,19	0,20	0,12	0,17	0,15	0,13	0,17	0,17	0,17	0,18
Αl	%, by mass a.r.	0,10	0,16	0,33	0,12	0,13	0,11	0,12	0,15	0,15	0,19
P	%, by mass a.r.	0,03	0,04	0,03	0,01	0,22	0,03	0,03	0,32	0,05	0,40
Si	%, by mass a.r.	1,2	1,9	1,6	1,0	0,9	0,8	1,2	1,0	1,4	1,3
Cl	%, by mass a.r.	0,30	0,26	0,27	0,29	0,30	0,29	0,36	0,38	0,40	0,29
S	%, by mass a.r.	0,34	0,36	0,29	0,33	0,43	3,27	0,40	0,53	0,49	0,68

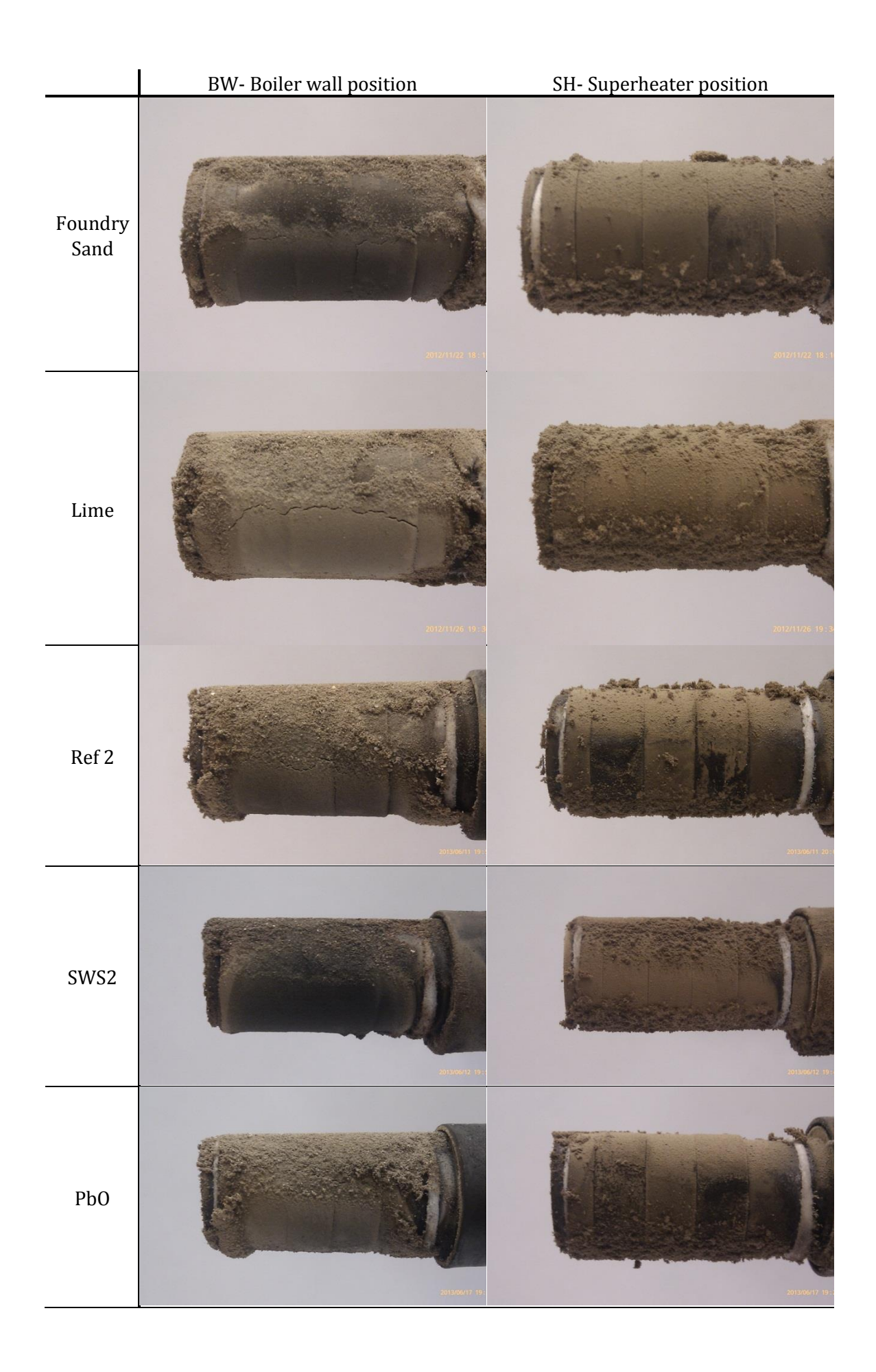
Table 27. Analysis of foundry sand provided by supplier

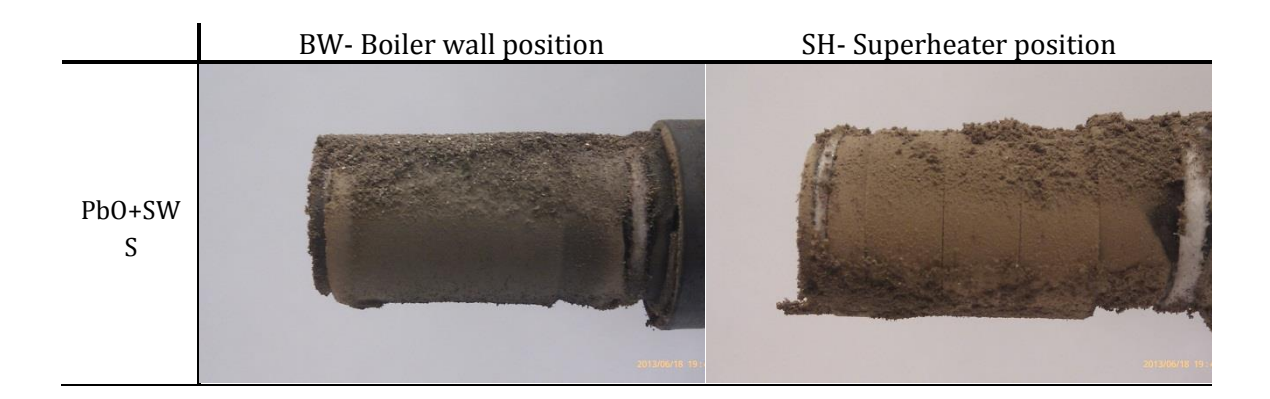
		Foun	dry Sand	Sewage Sludge		
		Min	Max			
Moisture	%, a.r.	0,2	2,8	8,1		
Ash	%, d.f.	96,2	97,1	33,8		
Cl	%, d.f.	<0,05	<0,05	0,07		
S	%, d.f.	0,01	0,06	1,3		
С	%, d.f.		3,3	36,5		
Н	%, d.f.			5,1		
N	%, d.f.		0,07	5,0		
0	%, d.f.			18,3		
LHV	MJ/kg, d.f.			15,1		
Ash-						
analysis						
Al	%, of dry fuel	0,39	0,67	1,55		
Si	%, of dry fuel			3,59		
Fe	%, of dry fuel	0,3	0,7	5,23		
Ti	%, of dry fuel			0,51		
Mn	%, of dry fuel	0,01	0,02	0,02		
Mg	%, of dry fuel	0,13	0,21	0,40		
Ca	%, of dry fuel	0,2	0,43	2,29		
Ва	%, of dry fuel					
Na	%, of dry fuel	0,17	0,2	0,19		
K	%, of dry fuel	0,02	0,14	0,35		
Р	%, of dry fuel	0,01	0,02	2,67		
Cu	mg/kg dry fuel	5	31	254		
V	mg/kg dry fuel	9	13	16		
Cr	mg/kg dry fuel	3	16	29		
Co	mg/kg dry fuel	2	2	4		
Ni	mg/kg dry fuel	3	16	15		
Zn	mg/kg dry fuel	11	160	451		
Pb	mg/kg dry fuel	3	5	12		
Cd	mg/kg dry fuel	0,04	0,1	0,6		
Мо	mg/kg dry fuel			7		
As	mg/kg dry fuel	0,6	1,4	2		

Foundry sand, average particle size about 0,25 mm, bentonite content 4,1-7 %.

Appendix D Photos of deposit probes directly after exposure







Appendix E XRD Diffraction Spectra

The raw data diffraction spectra from the analyses are given below. Pole spectra of identified compounds are added to the plots for reference. There are substantial background noises in the spectra, indicating the presence of non-crystalline materials in the samples alongside the identified compounds.

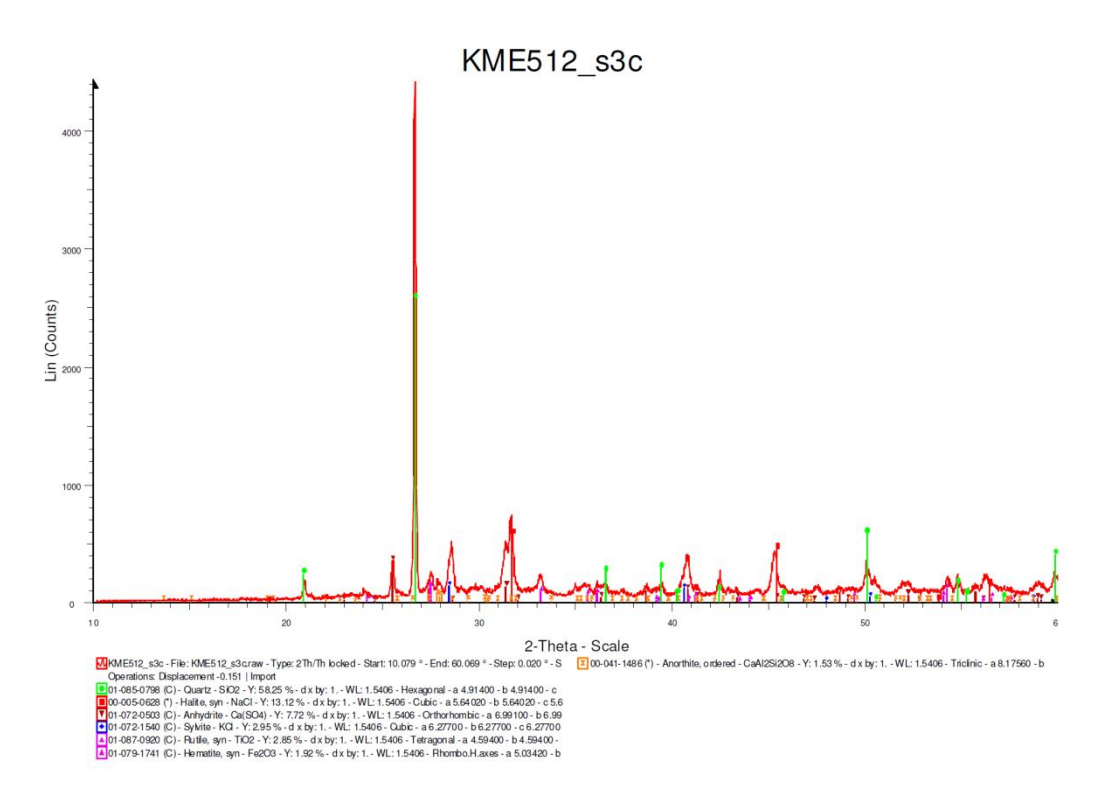


Figure 181. XRD-spectrum obtained from sample of loose deposits on BW probe, Ref 2.

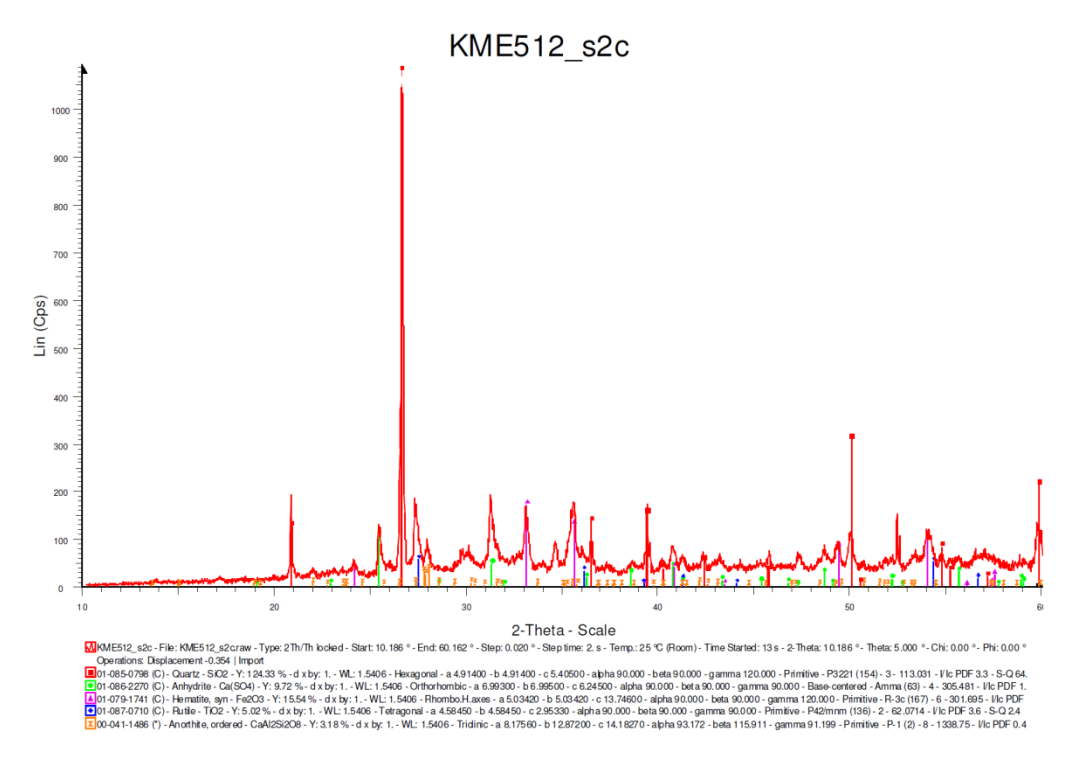


Figure 182. XRD-spectrum obtained from sample of loose deposits on BW probe, SWS2.

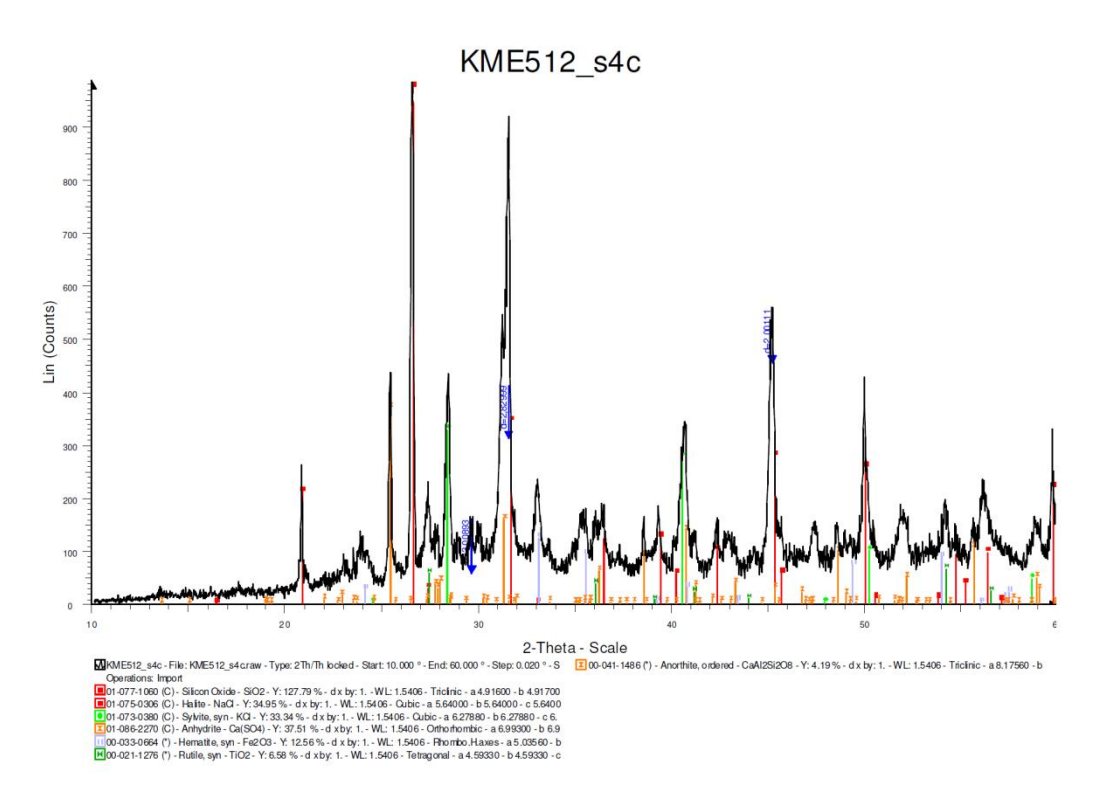


Figure 183. XRD-spectrum obtained from sample of loose deposits on BW probe, PbO.

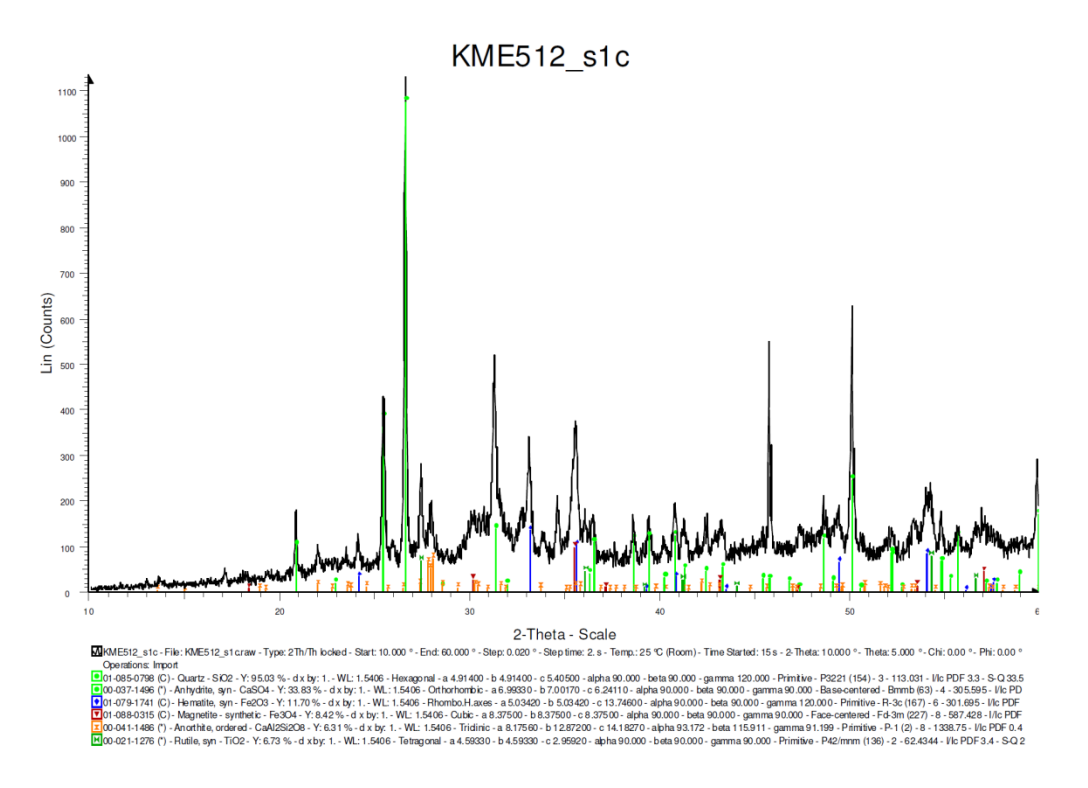


Figure 184. XRD-spectrum obtained from sample of loose deposits on BW probe, PbO+SWS.

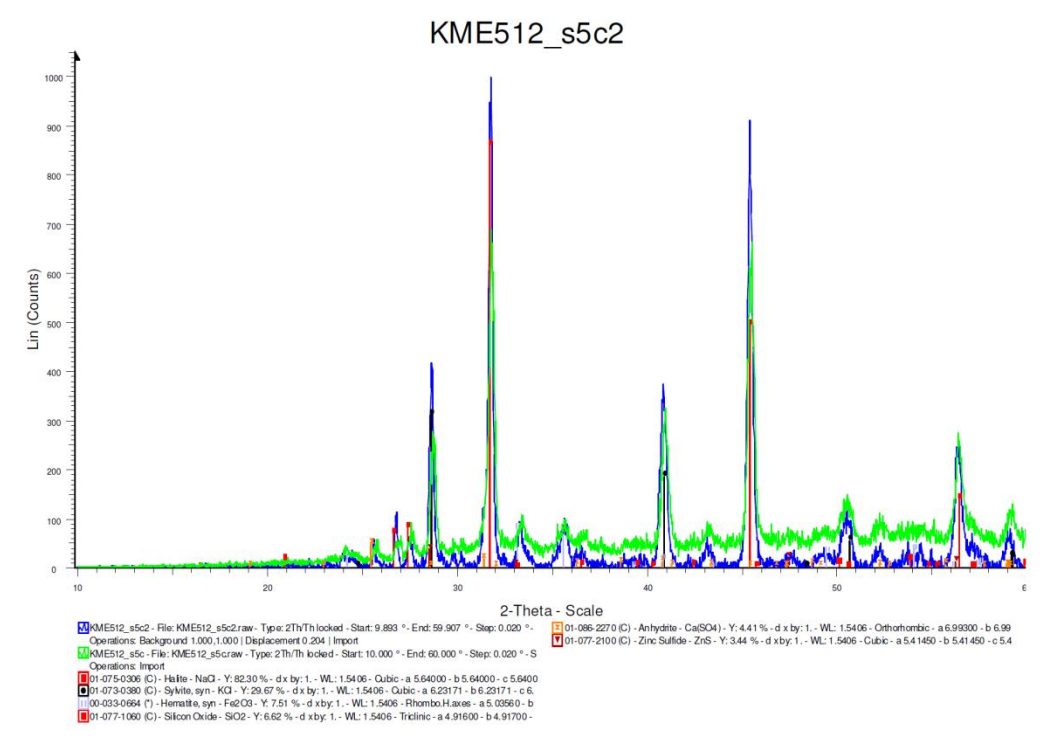


Figure 185. XRD-spectra obtained from sample of hard deposits on BW probe, PbO. Green line) milled sample, Blue Line) Non-milled sample with background subtracted to differentiate the graphs.

SP Technical Research Institute of Sweden

Our work is concentrated on innovation and the development of value-adding technology. Using Sweden's most extensive and advanced resources for technical evaluation, measurement technology, research and development, we make an important contribution to the competitiveness and sustainable development of industry. Research is carried out in close conjunction with universities and institutes of technology, to the benefit of a customer base of about 10000 organisations, ranging from start-up companies developing new technologies or new ideas to international groups.

